NASA TECHNICAL NOTE

NASA TN D-8332 c.1

NASA TN D-8332

TECH LIBRARY KAFB, NM
0134021

LOAN COPY: RETURN TO
AFWL TECHNICAL LIBRARY
KIRTLAND AFB, N. M.

BEHAVIOR OF AIRCRAFT ANTISKID BRAKING SYSTEMS ON DRY AND WET RUNWAY SURFACES

A Velocity-Rate-Controlled, Pressure-Bias-Modulated System

Sandy M. Stubbs and John A. Tanner

Langley Research Center
Hampton, Va. 23665

NATIONAL AERONAUTICS AND SPACE ADMINISTRATION • WASHINGTON, D. C. • DECEMBER 1976

TECH LIBRARY KAFB, NM

0134021

1. Report No.
NASA TN D-8332

2. Government Accession No.

3. Recipient's Catalog No.

4. Title and Subtitle
BEHAVIOR OF AIRCRAFT ANTISKID BRAKING SYSTEMS ON DRY AND WET RUNWAY SURFACES - A VELOCITY-RATE-CONTROLLED, PRESSURE-BIAS-MODULATED SYSTEM

5. Report Date
December 1976

6. Performing Organization Code

7. Author(s)
Sandy M. Stubbs and John A. Tanner

8. Performing Organization Report No.
L-10976

9. Performing Organization Name and Address
NASA Langley Research Center
Hampton, VA 23665

10. Work Unit No.
505-08-31-01

11. Contract or Grant No.

12. Sponsoring Agency Name and Address
National Aeronautics and Space Administration
Washington, DC 20546

13. Type of Report and Period Covered
Technical Note

14. Sponsoring Agency Code

15. Supplementary Notes

16. Abstract

An experimental investigation was conducted to study the braking and cornering response of a velocity-rate-controlled, pressure-bias-modulated, aircraft antiskid braking system on dry and wet runway surfaces. The investigation was conducted at the Langley aircraft landing loads and traction facility with one main wheel, brake, and tire assembly of a McDonnell Douglas DC-9 series 10 aircraft.

During maximum braking the average ratio of drag-force friction coefficient developed by the antiskid system to maximum drag-force friction coefficient available at the tire/runway interface was higher on dry surfaces than on wet surfaces; this drag-force ratio was not adversely affected by yaw angles up to 6°. The gross stopping power generated by the brake system on the dry surface was more than twice that obtained on the wet surfaces. With maximum braking applied, the average ratio of side-force friction coefficient developed by the tire under antiskid control to maximum side-force friction coefficient available at the tire/runway interface of a free-rolling yawed tire was shown to decrease with increasing yaw angle; but even with this lower performance ratio, the higher yaw angle gave greater cornering even power.

Braking reduced the side-force friction coefficient on a dry surface by 75 percent as the wheel slip ratio was increased to 0.3; on a flooded surface the coefficient dropped to near zero for the same slip ratio. Locked wheel skids were observed when the tire encountered a runway surface transition from dry to flooded, due in part to the response time required for the system to sense abrupt changes in the runway friction; however, the antiskid system quickly responded by reducing brake pressure and cycling normally during the remainder of the run on the flooded surface.

17. Key Words (Suggested by Author(s))
Cornering
Aircraft tires
Antiskid braking system

18. Distribution Statement
Unclassified - Unlimited

Subject Category 05

19. Security Classif. (of this report)	20. Security Classif. (of this page)	21. No. of Pages	22. Price*
Unclassified	Unclassified	129	$5.75

*For sale by the National Technical Information Service, Springfield, Virginia 22161

CONTENTS

BEHAVIOR OF AIRCRAFT ANTISKID BRAKING SYSTEMS ON DRY AND WET RUNWAY SURFACES

A VELOCITY-RATE-CONTROLLED, PRESSURE-BIAS-MODULATED SYSTEM

Sandy M. Stubbs and John A. Tanner
Langley Research Center

SUMMARY

An experimental investigation was conducted to study the braking and cornering response of a velocity-rate-controlled, pressure-bias-modulated aircraft antiskid braking system on dry and wet runway surfaces. The investigation was conducted at the Langley aircraft landing loads and traction facility with one main wheel, brake, and tire assembly of a McDonnell Douglas DC-9 series 10 aircraft.

During maximum braking, the average ratio of drag-force friction coefficient developed by the antiskid system to maximum drag-force friction coefficient available at the tire/runway interface was higher on dry surfaces than on wet surfaces; this drag-force ratio was not adversely affected by yaw angles up to 6°. The gross stopping power generated by the brake system on the dry surface was more than twice that obtained on the wet surfaces. With maximum braking applied, the average ratio of side-force friction coefficient developed by the tire under antiskid control to maximum side-force friction coefficient available at the tire/runway interface of a free-rolling yawed tire was shown to decrease with increasing yaw angle; but even with this lower performance ratio, the higher yaw angle gave greater cornering power.

Braking reduced the side-force friction coefficient on a dry surface by 75 percent as the wheel slip ratio was increased to 0.3; on a flooded surface the coefficient dropped to near zero for the same slip ratio. Locked wheel skids were observed when the tire encountered a runway surface transition from dry to flooded, due in part to the response time required for the system to sense abrupt changes in runway friction; however, the antiskid system quickly responded by reducing brake pressure and cycling normally during the remainder of the run on the flooded surface.

INTRODUCTION

Over the years the number and variety of aircraft using antiskid systems has steadily increased, with most current commercial and military jet airplanes being equipped with skid-control devices. The earliest antiskid systems were generally designed to prevent wheel lockups and excessive tire wear on dry pavements. Modern skid-control devices, however, are more sophisticated and are designed to provide maximum braking effort while maintaining full antiskid protection under all weather conditions. Operating statistics of modern jet aircraft indicate that these antiskid systems are both effective and dependable, and several million landings made each year in routine fashion with no serious operating problems attest to this fact. However, it has also been well established, both from flight tests and field experience, that the performance of these systems is subject to degradation when the runway becomes slippery; consequently, dangerously long rollout distances and reduced steering capability can result during some aircraft landing operations (refs. 1 to 5). There is a need to study different types of antiskid braking systems with the objective being to find sources of the degraded performance that occurs under adverse runway conditions; there is also a need to obtain data necessary in the development of more advanced systems so as to insure safe ground handling operations under all weather conditions.

In an effort to meet these needs, an experimental research program has been undertaken to study the performance of several, different aircraft antiskid braking systems under the controlled conditions afforded by the Langley aircraft landing loads and traction facility (formerly called the Langley landing loads track). The types of skid-control devices undergoing study in this program include a velocity-rate control system, a slip-ratio control system with inputs from an unbraked nose wheel, a slip-ratio control system without nose-wheel inputs, a slip-velocity control system, and a system which relies upon differential pump control. The investigation of these systems is being conducted with one main wheel, brake, and tire assembly from a McDonnell Douglas DC-9 series 10 aircraft.

The purpose of this paper is to present the results from a study of the performance of a velocity-rate-controlled, pressure-bias-modulated aircraft antiskid system during maximum-effort braking. The parameters varied in the study include: ground speed, tire loading and yaw angle, tire tread condition, system operating pressure, and runway slipperiness. A discussion of the effects of each of these parameters on the performance of the skid control system is presented. In addition, comparisons are made between data obtained with the skid control system and data from braking tests without antiskid protection.

SYMBOLS

Values are given in both SI and U.S. Customary Units. The measurements and calculations were made in U.S. Customary Units. Factors relating the two systems are given in reference 6.

F_x	drag force parallel to plane of wheel
F_y	side force perpendicular to plane of wheel
P	power
r	tire rolling radius
S	wheel slip ratio
t	time

V	test wheel speed (equivalent to carriage speed)
η	performance ratio
μ	friction coefficient
ψ	yaw angle
ω	test wheel angular velocity

Subscripts:

b	braking
c	cornering
d	drag
f	final value
g	gross
max	maximum value
o	initial value
r	free rolling
s	side
t	tire

A bar over a symbol denotes an average value.

APPARATUS AND TEST PROCEDURE

Test Tires

The tires used in this investigation were 40 × 14, type VII, bias-ply aircraft tires of 22 ply rating with a rated maximum speed of 200 knots (1 knot = 0.5144 m/sec). The tires were retreads with a six-groove tread pattern, and the study included both new and worn tread configurations. A photograph of two tires having new and worn treads is presented in figure 1. The new tread had a groove depth of 0.71 cm (0.28 in.) and was considered new until the groove depth decreased to 0.36 cm (0.14 in.). A commercially available tire grinding machine was then employed to remove tread rubber uniformly from the tire until only 0.05-cm (0.02-in.) groove depth remained. This simulated worn tire was probably in a worse wear condition than is normally experienced in aircraft operations. Throughout this investigation, the tire inflation pressure was maintained at 0.96 MPa (140 psi), which is the normal airline operational pressure.

Test Facility

The investigation was performed at the Langley aircraft landing loads and traction facility, described in reference 7, and utilized the main test carriage. Figure 2 is a photograph of the carriage with the test wheel assembly installed; figure 3 is a closeup view of the wheel and shows details of the instrumented dynamometer, which supports the wheel and brake assembly and measures the various axle loadings. A landing gear strut was not employed because the dynamometer was needed to provide an accurate measurement of the ground forces.

For the tests described in this paper, approximately a 244-m (800-ft) section of the 366-m (1200-ft) flat, concrete test runway was used to provide braking and cornering data on a dry surface, an artificially damp surface, an artificially flooded surface, and a natural-rain wet surface. With the exception of transient runway friction tests, the entire runway had a uniform surface condition, and antiskid cycling occurred for the entire 244 m (800 ft). The first 61 m (200 ft) of the test section were used for the initial wheel spinup and brake actuation, and 61 m (200 ft) were retained at the end of the test section for brake release. In order to obtain a damp condition, the test surface was wetted and the standing water swept away. For the flooded runway condition, the test section was surrounded by a dam and flooded to a depth of approximately 1 cm (0.4 in.). For the natural-rain surface condition, no attempt was made to dam or sweep the test section and no measure was made of water depth. The concrete surface in the test area had a light broom finish in a transverse direction, which produced a surface texture somewhat smoother than that of most operational concrete runways. The runway surface roughness for the 244-m (800-ft) test section was not uniform, as shown by the texture depth measurements in the following table:

Station		Average texture depth, μm
m	ft	
61	200	115
122	400	245
183	600	145
244	800	137
305	1000	155

Details of the texture-depth-measurement technique are presented in reference 8. The average texture depth of the test runway was 154 μm, which is slightly less than that of the typical operational runway (see ref. 9, for example). The test runway was quite level compared with airport runways and had no crown for drainage purposes. During the course of testing on the dry surface, rubber from the test tire was deposited on the runway, and it was necessary to periodically clean the runway, especially during yawed tests.

Skid Control System

A velocity-rate-controlled, pressure-bias-modulated skid control system, typical of that used on many commercial and military jet aircraft, was used to provide the braking inputs. This system was configured to simulate the braking system having hydraulic components for a single wheel of the dual-strut four-main-wheel McDonnell Douglas DC-9 series 10 aircraft. Figure 4 is a photograph of the major hydraulic components of the simulated braking system installed on the test carriage, and figure 5 is a schematic of the system. The brake system is activated by opening the pilot-operated metering valve (see fig. 5), which allows the brake fluid to flow from a high-pressure reservoir and pilot selector valve through the normally open antiskid control valve and a hydraulic fuse (passive for this test) to the brake. A pneumatic piston was used to open the pilot metering valve to its full stroke, thus providing maximum braking for all tests. During antiskid braking, an ac voltage (developed by a pulse count alternator driven by the braked wheel) proportional to wheel angular velocity is converted to a dc voltage and is differentiated in the electronic control box in order to obtain a measure of the wheel deceleration. This wheel deceleration is then compared to a preset velocity rate threshold of approximately 30 rad/sec^2. If the braking effort results in a wheel deceleration greater than the threshold value, then a skid signal (dc voltage) is transmitted to the antiskid control valve in order to reduce brake pressure to a low, possibly even zero, value. When the wheel recovers from the skid, the skid signal (dc voltage) is reduced to a level which is a function of the magnitude, duration, and number of preceding skid signals as retained by memory circuits in the electronic control box, which also control the rate of reapplication of brake pressure to the brake.

Typical time histories of the wheel speed, skid signal, brake pressure, and the resulting drag-force friction coefficient are presented in figure 6 to help describe the system operation. The dashed, vertical lines, and the points denoted by the letters "a" to "n" are used to highlight key events which occur during the skid cycles. In figure 6, the brake pressure is first applied rapidly (a to b) and results in a shallow skid, as noted by the wheel-speed trace (c). The skid, in turn, generates a skid signal voltage (d) proportional to the change in wheel speed that partially closes the antiskid control valve which, in turn, causes a reduction in pressure (e) to the brake and allows the wheel to spin up (f). When the wheel recovers from the skid, the signal dissipates (g) and opens the antiskid control valve to allow reapplication of brake pressure (h). Note that rapid successive shallow skids induce a residual skid signal which reduces the average brake pressure value. The deep skid at approximately 5 sec (i) into the run, due apparently to lower tire/runway friction (j), induces a high voltage skid signal (k) which, in turn, causes the brake pressure to reduce to a negligible value (l) and later to be reapplied at a much lower rate (m) since the skid signal level remains quite high (n).

Instrumentation

The tire/runway friction forces were measured by means of the dynamometer shown in figure 3 and illustrated schematically in figure 7. Strain gages were mounted on the five dynamometer support beams: two beams for vertical forces, two for drag forces parallel to the wheel plane, and a single beam for side force perpendicular to the wheel plane. Three accelerometers on the test wheel axle provided information for inertia corrections to the force data. The brake torque was measured independent of the drag force through the two torque links shown in figure 7. Transducers were installed in the hydraulic system to measure pressures at the pilot metering valve, the antiskid control valve, the hydraulic fuse, the brake, and in the return line between the brake and the hydraulic reservoir. A steel-reinforced, cogged, rubber belt was driven by the test wheel to turn an auxiliary axle which drove several pulse (ac) alternators and a dc generator to obtain a measure of the test wheel angular velocity. Signals from one of the ac alternators supplied wheel-speed information to the antiskid system. This signal and the skid signal produced by the antiskid system were recorded for examination of their characteristics. A light weight trailing wheel was mounted behind one of the carriage wheel assemblies as shown in figure 8, and a dc generator on its axle recorded the carriage speed. A radar unit was also employed to provide a measure of carriage speed. All of the data signals were fed into appropriate signal conditioning equipment and then into two frequency-modulated tape recorders. A time code was fed into the two recorders simultaneously to provide synchronization of the two sets of data.

Brake temperature measurements were provided by four thermocouples mounted to an inner stator, shown in figure 9, of the four-stator brake assembly. Signals from the thermocouples were fed through appropriate conditioning equipment to an oscillograph.

Test Procedure

The test technique for braking tests with and without antiskid protection consisted of setting the dynamometer and tire assembly to the preselected yaw angle, propelling the test carriage to the desired speed, applying a preselected vertical load on the tire, and recording the outputs from the onboard instrumentation. For antiskid runs, the brake was actuated by a pneumatic piston at the pilot metering valve, which gave full pedal or maximum braking, and the antiskid system controlled the braking effort. The runway surface condition was uniform over its entire length, and the brake was applied the full distance and was released just prior to carriage arrestment. For a typical braking test run without antiskid protection, the tire was subjected to three braking cycles, one each on dry, damp, and flooded areas of the runway. Each of these brake cycles consisted of applying sufficient brake pressure to bring the tire from a free-rolling condition to a locked-wheel skid and then releasing the brake to allow full tire spinup prior to the next cycle. The brake pressure was applied when the brake circuit was energized by means of triggering devices located along the test track. The nominal carriage speeds for both types of tests ranged from 40 to 100 knots, and the tire vertical loading was varied from approximately 58 kN (13 000 lbf) to 120 kN (27 000 lbf) which represented a nominal landing weight and a refused takeoff weight, respectively, for a single wheel. Tests were run at tire yaw angles of 0°, 3°, and 6° and at brake-system pressures of 14 MPa (2000 psi) and 21 MPa (3000 psi).

Data Reduction

Except for the ac alternator signals, all data recorded on magnetic tape were filtered to 60 Hz, digitized at 250 samples per second, and stored on tape. From these digitized data, direct measurements were obtained of carriage speed, braked-wheel angular velocity, skid signal generated by the antiskid system, brake pressure and torque, drag force F_x and side force F_y, vertical force applied to the tire, and accelerations of the dynamometer. Force data and accelerations (used to make inertial corrections to the force data) were combined to compute the drag-force friction coefficient μ_d parallel to the direction of motion and the side-force friction coefficient μ_s perpendicular to the direction of motion. The load transfer between the two drag-force beams provided a measure of the alining torque about the vertical or steering axis of the wheel (see fig. 7). A period counter was used to convert the braked-wheel alternator signal to wheel speed, which was combined with the carriage speed to yield wheel slip speed and wheel slip ratio. Time-history plots of some of the measured parameters for a typical antiskid braking test are presented in figure 10(a). The vertical and drag forces are each a summation of two data channels, with corrections made for acceleration effects. The time-history plots of figure 10(b) are the parameters computed from the data of figure 10(a). The brake-pressure time history is common to both figures 10(a) and 10(b).

DEFINITIONS

An adequate assessment of the performance behavior of the antiskid braking system, which was subjected to a wide variety of operational conditions during these tests, requires careful consideration of many variables. Two methods were developed to analyze the performance of the antiskid braking system - one based upon tire friction coefficients and one based upon generated stopping and cornering power. The various friction and power parameters which describe the antiskid-system performance are defined in the following paragraphs.

Tire Friction Terms

Time-history plots of wheel speed, drag-force friction coefficient μ_d, side-force friction coefficient μ_s, and brake pressure for a typical antiskid braking test are presented in figure 11 to help define those parameters which describe the tire frictional behavior under skid control. For the test illustrated, the brakes were applied at approximately 1 sec on the time scale, and four skid cycles were generated over the test-section length.

Drag-force friction coefficients.- The drag-force friction coefficient observed before the brakes are applied results from the tire rolling resistance and is labeled μ_r in figure 11. For those tests on flooded surfaces, μ_r also includes the resistance attributed to fluid drag. The drag-force friction coefficient $\mu_{d,max}$ is measured at the incipient wheel skid point and represents the maximum value of μ_d which the tire is capable of developing at that instant. The magnitude of $\mu_{d,max}$ during a test depends upon the local runway surface texture and the wetness condition, both of which can vary along the length of the test section. The temperature of the tire tread may also be a contributing factor in determining the magnitude of $\mu_{d,max}$, since in figure 11 some slight differences can be noted among the four values of this coefficient. In order to assign a single value to the maximum available drag-force friction coefficient, in light of these differences, all values of $\mu_{d,max}$ developed by the braking system throughout an individual braking test were averaged and are denoted by $\bar{\mu}_{d,max}$. Values of $\bar{\mu}_{d,max}$ are not available for the torque-limited braking tests because in those cases the maximum friction level was not reached. The term "torque limited" in this investigation refers to a situation on a high-friction surface where, for a given supply pressure, the brake torque is insufficient to develop the maximum friction available and cause a complete spindown of the tire. It is apparent that for these tests no antiskid cycling occurs.

The average drag-force friction coefficient $\bar{\mu}_d$ developed by the antiskid braking system during a given test is defined by the expression

$$\bar{\mu}_d = \frac{1}{t_f - t_o} \int_{t_o}^{t_f} \mu_d \, dt \qquad (1)$$

where t_o and t_f, identified in figure 11, enclose the time interval over which $\bar{\mu}_d$ is measured. The time t_o was chosen when the pressure at the brake reached the maximum system pressure or when the first skid occurred, and the time t_f was taken just prior to brake release at the end of the test section. The average drag-force friction coefficient was computed for each braking test with the use of numerical integration techniques.

Side-force friction coefficients.- The maximum side-force friction coefficient $\mu_{s,max}$ is observed in figure 11 to be developed when the yawed wheel is free rolling prior to brake application. The average side-force friction coefficient $\bar{\mu}_s$ developed by the antiskid braking system during braking is defined by an expression similar to that for $\bar{\mu}_d$. This expression

$$\bar{\mu}_s = \frac{1}{t_f - t_o} \int_{t_o}^{t_f} \mu_s \, dt \qquad (2)$$

was also solved by numerical integration techniques for each yawed wheel braking test.

Antiskid-System Effectiveness

Performance ratios.- It is a formidable task to evaluate an antiskid system in terms of efficiency or effectiveness. The ideal evaluation system would assign a single performance number to the system, but this is impossible because of the number of variables which must be considered. In an attempt to provide a rational and unbiased method of evaluating the performance of the antiskid braking system, the following performance ratios and power terms are offered. In order to obtain a measure of the braking performance of the antiskid system, the average friction coefficient developed by the system during a run was divided by the maximum friction coefficient developed by the system for that run. This braking performance ratio η_b is defined by the expression

$$\eta_b = \frac{\bar{\mu}_d - \mu_r}{\bar{\mu}_{d,max} - \mu_r} \tag{3}$$

where the tire-rolling resistance friction coefficient μ_r is subtracted from both the available and the developed friction coefficients to isolate the braking portion of the drag force.

A similar ratio involving the average and the maximum side-force coefficients was used to define a cornering performance ratio η_c:

$$\eta_c = \frac{\bar{\mu}_s}{\mu_{s,max}} \tag{4}$$

Power terms.- The performance of the antiskid system can also be expressed in terms of the gross stopping power developed by the braking system and by the stopping and cornering power dissipated by the tire. These various power terms are defined by expressions which involve the wheel speed V (equivalent to carriage speed), the drag force F_x parallel to the wheel plane, the side force F_y perpendicular to the wheel plane, the wheel yaw angle ψ, and the wheel slip ratio S. Slip ratio is defined as the instantaneous ratio of the slip speed of the braked wheel to the carriage speed; that is,

$$S = \frac{V - \omega r}{V}$$

where $r = 0.492$ m (1.613 ft) as determined by averaging the rolling radii from a number of free rolling tests conducted on the test tire. Time-history plots of some of these variables during a typical antiskid braking test are presented in figure 12. The power expressions are defined over the interval between t_o and t_f.

The gross stopping power $P_{d,g}$ developed by the antiskid system during a braking test is

$$P_{d,g} = \frac{1}{t_f - t_o} \int_{t_o}^{t_f} \left(F_x \cos \psi + F_y \sin \psi\right) V \, dt \tag{5}$$

where the term $F_x \cos \psi + F_y \sin \psi$ converts the measured drag and side forces noted in figure 12 to a single drag force opposing carriage motion. The product of velocity and time yields the distance through which the force acts and completes the work equation. Dividing the work by the duration provides a measure of the power being generated.

A measure of the stopping power $P_{d,t}$ dissipated by the tire is given by

$$P_{d,t} = \frac{1}{t_f - t_o} \int_{t_o}^{t_f} \left[\left(F_x \cos \psi + F_y \sin \psi\right) VS + F_y \sin \psi (1 - S) V\right] dt \tag{6}$$

where carriage speed is multiplied by slip ratio to obtain the slip speed (relative speed between tire and pavement). The last term in equation (6), $\int_{t_o}^{t_f} F_y \sin \psi(1 - S)V \, dt$, is an estimate of the work dissipated by the rolling resistance attributed to a yawed rolling tire.

The cornering power $P_{c,t}$ dissipated by the tire can be closely approximated by the expression

$$P_{c,t} = \frac{1}{t_f - t_o} \int_{t_o}^{t_f} \left(F_y \cos \psi - F_x \sin \psi\right)(1 - S)V \sin \psi \, dt \qquad (7)$$

where $F_y \cos \psi - F_x \sin \psi$ converts the measured side and drag forces to a single side force perpendicular to the direction of motion and $(1 - S)V$ is the braked wheel speed, which when multiplied by $\sin \psi$ yields the tire lateral slip speed.

If F_x, F_y, and V are measured in U.S. Customary Units, then the values determined from equations (5), (6), and (7) must be divided by 550 to express the power terms in units of horsepower.

RESULTS AND DISCUSSION

Pertinent data obtained from all the antiskid braking tests are presented in table I, together with parameters which describe each test condition. In addition, time-history plots of key parameters in all of the tests are presented in the appendix. The tabular data and appendix time histories are given for convenience of the user in plotting the data in ways other than those presented in the body of this report. After several iterations, the authors chose the method of data presentation that appears in the following sections. These sections describe the braking-system behavior, the tire friction behavior under skid control, and the antiskid-system performance under a variety of operating conditions.

Braking-System Behavior

In order to adequately study the performance of the antiskid system, it is first necessary to establish the response characteristics of the braking system and its components. The following paragraphs describe the brake pressure-temperature-torque response, brake hydraulic response, antiskid-system electronic response, and braking-system response to transient runway friction conditions.

Pressure-temperature-torque response.- The relationship between brake pressure, brake temperature, and torque developed by the brake is illustrated by the time-history plots of figure 13. The data presented in the figure are for a torque limited test, chosen so as to eliminate the effects of cyclic braking. For the test illustrated, braking was initiated about 2.5 sec into the test, and the brake pressure rapidly increased to the system operating pressure of 14 MPa (2000 psi). Since the brake did not produce sufficient brake torque to cause a wheel lockup, the brake pressure was not modulated by the antiskid system but remained constant for the remainder of the braking effort. The temperature at one of the brake inner stators at the start of the test was the ambient temperature 24° C (76° F), and after approximately 4 sec of heavy braking rose to 81° C (178° F). Approximately 5 min after the test (at zero speed and hence no air cooling), the stator reached a maximum temperature of 265° C (507° F). This time lag is indicative of the time required to transfer the heat generated at the brake pad surfaces to the thermocouples. The stator temperature gave a qualitative measure of the energy dissipated by the brake even though it did not give the temperature of the brake disk surfaces themselves.

The torque developed by the brake is shown in figure 13 to increase rapidly from zero to approximately 14 kN-m (10 000 ft-lb) when braking was initiated and then to increase gradually until the end of the test. This torque rise which occurred under a constant brake pressure is attributed to heating of the brake surfaces and indicates that the brake can develop torque more efficiently at an elevated temperature. No losses in torque attributed to brake fade were noted in this investigation.

Hydraulic response.- Time histories of pressure responses at the antiskid control valve and at the brake during a typical antiskid braking test are presented in figure 14. In this example, the brake is not torque limited and the antiskid system is actively modulating the brake pressure. Approximately 3 m (10 ft) of hydraulic line and a line fuse separate the two transducers, and no appreciable hydraulic lags are observed inasmuch as the spikes of both curves occur at approximately the same time.

Electronic response.- The electronic-response characteristics of the antiskid system can be described by examining the wheel-speed sensor (ac input signal) and the same signal after it has passed through an ac-dc converter within the antiskid control box. Typical time-history plots of these signals and the corresponding skid signal are presented in figure 15. The ac input signal is proportional to wheel speed and represents the actual or real-time angular velocity of the braked wheel. The ac-dc converted wheel-speed signal is used by the antiskid system to generate the skid signal voltage that operates the antiskid control valve. The plots in the figure indicate an approximate 40-msec lag between the input signal and the converted signal and, since it remains constant for all the skid cycles encountered, it appears to be a function of the system electronics. No time delays are detected between the ac-dc converted signal and the skid signal generated by the antiskid system during the skid cycles. Therefore, these data would indicate that a response time of approximately 40 msec is required for the antiskid system to react to a wheel spindown. A subsequent section will demonstrate how this reaction time can be especially critical to the braking system response to transient runway friction conditions.

Characteristics of the pressure-bias modulation employed by this antiskid system to control the braking effort are also illustrated in figure 15. Most prominent is the buildup in residual skid signal with repeated braking cycles. The function of this residual skid signal is to cause the application of brakes to be more gradual during subsequent brake cycles in an effort to reduce the severity of those skids. This residual skid signal is shown in figure 15 to decay at a constant rate following recovery of the wheel from a skid cycle. Hence, the re-application of brake pressure following a skid cycle is influenced by the skid cycles which precede it. The following section illustrates how the decay rate of this residual skid signal affects the response of the braking system to transient runway friction conditions.

Transient runway friction response.- Time-history plots of the wheel speed, skid signal, brake pressure, and drag-force friction coefficient are presented in figure 16 for two transient runway friction conditions to show the adaptive characteristics of the antiskid system. The response of the braking system to a single transition from a dry to a flooded runway surface is presented in figures 16(a) and 16(b) for nominal carriage speeds of 49 knots and 103 knots, respectively. At both test speeds, the brake pressure reached the maximum system operating pressure of 21 MPa (3000 psi) on the dry surface, and, upon entering the flooded section, the wheel rapidly decelerated to a locked wheel skid. At a speed of 49 knots, the antiskid system quickly responded by reducing brake pressure and cycling normally during the remainder of the run on the flooded surface. At a carriage speed of 103 knots, the wheel never did fully recover from the skid although some spinup was noted between 2 and 3 sec into the test. The inability of the antiskid system to prevent a locked wheel skid as the tire traversed a dry-to-flooded runway surface is attributed, at least in part, to the 30- to 40-msec response time required for the antiskid system to sense the abrupt change in the runway friction level. It should be noted that the predicted spinup hydroplaning speed for the tire was 91 knots (equivalent to a wheel speed of 15.16 rps) based on a tire inflation pressure of 0.96 MPa (140 psi) (see ref. 5). Thus, once the tire had spun down, there was insufficient torque to spin the tire up again even though brake pressure had dropped to negligible values.

Time histories of test runs selected to illustrate the response of the braking system in transition from a flooded to a dry runway surface are presented in figures 16(c) and 16(d) for nominal carriage speeds of 50 knots and 101 knots, respectively. In both tests the wheel was spun up to carriage speed on a dry surface before entering the flooded test section where braking was applied. Figure 16(c) shows that at 50 knots the antiskid system properly controlled the braking action on the flooded portion of the test section. Following an initial deep skid, cyclic braking occurred wherein the brake pressure never exceeded a level of approximately 9 MPa (1270 psi). Upon reaching the dry portion, the brake pressure increased almost linearly over a 3-sec interval (a slow rate commensurate with information from previous skid signals) until a pressure of approximately 16 MPa (2360 psi) produced the first skid cycle on that surface. For the test run at a nominal carriage speed of 101 knots (fig. 16(d)), the wheel, due to dynamic tire hydroplaning, commenced to spin down on the flooded section before brakes were applied at a speed of 113 knots. The predicted tire spindown hydroplaning speed was 106 knots (equivalent wheel speed, 17.66 rps) based on an inflation pressure of 0.96 MPa (140 psi) (see ref. 5). Upon reaching the dry section, the wheel rapidly spun up to the carriage speed, and approximately 2.5 sec later the brake pressure had increased to approximately 14 MPa (2000 psi). A maximum operating pressure of 21 MPa (3000 psi) was available to the system. The relatively slow increase in brake pressure after the transition from the flooded to the dry runway surface is a function of the decay rate of the residual skid signal built up by the antiskid system's pressure-bias modulation circuit on the flooded portion of the runway.

Tire Frictional Behavior Under Skid Control

Effect of cyclic braking on maximum drag-force friction coefficient.- Values of the maximum drag-force friction coefficient $\mu_{d,max}$ obtained from antiskid braking tests on the various runway conditions are presented as a function of carriage speed in figure 17. Data are presented for each test condition at nominal carriage speeds of 50, 75, and 100 knots. The values of $\mu_{d,max}$ are plotted for the individual brake cycles and are numbered sequentially for each braking test. For example, under natural-rain conditions, 5 brake cycles occurred during the nominal 50- and 75-knot tests and 4 cycles were noted at 100 knots. The data on the flooded surface indicated very little change in $\mu_{d,max}$ between first and last brake cycles. The data obtained in the damp and natural-rain conditions indicate that the value of $\mu_{d,max}$ generally decreases from the first to the last brake cycle. This trend was initially attributed to tire heating. However, the data from the dry runway tests, where it would appear that heating effects would be much more pronounced, did not exhibit a similar trend. Thus the variation in $\mu_{d,max}$ for the individual brake cycles would appear to be unpredictable, and the variation is not explained on the basis of temperature effects alone. Indeed, such other factors as tire scrubbing, which exposes new and possibly cooler rubber to the footprint, and runway-surface texture variations may play an important role.

A comparison between the value of $\mu_{d,max}$ measured during single-cycle braking tests, run without antiskid protection, and the average of corresponding values measured under identical test conditions but with the antiskid system operational is presented in figure 18. The data are presented separately for dry, damp, flooded, and combined test conditions, and the data for each condition are faired by a least-squares fit through the plot origins. The data indicate that the maximum drag-force friction coefficients obtained from single-cycle braking tests tend to overestimate the average maximum coefficients developed by the antiskid system on the dry and flooded surfaces and to underestimate those on a damp surface. When the data from all three surface wetness conditions are compared simultaneously, the tendency is for the single-cycle data to overestimate the maximum drag coefficient available to the antiskid system. These results imply that braking performance calculations based upon values of $\bar{\mu}_{d,max}$ obtained from a number of antiskid cycles should be better defined than performance based on $\mu_{d,max}$ from a single brake cycle because the latter neglects runway-surface variations and tire heating effects, for example.

Effect of test parameters on maximum drag-force friction coefficient.- The average maximum drag-force friction coefficient $\bar{\mu}_{d,max}$ as developed by the unyawed tire under dry, damp, flooded, and natural-rain conditions is presented as a function of carriage speed in figure 19. The fairings in the figure are linear least-squares curve fits of the data. Also noted on the figure is the maximum value of the drag-force friction coefficient, 0.78, predicted from the empirical expression developed in reference 10 at very low speeds. The dry data for $\bar{\mu}_{d,max}$ tend to substantiate this prediction if extrapolated to zero speed. As expected, $\bar{\mu}_{d,max}$ values for the wet runway surfaces are substantially lower than those for the dry runway and the difference becomes greater with increasing water depth, particularly at the higher speeds. The values of $\bar{\mu}_{d,max}$ are shown in figure 19 to approach negligible values on the flooded runway near the predicted tire spindown hydroplaning speed of 106 knots. It is interesting to note that the values of $\bar{\mu}_{d,max}$ for the natural-rain test condition are fairly well bracketed by the values for the damp and flooded runway test conditions.

The data of figure 19 were obtained at 0° yaw angle. The fairings of these data for the dry, damp, and flooded conditions are reconstructed in figure 20, together with corresponding data obtained at yaw angles of 3° and 6°, to show the effect of yaw angle on $\bar{\mu}_{d,max}$. Figure 20 shows that the effect of yaw angle is dependent upon the surface wetness condition. A reduction in $\bar{\mu}_{d,max}$ is noted on the dry surface with the introduction of yaw; however, this reduction is less pronounced on the damp surface, and no significant reduction in $\mu_{d,max}$ values with yaw angle was observed on the flooded surface.

The effect of tire tread wear on $\bar{\mu}_{d,max}$ is shown in figure 21 where the values of $\mu_{d,max}$ are plotted as a function of carriage speed on dry, damp, and flooded runway surfaces. The new-tread data were again obtained from the faired curves of figure 19. Figure 21 indicates that, when the new tread is replaced by a worn tread, the average maximum drag coefficient is reduced during damp or flooded runway conditions. The tread condition appears to have no effect on $\bar{\mu}_{d,max}$ during dry runway operations, which agrees with a similar trend noted in reference 2.

Effect of test parameters on maximum available side-force friction coefficient.- The maximum side-force friction coefficients available to the tire under dry, damp, and flooded conditions are plotted as a function of carriage speed in figure 22. The fairings in the figure are linear least-squares curve fits of the data. The $\mu_{s,max}$ values for the wet runway surfaces are lower than those for the dry runway, and the difference becomes greater with increasing water depth. The values of $\mu_{s,max}$ are shown in the figure to be zero on the flooded runway near the predicted tire spindown hydroplaning speed of 106 knots. As expected, the values of $\mu_{s,max}$ at a 6° yaw angle are substantially higher than those at a 3° yaw angle on the dry and the damp runway surfaces. An opposite trend, however slight, was observed on the flooded surface, which indicates that the side force reached a maximum value at some yaw angle between 3° and 6°.

The effect of tire tread wear on $\mu_{s,max}$ is shown in figure 23 where the values of $\mu_{s,max}$ at a 6° yaw angle on damp and flooded runway surfaces are plotted as a function of carriage speed. The new-tread data were obtained from the faired curves for the 6° yaw angle from figure 22. The data from figure 23 indicate that $\mu_{s,max}$ decreases more rapidly with carriage velocity for the worn tread than for the new tread on the wet runway surfaces.

Interaction between braking and cornering.- Typical tire frictional response to antiskid braking on dry and flooded runway surfaces is presented in figure 24. The drag- and side-force friction coefficients μ_d and μ_s for the tire yawed to 6° and, operating at a nominal carriage speed of 75 knots, are plotted as a function of wheel slip ratio. The data presented in figure 24 illustrate the irregular nature of the antiskid braking control. The random perturbations can be attributed to a combination of such factors as small fluctuations in the tire vertical load due to runway unevenness, flexibility in the wheel support which would be reflected in the measured drag and side forces, variations in the runway surface friction characteristics, and spring coupling between the wheel and the pavement provided by the tire. Reference 11 discusses some of these factors.

The data presented in figure 24 illustrate the traction losses associated with flooded-runway operations. For example, on the dry surface the maximum value of μ_d is slightly greater than 0.55 but it never exceeds 0.2 on the flooded surface. A similar loss is noted in the side-force friction coefficients where the maximum value of approximately 0.4 on the dry runway reduces to approximately 0.2 when the runway was flooded. The figure also demonstrates the rapid deterioration in the tire cornering capability with increased braking effort (tire slip). The value of μ_s is reduced approximately 75 percent on the dry runway at a slip ratio of only 0.3, the maximum reached in the test illustrated, and is reduced to a negligible value at that slip ratio on the flooded surface. These trends are consistent with those noted for similar antiskid braking tests reported in reference 1.

Antiskid-System Performance

Braking performance.- In this section, two terms are used to present a measure of antiskid performance: (1) the performance ratio, which assesses the ability of the antiskid system to use the friction that is available at the tire/runway interface; and (2) the total stopping power developed by the antiskid system, which essentially describes the extent of the braking effort.

Antiskid braking performance ratios η_b were computed for all braking tests except those which were torque limited, involved tire hydroplaning, or were performed under transient runway friction conditions. Values of η_b are listed in table I and are plotted in figure 25 as a function of the average maximum available drag-force friction coefficient $\bar{\mu}_{d,max}$. In figure 25, data for all surface conditions are plotted, and the wide range of test variables (surface condition, yaw angle, carriage speed, tire wear, etc.) resulted in the scatter shown. The braking performance ratio for all damp, flooded, and natural-rain tests varied from approximately 0.4 to 0.8, with an average value of 0.65; and the magnitude of $\bar{\mu}_{d,max}$ on these surfaces never exceeded 0.41. The braking performance ratio for all dry-surface tests varied from approximately 0.75 to 0.95, with an average value of 0.83, and the range of $\bar{\mu}_{d,max}$ extended from 0.43 to 0.74. Thus, the antiskid braking system suffers a loss in performance on wet surfaces, the surfaces that have the greatest need for good performance since they have lower friction coefficients.

Figure 26 presents bar-graph data describing the effect of the various test variables on $\bar{\eta}_b$. The value of $\bar{\eta}_b$ is a numerical average of all the data from a given test condition. For example, the dry, 50-knot bar graph (fig. 26(a)) is the average of all dry runs conducted at 50 knots, including the various yaw angles, vertical forces, tire configurations, and system pressures. Data for all test conditions are presented in table I and in the appendix. To illustrate the characteristics of the antiskid system, the authors have chosen to present the data in bar-graph form as shown, for example, in figure 26. On the dry surface, $\bar{\eta}_b$ is shown to increase with carriage speed, yaw angle, and tire vertical force, to decrease when the new tread is replaced by a worn tread, and to be insensitive to variations in the system operating pressure for the two pressures tested. On the wet runway surfaces, $\bar{\eta}_b$ decreases with carriage speed, tread wear, and system operating pressure, $\bar{\eta}_b$ is slightly higher when the tire is yawed 3° but then decreases for the 6° yaw angle, and $\bar{\eta}_b$ increases with tire vertical force. The variation of $\bar{\eta}_b$ with speed on the different surfaces is in agreement with trends reported in reference 1 on a similar antiskid system. The data depicted in figure 26 imply that the braking performance of this antiskid system would not be degraded during crosswind operations (yaw-angle effects) but might be adversely affected by excessive wing lift during the landing rollout (vertical-force effects). These results also indicate that the antiskid-system braking performance may be adversely affected by excessive tire wear and that the antiskid system may perform more effectively on slippery runways at reduced system operating pressures.

The gross stopping power $P_{d,g}$ developed by the antiskid system, which is a measure of the overall antiskid braking effort, is listed in table I for each test condition. Bar graphs which average these data are presented in figure 27 to describe the effects of test parameter variations. The data from torque-limited tests and from tests involving tire hydroplaning are included in the figure but not the data from tests performed under transient runway friction conditions. As expected, because of higher available friction coefficient, $\bar{P}_{d,g}$ on the dry runway surface is more than double the value on the wet runway surfaces. On the dry surface, $\bar{P}_{d,g}$ is shown to increase with carriage speed, yaw angle, tire vertical force, tread wear, and system operating pressure. On the wet runway surfaces, $\bar{P}_{d,g}$ is shown to be insensitive to variations in the carriage speed, to decrease with yaw angle, tread wear, and system operating pressure, and to be higher for tire vertical forces in excess of 89 kN (20 000 lbf) than for the lower tire vertical forces in the range 71 kN to 89 kN. In general, the trends for $\bar{P}_{d,g}$ are in agreement with the trends noted for $\bar{\eta}_b$ in figure 26; however, there are some notable exceptions. For example, on the dry runway, increases in tread wear and system operating pressure are shown in figure 27 to result in increases in $\bar{P}_{d,g}$ which are not reflected in $\bar{\eta}_b$ because torque-limited data are not included in the latter. Similarly, on the wet surfaces, $\bar{P}_{d,g}$ decreases with yaw angle although $\bar{\eta}_b$ is shown in figure 26 to be higher for 3° and 6° than for 0°. This result indicates that the increase in $\bar{\eta}_b$ with yaw angle does not completely offset the loss in $\bar{\mu}_{d,max}$ with yaw angle (see fig. 20).

The stopping power $P_{d,t}$ dissipated by the tire alone provides a measure of the increased tread wear associated with the braking effort; thus, the ideal antiskid braking system would maximize $P_{d,g}$ and minimize $P_{d,t}$. Values of $P_{d,t}$ are listed in table I for each test condition, and bar graphs describing the effects attributed to test parameter variations are presented in figure 28. Data from tests performed under transient runway friction conditions are not included in the figure. It should be noted that $P_{d,t}$ is only a small fraction of $P_{d,g}$, and the trends shown in figure 28 are not as conclusive as those shown for $P_{d,g}$. For corresponding conditions, $P_{d,t}$ is shown to be higher on the dry surfaces than on the wet surfaces. The stopping power $P_{d,t}$ on the dry surface generally increases with carriage speed and yaw angle, is lower for tire vertical forces greater than 89 kN (20 000 lbf) than for the other test loading conditions, decreases when the new tread is replaced by a worn tread, and decreases slightly with increasing system operating pressure. The low values of $\bar{P}_{d,t}$ on the dry runway for tire vertical loadings greater than 89 kN (20 000 lb) are attributed to torque-limited braking. On the wet runway surface, $\bar{P}_{d,t}$ increases with carriage speed and yaw angle, is higher for vertical forces between 71 and 89 kN (16 000 and 20 000 lbf) than for the other test loading conditions, decreases with system operating pressure, and is insensitive to variations in tread wear. Figure 28 indicates that the most severe tread wear will occur during combined braking and cornering operations on a dry surface.

The ratio of tire stopping power to gross stopping power for each test is plotted as a function of $\bar{\mu}_{d,max}$ in figure 29. Data are not included in the figure for torque-limited tests or for tests performed under transient runway friction conditions. The faired curves represent the least-squares fit to the data for $\bar{\mu}_{d,max}$ values greater than 0.15. The data indicate that as yaw angle is increased a greater percentage of the gross stopping power is dissipated by the tire, thus indicating increased tire wear. This was evidenced by rubber deposits on the runway during yawed tests. The marked increase in power ratio when the runway is quite slippery indicates that most of the gross stopping power is associated with tire skidding on the low-friction surface. This does not necessarily indicate increased tire wear, however, since both terms of the power ratio have been greatly reduced by hydroplaning effects.

Cornering performance.- Antiskid systems are not designed to maximize cornering performance because good cornering is not compatible with heavy braking, but cornering is important for directional control, especially when crosswinds are present.

The antiskid-system cornering performance ratios η_c for the individual braking tests at yaw angles of 3° and 6° are listed in table I, and bar-graph data for the average values for each set of test conditions are presented in figure 30. The data indicate that $\bar{\eta}_c$ was higher on the dry surface than on the wet surfaces. In addition, $\bar{\eta}_c$ is shown to decrease with increasing yaw angle. There was no discernible trend for speed variations on the dry surface, but on the wet surfaces $\bar{\eta}_c$ decreased with increasing speed. The effect of tread wear on $\bar{\eta}_c$ was negligible.

The cornering power dissipated by the tire $P_{c,t}$ not only is indicative of the overall cornering capability of the tire during the antiskid controlled braking but also provides an indication of the increased tread wear associated with the steering effort (see table I). Bar-graph data describing the effects of test parameter variations on $\bar{P}_{c,t}$ are presented in figure 31. The figure shows that $\bar{P}_{c,t}$ values are higher on the dry surface than on the wet surfaces, as expected, and increase with increasing yaw angle and speed on both surfaces. The effect of tread wear, obtained only on the wet surfaces, also appears to be negligible. Although the performance ratio decreased with increasing yaw angle on the wet surfaces, the average cornering power doubled when the yaw angle was changed from 3° to 6° (fig. 31), thus illustrating the need for a power term in addition to performance ratio when studying the characteristics of antiskid systems.

CONCLUDING REMARKS

An experimental investigation was conducted to study the braking and cornering response of a velocity-rate-controlled, pressure-bias-modulated aircraft antiskid braking system during maximum braking effort on dry and wet runway surfaces. The investigation was conducted at the Langley aircraft landing loads and traction facility with one main wheel, brake, and tire assembly from a McDonnell Douglas DC-9 series 10 aircraft.

The results indicated that the capability of the braking system to develop torque is a function of brake temperature as well as system pressure. There were no apparent hydraulic lags during antiskid cycling, but an electronic lag of approximately 40 msec was required for the antiskid system to respond to a skid cycle; the residual skid signal built up by the antiskid system on slippery runways was shown to decay at a constant rate following recovery of the wheel from a skid cycle. Locked wheel skids were observed when the tire encountered a runway surface transition from dry to flooded, due in part to the response time required for the system to sense abrupt changes in runway friction; however, the antiskid system quickly responded, reducing brake pressure, and cycling normally during the remainder of the run on the flooded surface. A relatively slow brake pressure recovery was observed following transition from a flooded-to-dry runway surface, which was shown to be a function of the decay rate of the residual skid signal built up by the antiskid system on the flooded runway.

The maximum drag-force and side-force friction coefficients available to the braking system were shown to decrease with increased surface wetness, particularly at high carriage speeds. This trend was more pronounced for the worn-tread tire than for the new-tread tire. The effect of yaw angle was to reduce the drag-force friction coefficient available on the dry and damp runway surfaces. The side-force friction coefficient was reduced by as much as 75 percent on the dry runway and to negligible values on the flooded runway during portions of the antiskid braking cycle. The results also indicated that antiskid performance based upon an average of the maximum drag-force friction coefficients obtained from a number of antiskid cycles should be better defined than performance based upon the maximum friction coefficient developed during a single brake cycle.

The average ratio of drag-force friction coefficient developed by the antiskid system to the maximum friction coefficient available at the tire/runway interface during maximum braking was shown (1) to be higher on the dry surface than on the wet surfaces, (2) not to be adversely affected by yaw angles up to 6°, and (3) to be reduced with lighter vertical loads (wing lift) and worn tires. The average of the gross stopping power values generated by the brake system on the dry surface was more than twice that obtained on the wet surfaces. The stopping power dissipated by the tire, which is indicative of the amount of tire wear, was the greatest during combined braking and cornering on dry runway surfaces.

With maximum applied braking, the average ratio of the side-force friction coefficient developed by the tire under antiskid control to the maximum side-force friction coefficient available at the tire/runway interface of a free-rolling tire was shown (1) to decrease with increasing yaw angle, (2) to decrease with increasing velocity on wet surfaces, and (3) to decrease with increasing yaw angle on wet surfaces. Although this ratio decreased with increasing yaw angle on wet surfaces, the average cornering power doubled when yaw angle was changed from 3° to 6°.

Langley Research Center
National Aeronautics and Space Administration
Hampton, VA 23665
September 30, 1976

REFERENCES

1. Tanner, John A.: Performance of an Aircraft Tire Under Cyclic Braking and of a Currently Operational Antiskid Braking System. NASA TN D-6755, 1972.

2. Horne, Walter B.; and Leland, Trafford J. W.: Influence of Tire Tread Pattern and Runway Surface Condition on Braking Friction and Rolling Resistance of a Modern Aircraft Tire. NASA TN D-1376, 1962.

3. Tracy, William V., Jr.: Wet Runway Aircraft Control Project (F-4 Rain Tire Project). ASD-TR-74-37, U.S. Air Force, Oct. 1974. (Available from DDC as AD A004 768.)

4. Danhof, Richard H.; and Gentry, Jerauld R.: RF-4C Wet Runway Performance Evaluation. FTC-TR-66-6, U.S. Air Force, May 1966. (Available from DDC as AD 486 049.)

5. Horne, Walter B.; McCarty, John L.; and Tanner, John A.: Some Effects of Adverse Weather Conditions on Performance of Aircraft Antiskid Braking Systems. NASA TN D-8202, 1976.

6. Metric Practice Guide. E 380-72, American Soc. Testing & Mater., June 1972.

7. Tanner, John A.: Fore-and-Aft Elastic Response Characteristics of 34 x 9.9, Type VII, 14 Ply-Rating Aircraft Tires of Bias-Ply, Bias-Belted, and Radial-Belted Design. NASA TN D-7449, 1974.

8. Leland, Trafford J. W.; Yager, Thomas J.; and Joyner, Upshur T.: Effects of Pavement Texture on Wet-Runway Braking Performance. NASA TN D-4323, 1968.

9. Yager, Thomas J.; Phillips, W. Pelham; Horne, Walter B.; and Sparks, Howard C. (appendix D by R. W. Sugg): A Comparison of Aircraft and Ground Vehicle Stopping Performance on Dry, Wet, Flooded, Slush-, Snow-, and Ice-Covered Runways. NASA TN D-6098, 1970.

10. Smiley, Robert F.; and Horne, Walter B.: Mechanical Properties of Pneumatic Tires With Special Reference to Modern Aircraft Tires. NASA TR R-64, 1960. (Supersedes NACA TN 4110.)

11. Batterson, Sidney A.: A Study of the Dynamics of Airplane Braking Systems as Affected by Tire Elasticity and Brake Response. NASA TN D-3081, 1965.

TABLE I.- SUMMARY OF ANTI

Run	Tire-tread condition	Brake supply pressure		Yaw angle, deg	Surface condition	Vertical load		Nominal speed, knots	Brake torque limited	$\bar{\mu}_d$	$\bar{\mu}_{d,max}$	μ_r
		MPa	psi			kN	lbf					
1	New	14	2000	0	Dry	54.7	12 300	46	No	0.56	0.74	0.027
2						59.6	13 400	44		.51	.67	.048
3						60.5	13 600	73		.52	.66	.027
4						60.9	13 700	98		.62	.66	.041
5						72.5	16 300	46		.58	.72	.075
6						85.0	19 100	102	Yes	.46		.041
7					Damp	56.9	12 800	52	No	.20	.38	.014
8						61.4	13 800	99		.22	.38	.062
9						56.9	12 800	100		.17	.33	.070
10						77.0	17 300	50		.25	.41	.027
11						75.6	17 000	74		.25	.38	.027
12						79.6	17 900	98		.23	.37	.048
13						99.2	22 300	32		.31	.37	.027
14						93.9	21 100	98		.17	.26	.027
15						120.6	27 100	59		.29	.40	.041
16					Flooded	57.8	13 000	98		.05	.06	
17						92.1	20 700	47		.26	.33	.034
18						104.5	23 500	50		.26	.31	.034
19						118.3	26 600	48		.28	.35	.062
20						114.3	25 700	76		.14	.19	.055
21					Natural rain	120.6	27 100	45		.26	.32	.027
22						120.1	27 000	72		.22	.31	.027
23						122.3	27 500	103		.09	.16	.027
24					Flooded/Dry	79.6	17 900	52		.27	.30/.45	
25					Dry/Flooded	78.7	17 700	72	Yes/No	.33	---/.19	
26					Dry/Flooded	79.2	17 800	98	No	.20	.58/.05	
27				3	Dry	61.8	13 900	46	No	.51	.60	.041
28					Dry	72.1	16 200	74	Yes	.54		.041
29					Dry	75.6	17 000	100	Yes	.48		.041
30					Damp	76.5	17 200	48	No	.25	.34	.041
31					Damp	81.0	18 200	75		.21	.28	.034
32					Damp	81.0	18 200	99		.19	.24	.048
33					Flooded	76.1	17 100	48		.23	.30	.041
34					Flooded	74.7	16 800	75		.14	.18	.068

SKID-BRAKING TEST RESULTS

Braking performance ratio, η_b	$\bar{\mu}_s$	$\mu_{s,max}$	Cornering performance ratio, η_c	Brake-temperature rise		Average slip ratio	Gross stopping power		Tire stopping power		Tire cornering power	
				°C	°F		kW	hp	kW	hp	kW	hp
0.75	0.03			273	491	0.11	708	949	78	105		
.74	.03			242	435	.13	677	908	89	120		
.78	.01			250	450	.13	1228	1513	142	191		
.93	0					.15						
.78	.03					.09	924	1239	84	113		
	.03			221	398	.07	1959	2627	136	183		
.51				112	201	.10	312	419	32	43		
.50						.25	620	832	73	98		
.38						.11						
.58				189	340							
.63				292	526	.12	770	1033	93	125		
.56						.09	808	1082	75	101		
.83						.13	420	563	38	51		
.61						.07	770	1033	54	73		
.70				272	489	.07	910	1220	60	80		
.76						.09	585	785	51	68		
.82				183	330	.07	682	915	46	62		
.76						.10	818	1097	81	109		
.63				69	156	.07	597	800	43	58		
.80						.08	705	945	54	73		
.68						.07	976	1309	63	85		
.47						.09	552	740	48	64		
						.10	562	754	55	74		
						.13	1013	1359	133	179		
							808	1083				
.84	.23	0.32	0.72	263	474	.17	722	968	118	158	13	17
	.28	.32	.84	296	533	.10	1450	1944	179	240	31	41
	.27	.29	.93	239	431	.10	1824	2446	227	305	43	57
.70	.16	.25	.64			.15	490	657	85	114	13	17
.71	.17	.26	.65	121	217	.09	667	895	87	116	23	31
.74	.15	.22	.68	92	165	.09	775	1039	96	129	26	35
.73	.14	.15	.93	94	169	.12	433	580	64	86	11	15
.64	.07	.10	.70			.16	422	566	75	101	8	11

TABLE I.-

Run	Tire-tread condition	Brake supply pressure		Yaw angle, deg	Surface condition	Vertical load		Nominal speed, knots	Brake torque limited	$\bar{\mu}_d$	$\bar{\mu}_{d,max}$	μ_r
		MPa	psi			kN	lbf					
35	New	14	2000	3	Flooded	74.3	16 700	102	No	0.05	0.05	0.05
36				6	Dry	83.6	18 800	46		.48	.57	.062
37					Dry	81.4	19 300	74		.44	.46	.068
38					Dry	83.2	18 700	100		.38	.43	.062
39					Damp	82.3	18 500	50		.27	.34	.055
40					Damp	81.8	18 400	75		.20	.26	.041
41					Damp	76.5	17 200	100		.14	.20	.048
42					Flooded	80.5	18 100	52		.17	.22	.041
43					Flooded	80.1	18 000	75		.11	.13	.062
44	↓			↓	Flooded	80.1	18 000	101	↓	.06	.07	.048
45	Worn			0	Dry	80.1	18 000	50	Yes	.55		.027
46					Dry	96.5	21 700	100	Yes	.41		.021
47					Damp	80.1	18 000	50	No	.26	.36	.027
48					Damp	80.1	18 000	76		.14	.21	.034
49					Damp	82.3	18 500	102		.10	.16	.021
50					Flooded	81.0	18 200	48		.16	.20	.055
51					Flooded	78.7	17 700	75		.07	.10	.068
52				↓	Flooded	81.4	18 300	99		.06	.08	.06
53				6	Damp	80.1	18 000	52		.23	.32	.068
54					Damp	79.6	17 900	77		.17	.24	.048
55					Damp	82.7	18 600	102		.14	.21	.055
56					Flooded	80.1	18 000	47		.13	.16	.055
57					Flooded	78.7	17 700	76		.08	.10	.055
58	↓	↓	↓	↓	Flooded	81.4	18 300	100		.04	.05	.034
59	New	21	3000	0	Flooded/Dry	78.3	17 600	50	↓	.40	.38/.62	.027
60					Flooded/Dry	80.1	18 000	101	No/Yes	.18	.08/---	.027
61					Dry/Flooded	78.3	17 600	49	Yes/No	.61/.24	---/.39	.027
62				↓	Dry/Flooded	79.6	17 900	103	Yes/No	.11	---/.05	.027
63				6	Dry	79.6	17 900	75	No	.50	.55	.068
64	↓			6	Flooded	78.3	17 600	80		.14	.16	.055
65	Worn			0	Dry	62.3	14 000	49		.55	.70	.021
66					Dry	79.6	17 900	48	↓	.53	.66	.027
67					Dry	99.6	22 400	100	Yes	.45		.021
68	↓	↓	↓	↓	Flooded	79.6	17 900	76	No	.06	.08	.048

Concluded

Braking performance ratio, n_b	$\bar{\mu}_s$	$\mu_{s,max}$	Cornering performance ratio, n_c	Brake-temperature rise		Average slip ratio	Gross stopping power		Tire stopping power		Tire cornering power	
				°C	°F		kW	hp	kW	hp	kW	hp
	0.01	0	0			0.71	190	255	133	179	1	1
0.82	.31	.43	.72			.12	886	1188	160	214	43	57
.95		.43		253	456	.15	1421	1905	256	343		
.86	.23	.40	.58	178	321	.14	1576	2113	313	420	69	93
.75	.24	.38	.63	165	297	.17	601	806	147	197	38	51
.73	.23	.36	.64	104	188	.12	627	841	137	184	57	77
.61	.19	.36	.53	60	108	.09	553	741	117	157	62	83
.72	.08	.12	.67	48	86	.22	392	526	98	132	11	15
.71	.03	.07	.43			.18	342	458	71	95	5	7
.55	0	0	0			.84	239	320	201	269	0	0
	0			398	716	.11						
	0			393	527	.03	1967	2638	67	90		
.70						.04						
.60	0					.06						
.57	0					.07	441	591	33	44		
.72	0					.08	321	430	25	33		
	0					.19						
	0					.74						
.64	.26	.47	.55			.08	497	667	95	127	45	61
.64	.22	.36	.61			.09	540	724	110	147	57	76
.55	.19	.29	.66			.08	600	804	124	166	70	94
.71	.07	.08	.88			.13	293	393	55	74	10	14
	.02	0	0			.26	262	351	72	96	3	4
	.02	0	0			.79	198	266	154	206	1	2
	0					.10	784	1052	80	107		
	0					.20	781	1047	156	209		
						.09						
						.42	518	694	215	288		
.90	.30	.47	.64	301	542	.14	1508	2022	288	386	25	34
.81	.08	.16	.50			.16	466	625	97	130	17	23
.78	0			294	529	.11	869	1165	95	128		
.79	0			396	712		975	1308	23	31		
	0			381	685	.02	2154	2889	48	64		
.38	0						201	269	31	42		

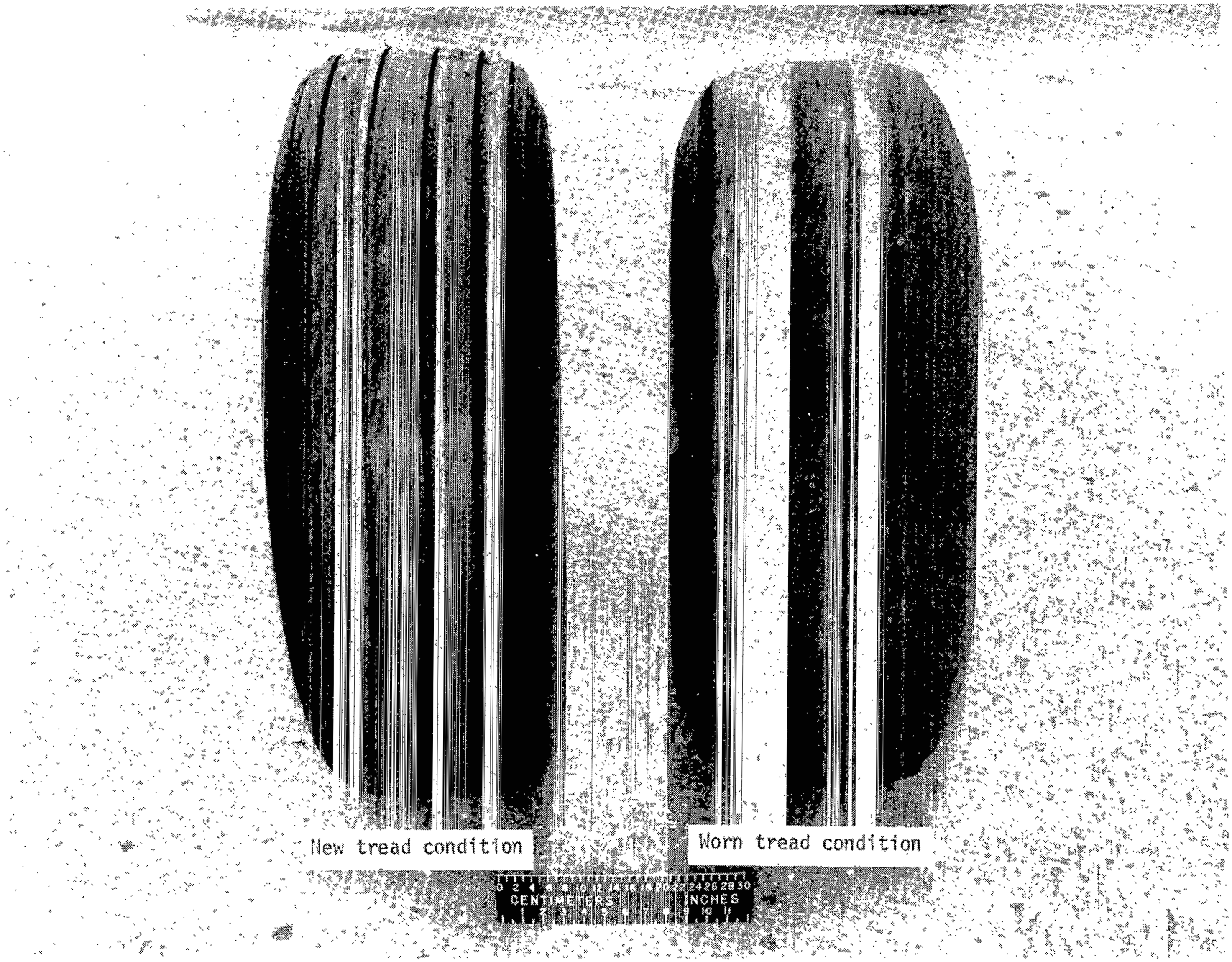

L-76-1704.1

Figure 1.- New and worn tread condition of six-groove, 40 × 14, type VII aircraft test tires.

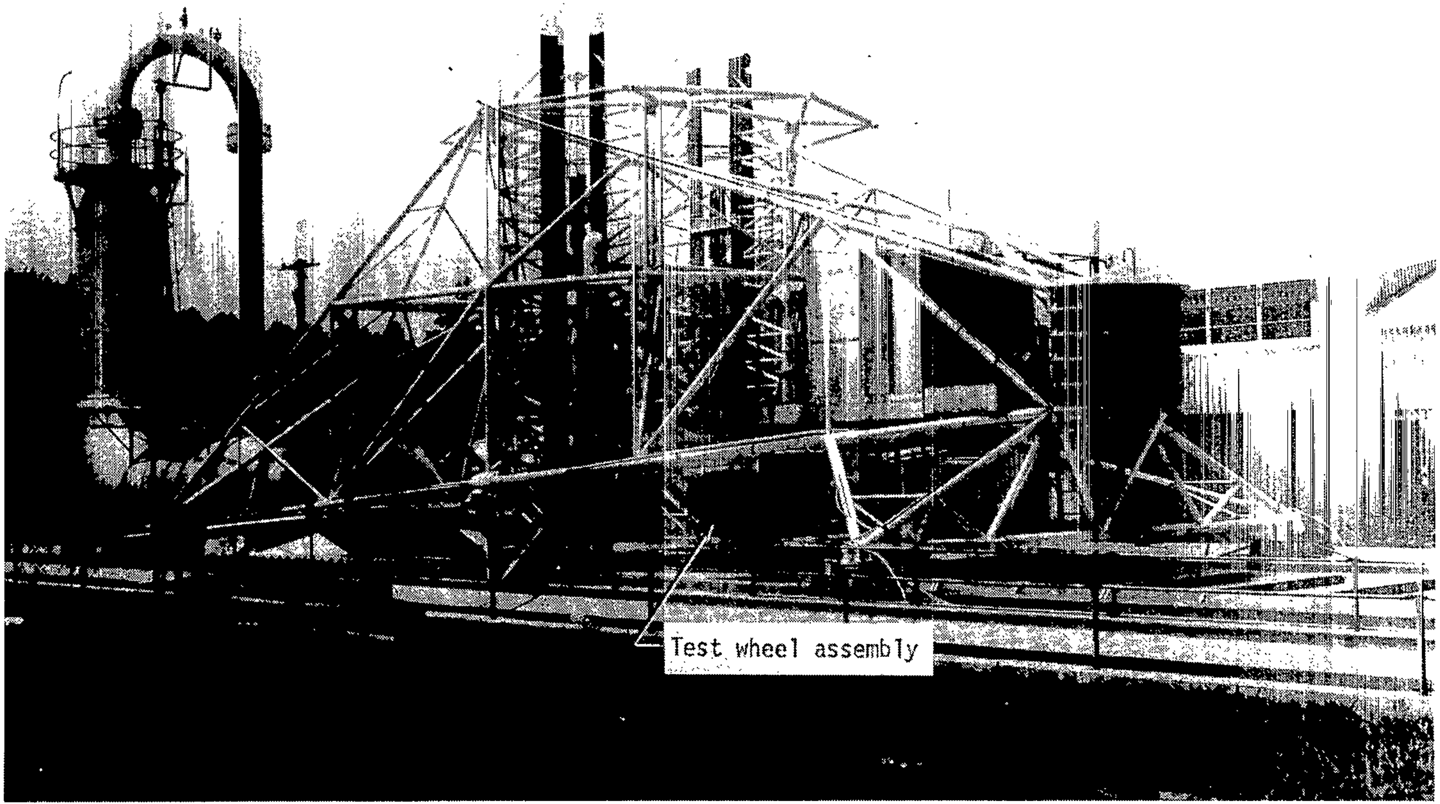

L-69-5860.2

Figure 2.- Photograph of test carriage.

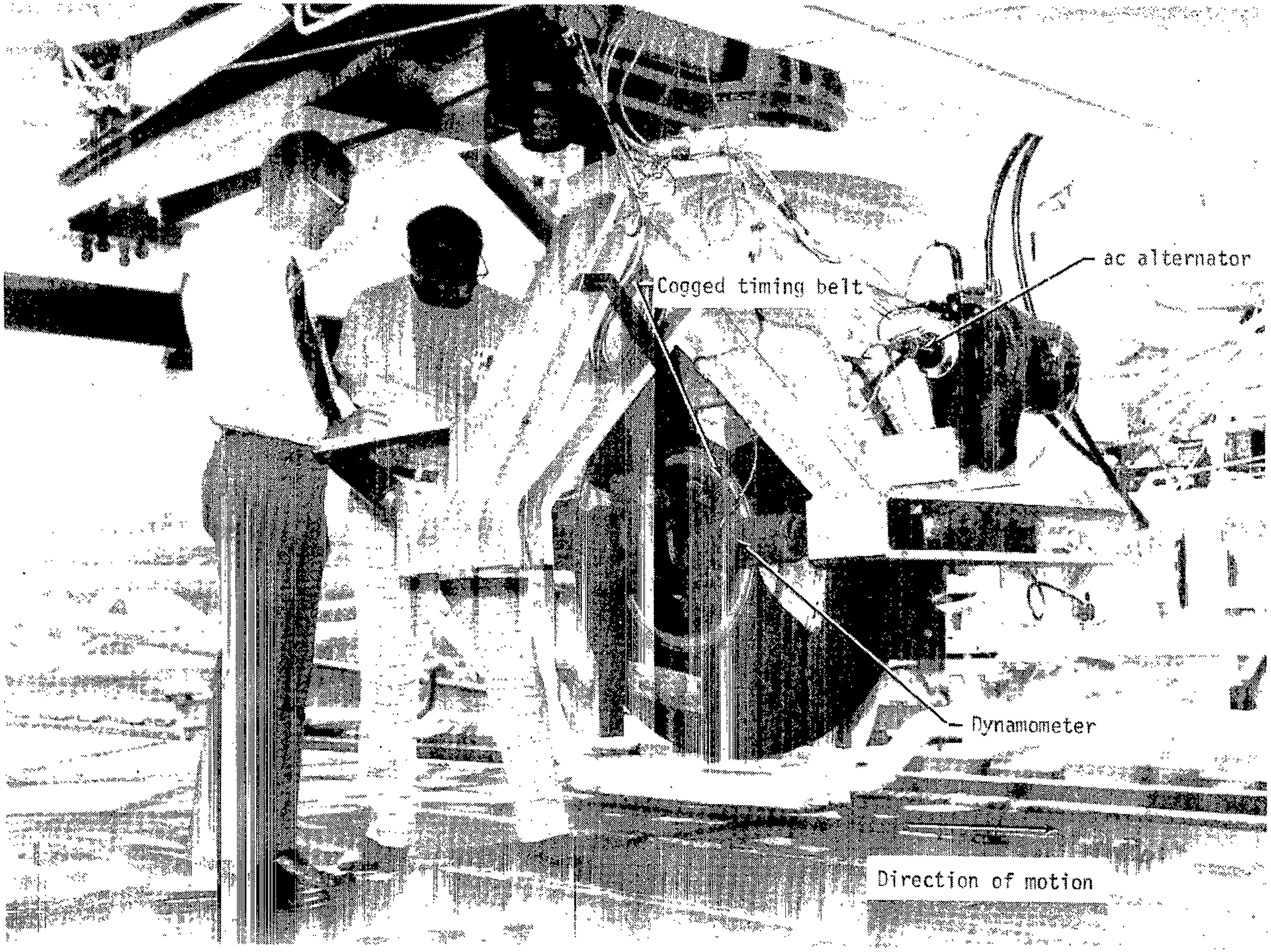

L-75-3427.1

Figure 3.- Test tire and instrumented dynamometer.

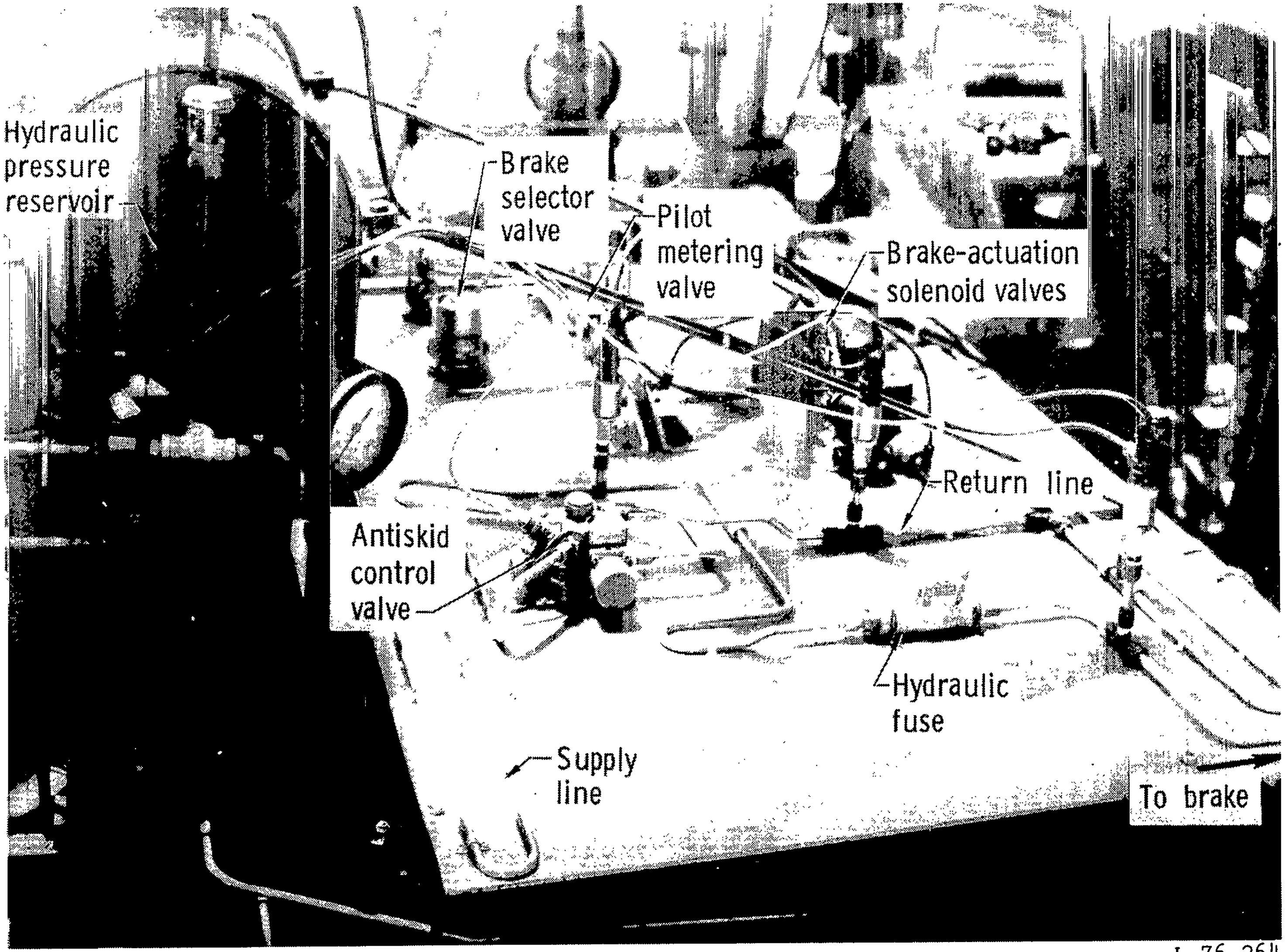

L-76-264

Figure 4.- Layout of simulated braking system on test carriage.

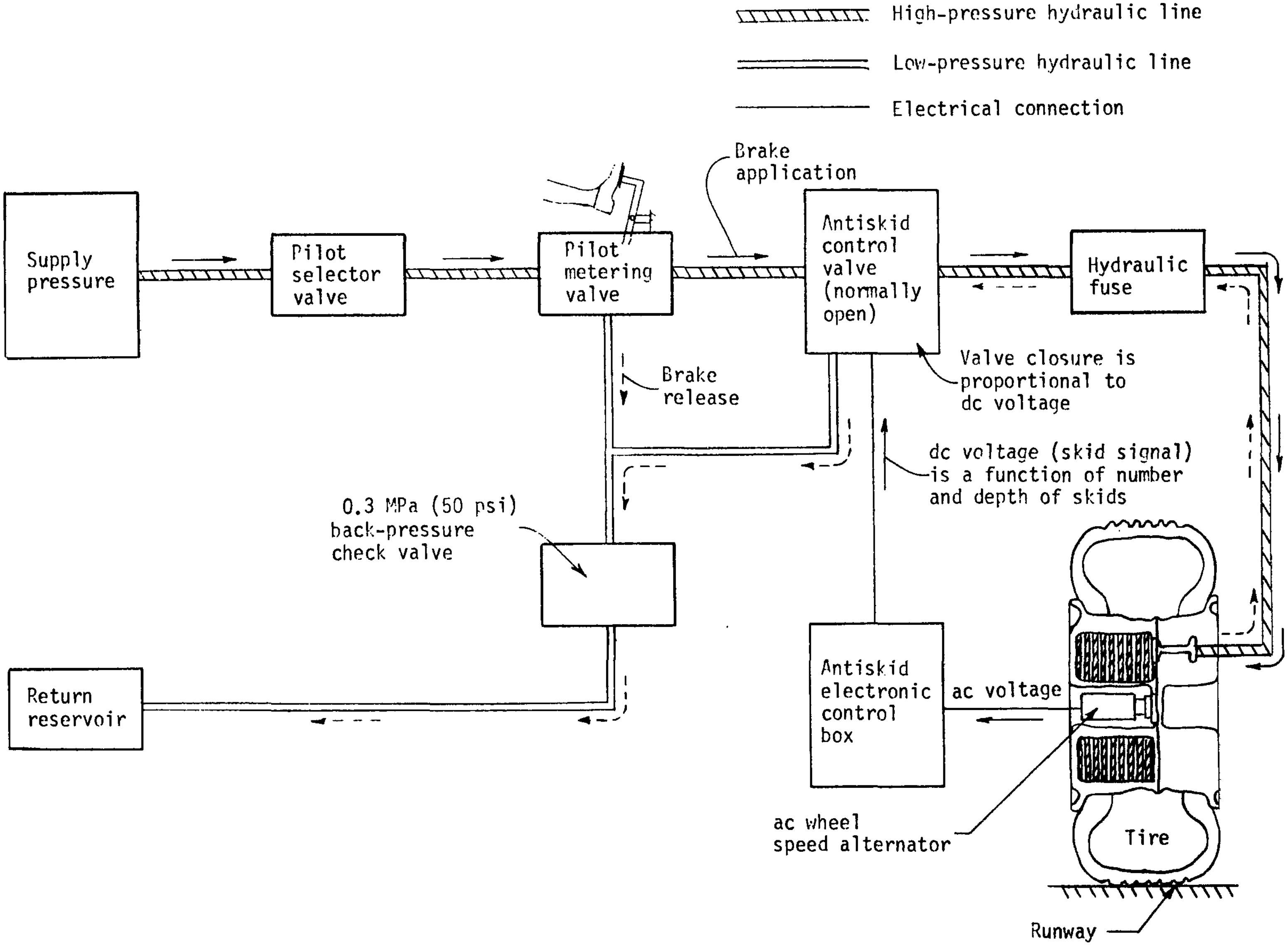

Figure 5.- Schematic of skid control system.

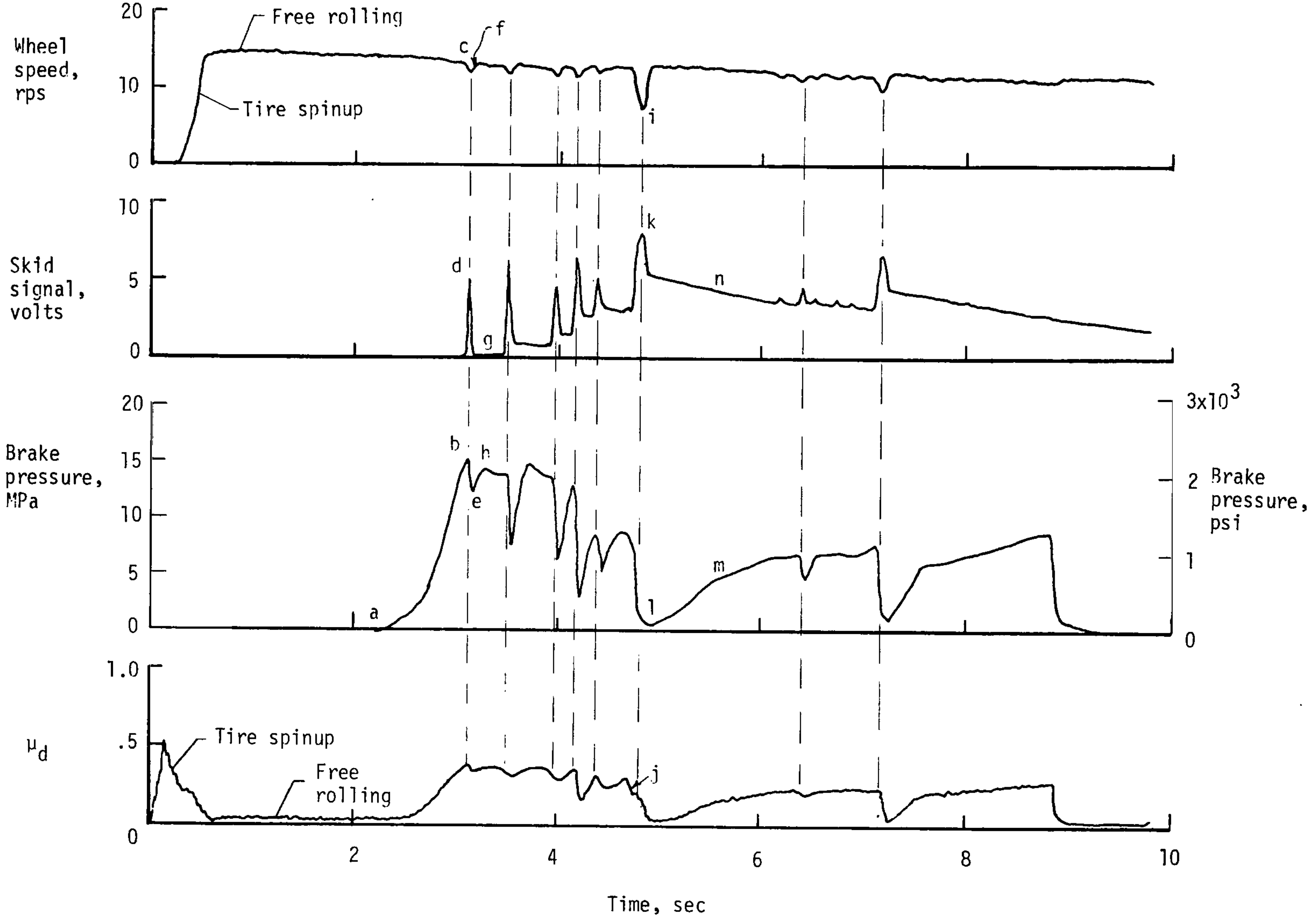

Figure 6.- Typical time histories of parameters useful in describing operation of antiskid system. Run 22; 0° yaw; 120 kN (27 000 lbf) vertical load; 14 MPa (2000 psi) brake supply pressure; new tread condition; 72 knots nominal carriage speed; natural-rain condition.

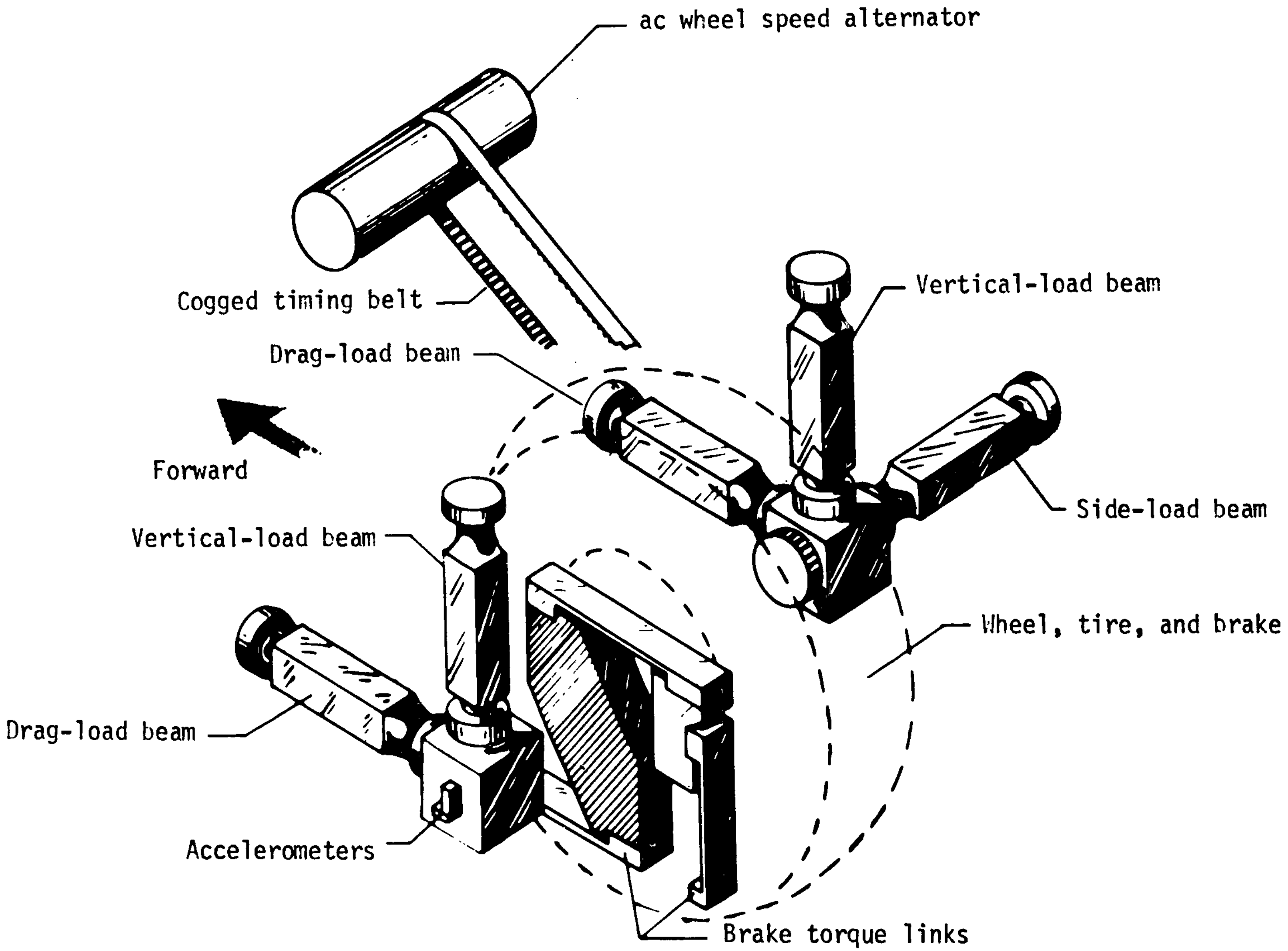

Figure 7.- Sketch of dynamometer details.

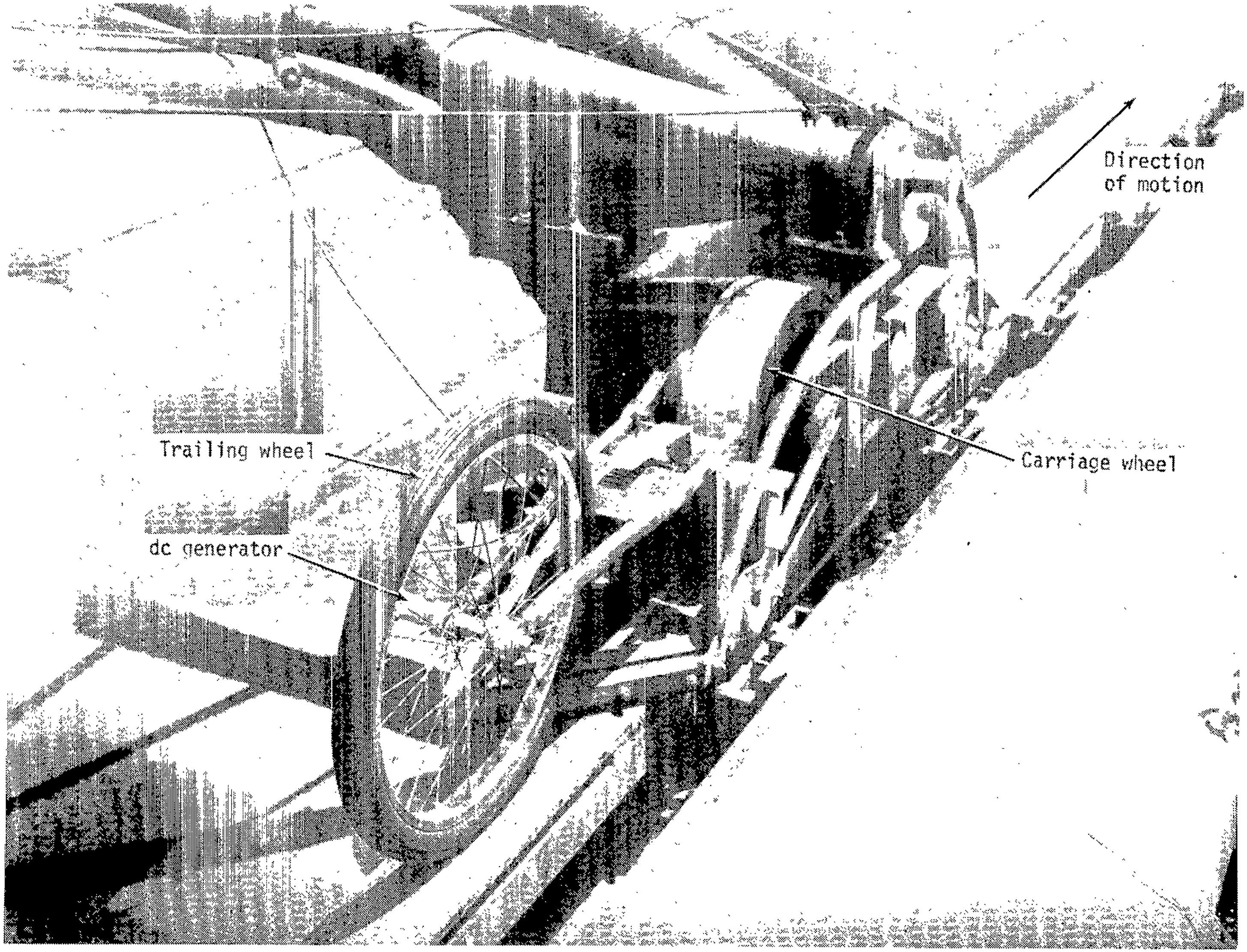

L-74-8858.1

Figure 8.- Photograph of trailing wheel used to obtain carriage speed.

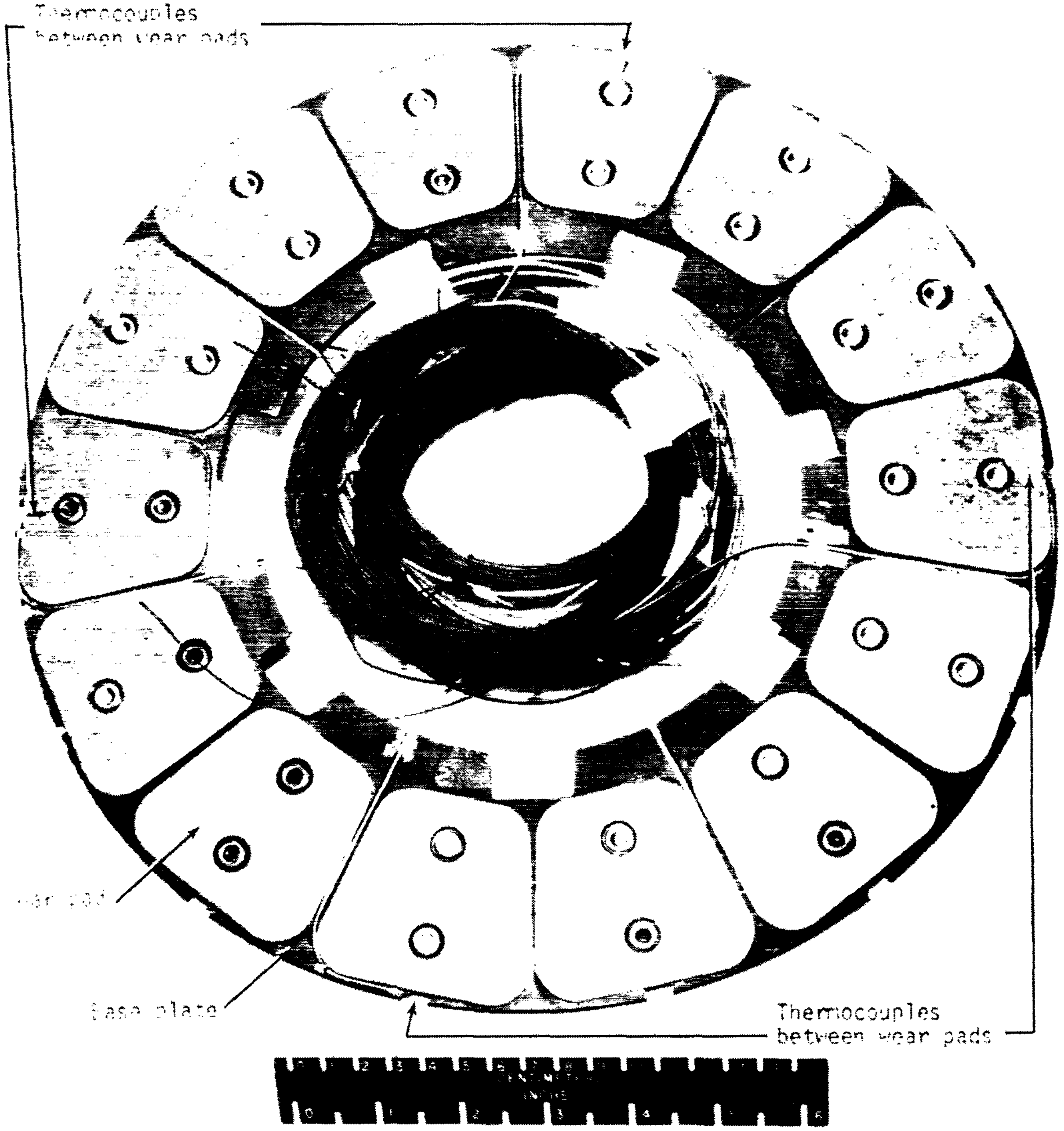

L-74-330.1

Figure 9.- Photograph of inner brake stator with thermocouples mounted between brake pads for measuring brake temperature.

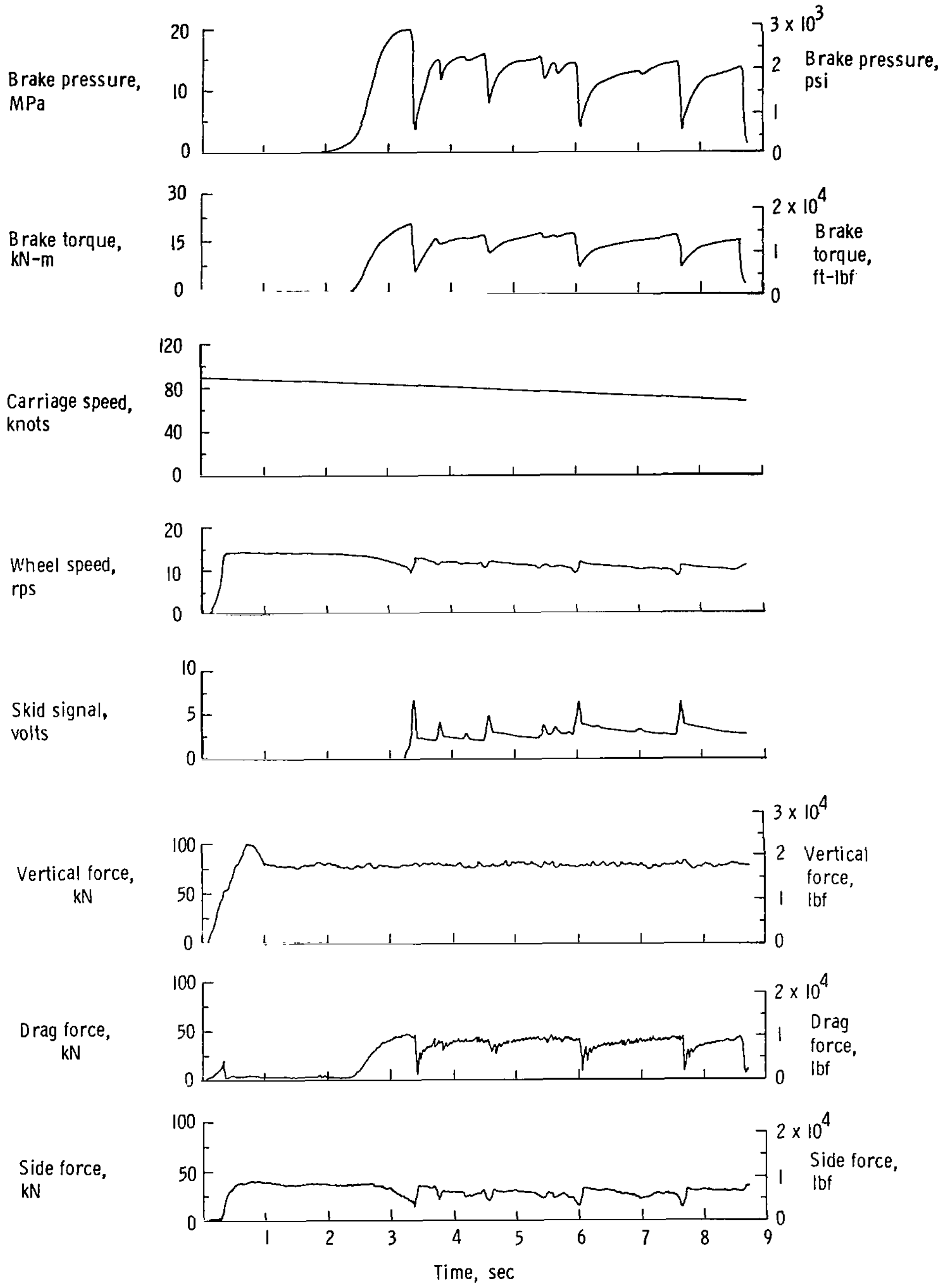

(a) Measured parameters.

Figure 10.- Typical time histories of basic test variables. Run 63; 6° yaw; 79.6 kN (17 900 lbf) vertical load; 21 MPa (3 000 psi) brake supply pressure; new tread condition; 75 knots nominal carriage speed; dry surface.

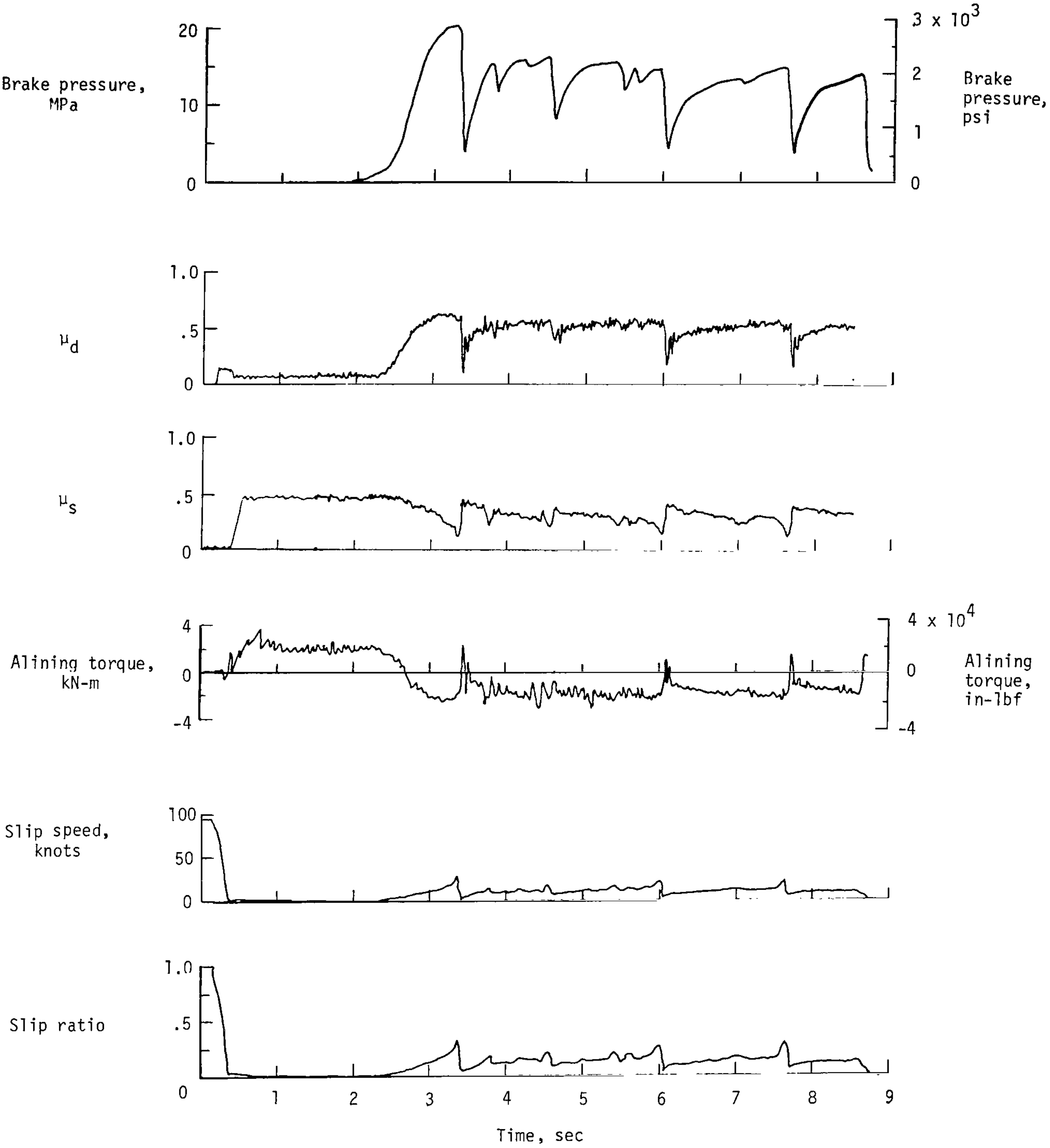

(b) Computed parameters.

Figure 10.- Concluded.

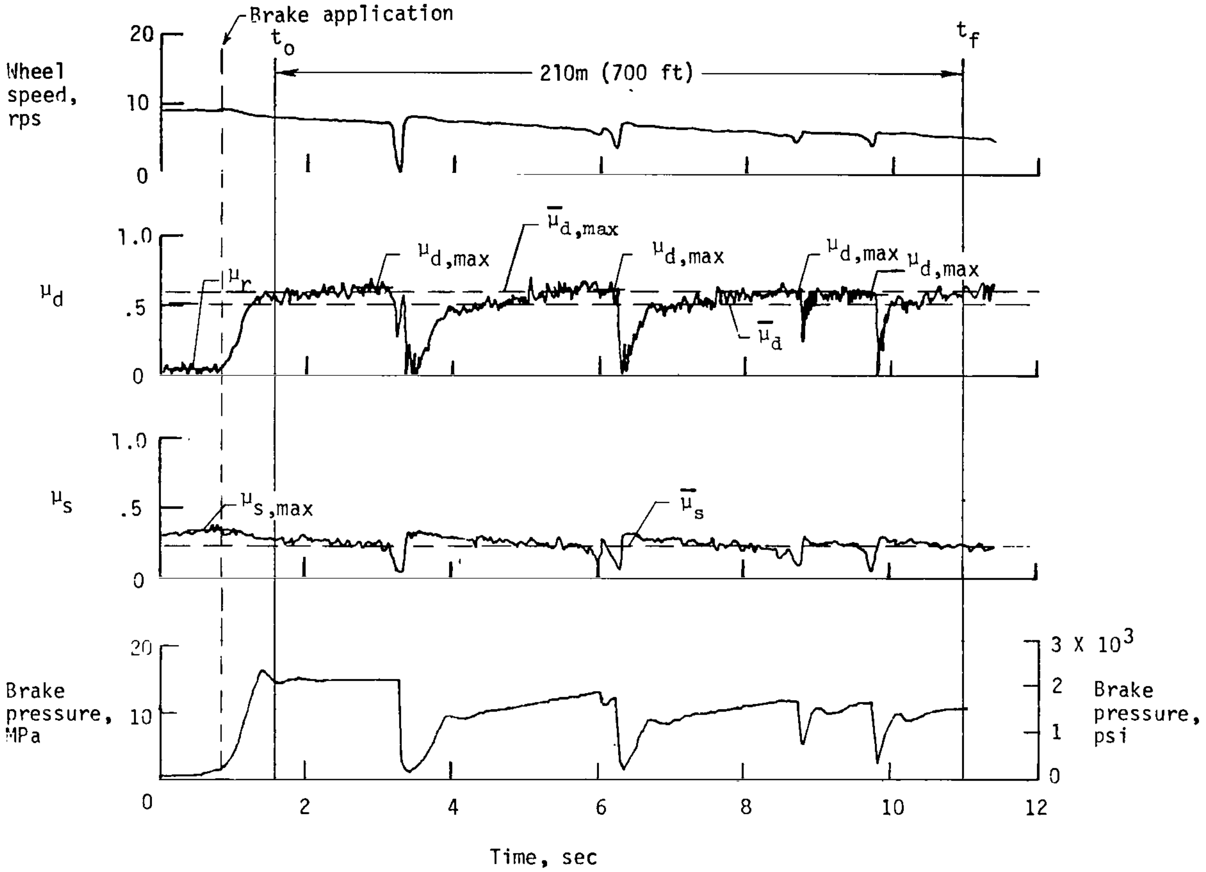

Figure 11.- Typical friction response of antiskid braking system. Run 27; 3^o yaw; 61.8 kN (13 900 lbf) vertical load; 14 MPa (2000 psi) brake supply pressure; new tread condition; 46 knots nominal carriage speed; dry surface.

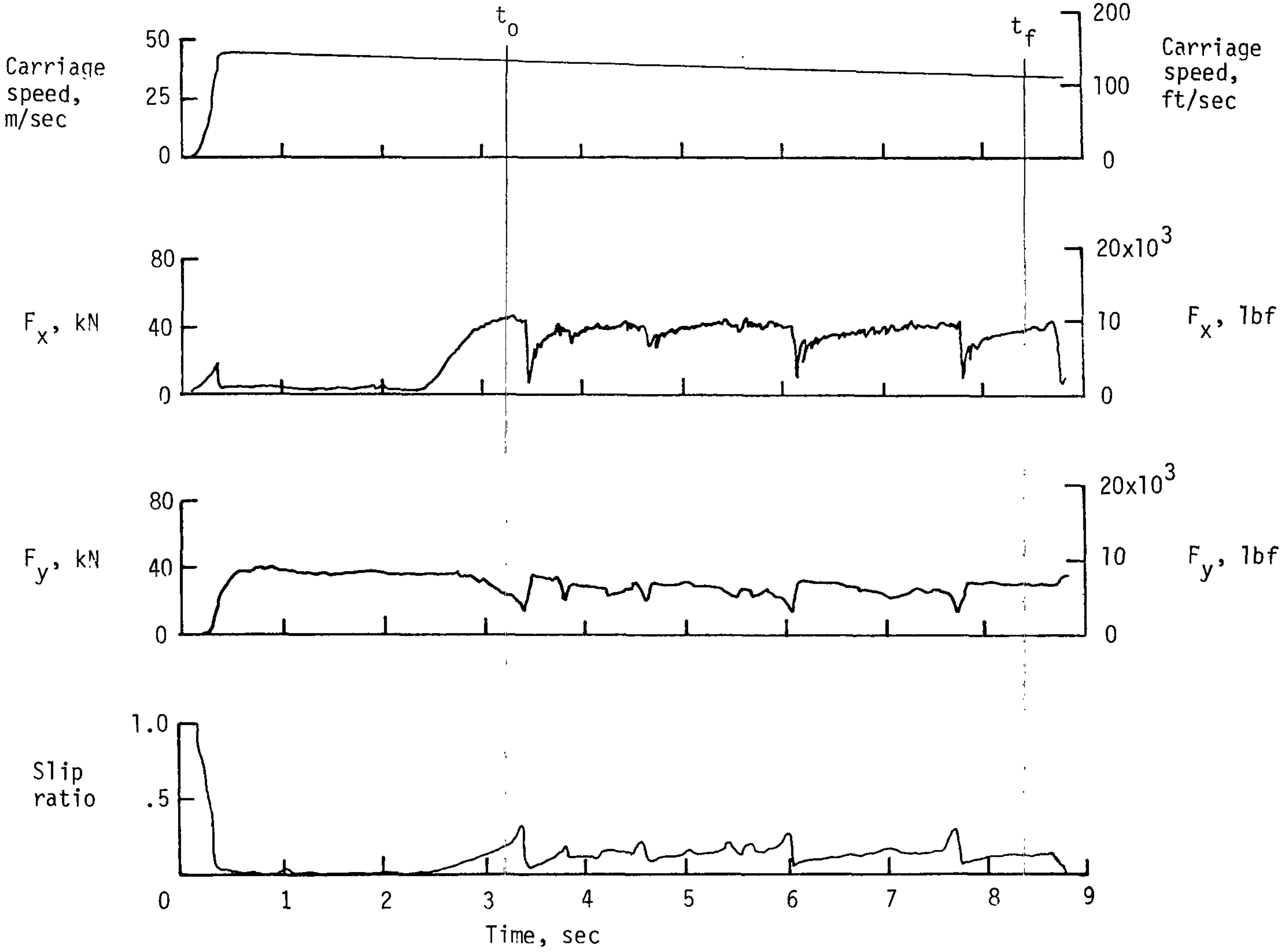

Figure 12.- Typical time histories of variables used to obtain power terms. Run 63; 6° yaw; 79.6 kN (17 900 lbf) vertical load; 21 MPa (3000 psi) brake supply pressure; new tread condition; 75 knots nominal carriage speed; dry surface.

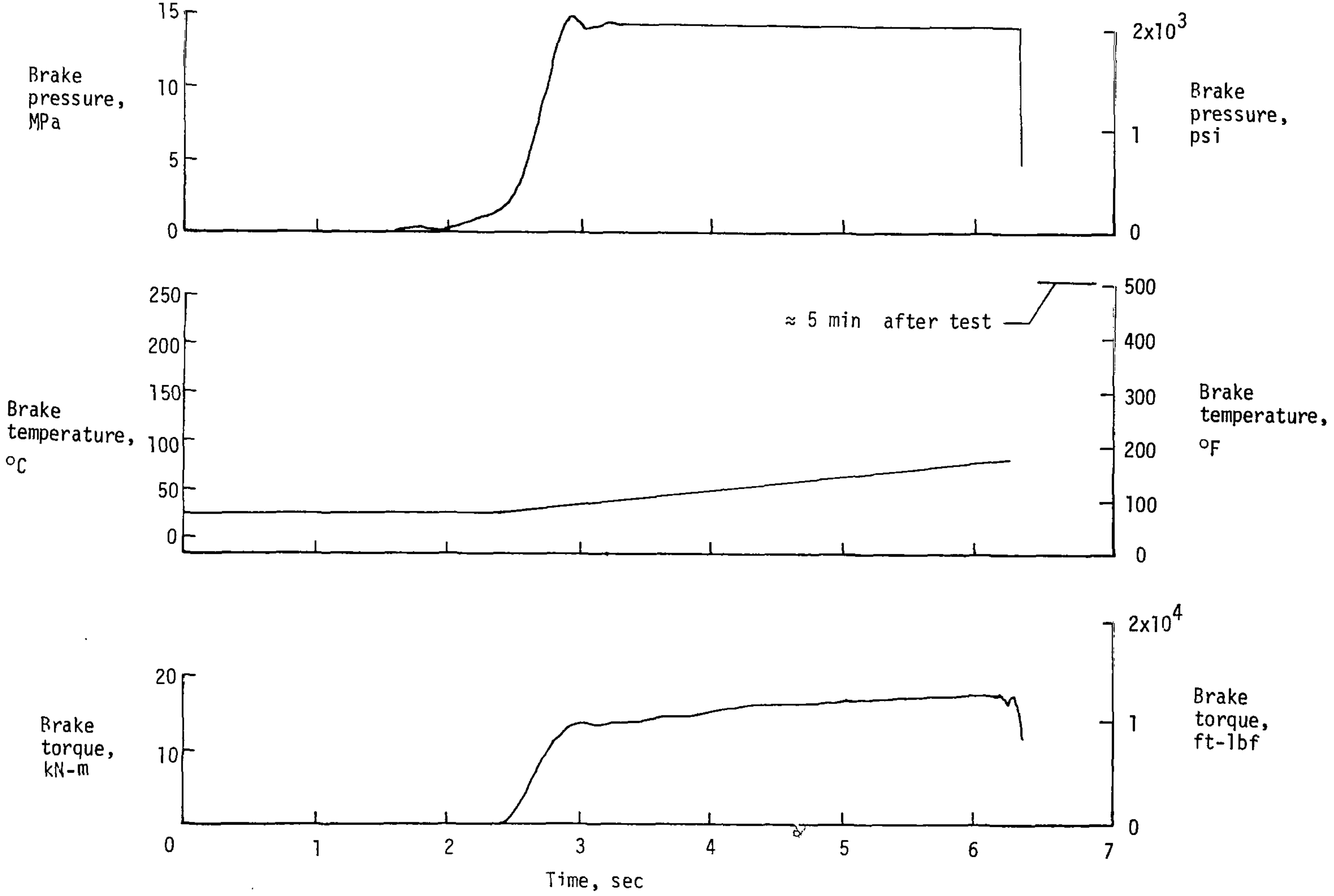

Figure 13.- Brake pressure-temperature-torque relationship. Run 29; 3° yaw; 75.6 kN (17 000 lbf) vertical load; 14 MPa (2000 psi) brake supply pressure; new tread condition; 100 knots nominal carriage speed; dry surface.

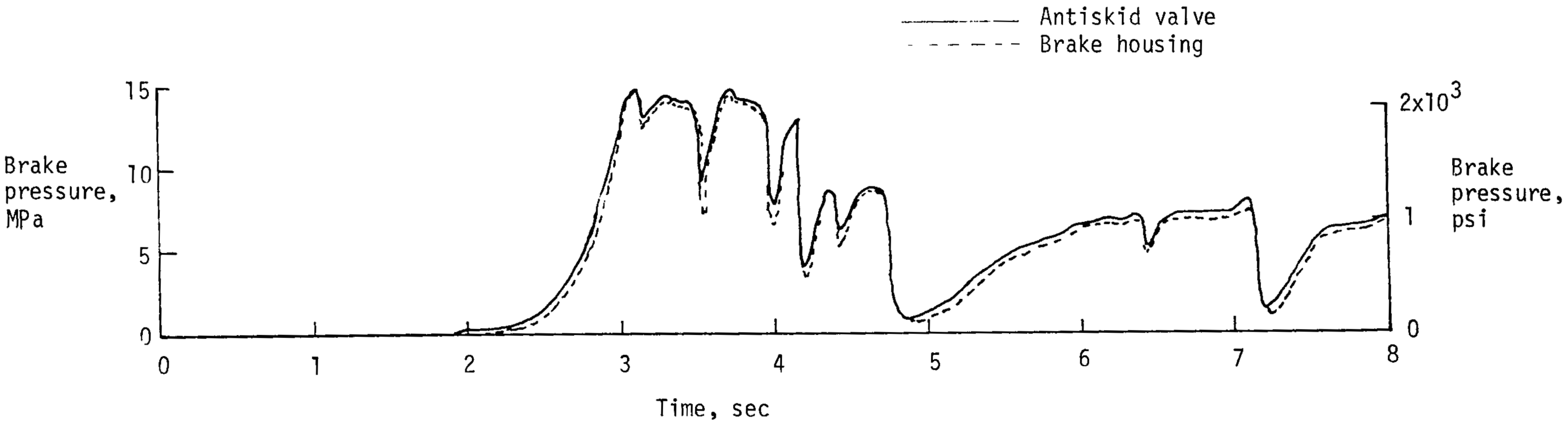

Figure 14.- Typical brake-system hydraulic response. Run 22; 0° yaw; 114.3 kN (25 700 lbf) vertical load; 14 MPa (2000 psi) brake supply pressure; new tread condition; 76 knots nominal carriage speed; flooded surface.

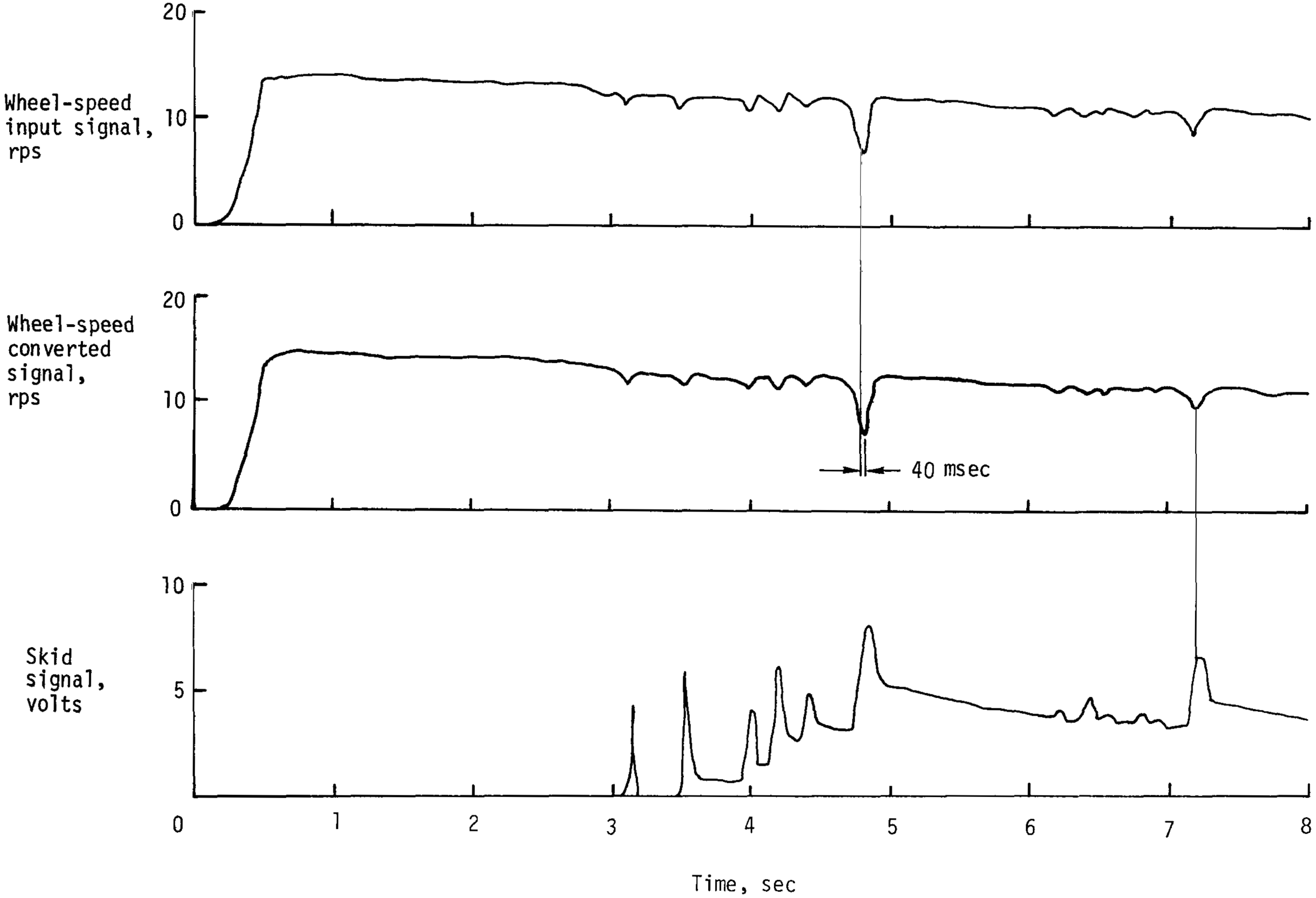

Figure 15.- Typical brake-system electronic response. Run 22; 0° yaw; 114.3 kN (25 700 lbf) vertical load; 14 Mpa (2000 psi) brake supply pressure; new tread; 76 knots nominal carriage speed; flooded surface.

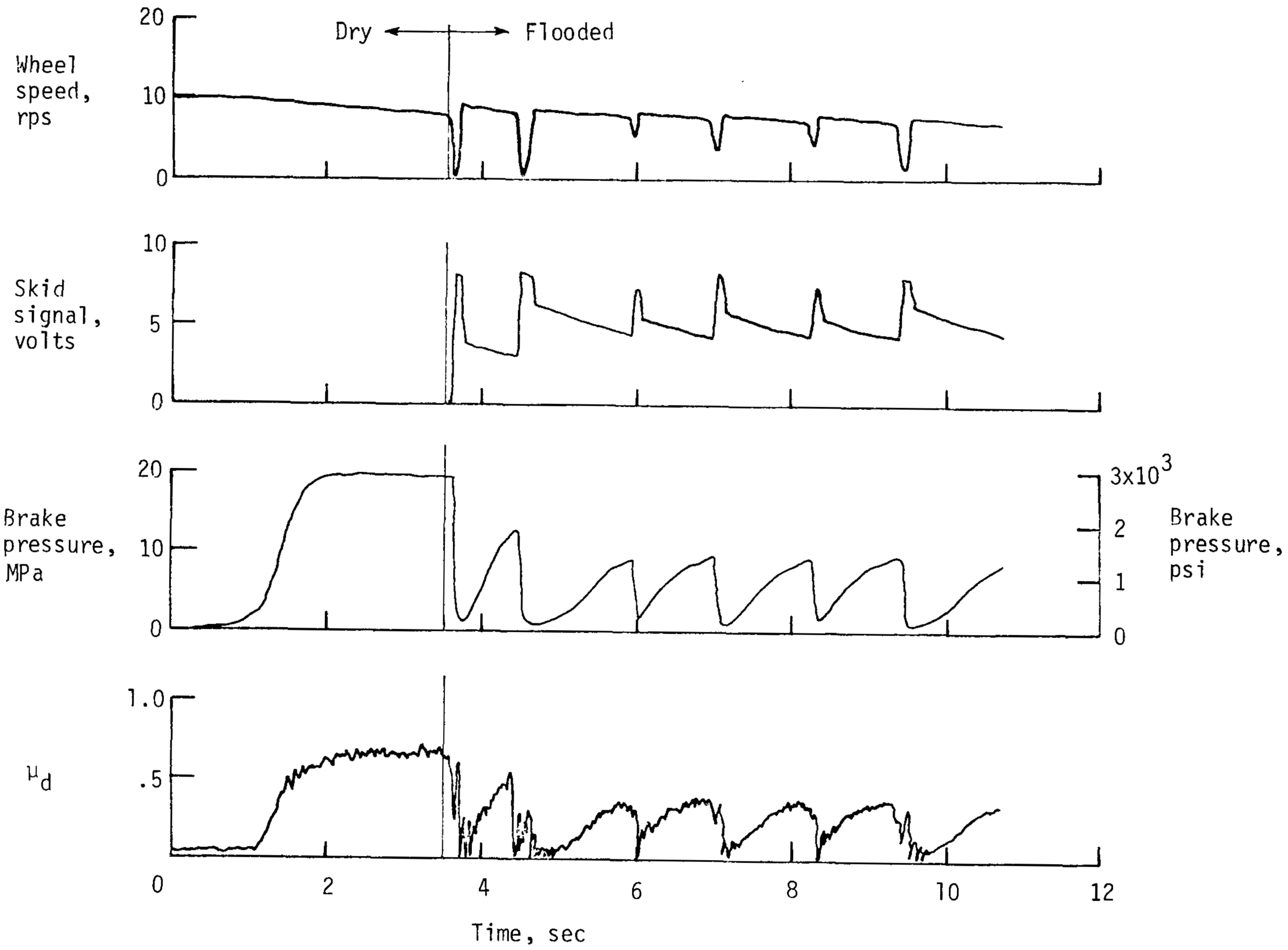

(a) Dry-to-flooded transition; 49 knots nominal carriage speed; run 61.

Figure 16.- Typical antiskid system response to transient runway conditions. 0° yaw; 79.2 kN (17 800 lbf) nominal vertical load; 21 MPa (3000 psi) brake sypply pressure; new tread condition.

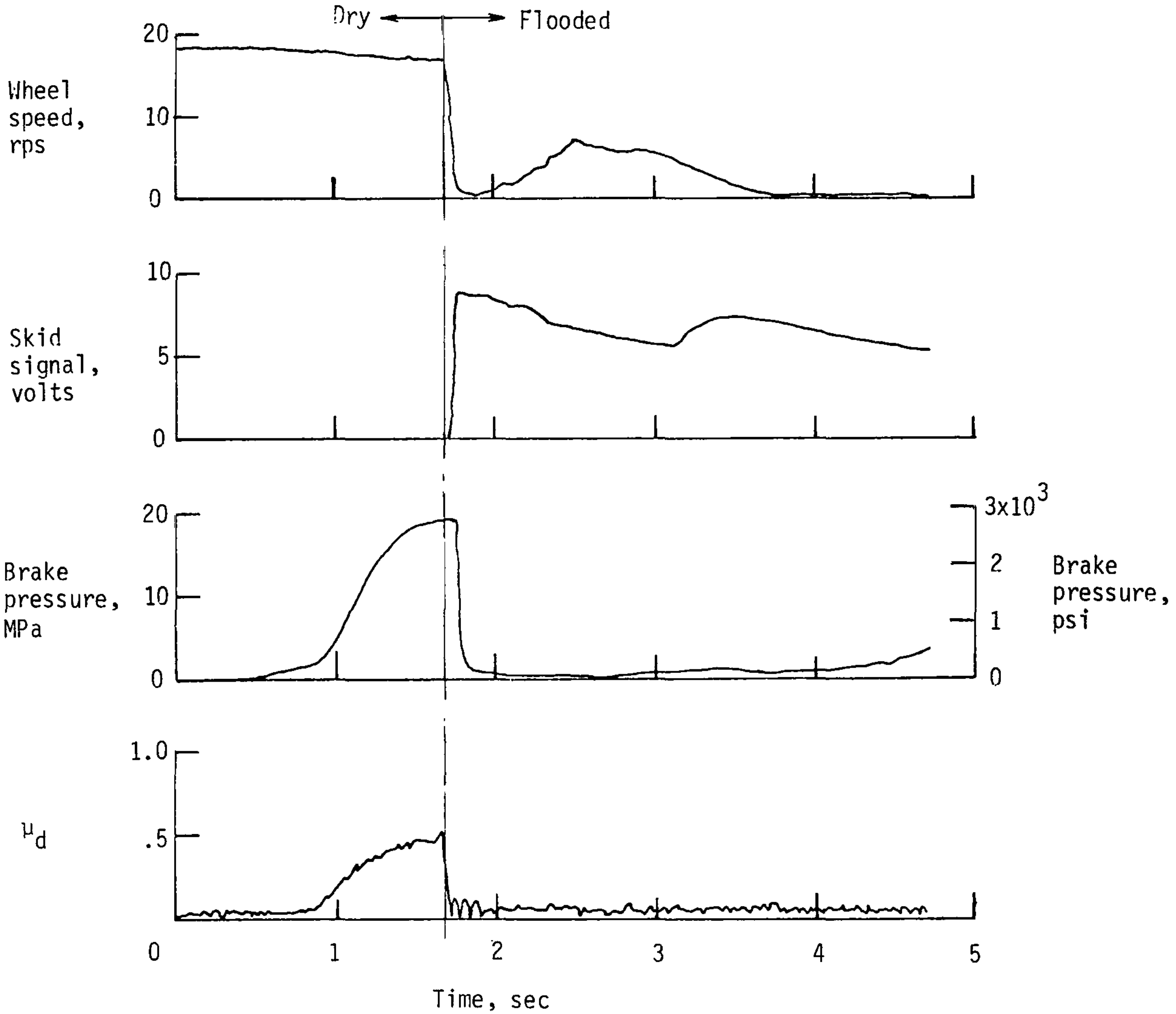

(b) Dry-to-flooded transition; 103 knots nominal carriage speed; run 62.

Figure 16.- Continued.

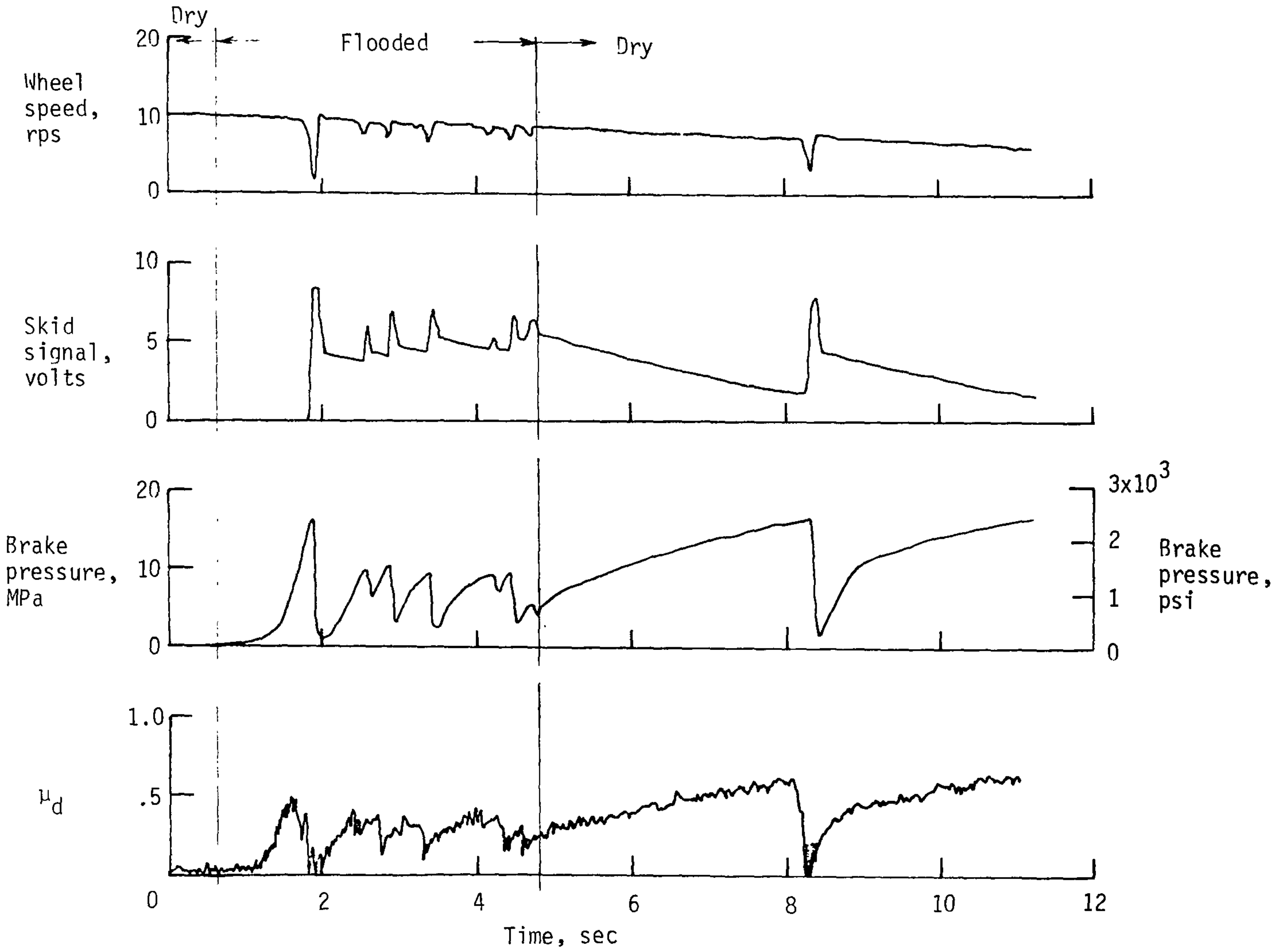

(c) Flooded-to-dry transition; 50 knots nominal carriage speed; run 59.

Figure 16.- Continued.

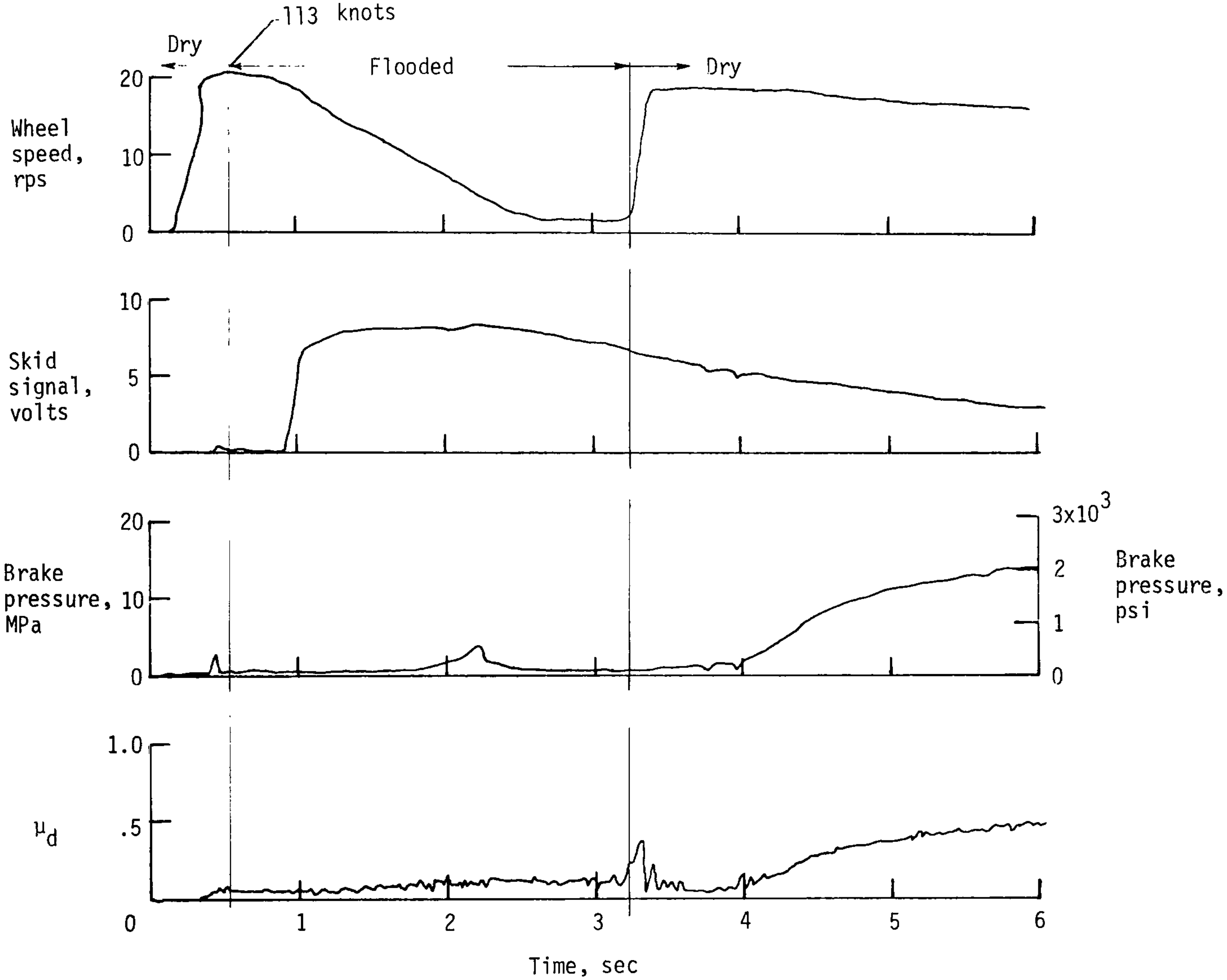

(d) Flooded-to-dry transition; 101 knots nominal carriage speed; run 60.

Figure 16.- Concluded.

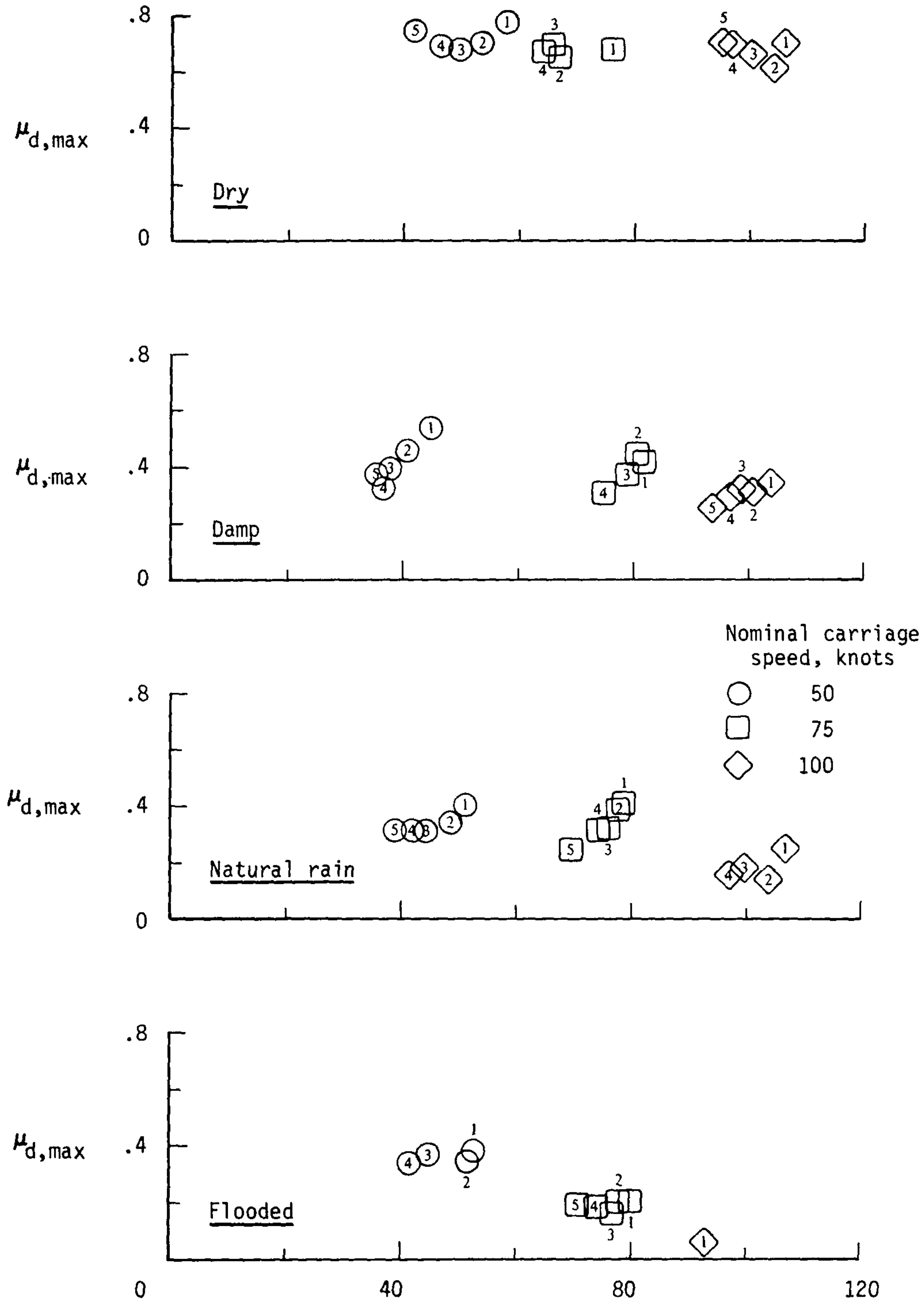

Figure 17.- Effect of cyclic braking on $\mu_{d,max}$. (Individual brake cycles are numbered sequentially for each test condition.)

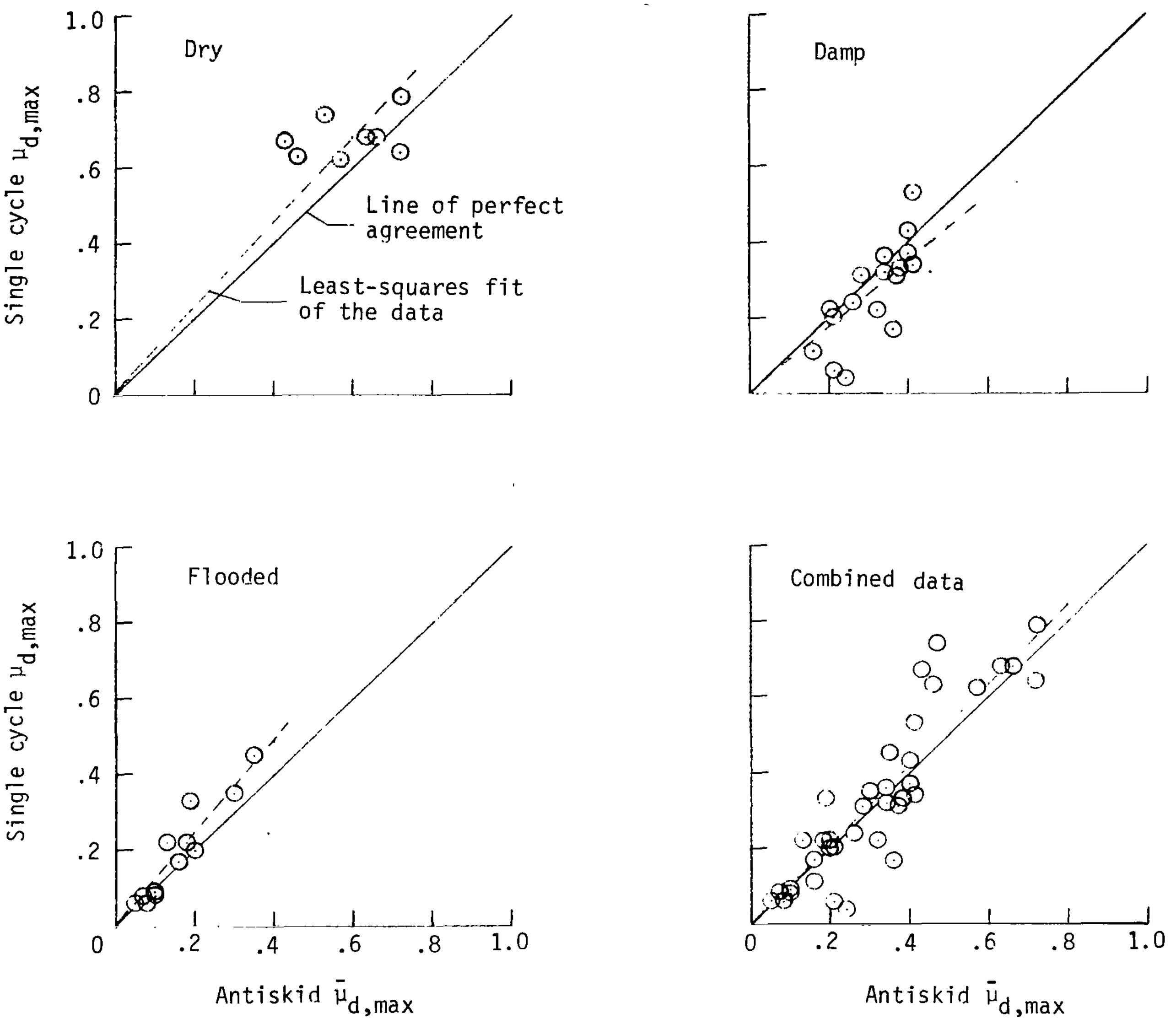

Figure 18.- A comparison between values of the maximum available friction coefficient for single-cycle braking and antiskid braking.

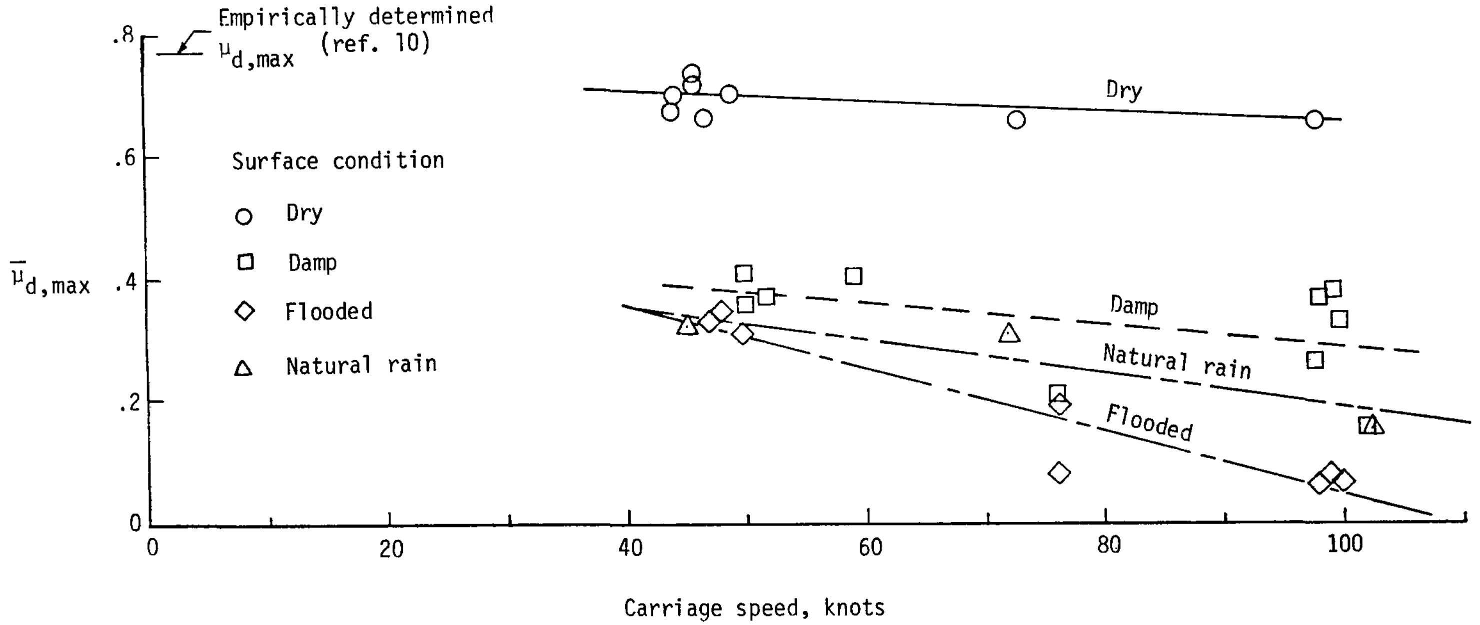

Figure 19.- Average maximum friction coefficients available for the various surface conditions. 0° yaw; new tread condition.

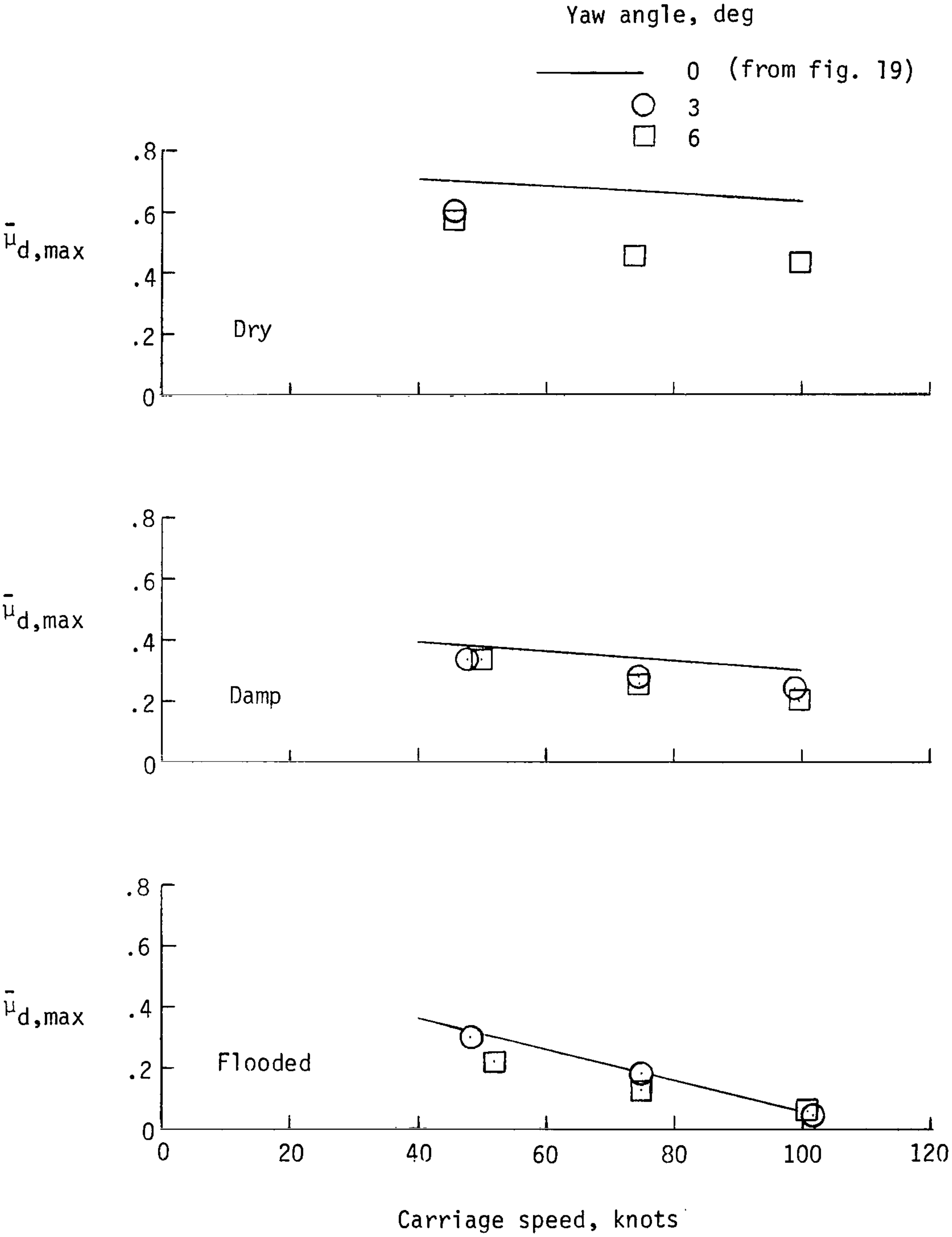

Figure 20.- Average maximum friction coefficients available for various yaw angles. New tread condition.

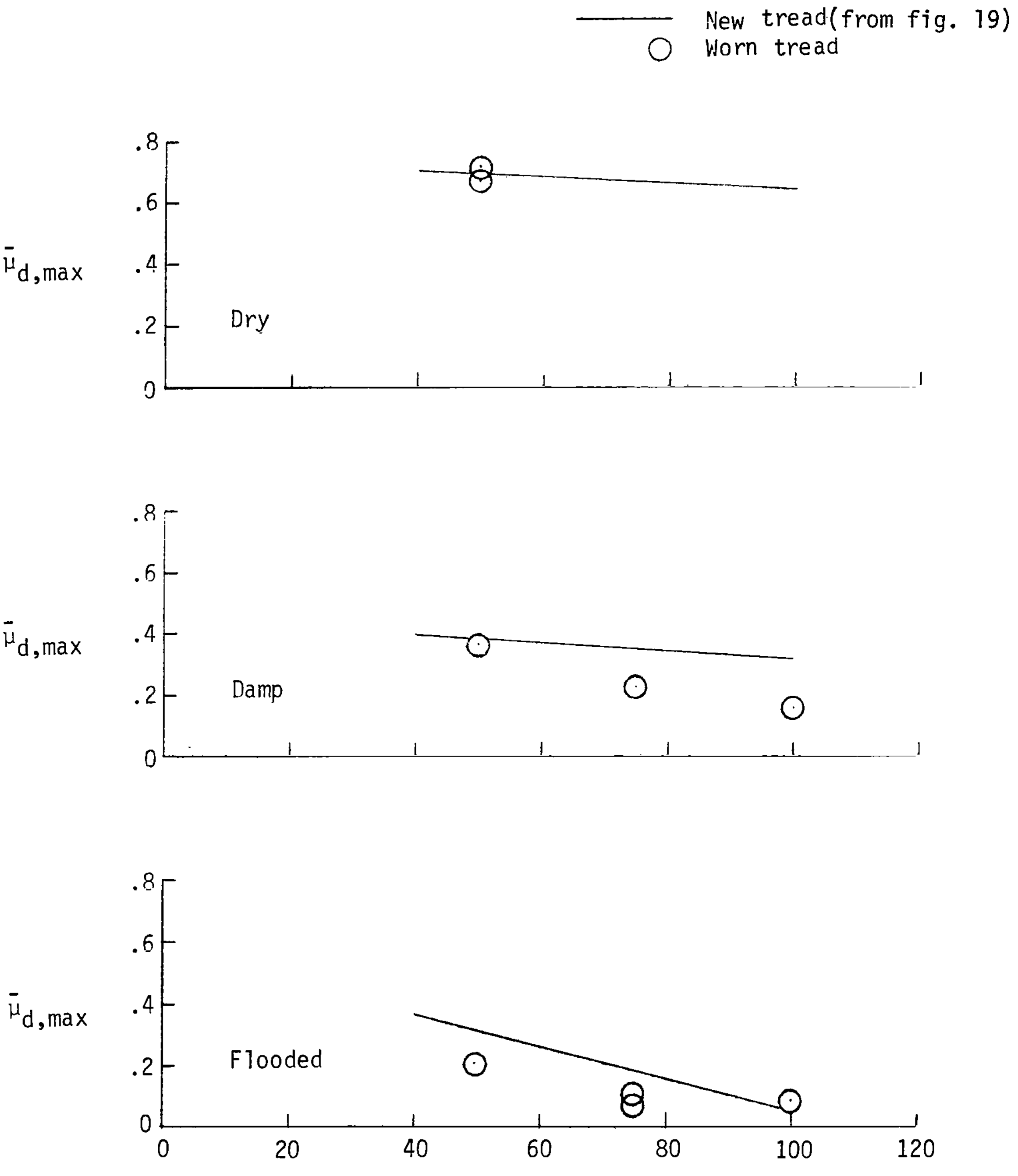

Figure 21.- Effect of tread wear on average maximum available friction coefficient. 0° yaw.

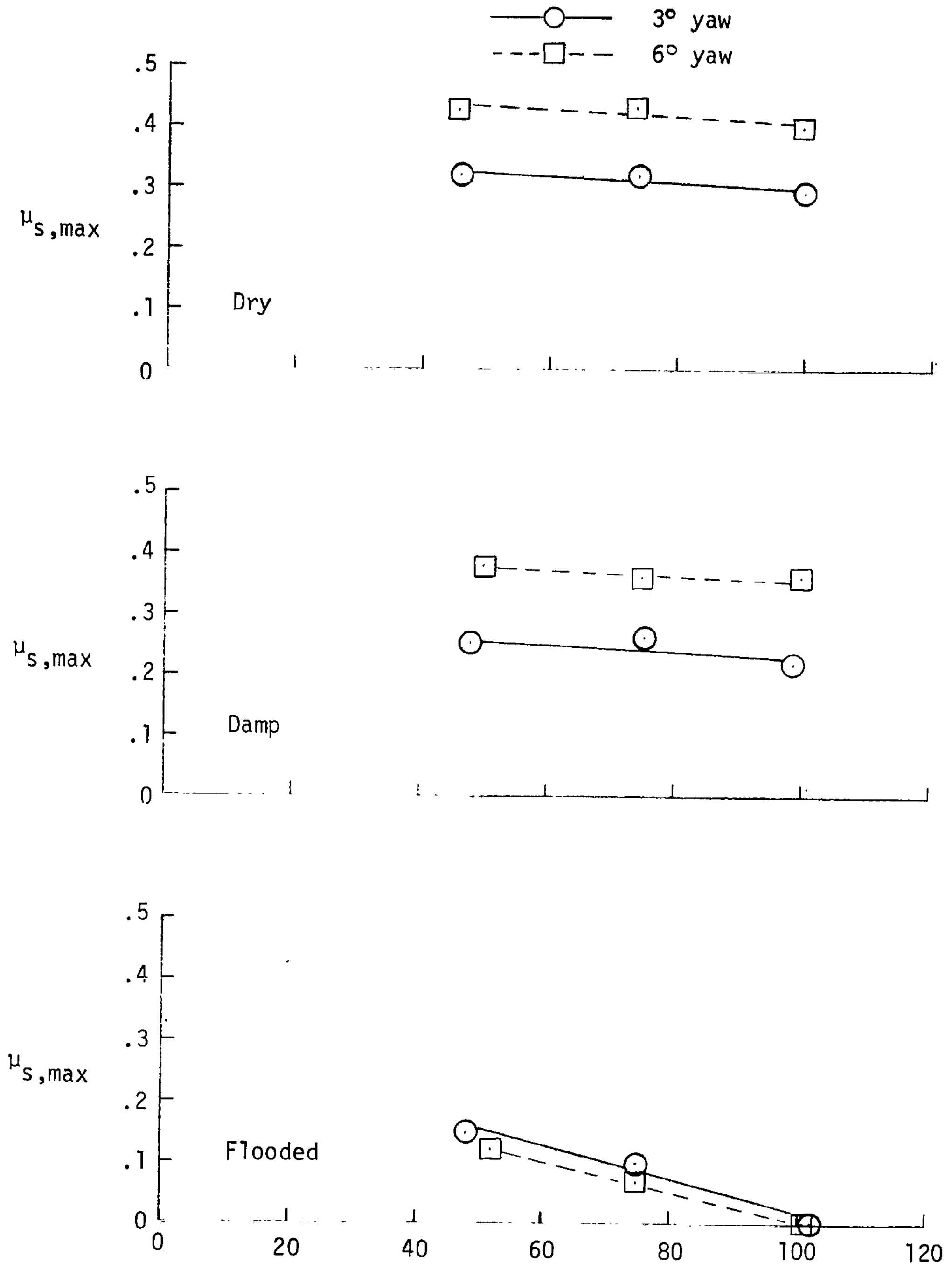

Figure 22.- Maximum unbraked side-force coefficient for 3° and 6° yaw. New tread condition.

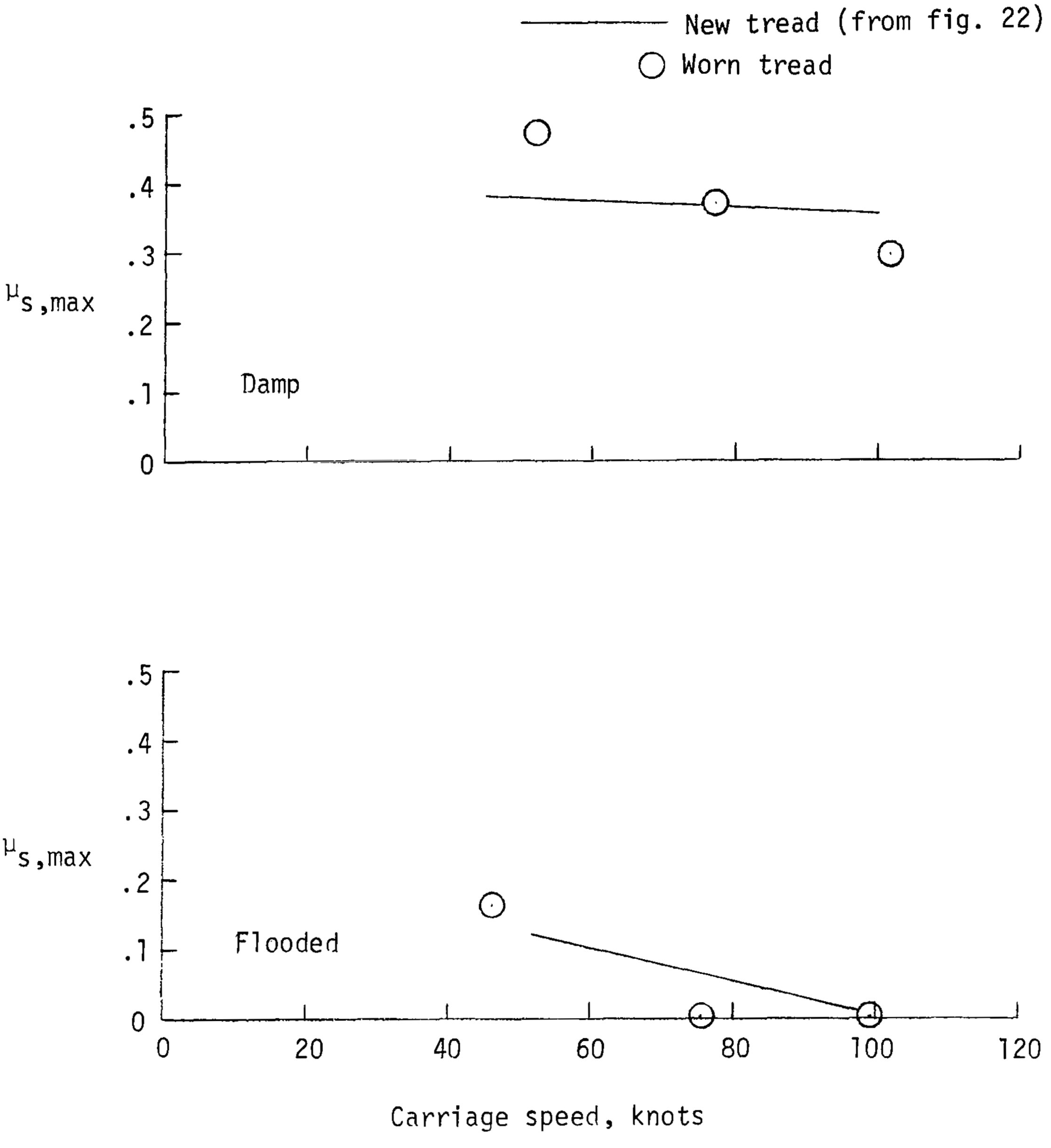

Figure 23.- Effect of tread wear on maximum side friction coefficient for 6° yaw.

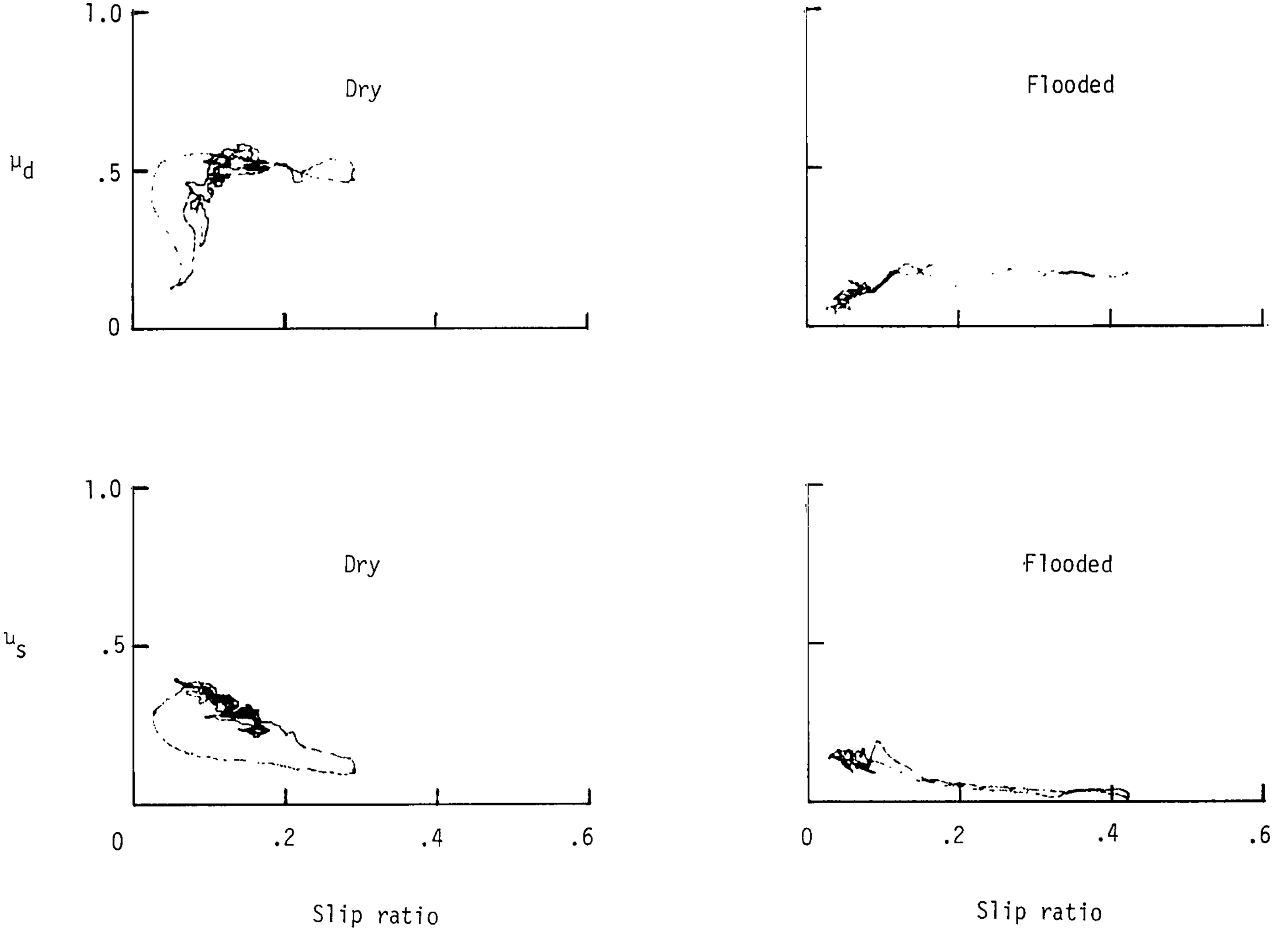

(a) Run 63.

(b) Run 64.

Figure 24.- Friction coefficients during cyclic braking. 6° yaw; 78.3 kN (17 800 lbf) nominal vertical load; 21 MPa (3000 psi) brake supply pressure; new tread condition.

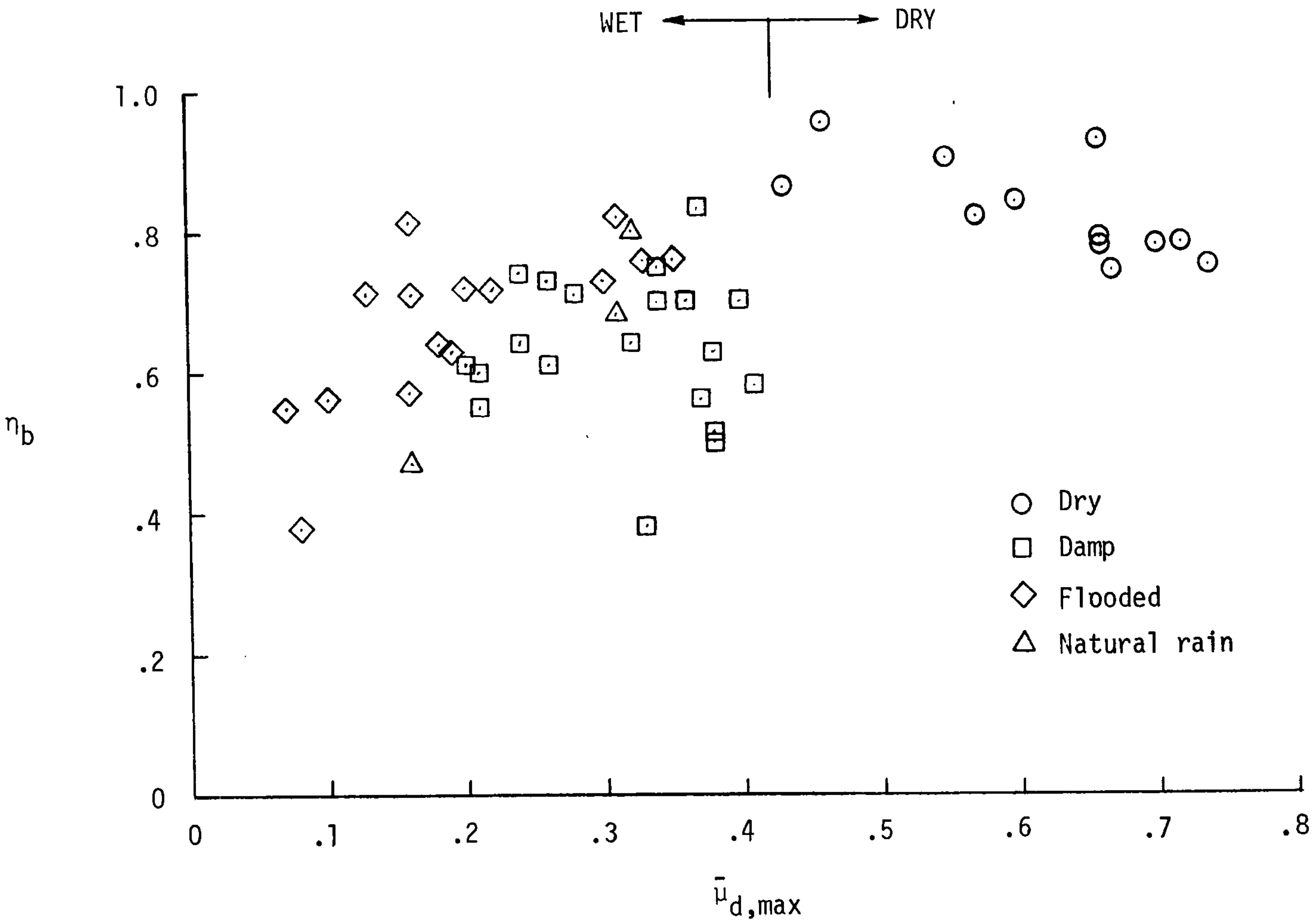

Figure 25.- Antiskid braking performance ratios for various surface conditions.

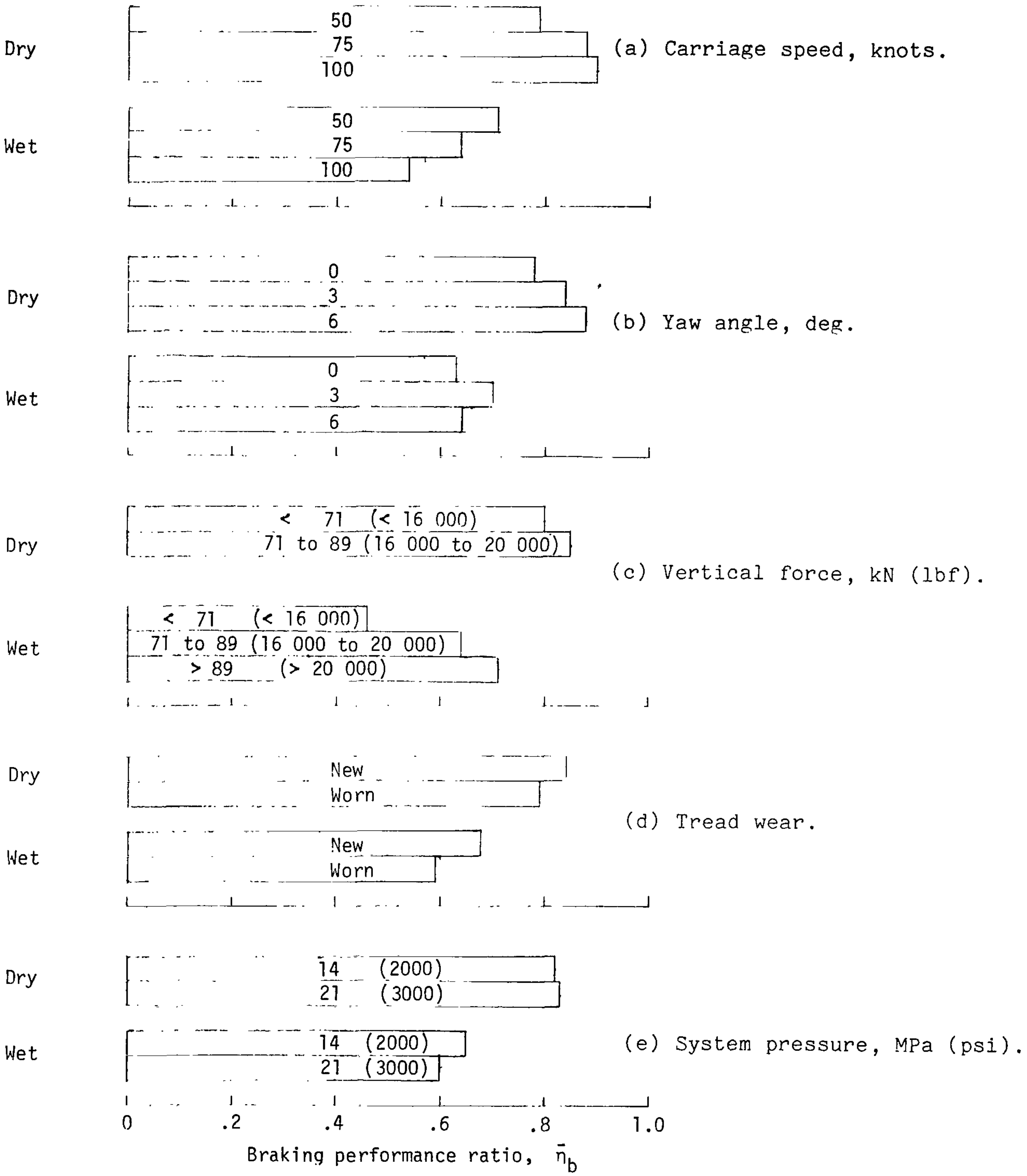

Figure 26.- Effect of test parameter variations on antiskid braking performance ratio.

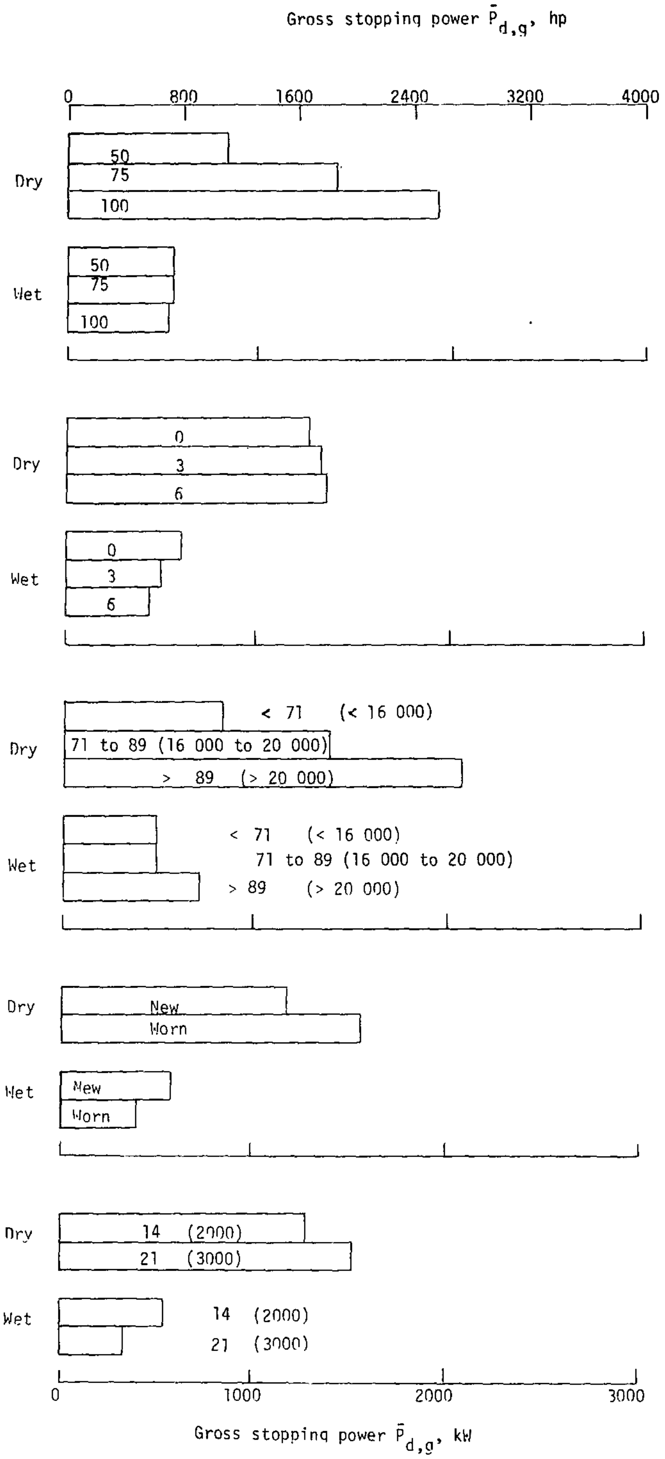

(a) Carriage speed, knots.

(b) Yaw angle, deg.

(c) Vertical force, kN (lbf).

(d) Tread wear.

(e) System pressure, MPa (psi).

Figure 27.- Effect of test parameter variations on gross stopping power.

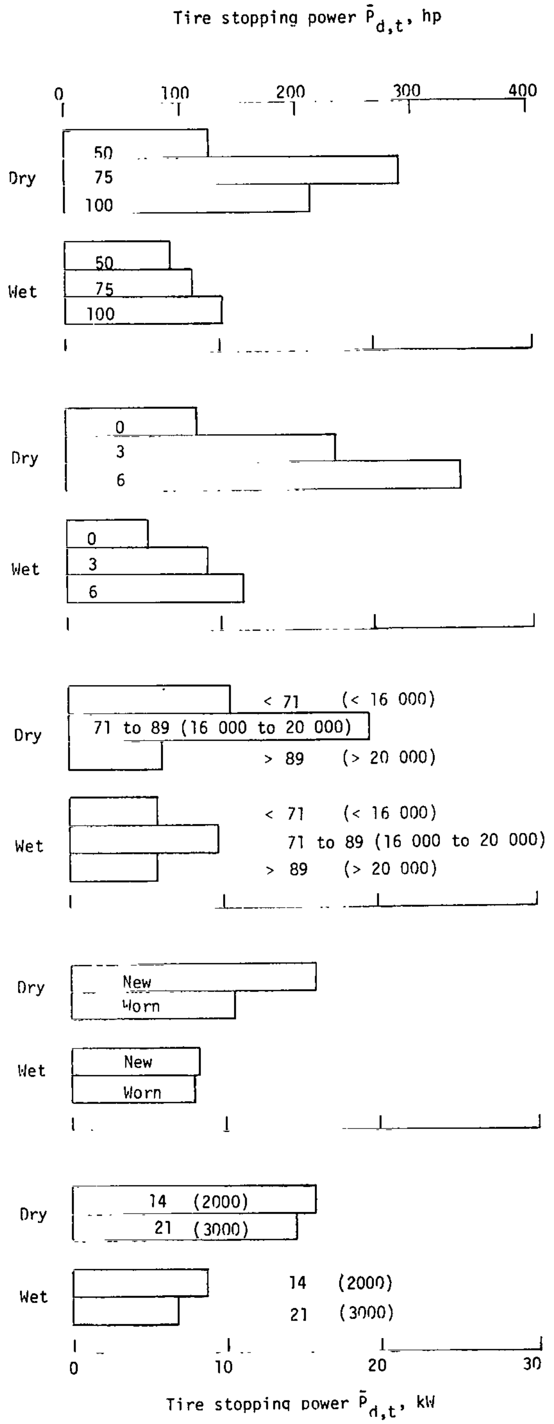

(a) Carriage speed, knots.

(b) Yaw angle, deg.

(c) Vertical force, kN (lbf).

(d) Tread wear.

(e) System pressure, MPa (psi).

Figure 28.- Effect of test parameter variations on tire stopping power.

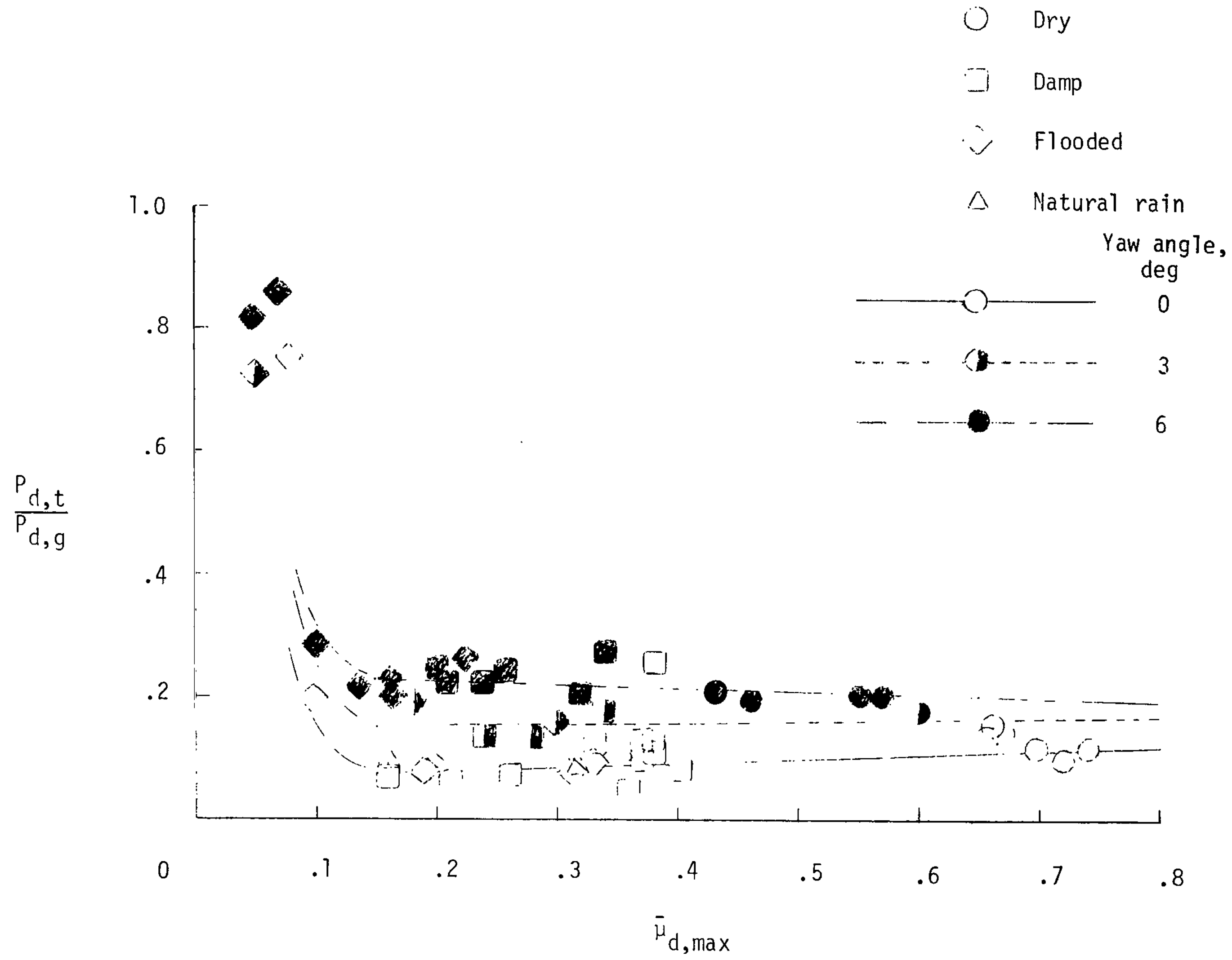

Figure 29.- Ratio of tire stopping power to gross stopping power for various surface conditions and yaw angles.

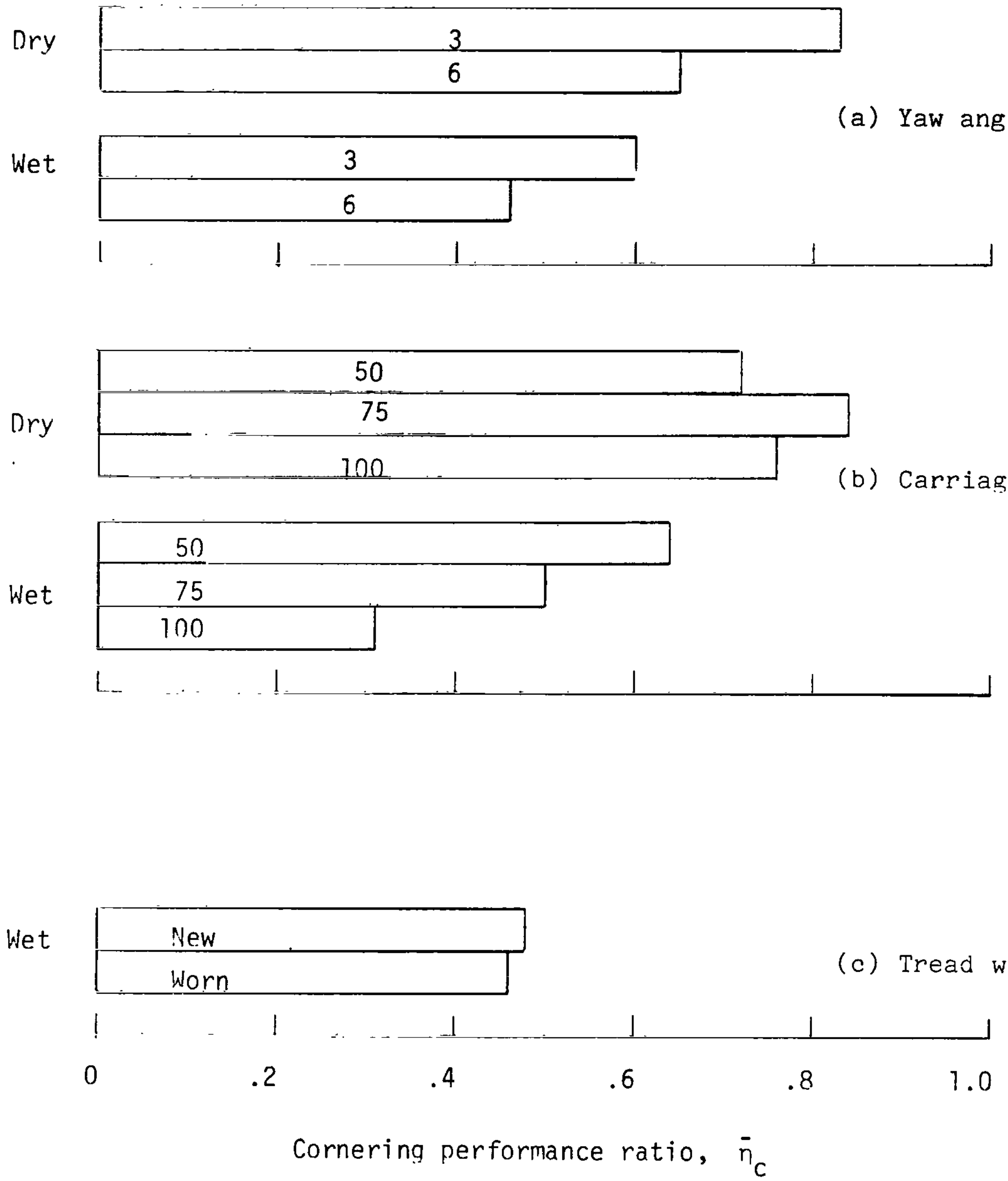

(a) Yaw angle, deg.

(b) Carriage speed, knots.

(c) Tread wear.

Figure 30.- Effect of test parameter variations on cornering performance ratio.

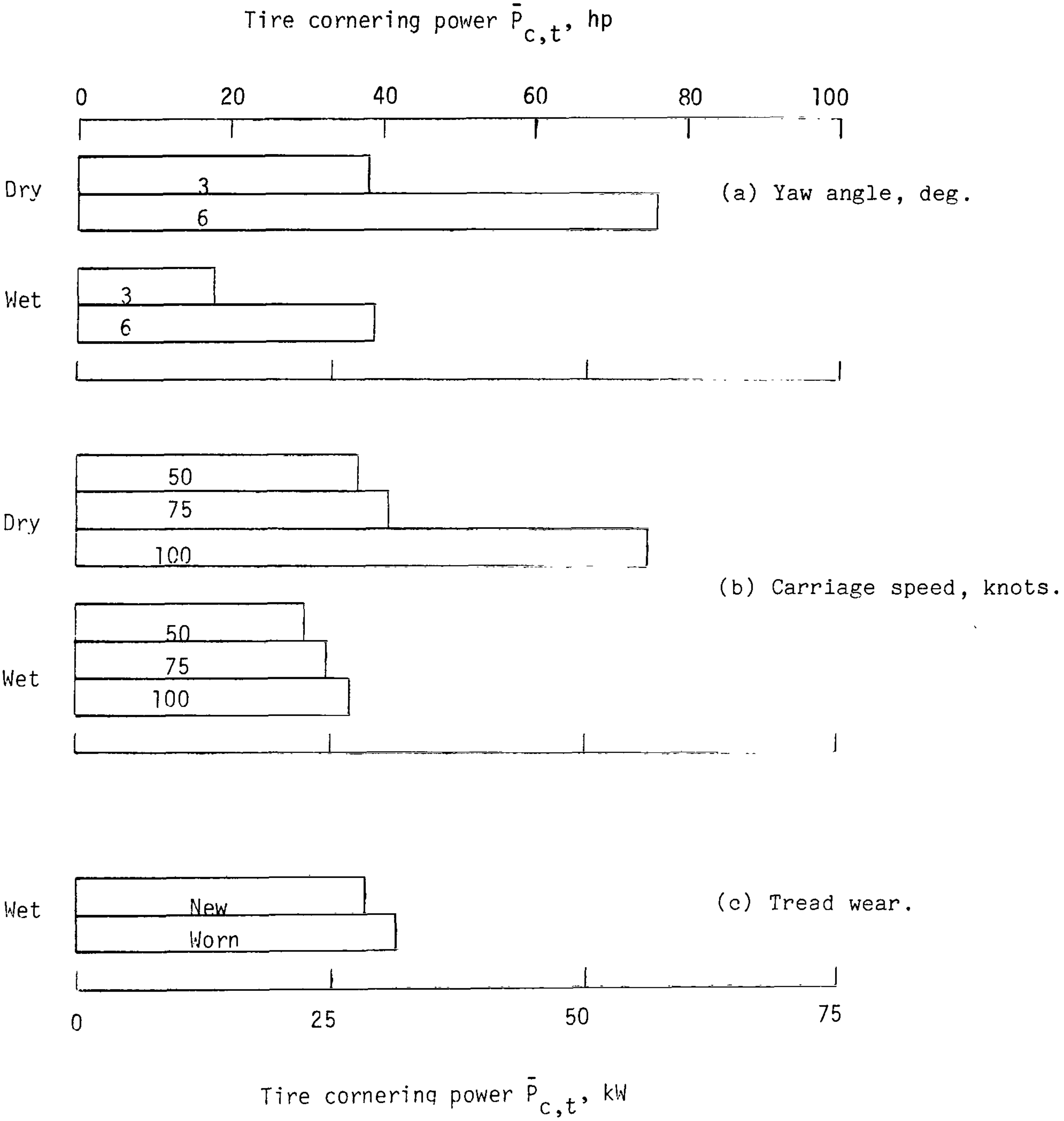

Figure 31.- Effect of test parameter variations on tire cornering power.

APPENDIX

TIME-HISTORY PLOTS

Time-history plots of eight parameters describing the behavior of the antiskid system during each test condition are presented in this appendix. The eight parameters are wheel speed, skid signal, brake pressure, brake torque, drag-force friction coefficient, side-force friction, alining torque, and slip ratio. The time histories are given for the convenience of the user in plotting the data and are presented in figures A1 to A68.

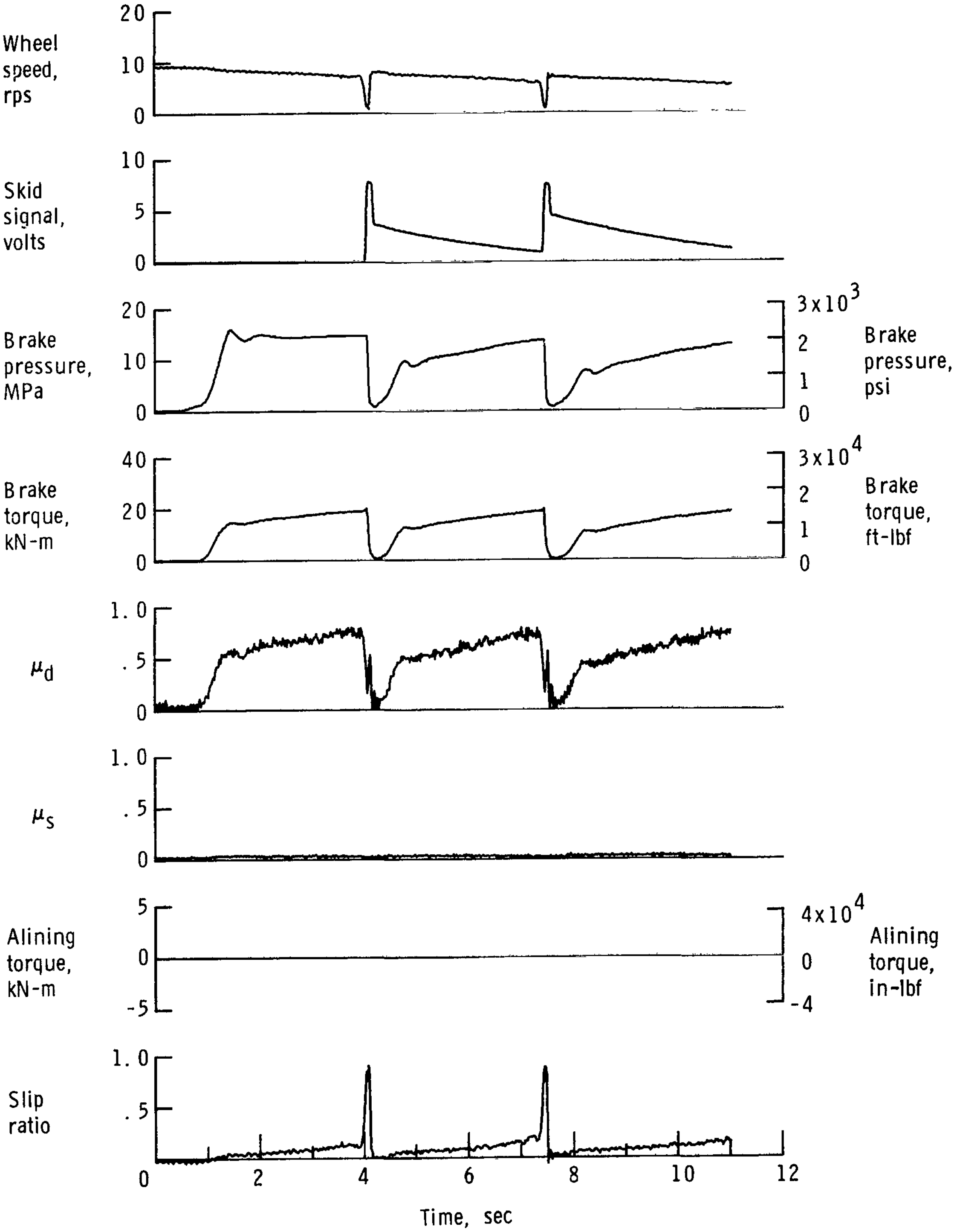

Figure A1.- Time histories for run 1; nominal carriage speed, 46 knots; vertical load, 54.7 kN (12 300 lbf); yaw angle, 0°; surface condition, dry; tire condition, new; brake pressure, 14 MPa (2000 lbf/in^2).

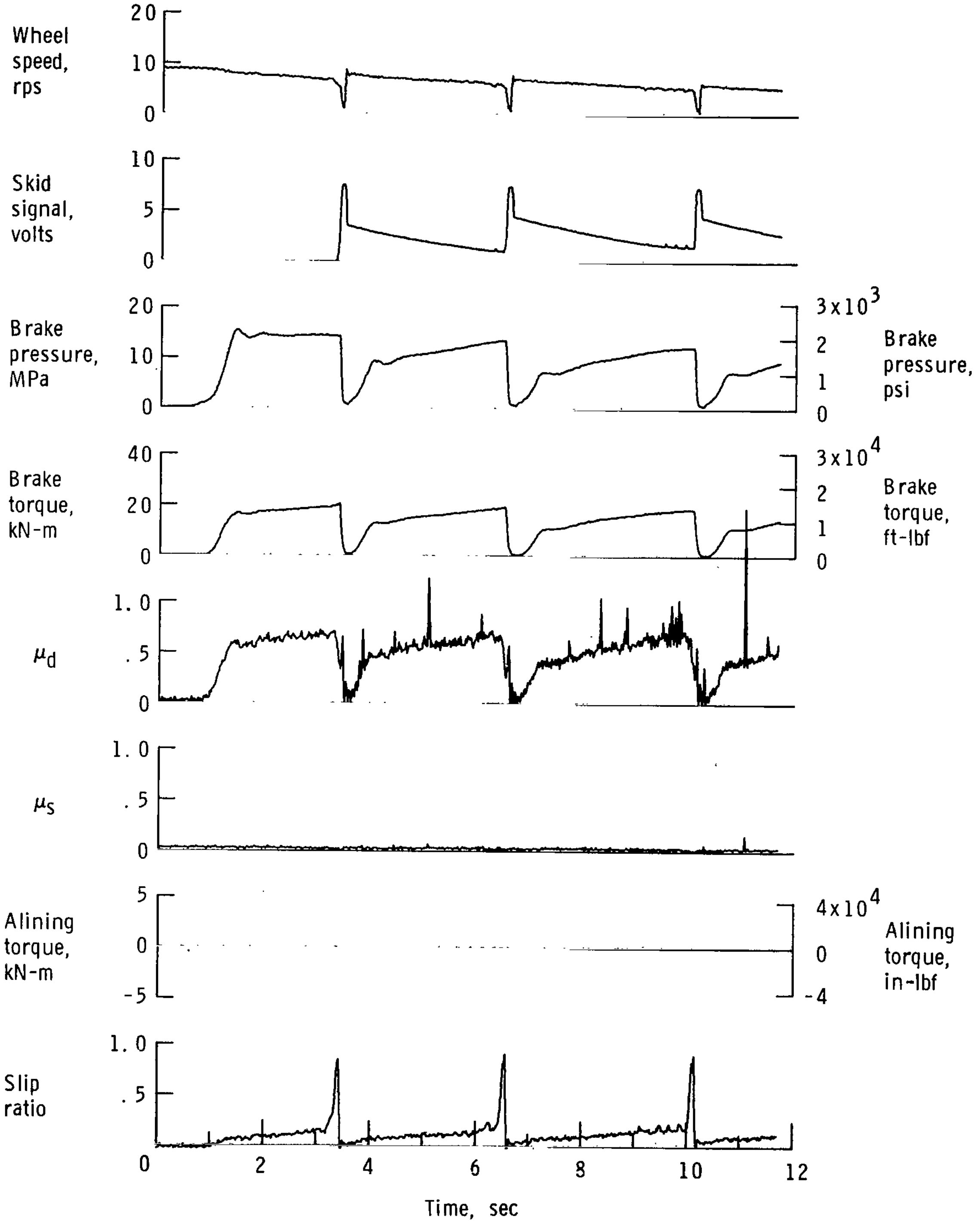

Figure A2.- Time histories for run 2; nominal carriage speed, 44 knots; vertical load, 59.6 kN (13 400 lbf); yaw angle, 0°; surface condition, dry; tire condition, new; brake pressure, 14 MPa (2000 lbf/in^2).

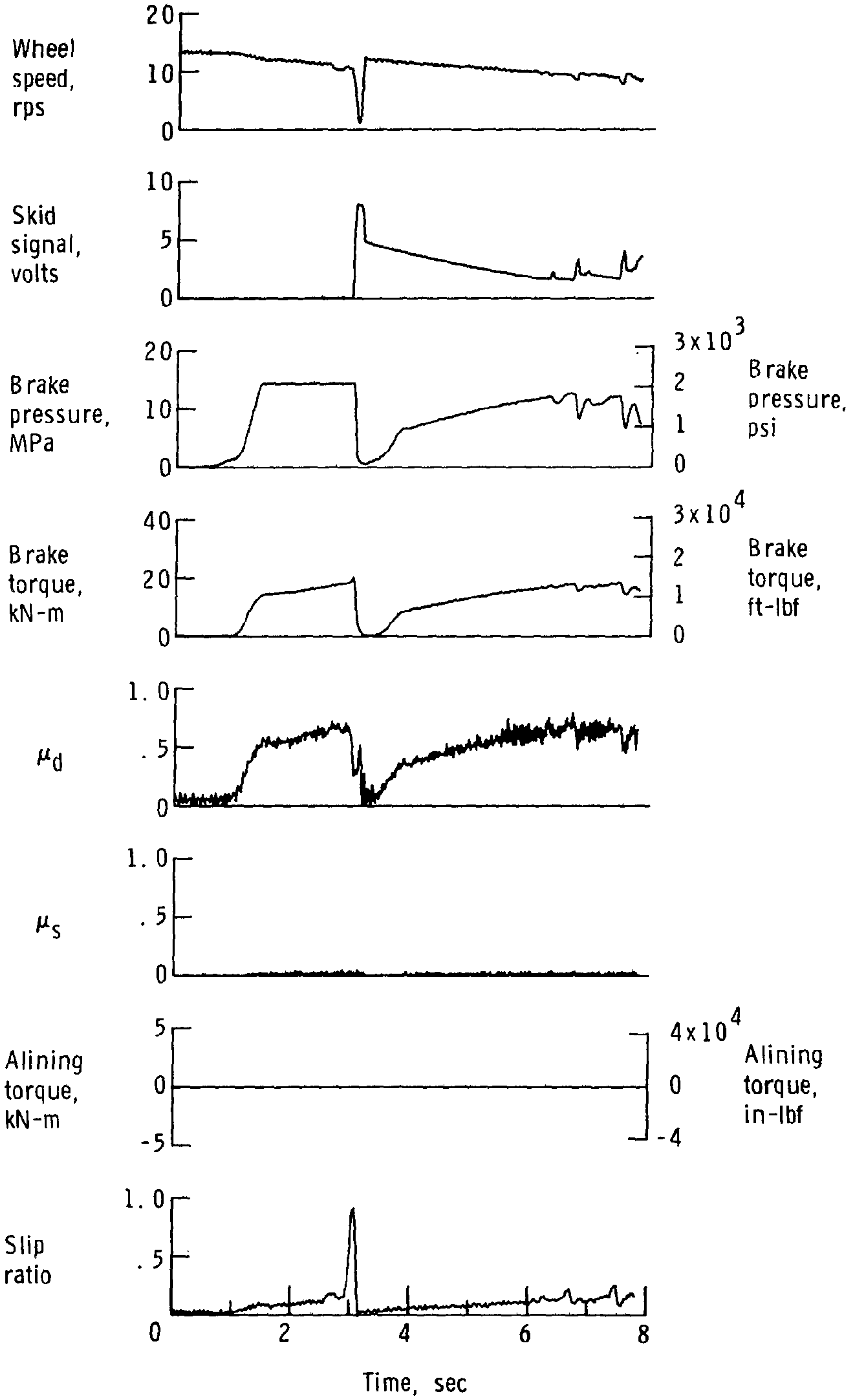

Figure A3.- Time histories for run 3; nominal carriage speed, 73 knots; vertical load, 60.5 kN (13 600 lbf); yaw angle, 0°; surface condition, dry; tire condition, new; brake pressure, 14 MPa (2000 lbf/in^2).

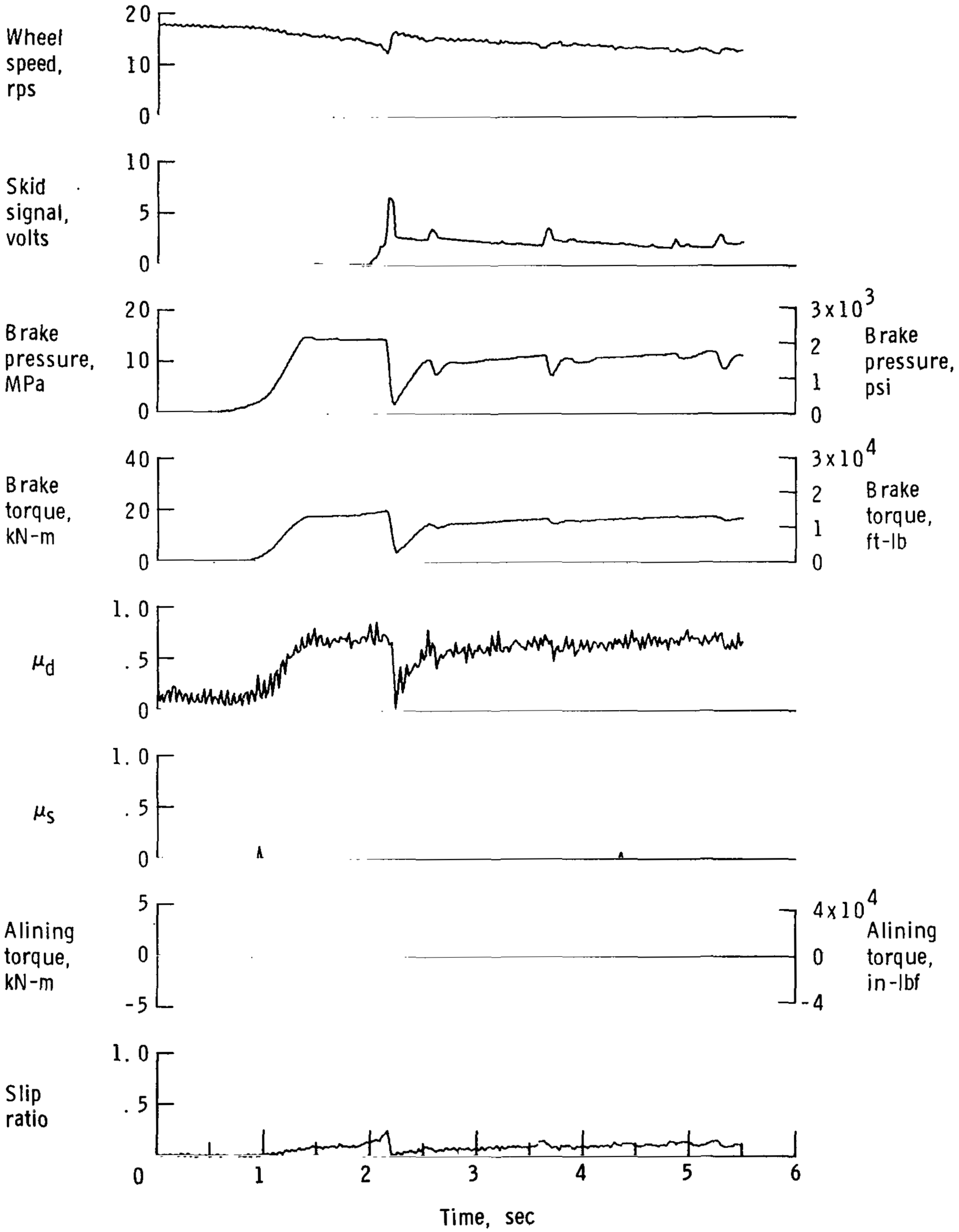

Figure A4.- Time histories for run 4; nominal carriage speed, 98 knots; vertical load, 60.9 kN (13 700 lbf); yaw angle, 0°; surface condition, dry; tire condition, new; brake pressure, 14 MPa (2000 lbf/in^2).

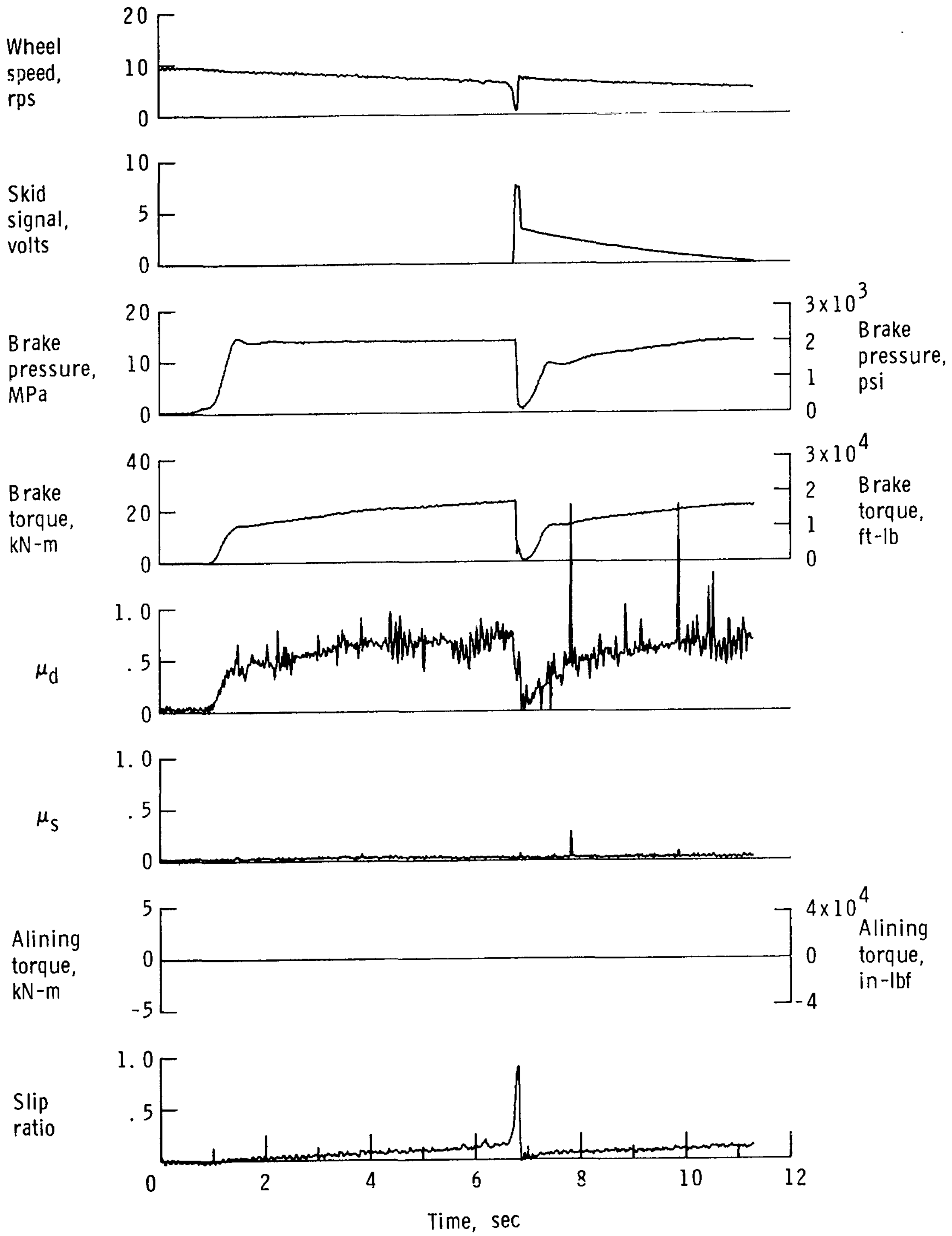

Figure A5.- Time histories for run 5; nominal carriage speed, 46 knots; vertical load, 72.5 kN (16 300 lbf); yaw angle, 0°; surface condition, dry; tire condition, new; brake pressure, 14 MPa (2000 lbf/in^2).

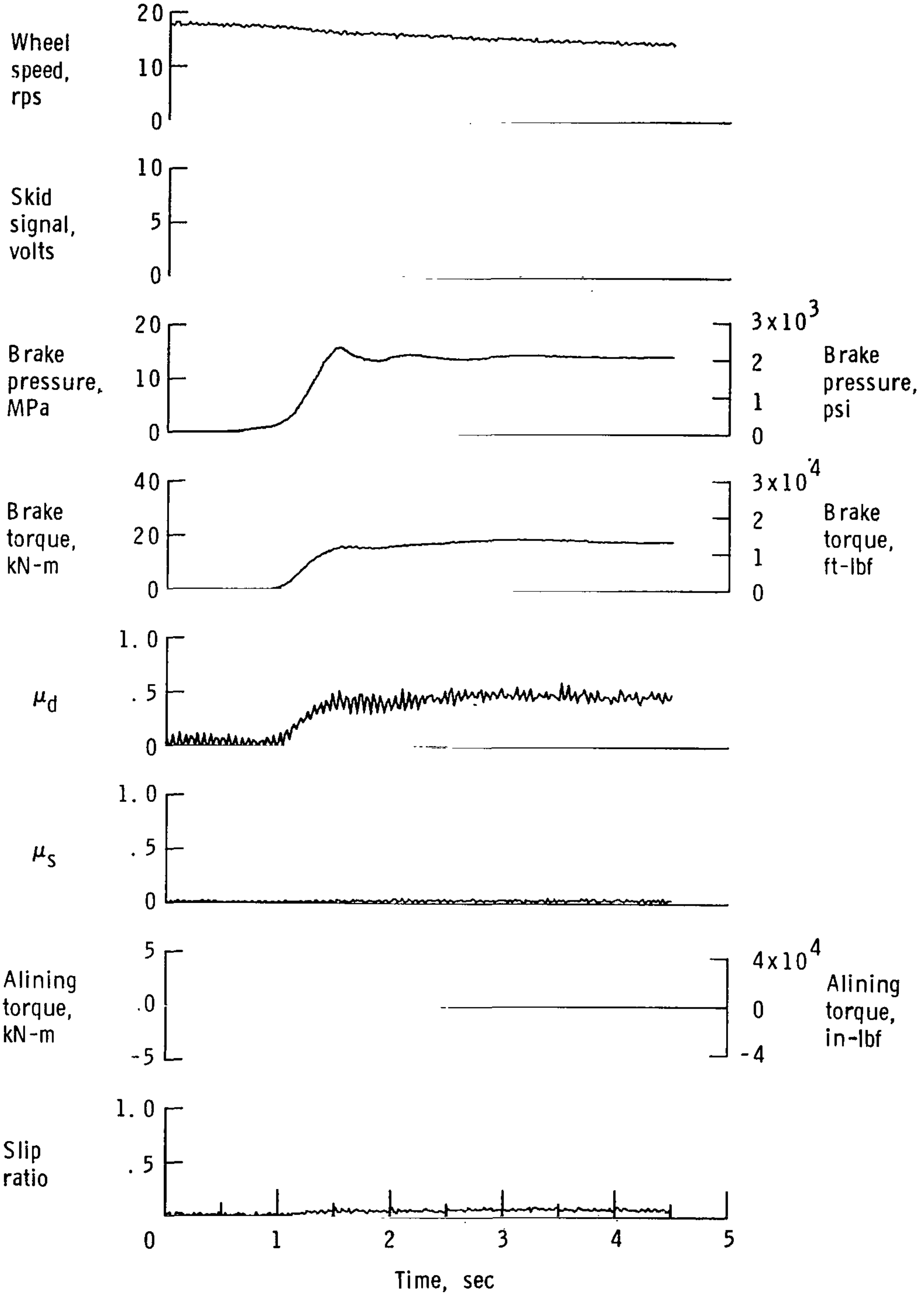

Figure A6.- Time histories for run 6; nominal carriage speed, 102 knots; vertical load, 85.0 kN (19 100 lbf); yaw angle, 0°; surface condition, dry; tire condition, new; brake pressure, 14 MPa (2000 lbf/in^2).

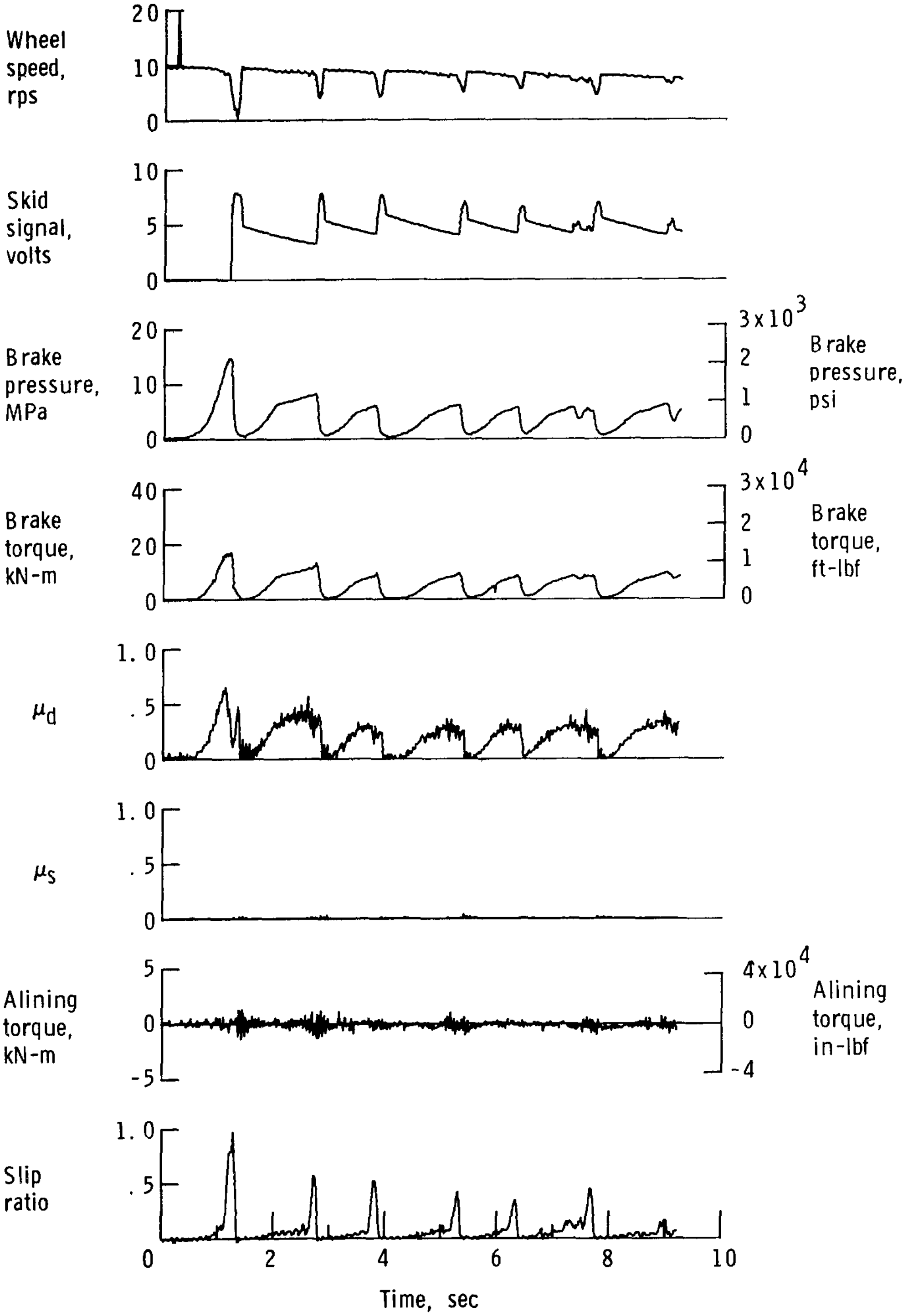

Figure A7.- Time histories for run 7; nominal carriage speed, 52 knots; vertical load, 56.9 kN (12 800 lbf); yaw angle, 0°; surface condition, damp; tire condition, new; brake pressure, 14 MPa (2000 lbf/in^2).

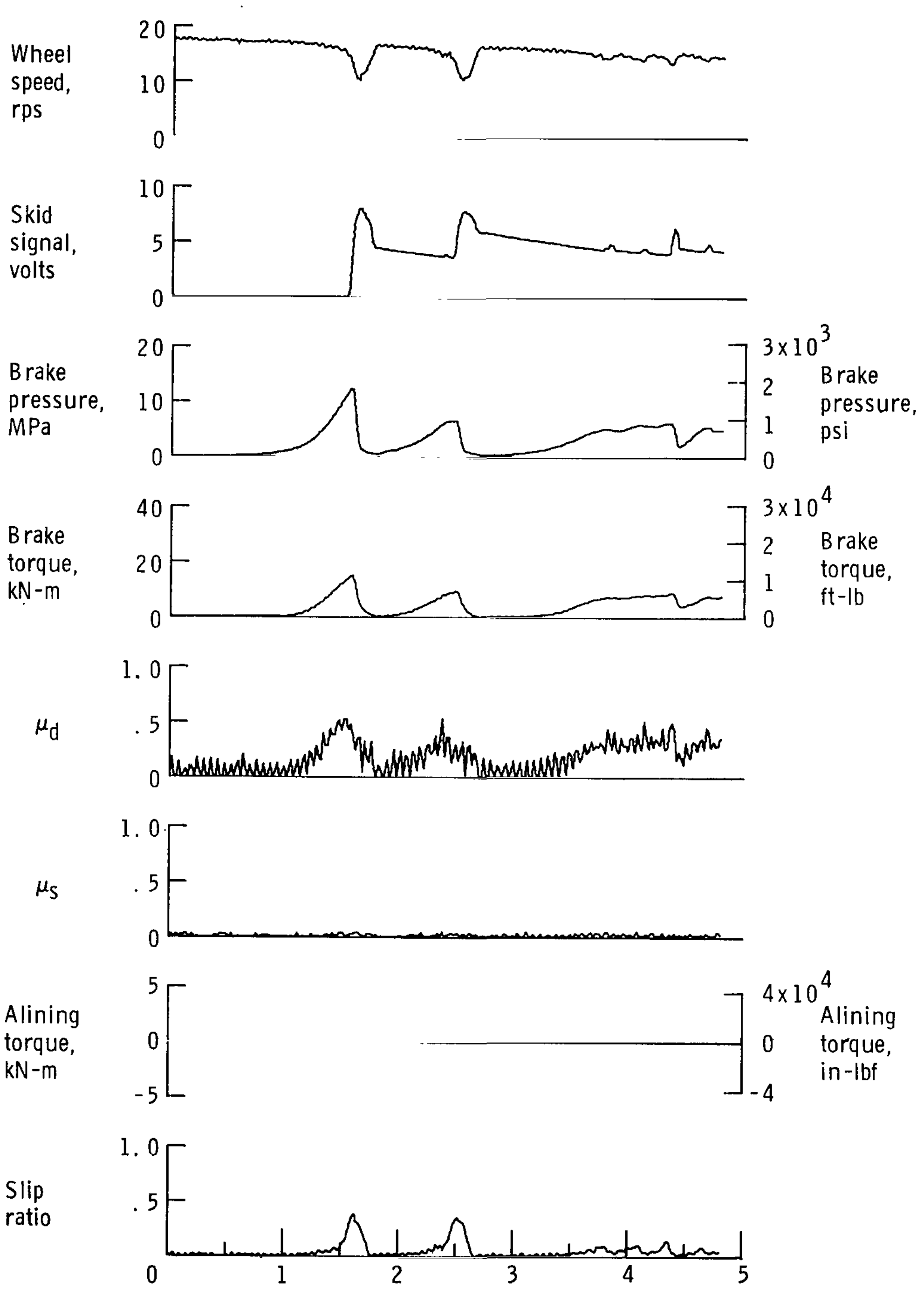

Figure A8.- Time histories for run 8; nominal carriage speed, 99 knots; vertical load, 61.4 kN (13 800 lbf); yaw angle, 0°; surface condition, damp; tire condition, new; brake pressure, 14 MPa (2000 lbf/in^2).

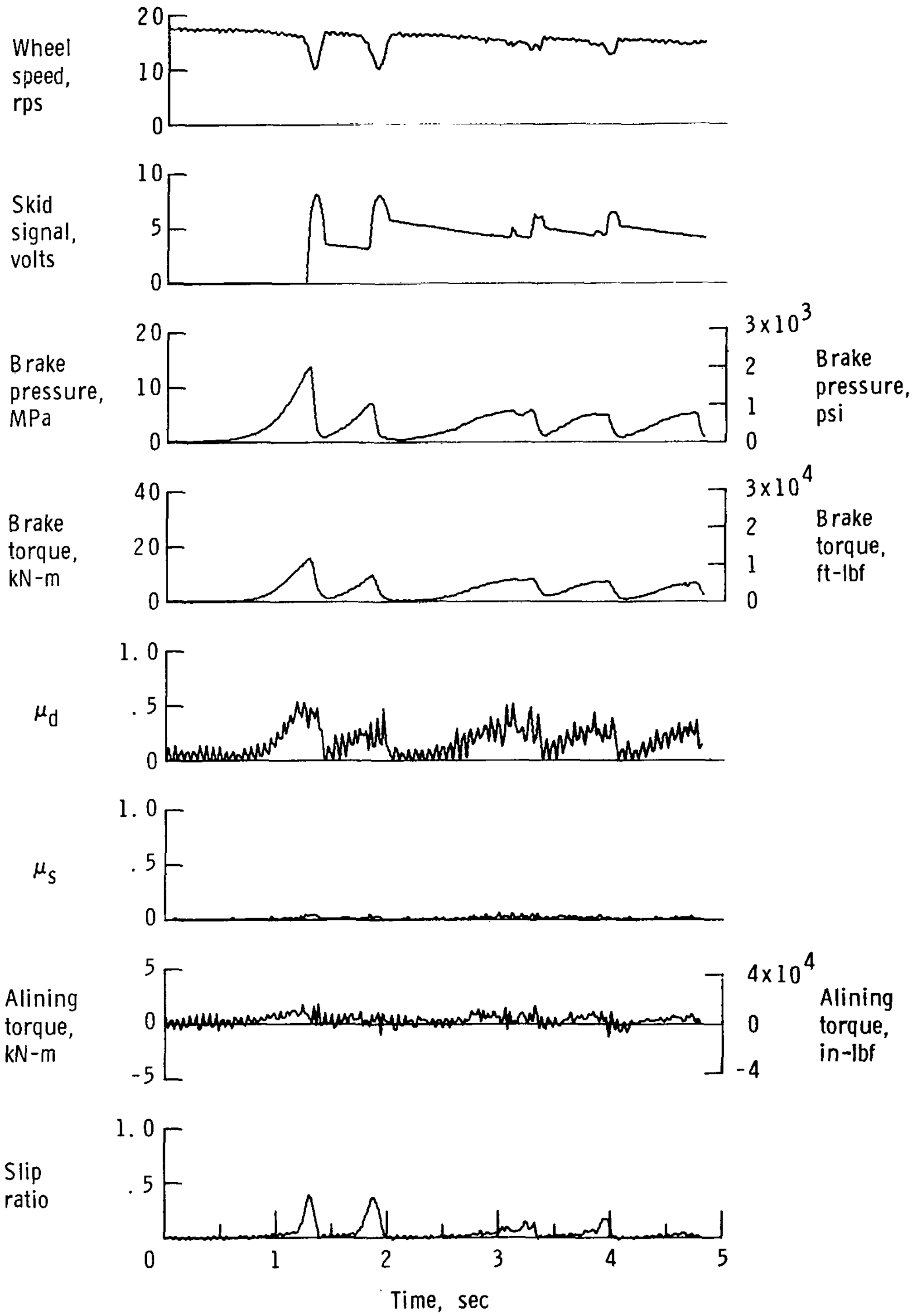

Figure A9.- Time histories for run 9; nominal carriage speed, 100 knots; vertical load, 56.9 kN (12 800 lbf); yaw angle, 0°; surface condition, damp; tire condition, new; brake pressure, 14 MPa (2000 lbf/in^2).

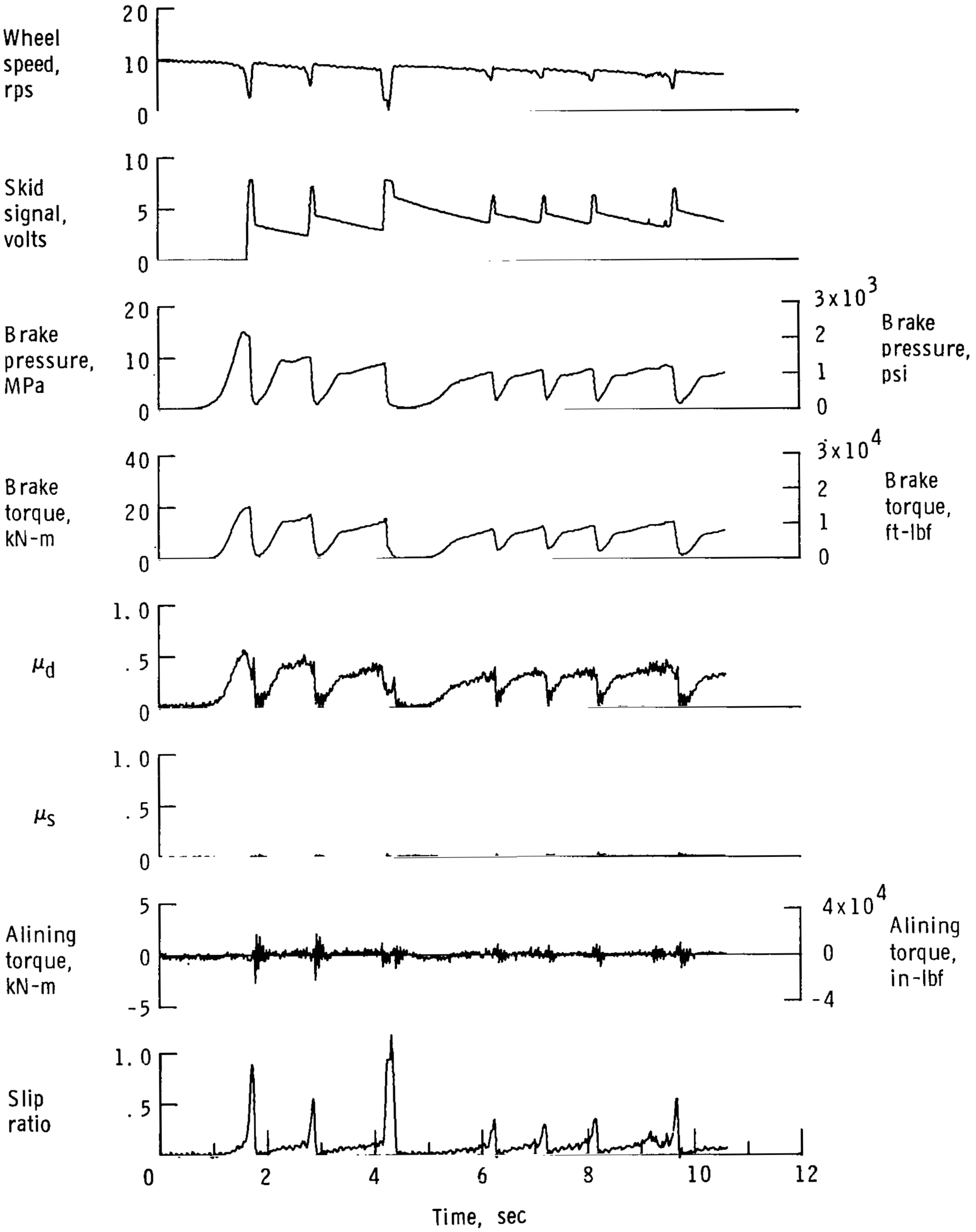

Figure A10.- Time histories for run 10; nominal carriage speed, 50 knots; vertical load, 77.0 kN (17 300 lbf); yaw angle, 0°; surface condition, damp; tire condition, new; brake pressure, 14 MPa (2000 lbf/in^2).

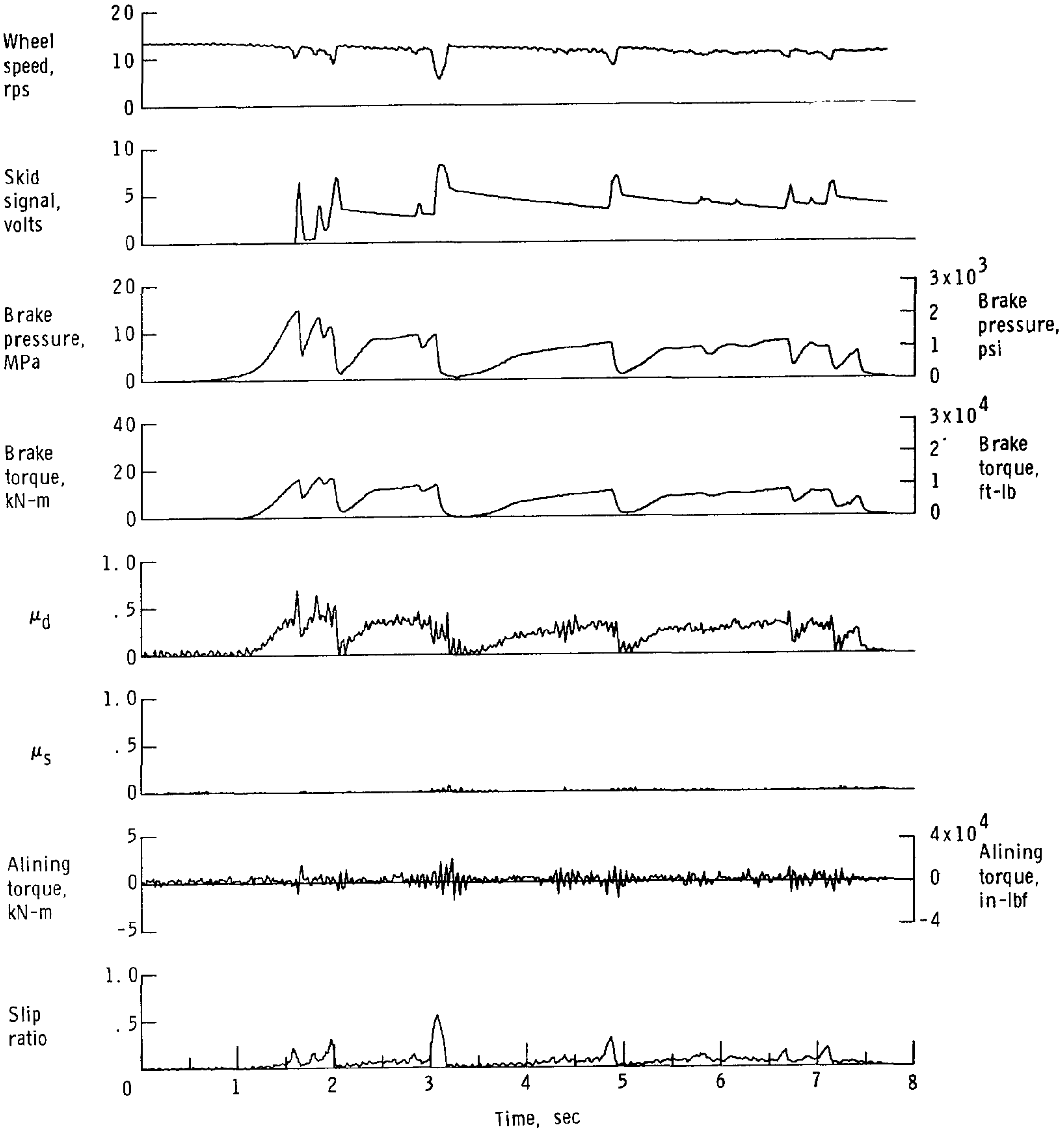

Figure A11.- Time histories for run 11; nominal carriage speed, 74 knots; vertical load, 75.6 kN (17 000 lbf); yaw angle, 0°; surface condition, damp; tire condition, new; brake pressure, 14 MPa (2000 lbf/in^2).

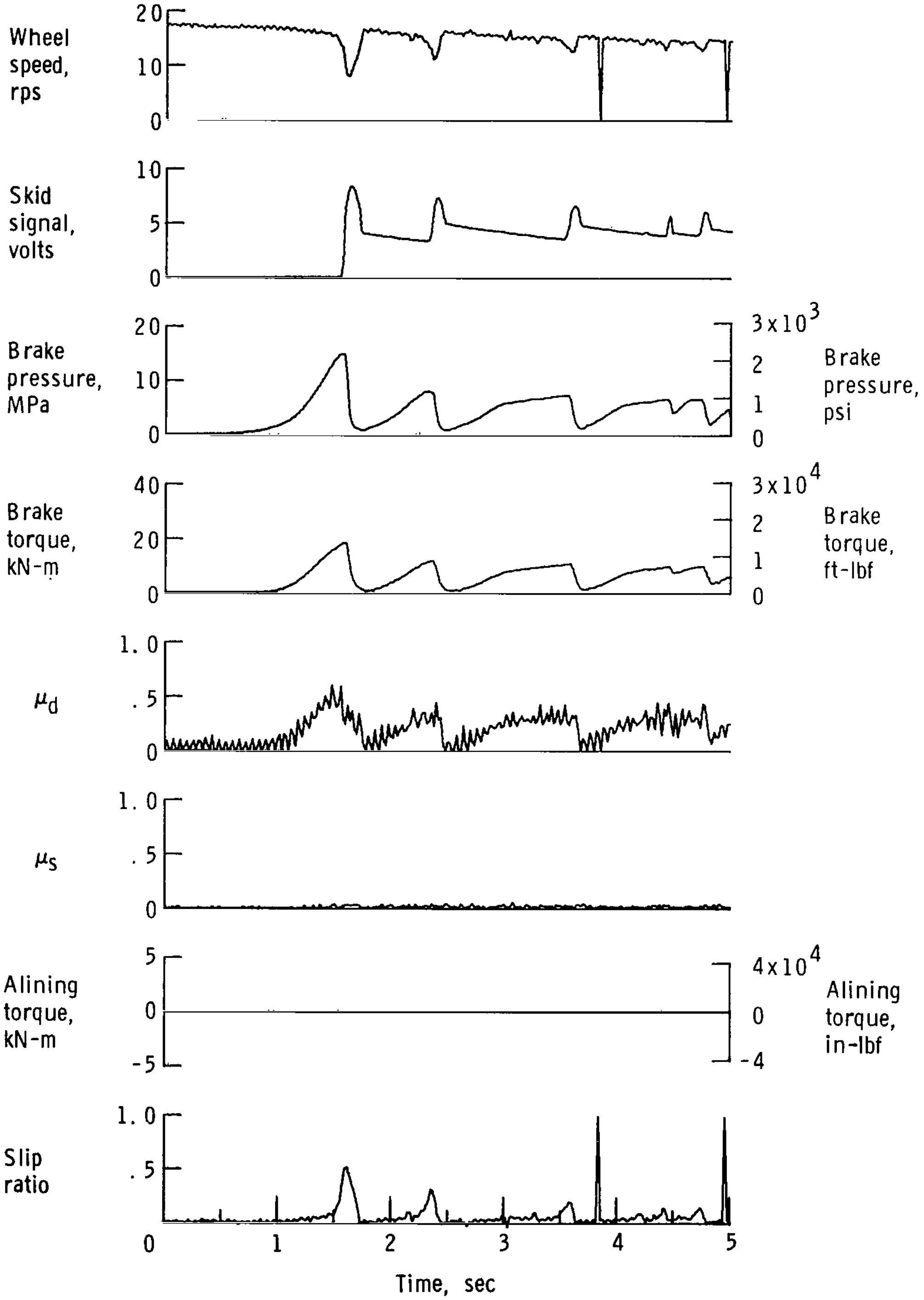

Figure A12.- Time histories for run 12; nominal carriage speed, 98 knots; vertical load, 79.6 kN (17 900 lbf); yaw angle, 0°; surface condition, damp; tire condition, new; brake pressure, 14 MPa (2000 lbf/in^2).

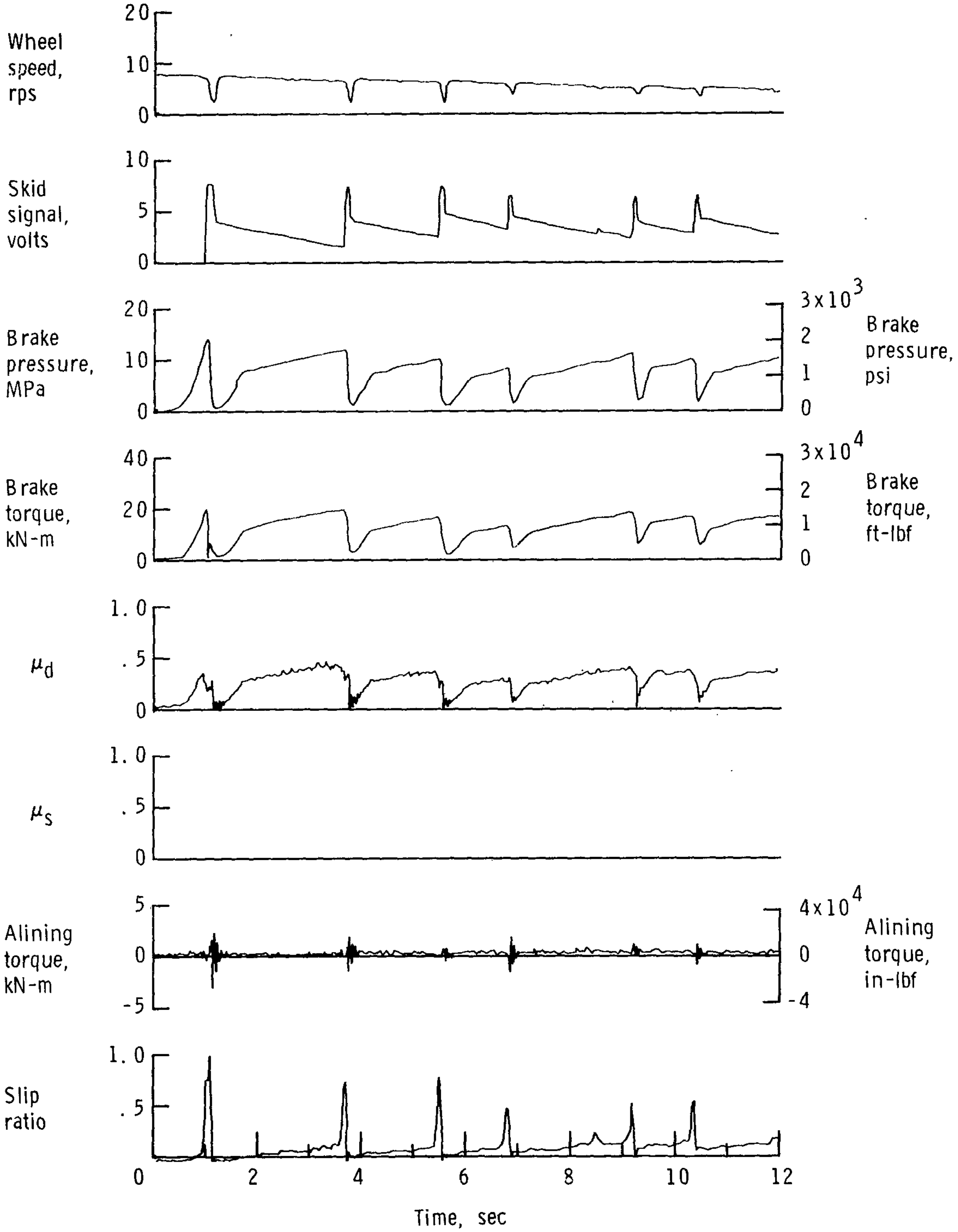

Figure A13.- Time histories for run 13; nominal carriage speed, 32 knots; vertical load, 99.2 kN (22 300 lbf); yaw angle, 0°; surface condition, damp; tire condition, new; brake pressure, 14 MPa (2000 lbf/in^2).

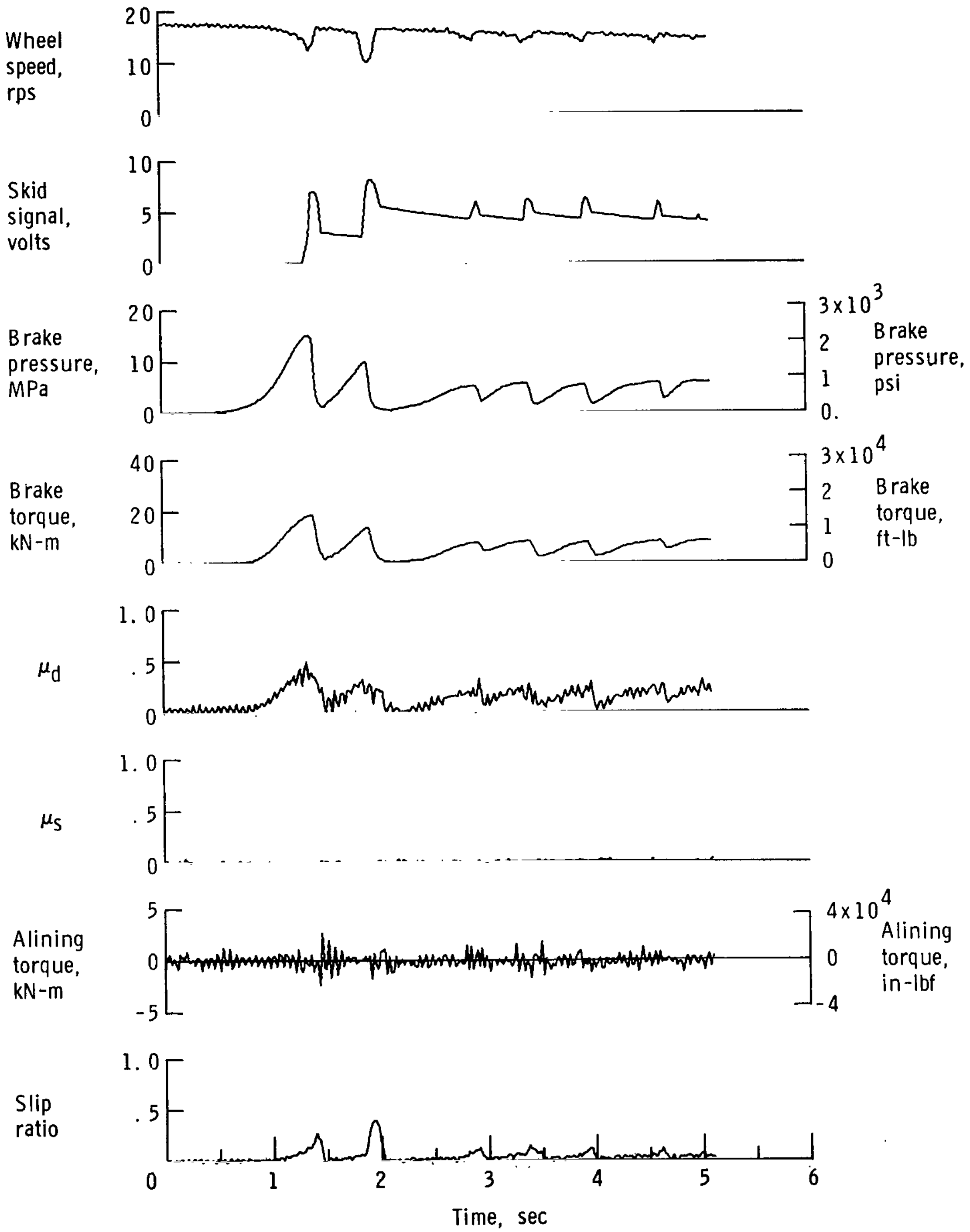

Figure A14.- Time histories for run 14; nominal carriage speed, 98 knots; vertical load, 93.9 kN (21 100 lbf); yaw angle, 0°; surface condition, damp; tire condition, new; brake pressure, 14 MPa (2000 lbf/in^2).

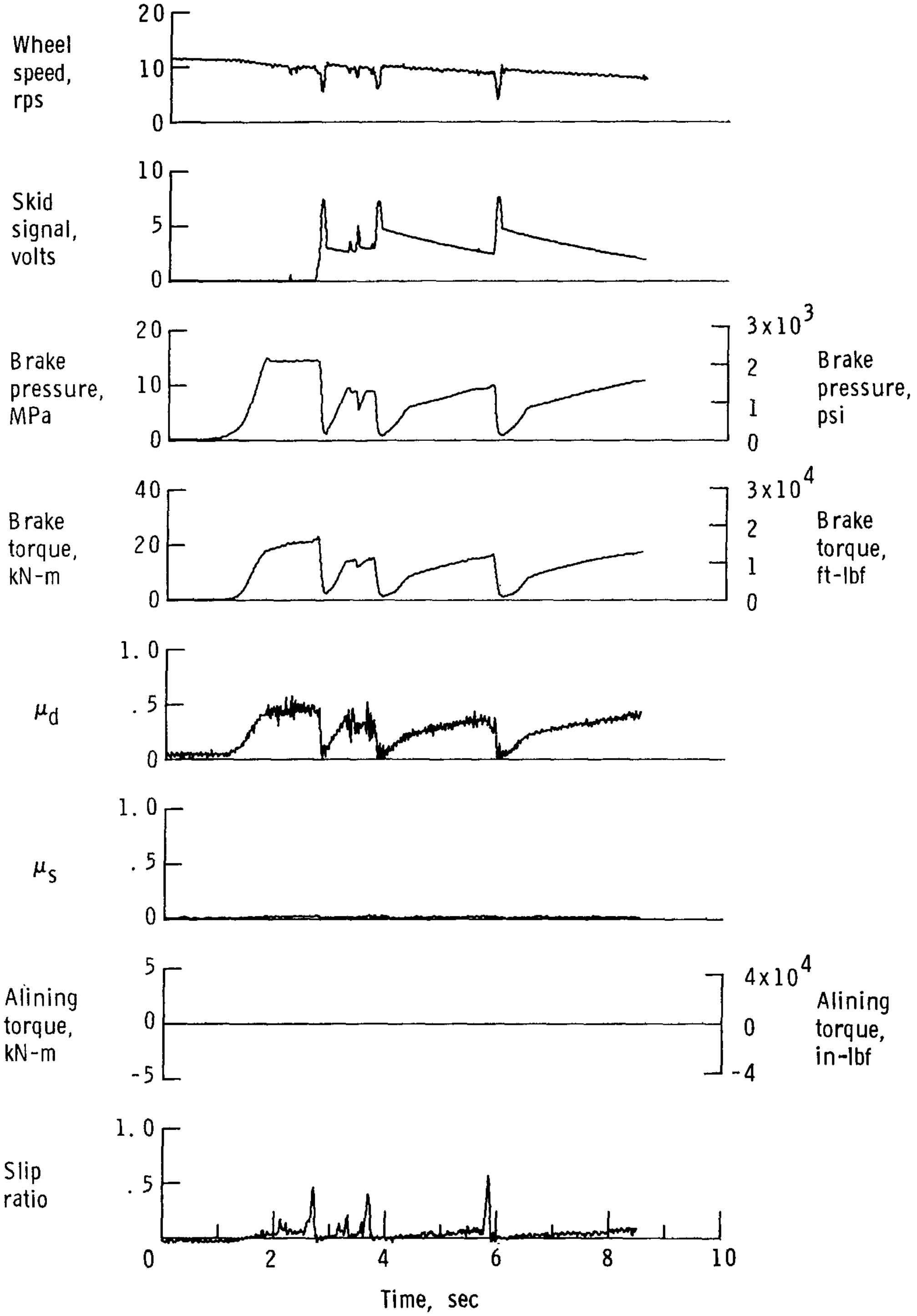

Figure A15.- Time histories for run 15; nominal carriage speed, 59 knots; vertical load, 120.6 kN (27 100 lbf); yaw angle, 0°; surface condition, damp; tire condition, new; brake pressure, 14 MPa (2000 lbf/in^2).

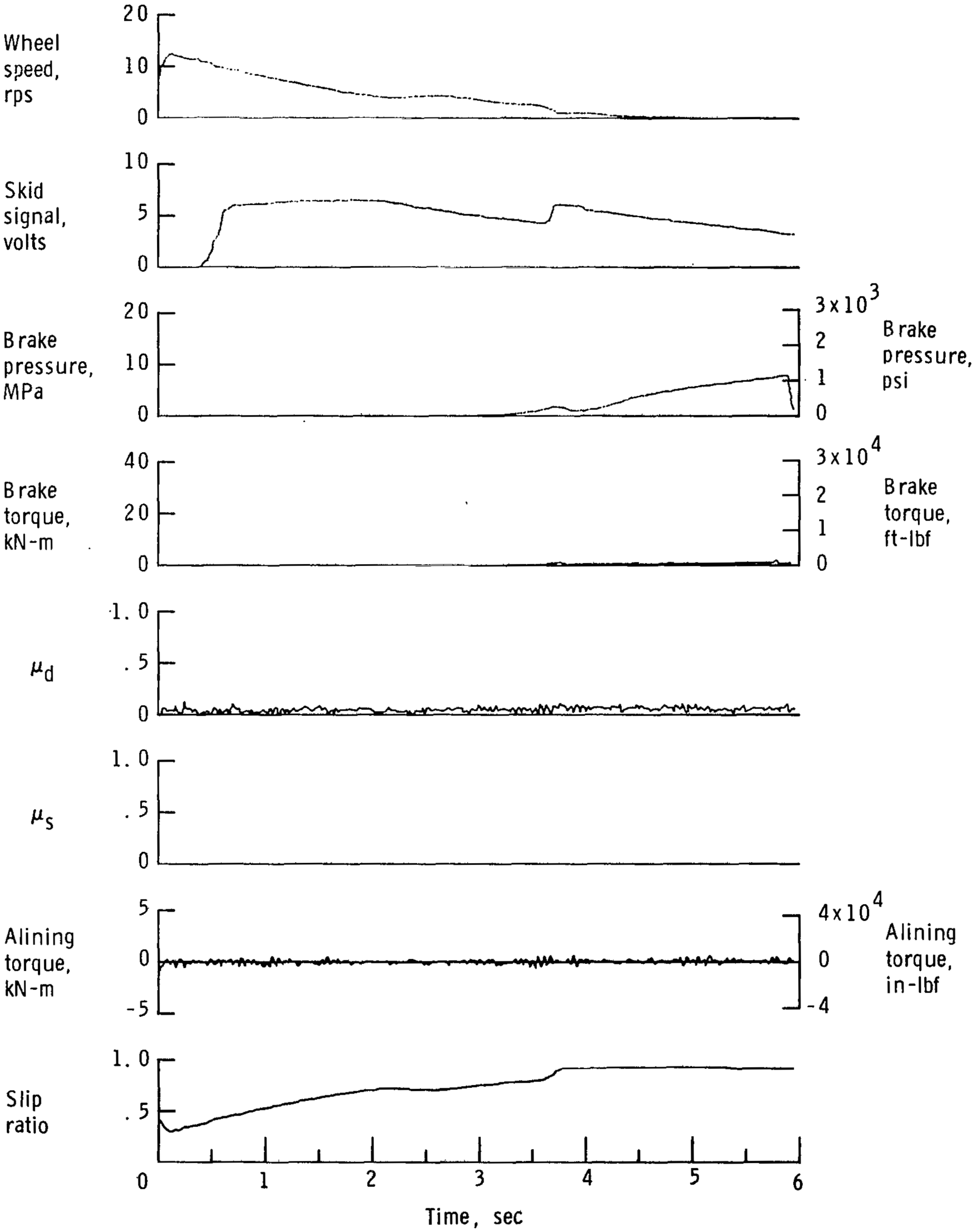

Figure A16.- Time histories for run 16; nominal carriage speed, 98 knots; vertical load, 57.8 kN (13 000 lbf); yaw angle, 0°; surface condition, flooded; brake pressure, 14 MPa (2000 lbf/in^2).

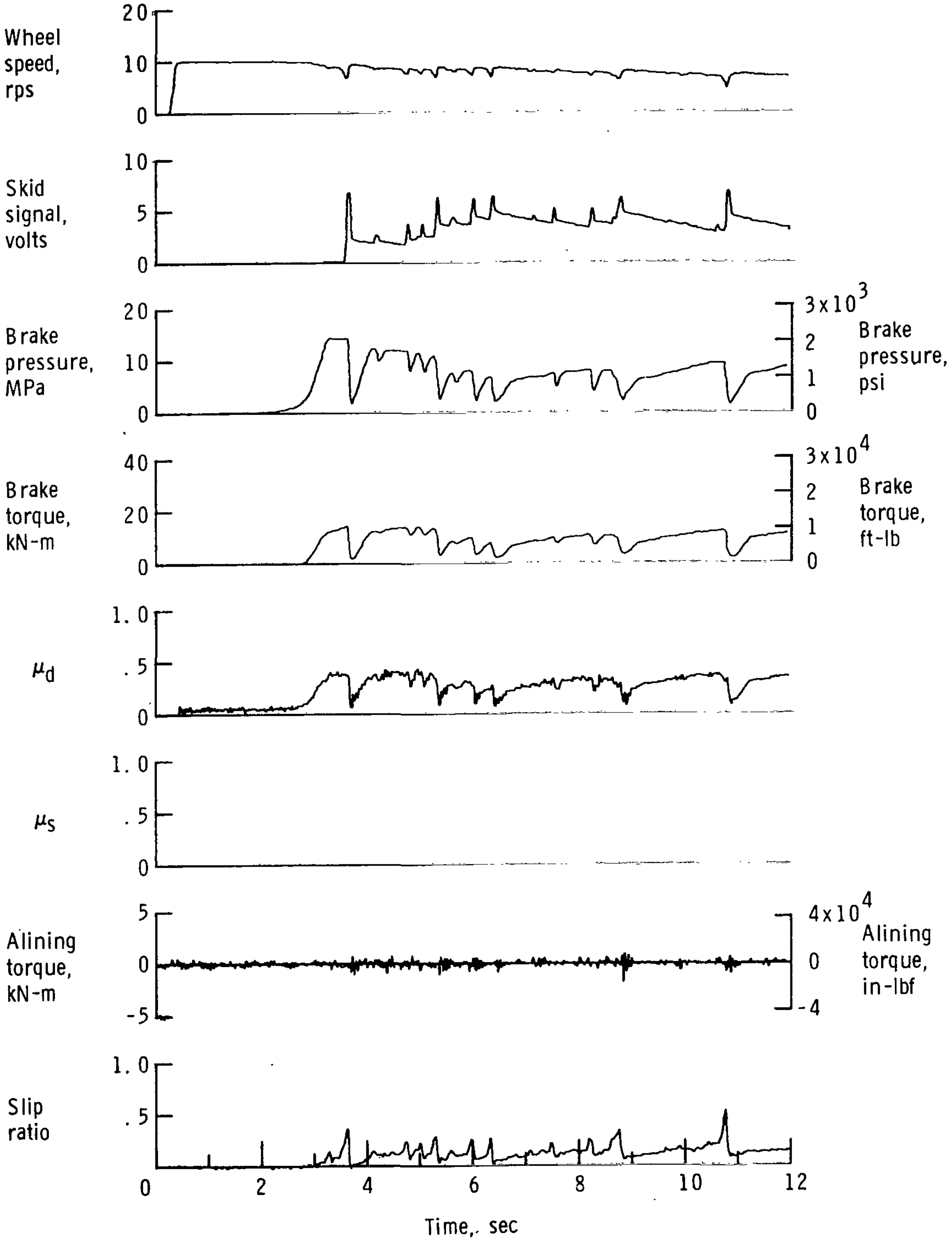

Figure A17.- Time histories for run 17; nominal carriage speed, 47 knots; vertical load, 92.1 kN (20 700 lbf); yaw angle, 0°; surface condition, flooded; brake pressure, 14 MPa (2000 lbf/in^2).

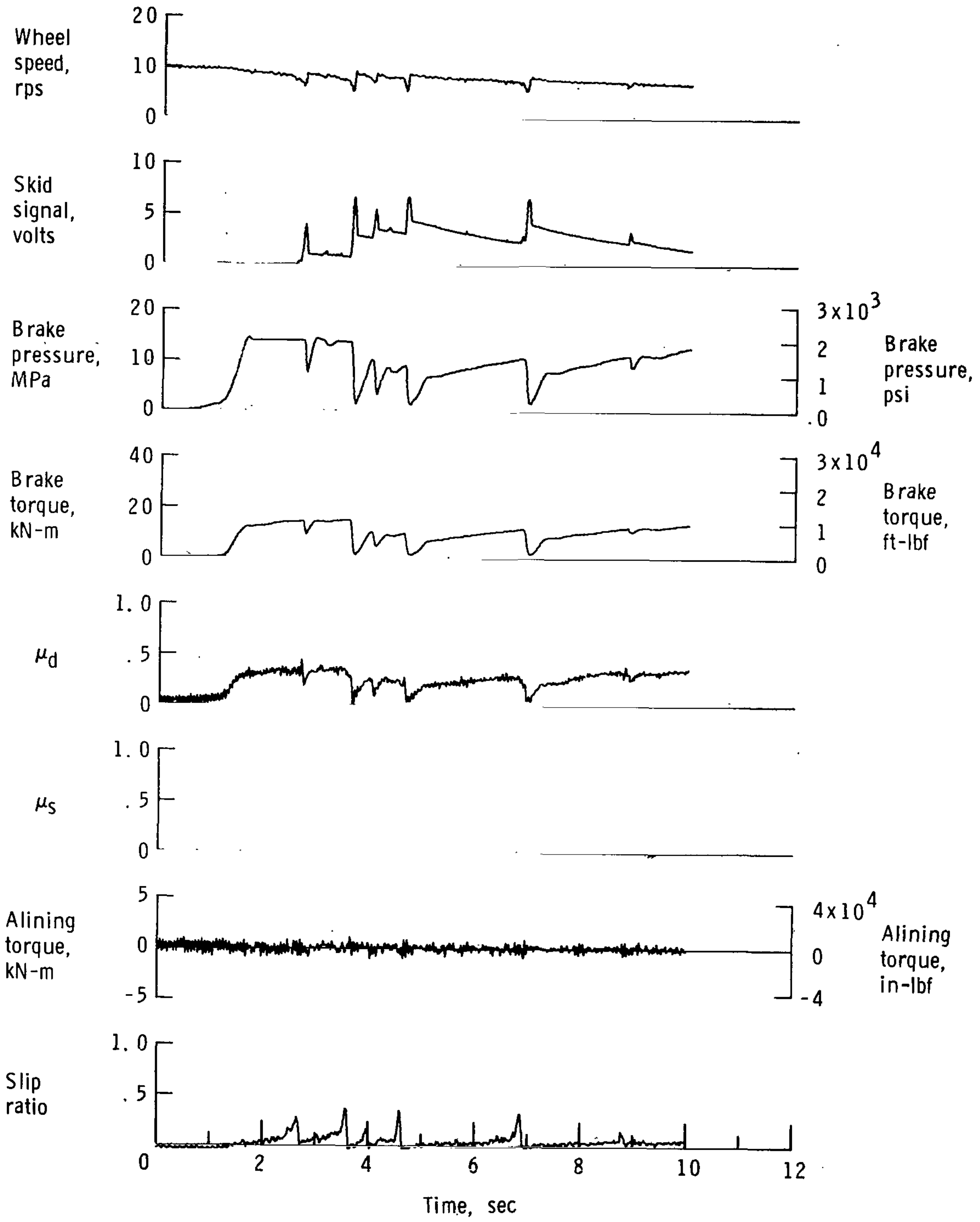

Figure A18.- Time histories for run 18; nominal carriage speed, 50 knots; vertical load, 104.5 kN (23 500 lbf); yaw angle, 0°; surface condition, flooded; brake pressure, 14 MPa (2000 lbf/in^2).

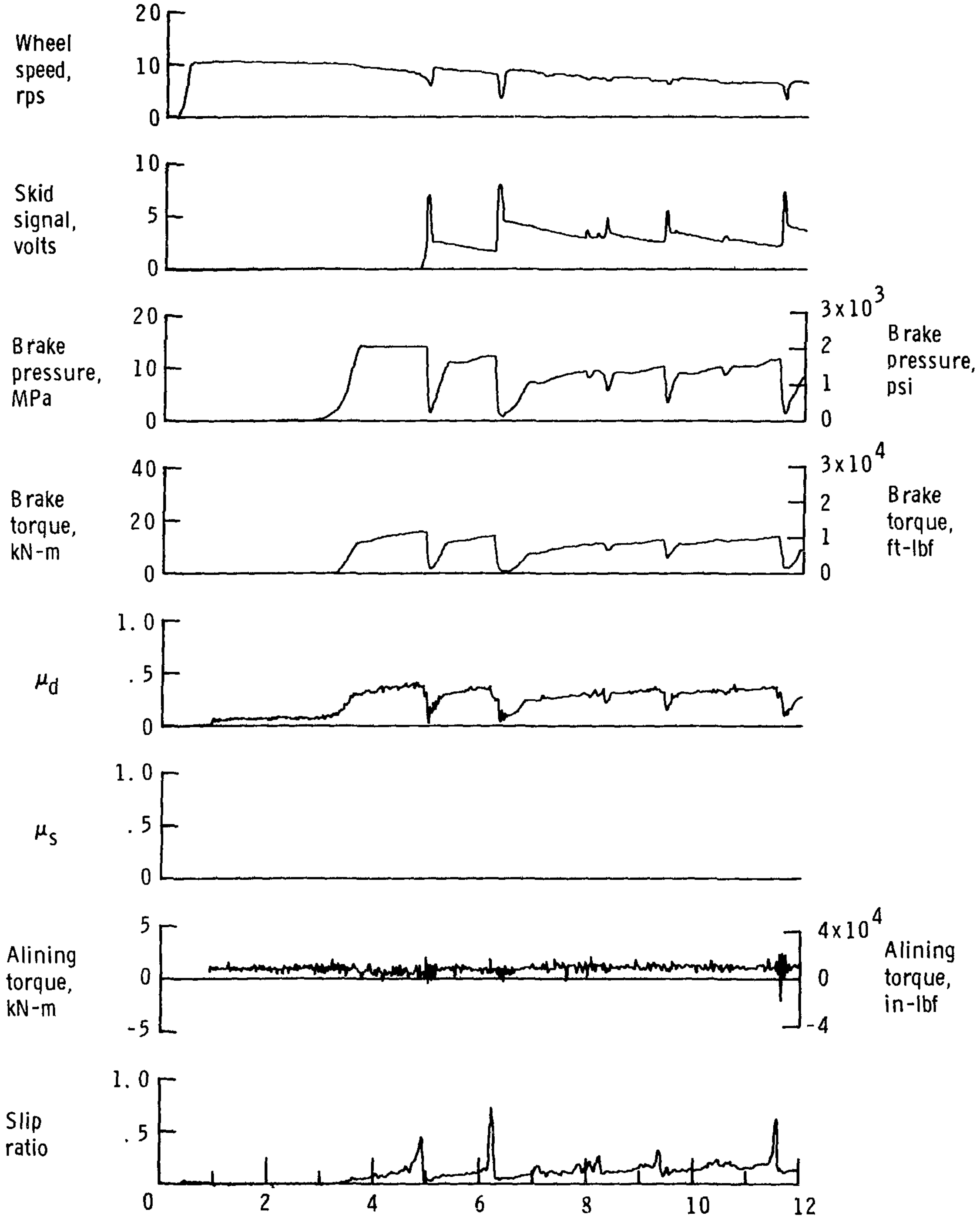

Figure A19.- Time histories for run 19; nominal carriage speed, 46 knots; vertical load, 118.3 kN (26 600 lbf); yaw angle, 0°; surface condition, flooded; brake pressure, 14 MPa (2000 lbf/in^2).

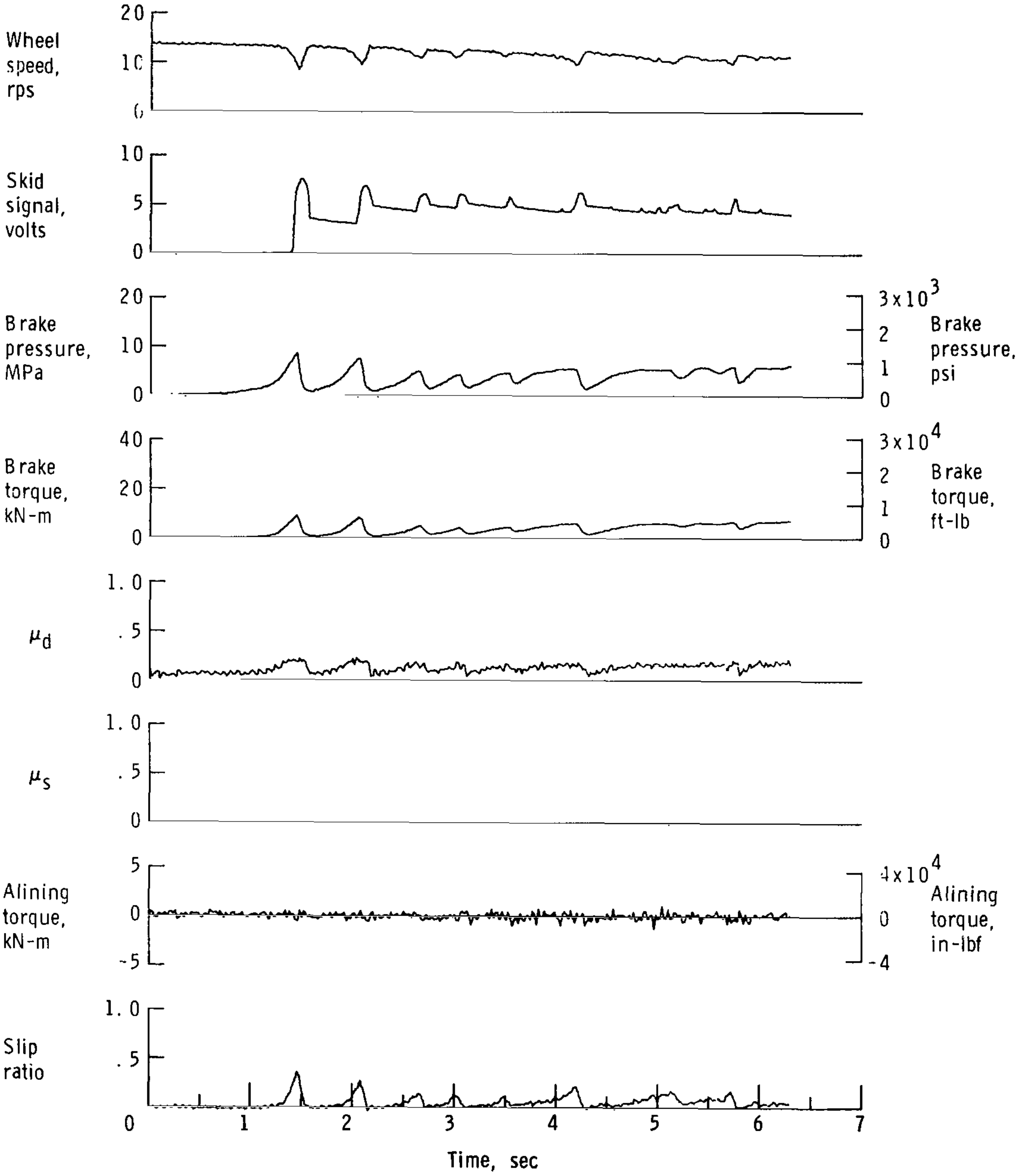

Figure A20.- Time histories for run 20; nominal carriage speed, 76 knots; vertical load, 114.3 kN (25 700 lbf); yaw angle, 0°; surface condition, flooded; brake pressure, 14 MPa (2000 lbf/in^2).

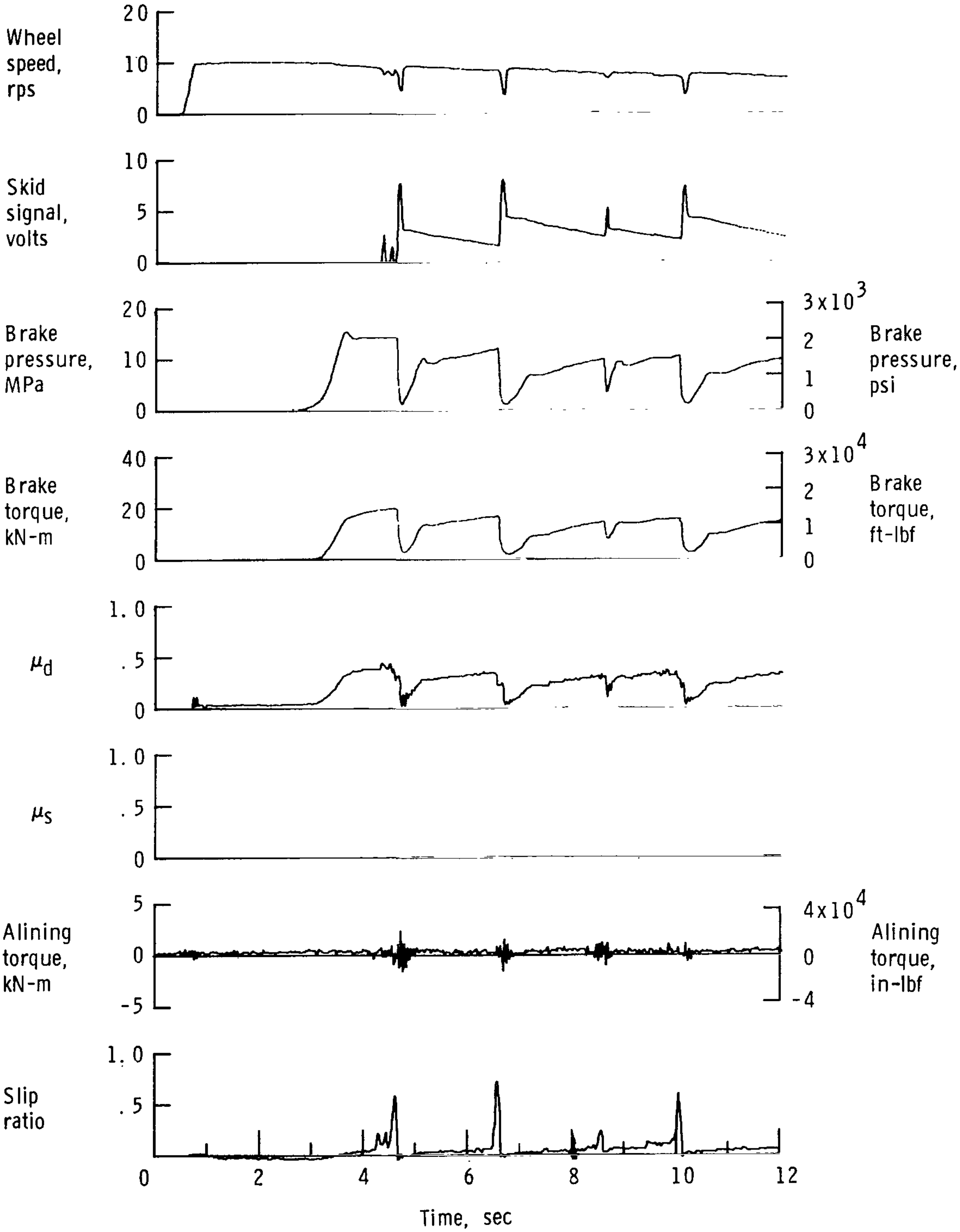

Figure A21.- Time histories for run 21; nominal carriage speed, 45 knots; vertical load, 120.6 kN (27 100 lbf); yaw angle, 0°; surface condition, natural rain; brake pressure, 14 MPa (2000 lbf/in^{2}).

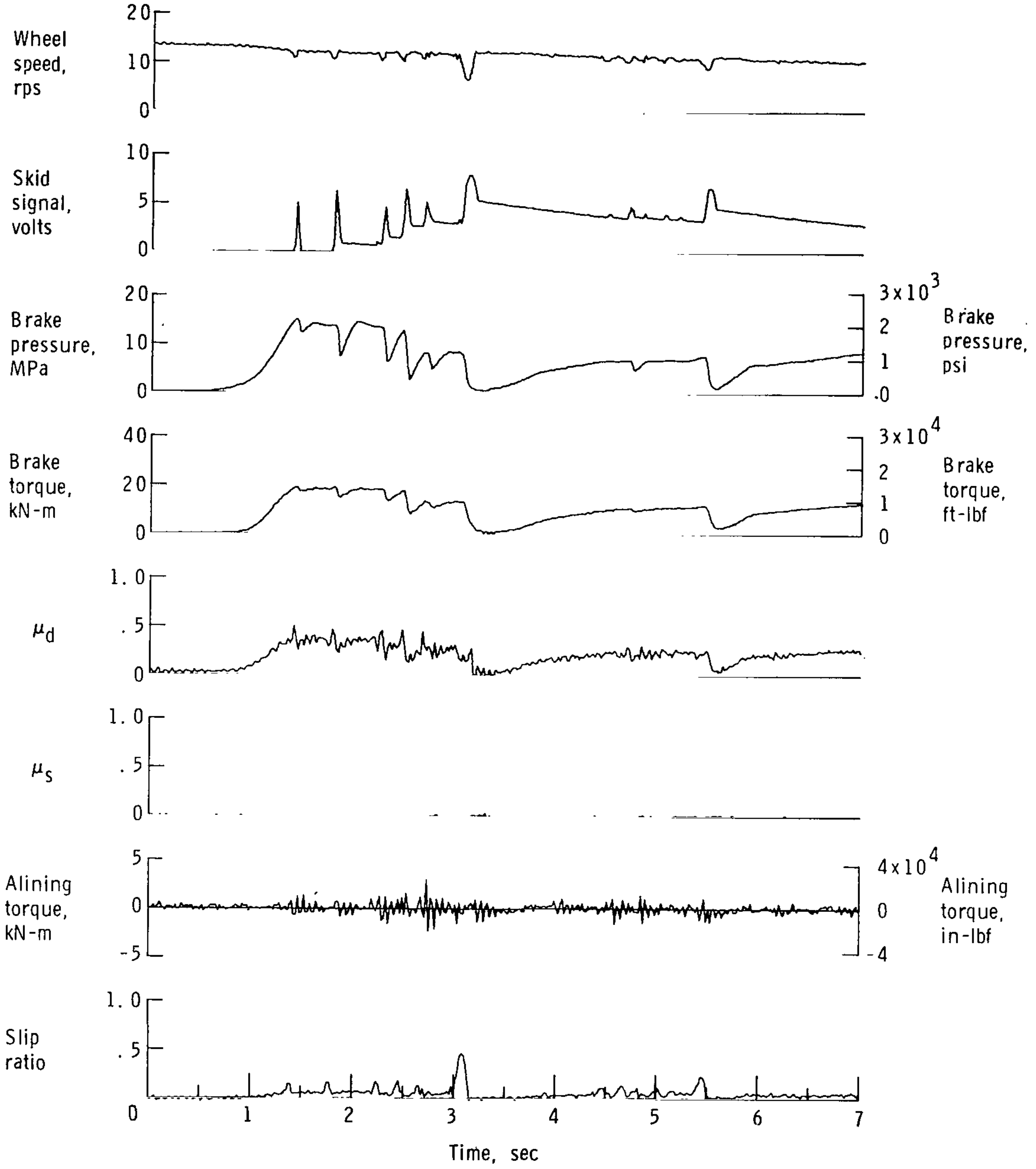

Figure A22.- Time histories for run 22; nominal carriage speed, 72 knots; vertical load, 120.1 kN (27 000 lbf); yaw angle, 0°; surface condition, natural rain; brake pressure, 14 MPa (2000 lbf/in^2).

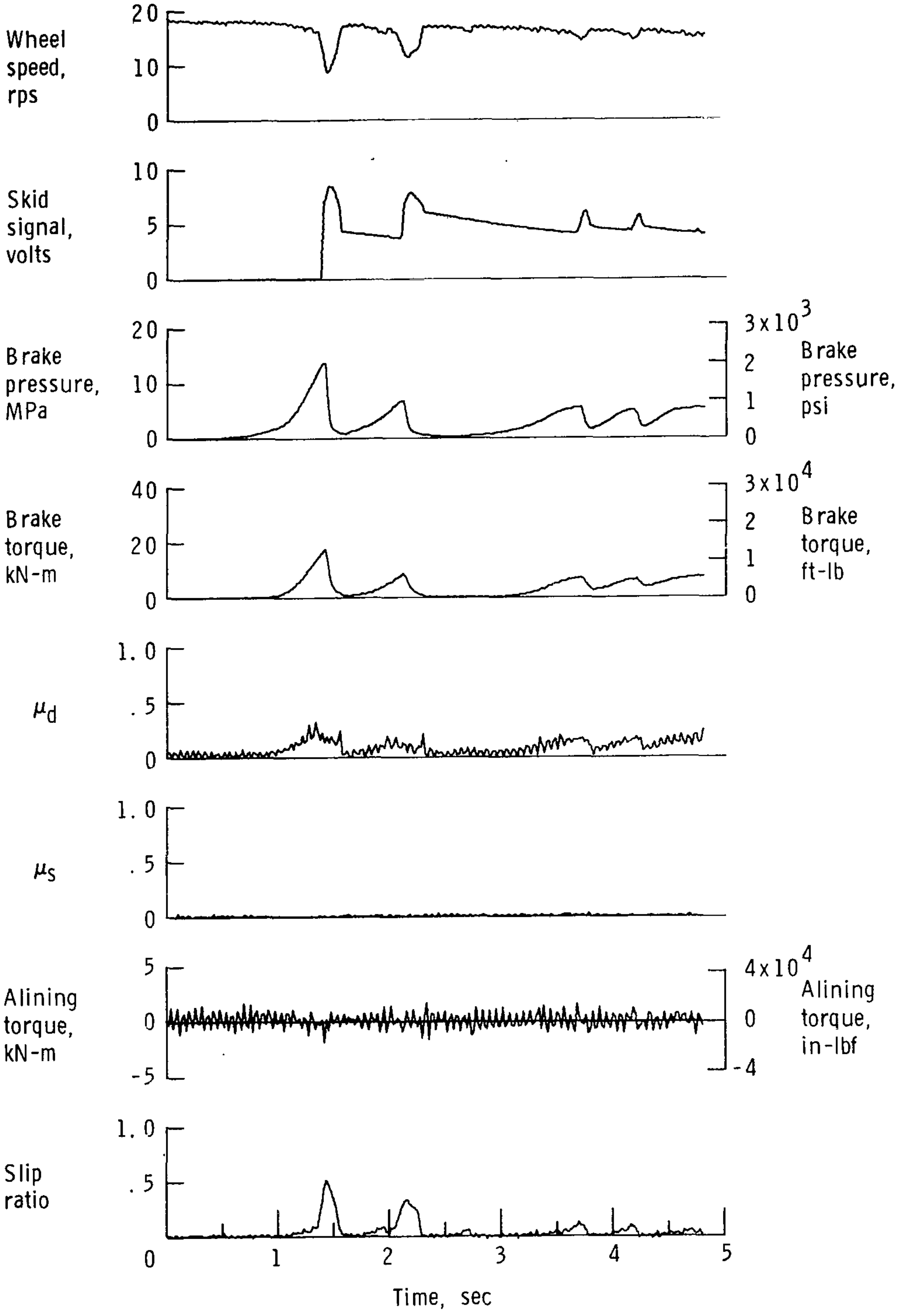

Figure A23.- Time histories for run 23; nominal carriage speed, 103 knots; vertical load, 122.3 kN (27 500 lbf); yaw angle, 0°; surface condition, natural rain; brake pressure, 14 MPa (2000 lbf/in^2).

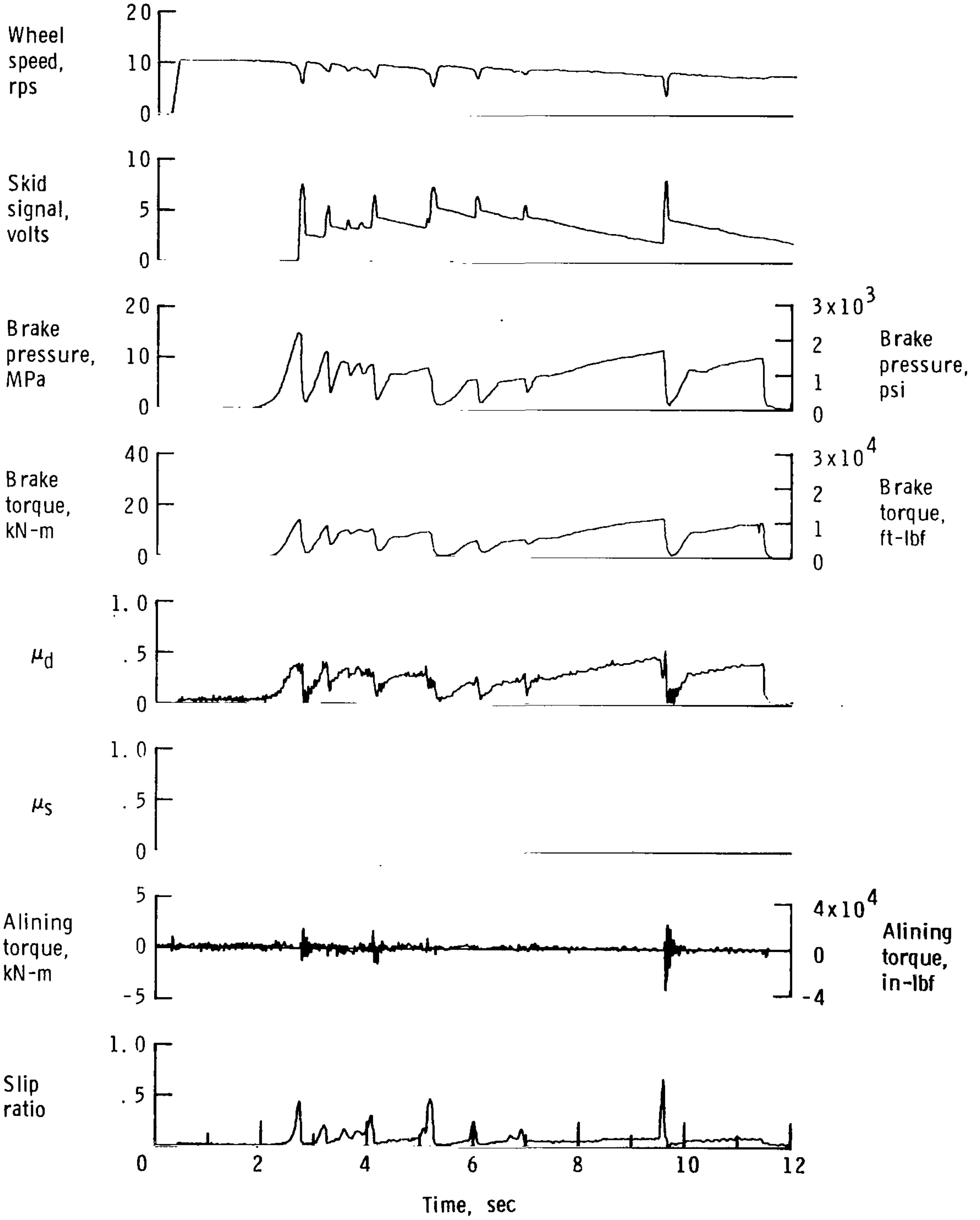

Figure A24.- Time histories for run 24; nominal carriage speed, 52 knots; vertical load, 79.6 kN (17 900 lbf); yaw angle, 0°; surface condition, flooded/dry; brake pressure, 14 MPa (2000 lbf/in^2).

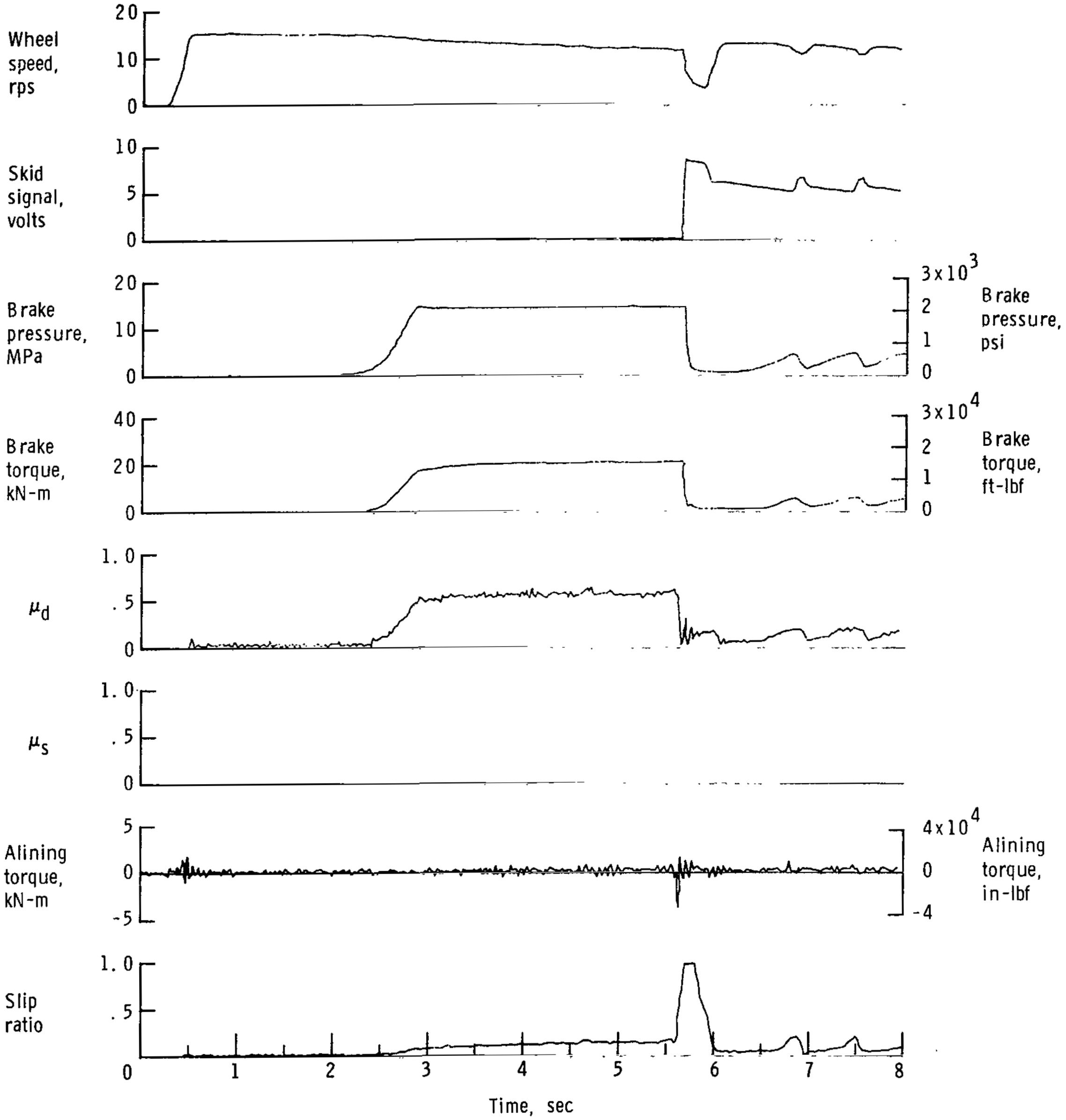

Figure A25.- Time histories for run 25; nominal carriage speed, 72 knots; vertical load, 78.7 kN (17 700 lbf); yaw angle, 0°; surface condition, dry/flooded; brake pressure, 14 MPa (2000 lbf/in^2).

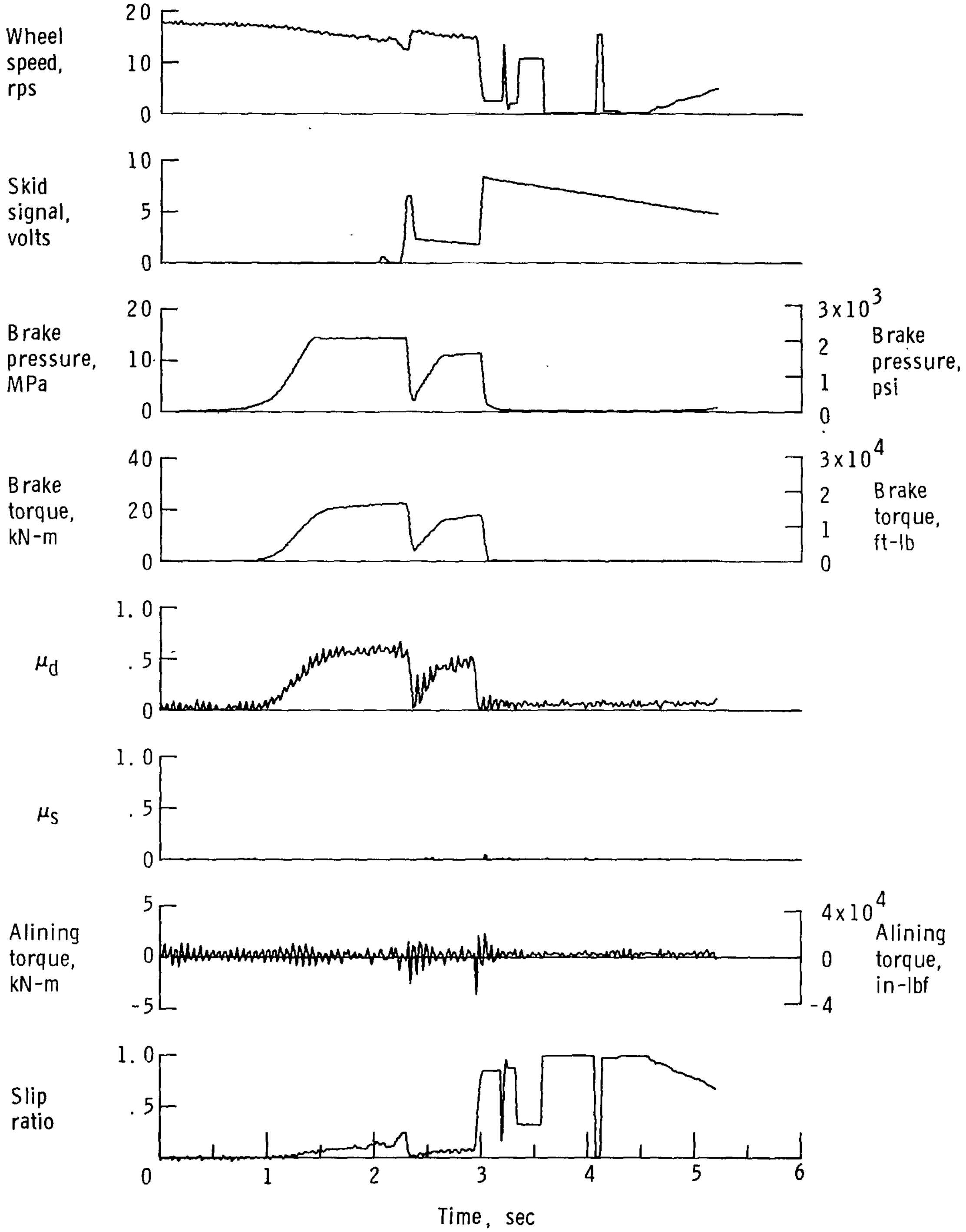

Figure A26.- Time histories for run 26; nominal carriage speed, 98 knots; vertical load, 79.2 kN (17 800 lbf); yaw angle, 0°; surface condition, dry/flooded; tire condition, new; brake pressure, 14 MPa (2000 lbf/in^2).

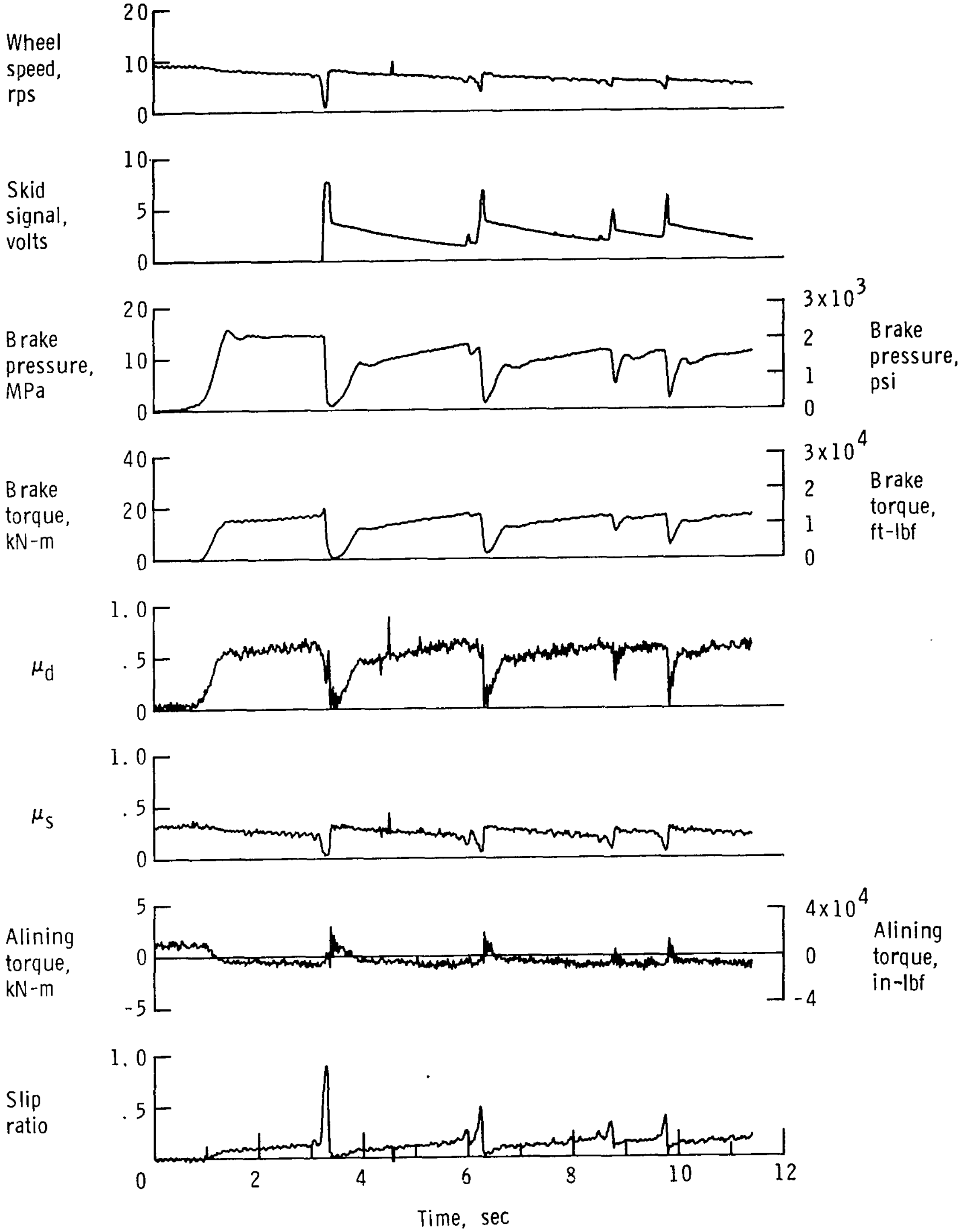

Figure A27.- Time histories for run 27; nominal carriage speed. 46 knots; vertical load, 61.8 kN (13 900 lbf); yaw angle, 3°; surface condition, dry; tire condition, new; brake pressure, 14 MPa (2000 lbf/in^2).

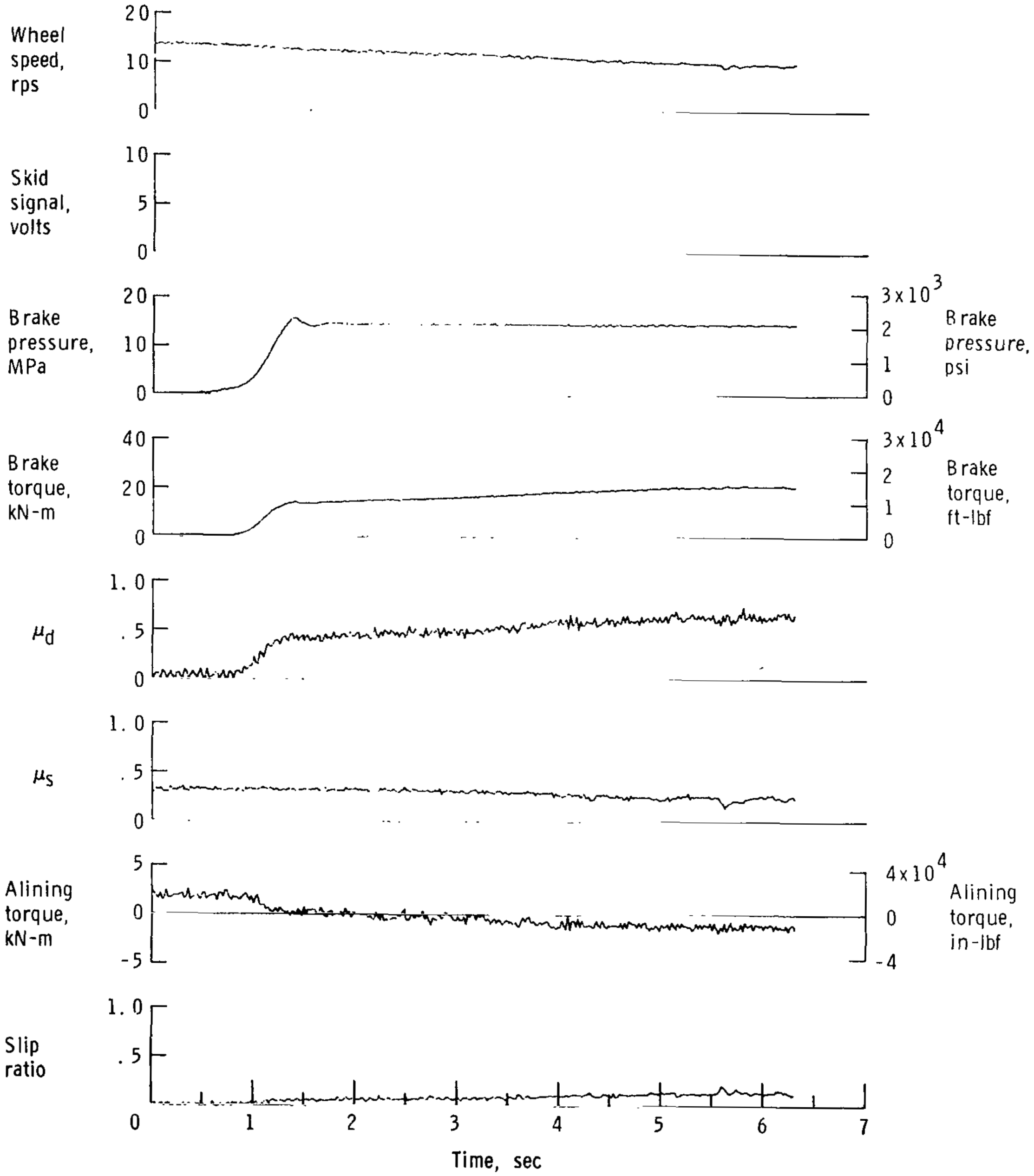

Figure A28.- Time histories for run 28; nominal carriage speed, 74 knots; vertical load, 72.1 kN (16 200 lbf); yaw angle, 3°; surface condition, dry; tire condition, new; brake pressure, 14 MPa (2000 lbf/in^2).

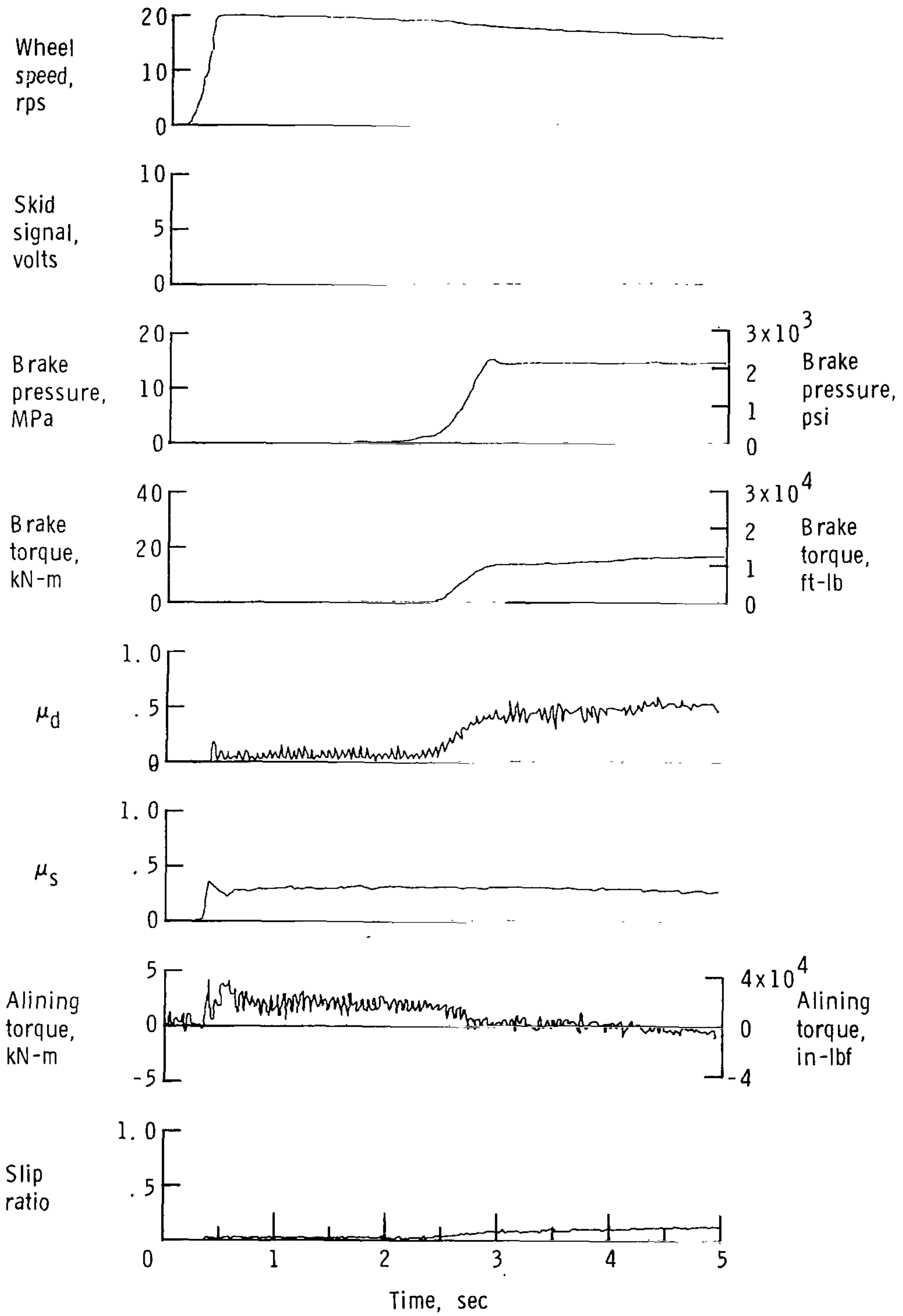

Figure A29.- Time histories for run 29; nominal carriage speed, 100 knots; vertical load, 75.6 kN (17 000 lbf); yaw angle, 3°; surface condition, dry; tire condition, new; brake pressure, 14 MPa (2000 lbf/in^2).

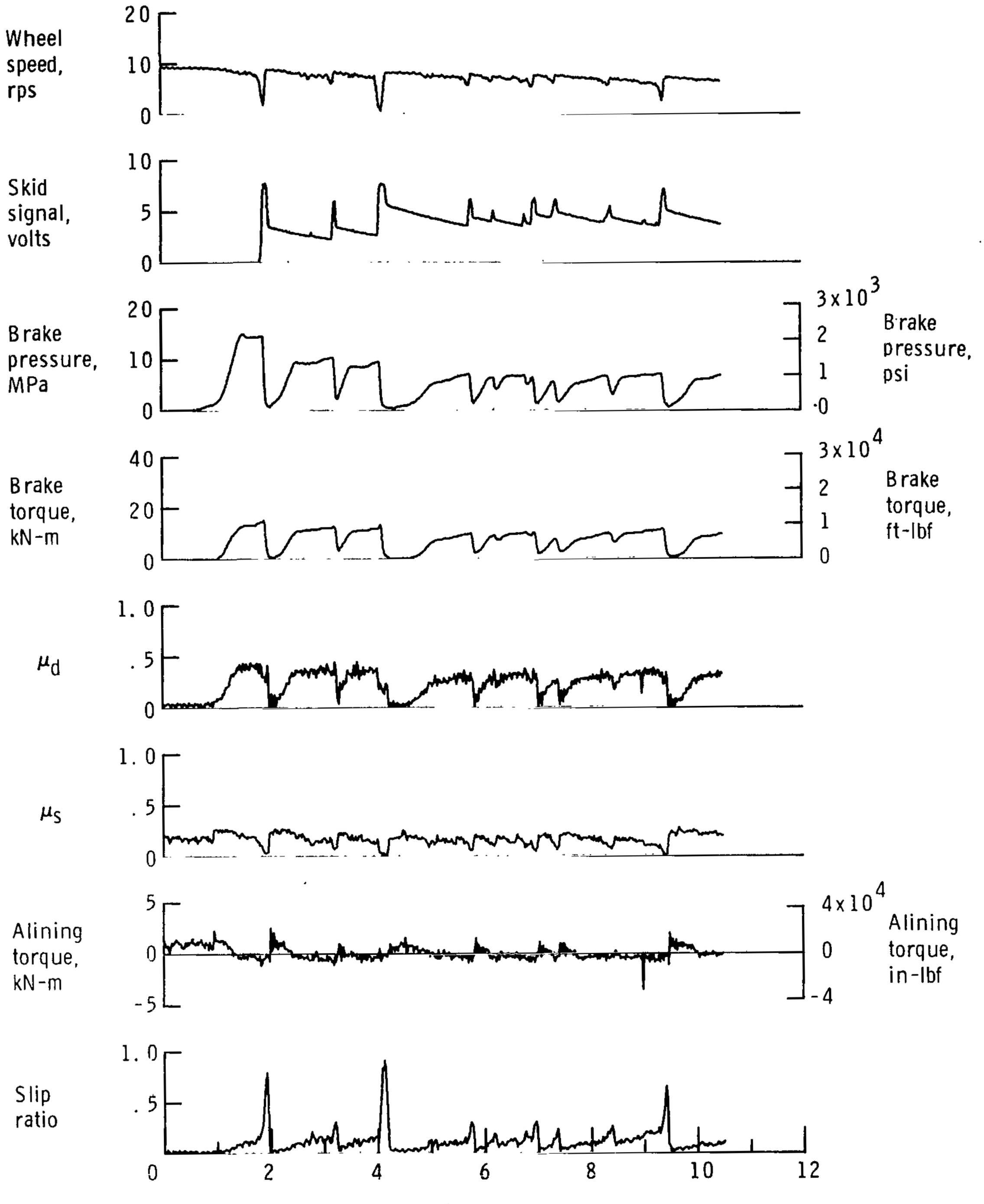

Figure A30.- Time histories for run 30; nominal carriage speed, 48 knots; vertical load, 76.5 kN (17 200 lbf); yaw angle, 3°; surface condition, damp; tire condition, new; brake pressure, 14 MPa (2000 lbf/in^2).

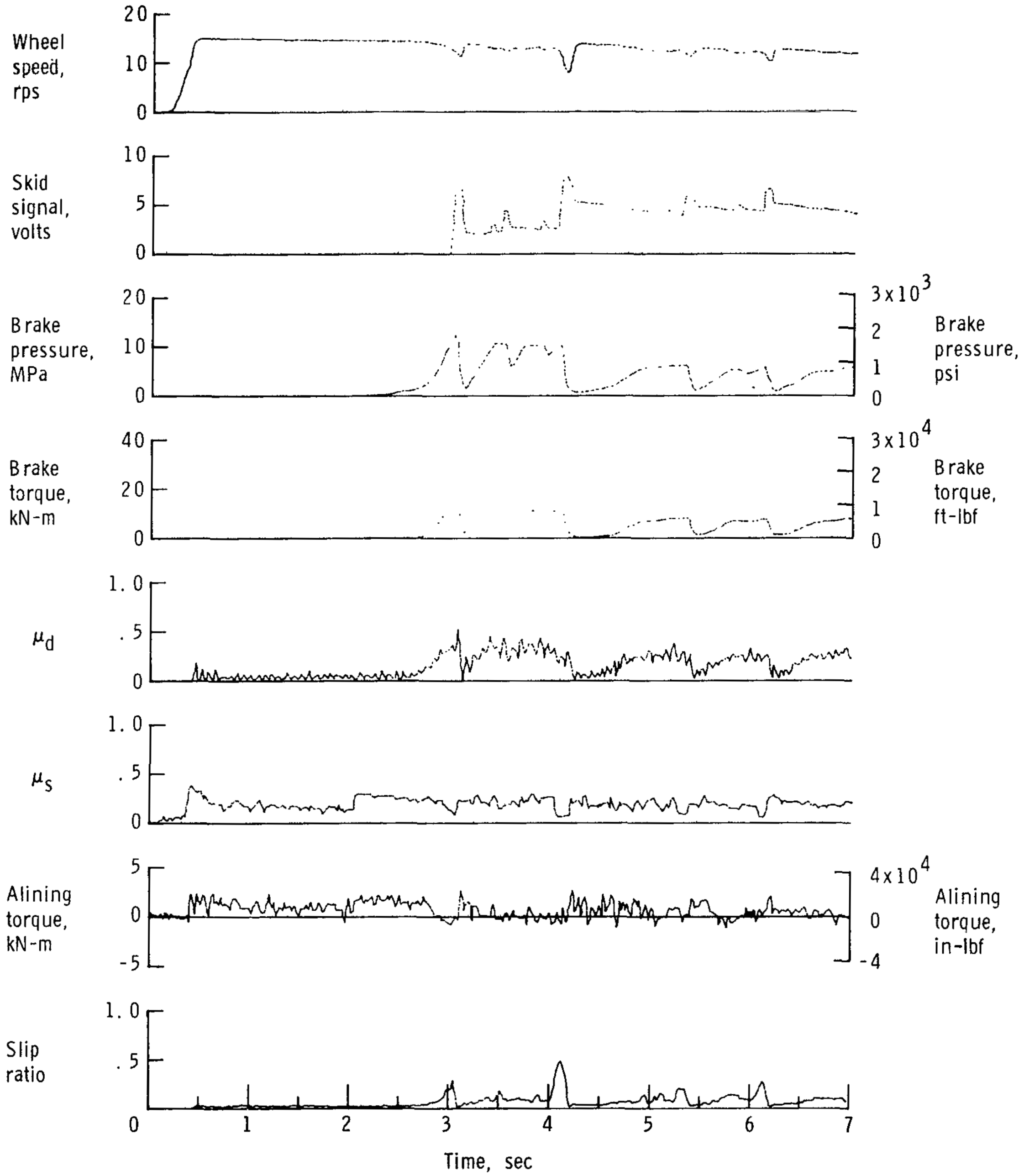

Figure A31.- Time histories for run 31; nominal carriage speed, 75 knots; vertical load, 81.0 kN (18 200 lbf); yaw angle, 3°; surface condition, damp; tire condition, new; brake pressure, 14 MPa (2000 lbf/in^2).

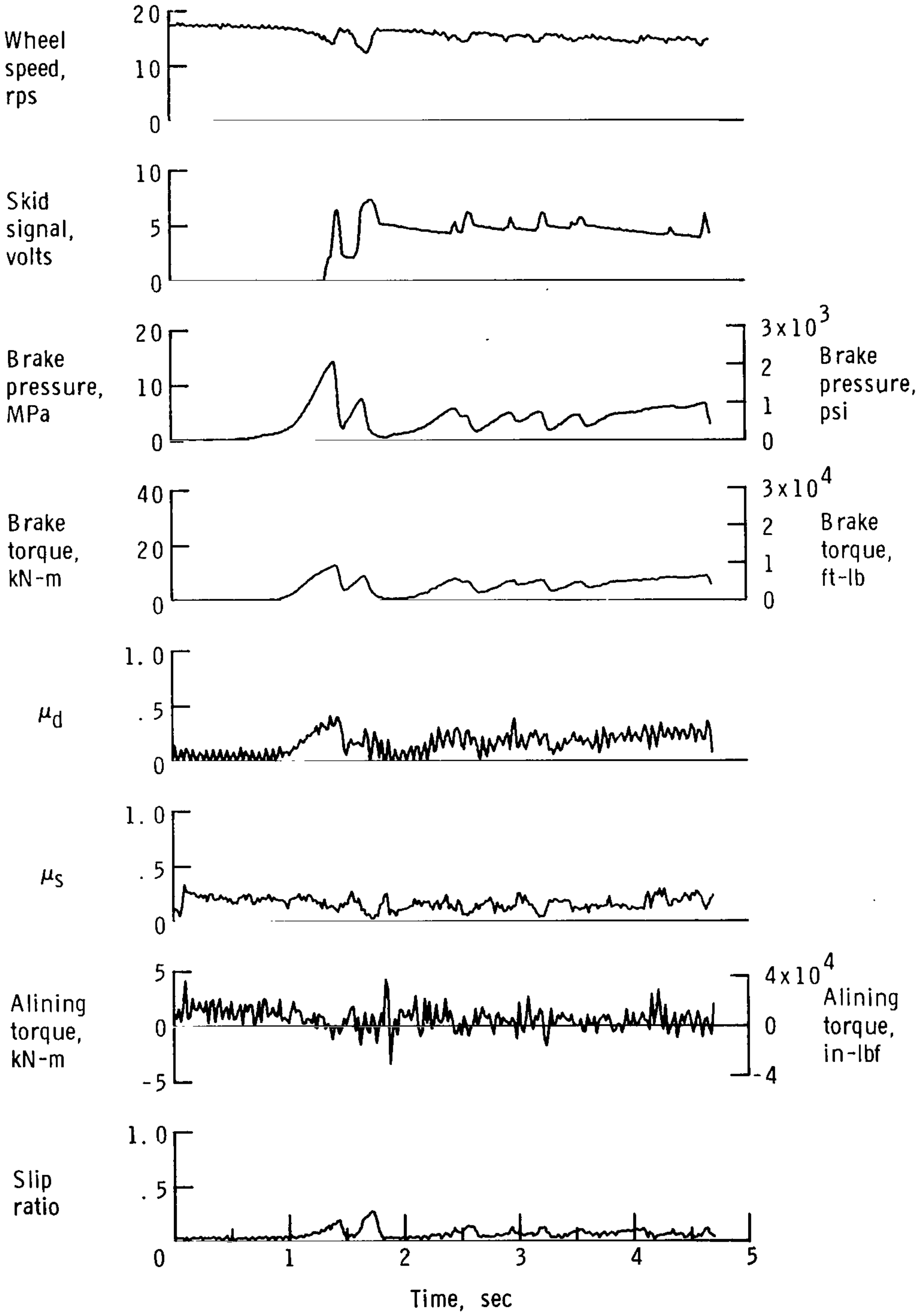

Figure A32.- Time histories for run 32; nominal carriage speed, 99 knots; vertical load, 81.0 kN (18 200 lbf); yaw angle, 3°; surface condition, damp; tire condition, new; brake pressure, 14 MPa (2000 lbf/in^2).

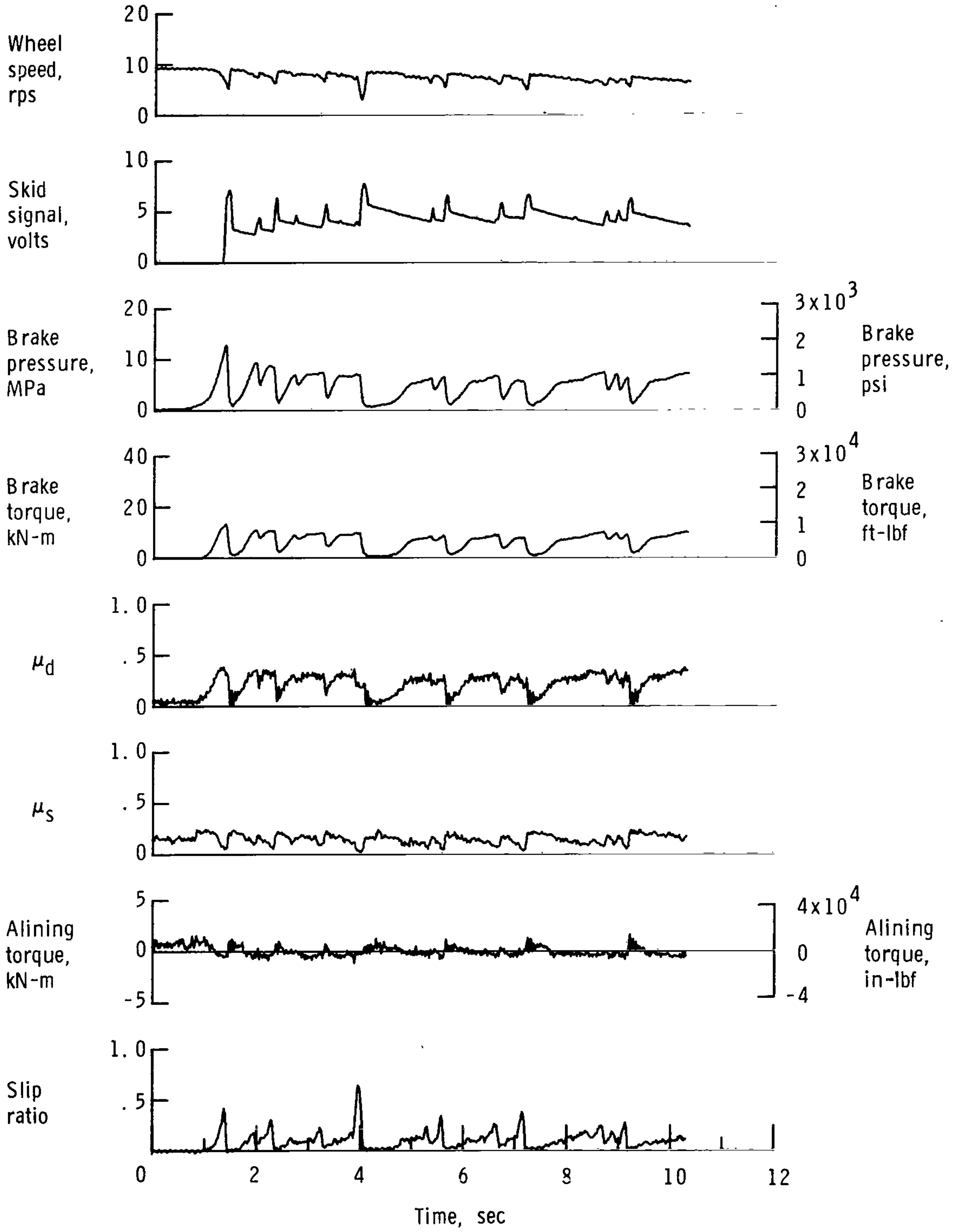

Figure A33.- Time histories for run 33; nominal carriage speed, 48 knots; vertical load, 76.1 kN (17 100 lbf); yaw angle, 3°; surface condition, flooded; tire condition, new; brake pressure, 14 MPa (2000 lbf/in^2).

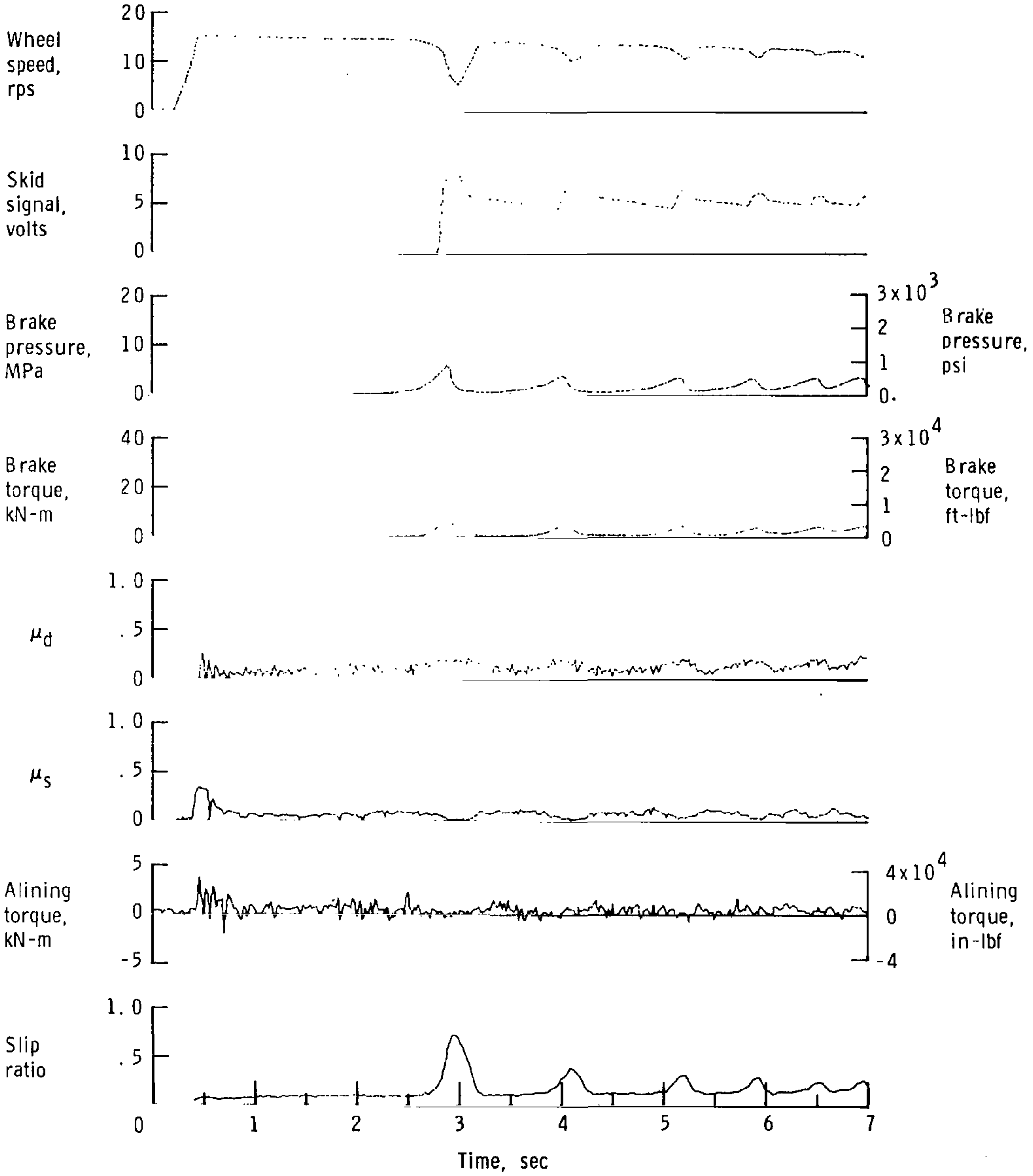

Figure A34.- Time histories for run 34; nominal carriage speed, 75 knots; vertical load, 74.7 kN (16 800 lbf); yaw angle, 3°; surface condition, flooded; tire condition, new; brake pressure, 14 MPa (2000 lbf/in^2).

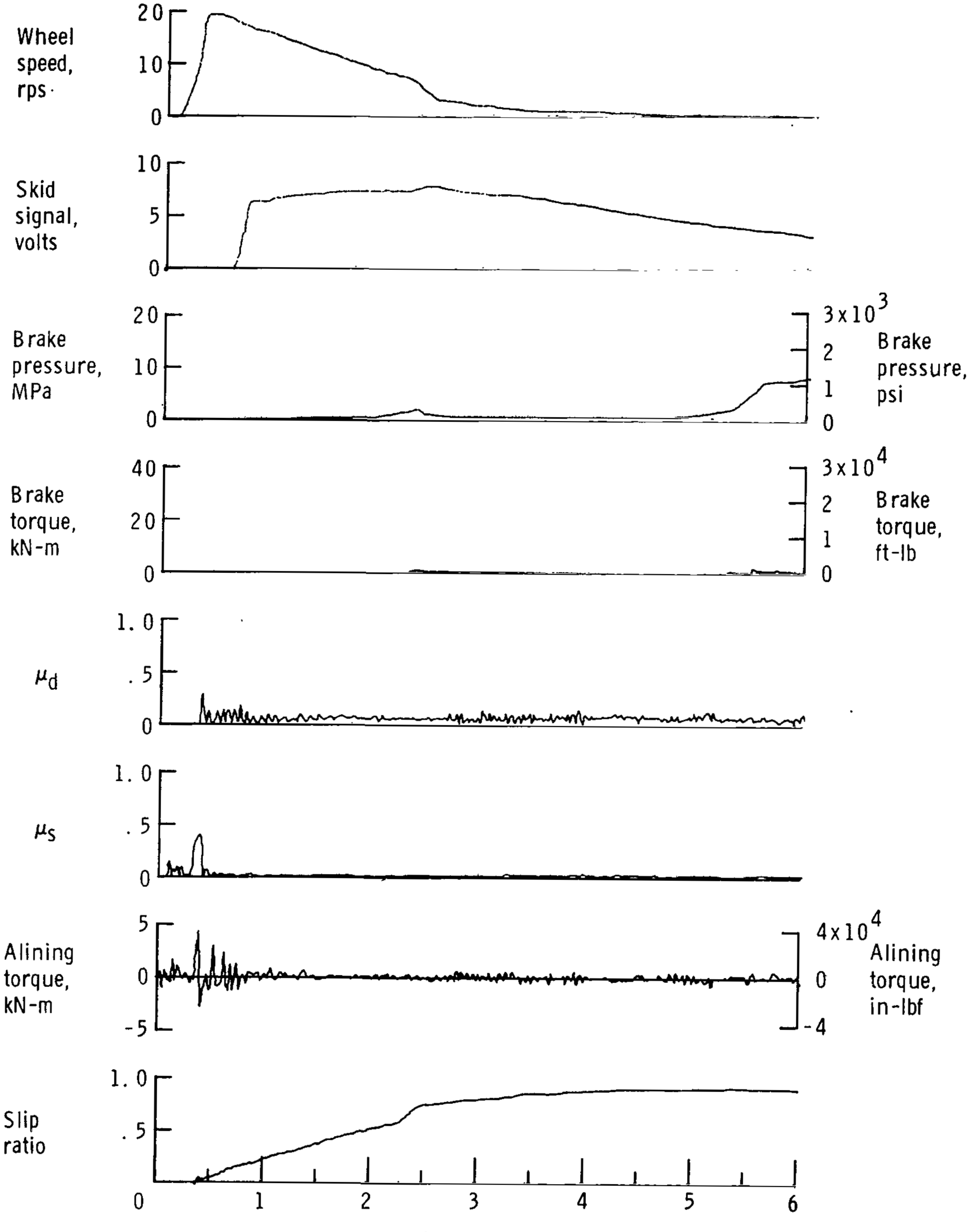

Figure A35.- Time histories for run 35; nominal carriage speed, 102 knots; vertical load, 74.3 kN (16 700 lbf); yaw angle, 3°; surface condition, flooded; tire condition, new; brake pressure, 14 MPa (2000 lbf/in^2).

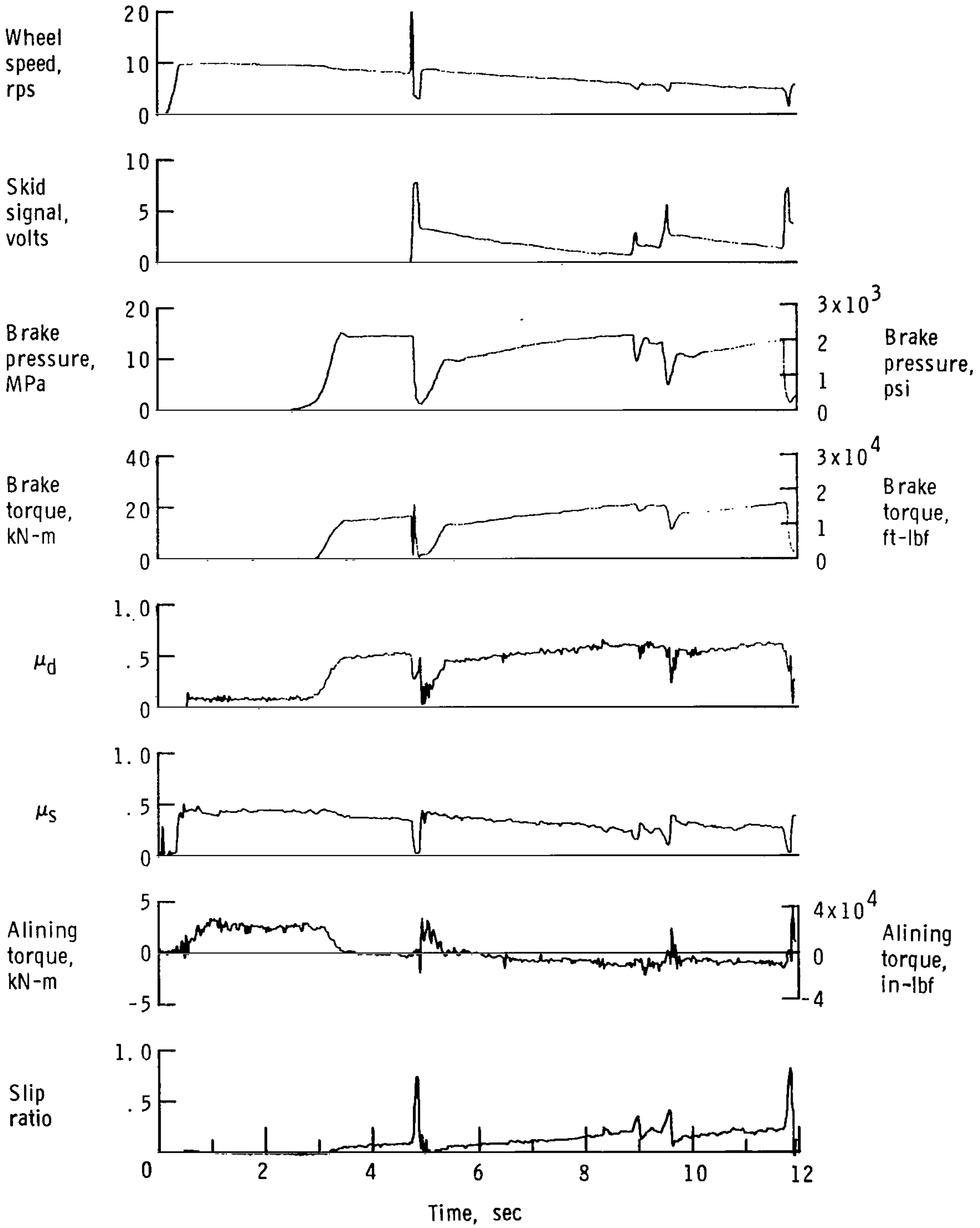

Figure A36.- Time histories for run 36; nominal carriage speed, 46 knots; vertical load, 83.6 kN (18 800 lbf); yaw angle, 6°; surface condition, dry; tire condition, new; brake pressure, 14 MPa (2000 lbf/in^2).

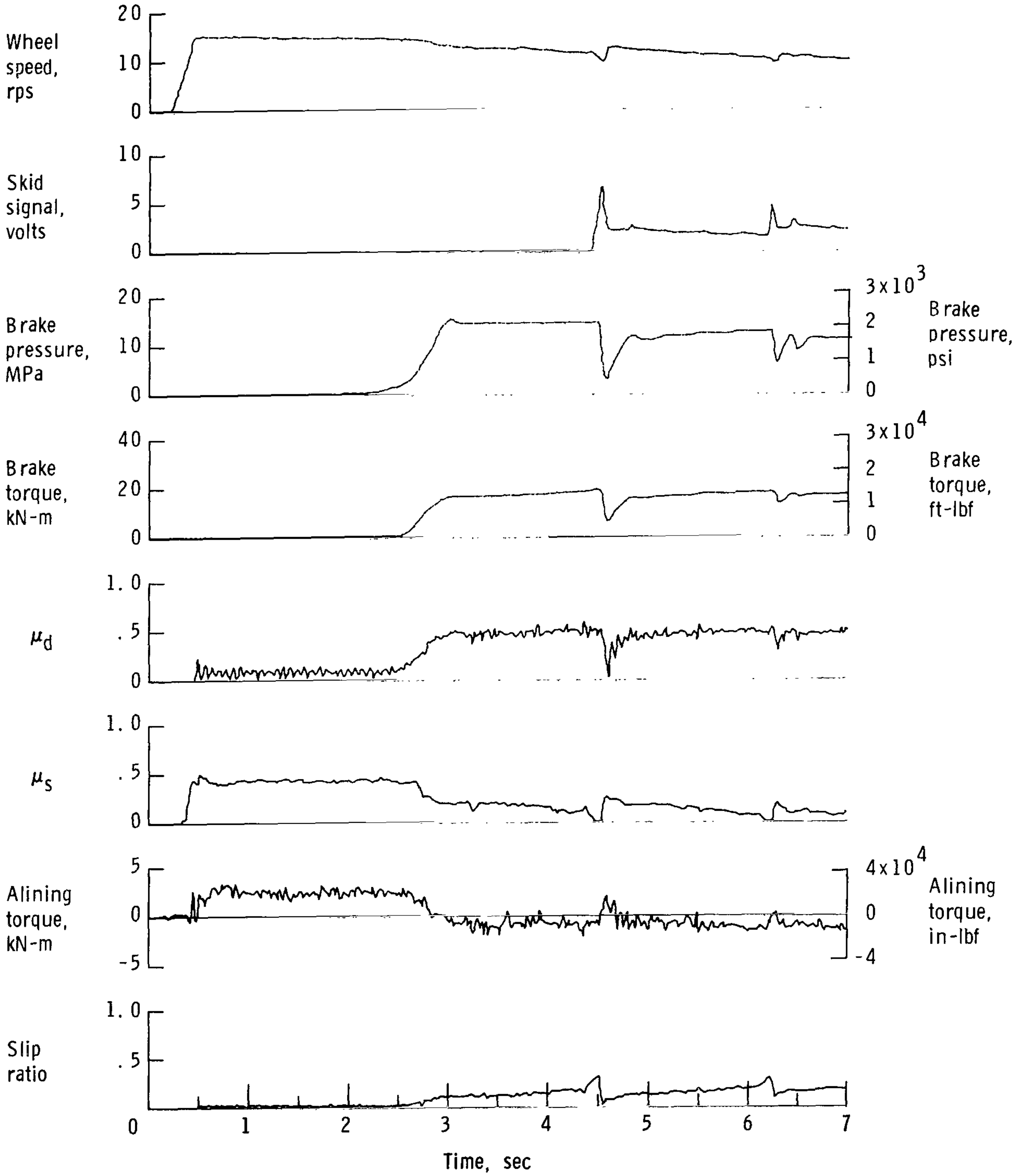

Figure A37.- Time histories for run 37; nominal carriage speed, 74 knots; vertical load, 81.4 kN (19 300 lbf); yaw angle, 6°; surface condition, dry; tire condition, new; brake pressure, 14 MPa (2000 lbf/in^2).

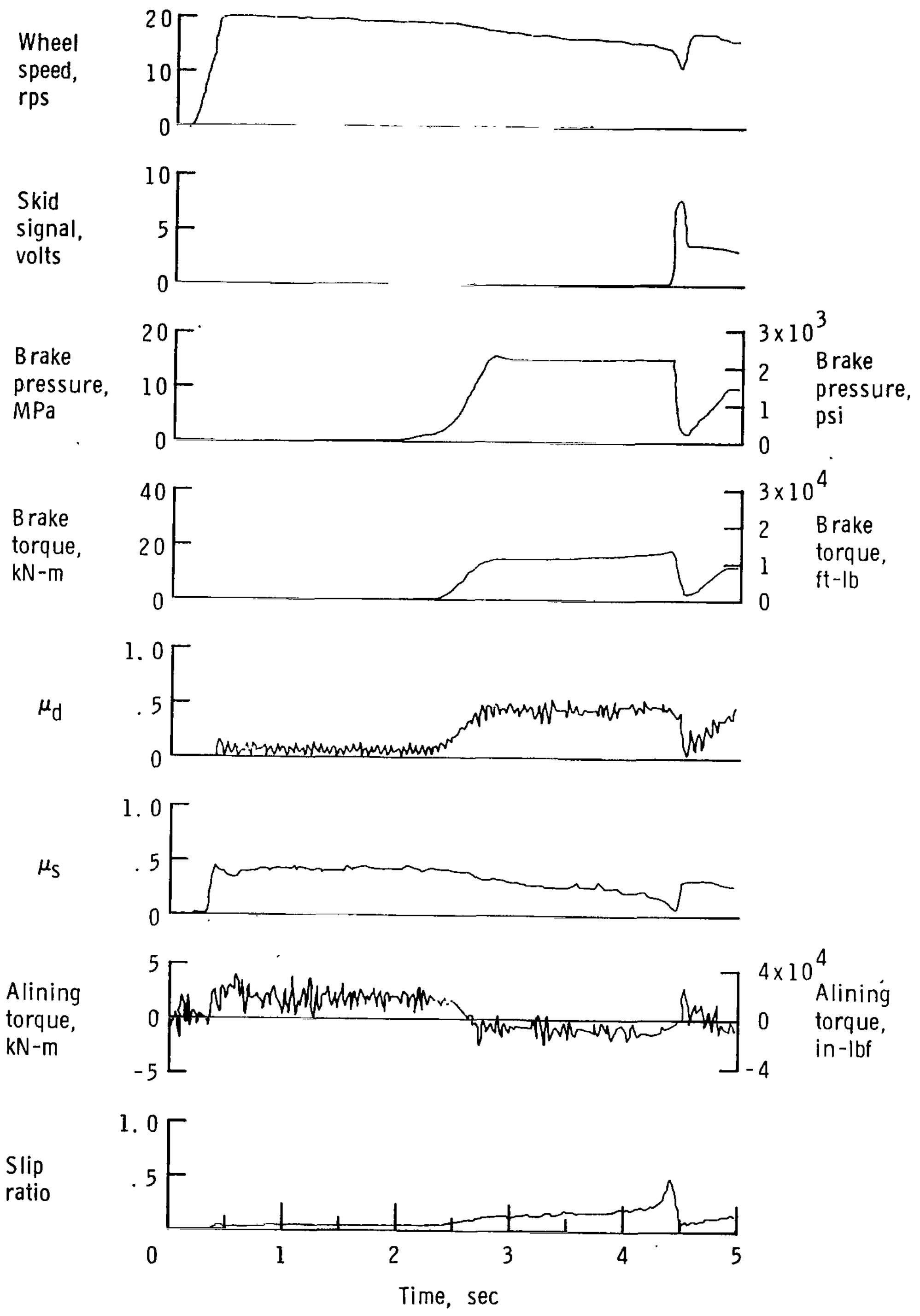

Figure A38.- Time histories for run 38; nominal carriage speed, 100 knots; vertical load, 83.2 kN (18 700 lbf); yaw angle, 6°; surface condition, dry; tire condition, new; brake pressure, 14 MPa (2000 lbf/in^2).

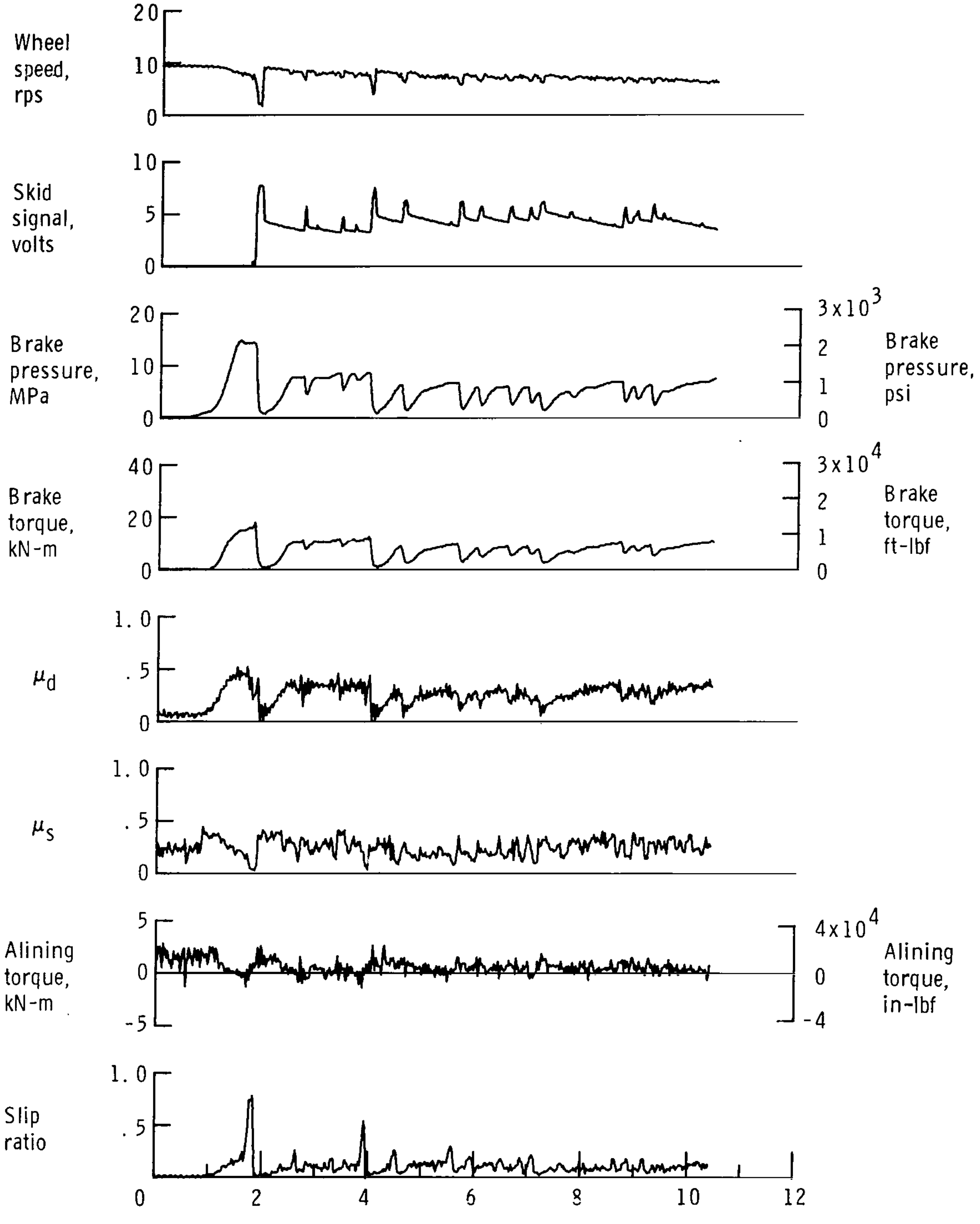

Figure A39.- Time histories for run 39; nominal carriage speed, 50 knots; vertical load, 82.3 kN (18 500 lbf); yaw angle, 6°; surface condition, damp; tire condition, new; brake pressure, 14 MPa (2000 lbf/in^2).

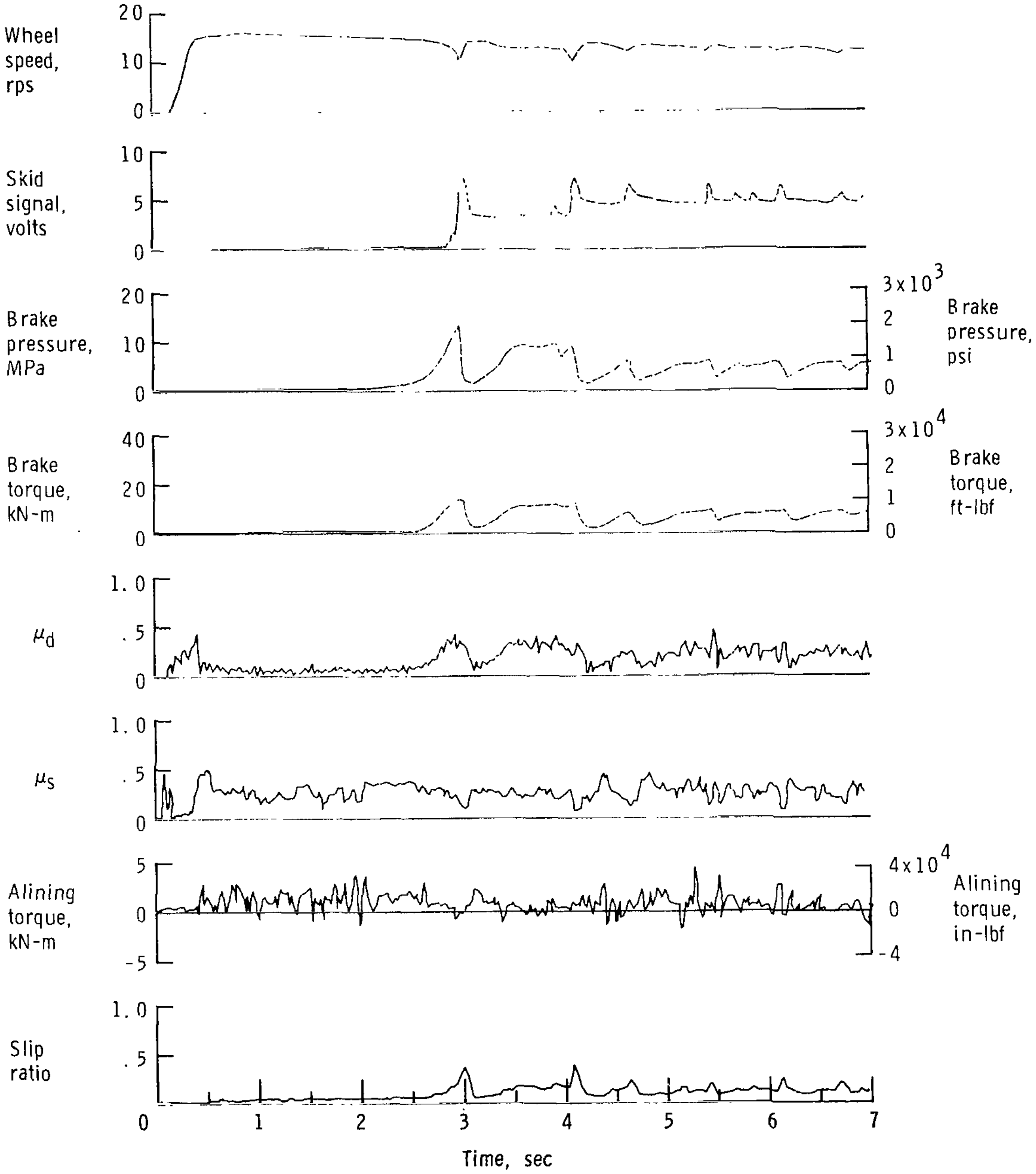

Figure A40.- Time histories for run 40; nominal carriage speed, 75 knots; vertical load, 81.8 kN (18 400 lbf); yaw angle, 6°; surface condition, damp; tire condition, new; brake pressure, 14 MPa (2000 lbf/in^2).

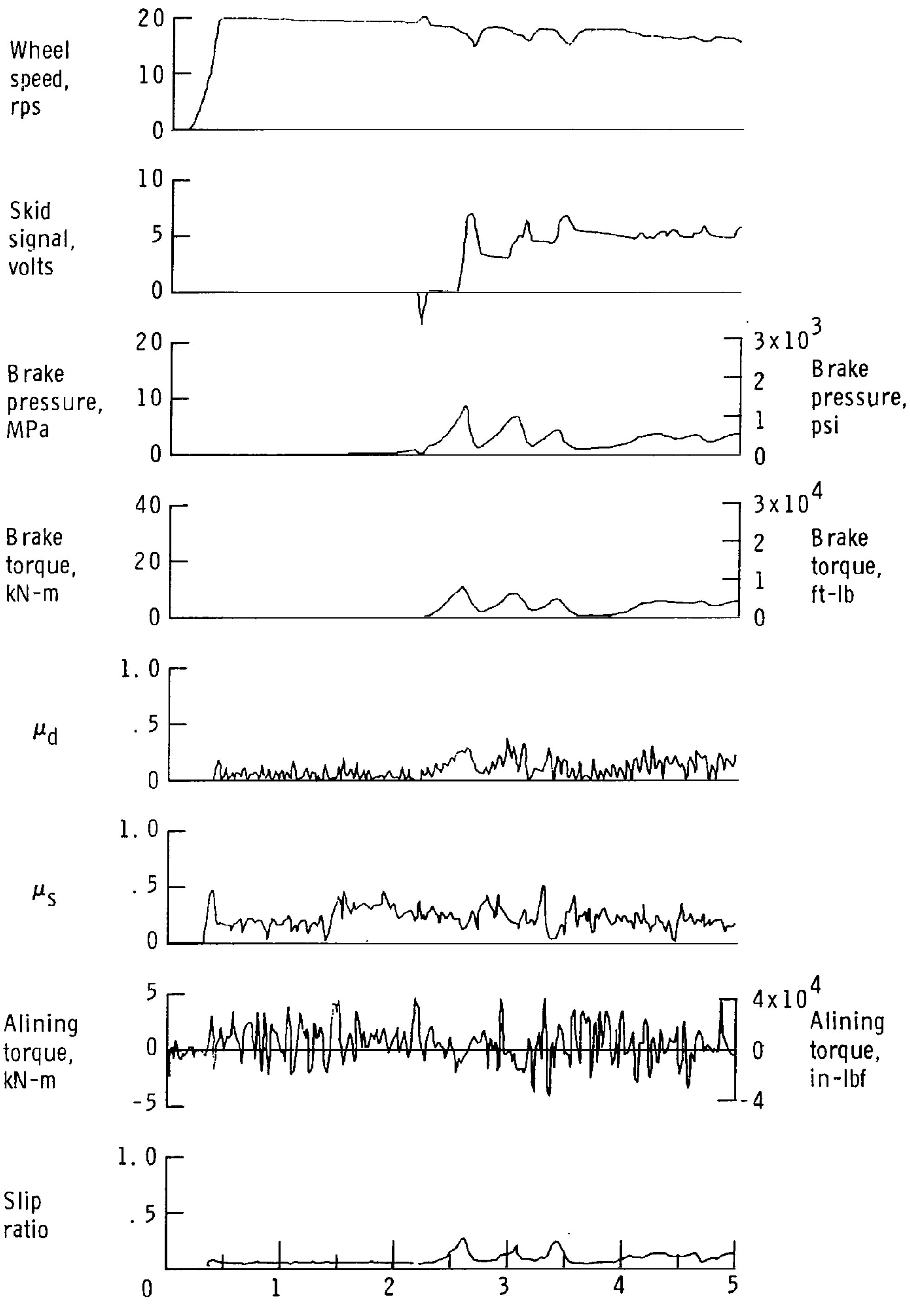

Figure A41.- Time histories for run 41; nominal carriage speed, 100 knots; vertical load, 76.5 kN (17 200 lbf); yaw angle, 6°; surface condition, damp; tire condition, new; brake pressure, 14 MPa (2000 lbf/in^2).

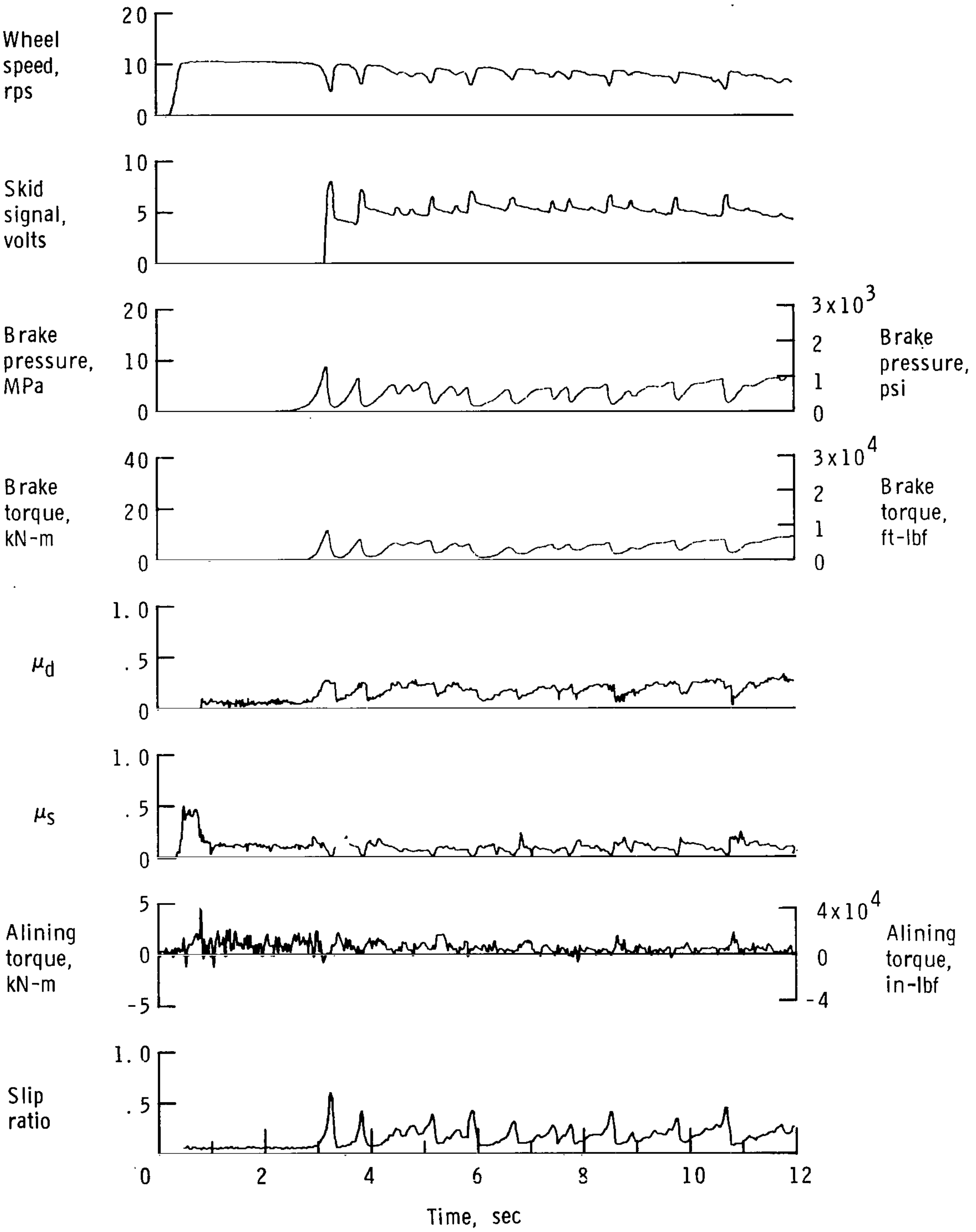

Figure A42.- Time histories for run 42; nominal carriage speed, 52 knots; vertical load, 80.5 kN (18 100 lbf); yaw angle, 6°; surface condition, flooded; tire condition, new; brake pressure, 14 MPa (2000 lbf/in^2).

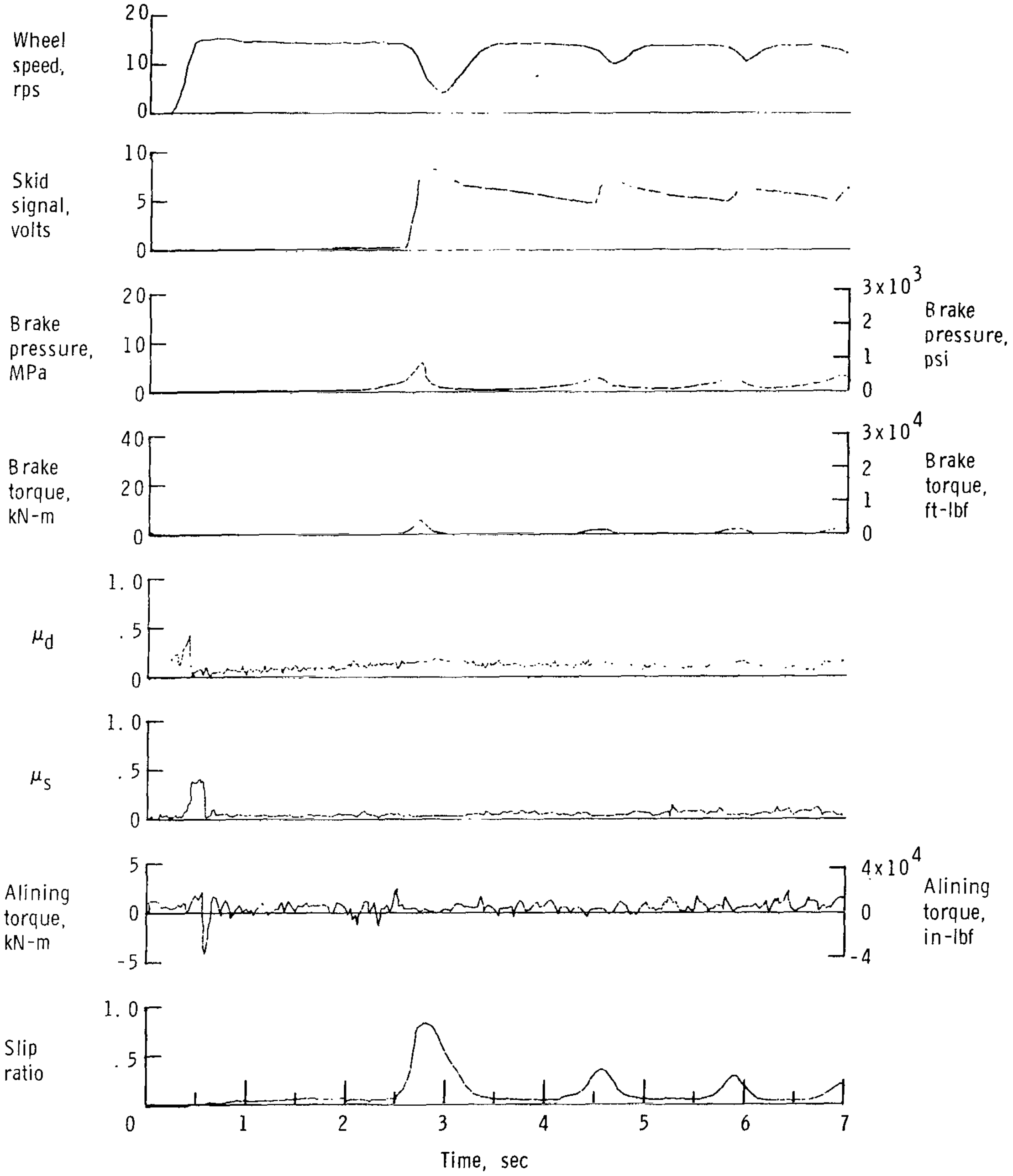

Figure A43.- Time histories for run 43; nominal carriage speed, 75 knots; vertical load, 80.1 kN (18 000 lbf); yaw angle, 6°; surface condition, flooded; tire condition, new; brake pressure, 14 MPa (2000 lbf/in^2).

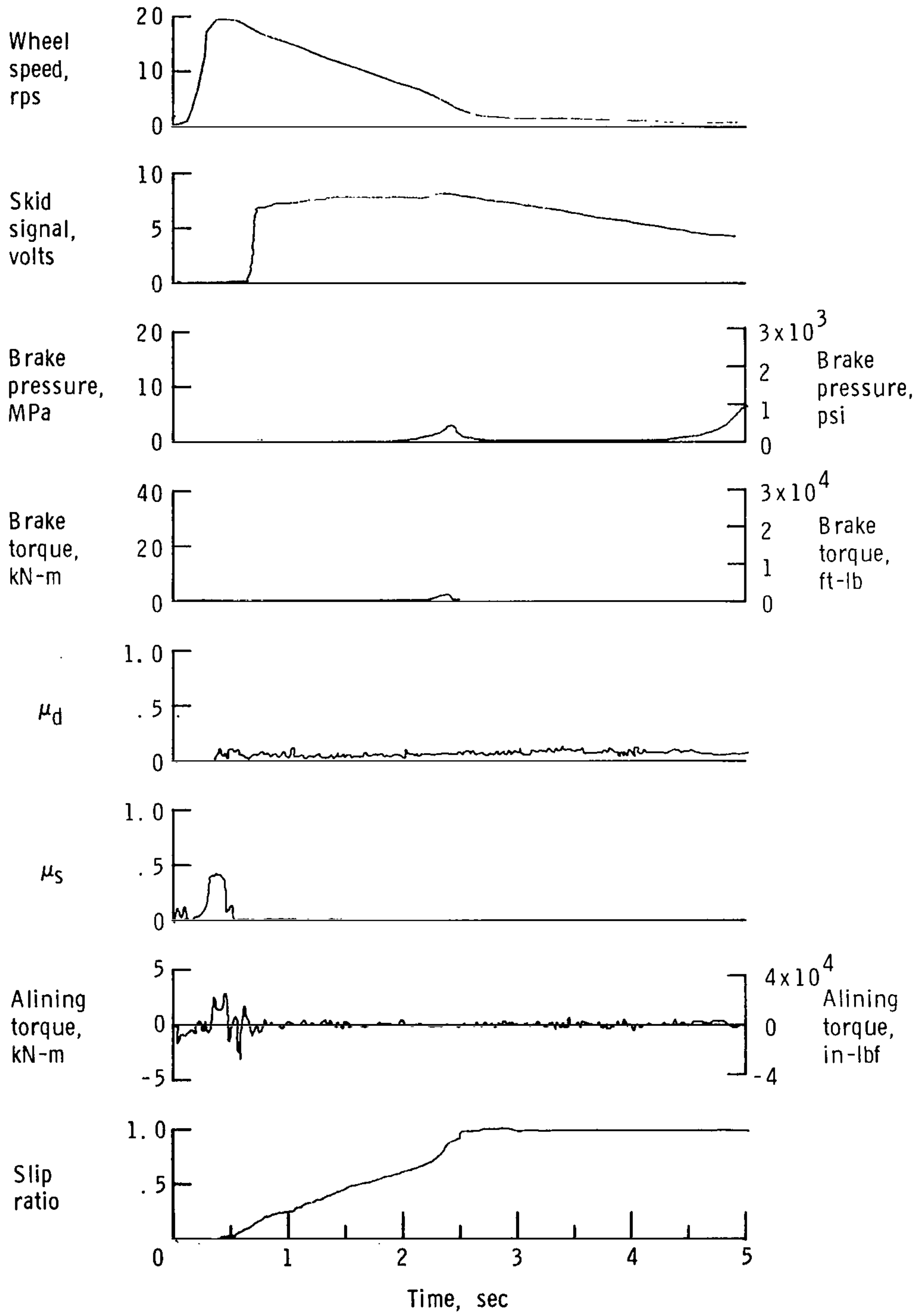

Figure A44.- Time histories for run 44; nominal carriage speed, 101 knots; vertical load, 80.1 kN (18 000 lbf); yaw angle, 6°; surface condition, flooded; tire condition, new; brake pressure, 14 MPa (2000 lbf/in^2).

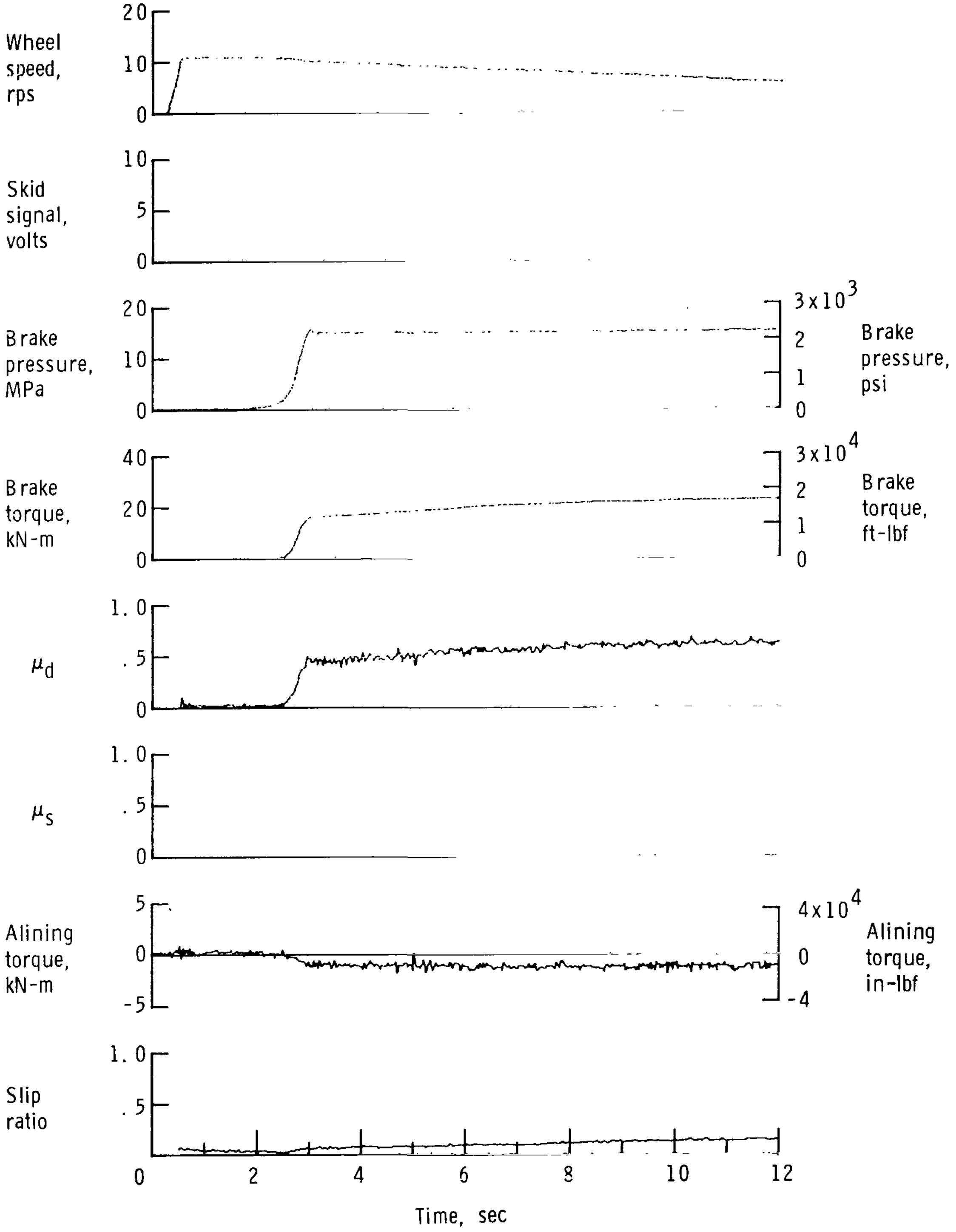

Figure A45.- Time histories for run 45; nominal carriage speed, 50 knots; vertical load, 80.1 kN (18 000 lbf); yaw angle, 0°; surface condition, dry; tire condition, worn; brake pressure, 14 MPa (2000 lbf/in^{2}).

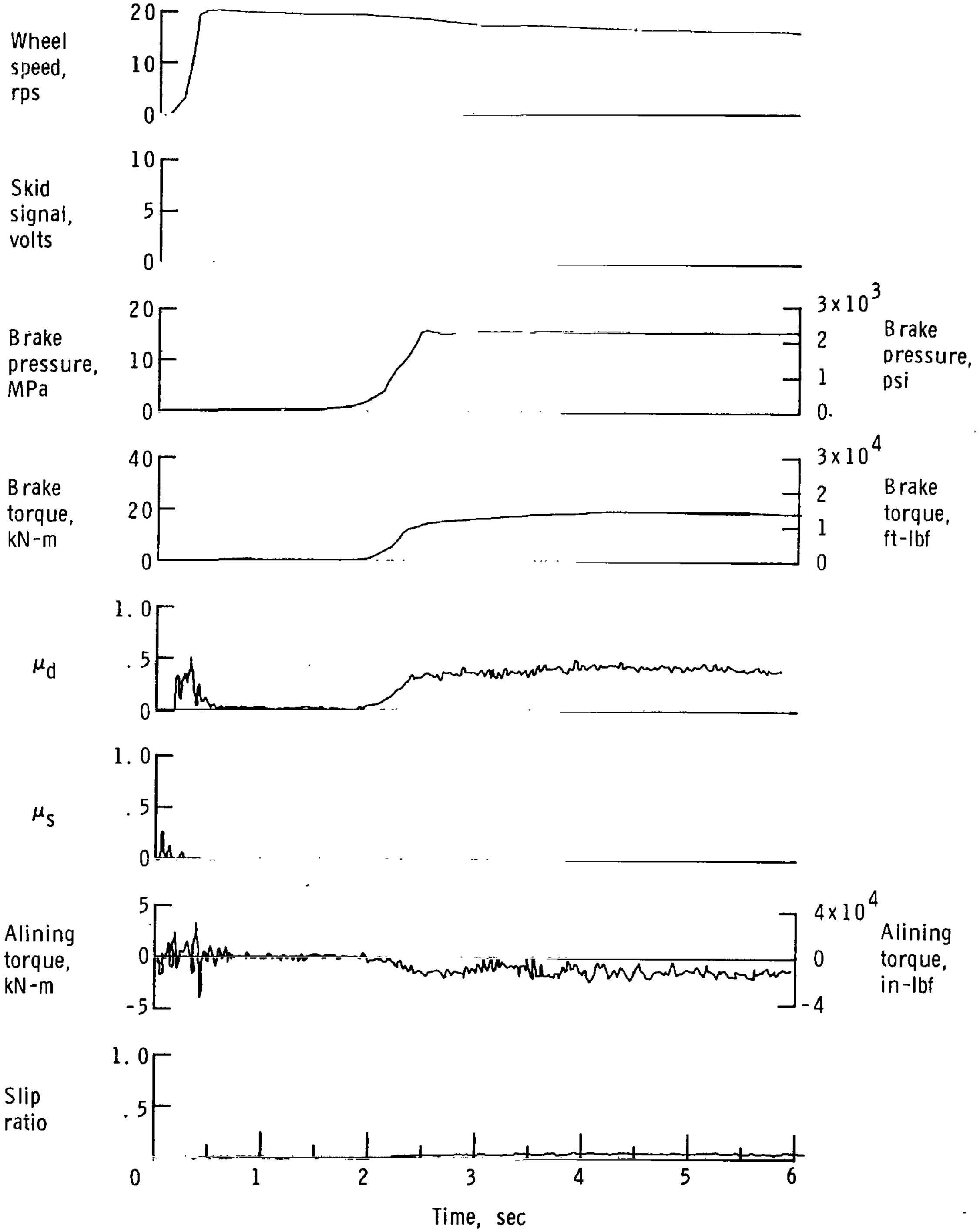

Figure A46.- Time histories for run 46; nominal carriage speed, 100 knots; vertical load, 96.5 kN (21 700 lbf); yaw angle, 0°; surface condition, dry; tire condition, worn; brake pressure, 14 MPa (2000 lbf/in^2).

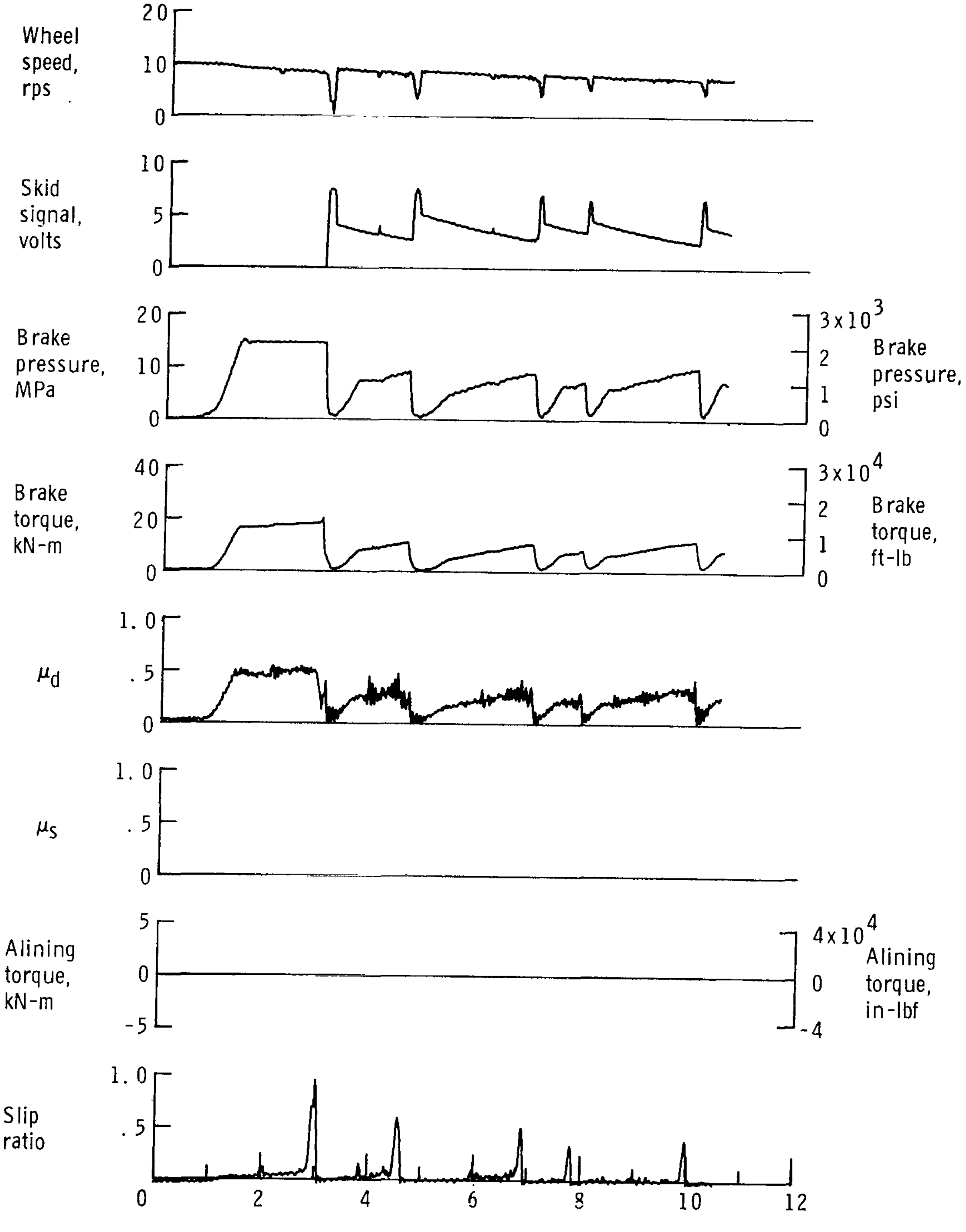

Figure A47.- Time histories for run 47; nominal carriage speed, 50 knots; vertical load, 80.1 kN (18 000 lbf); yaw angle, 0°; surface condition, damp; tire condition, worn; brake pressure, 14 MPa (2000 lbf/in^2).

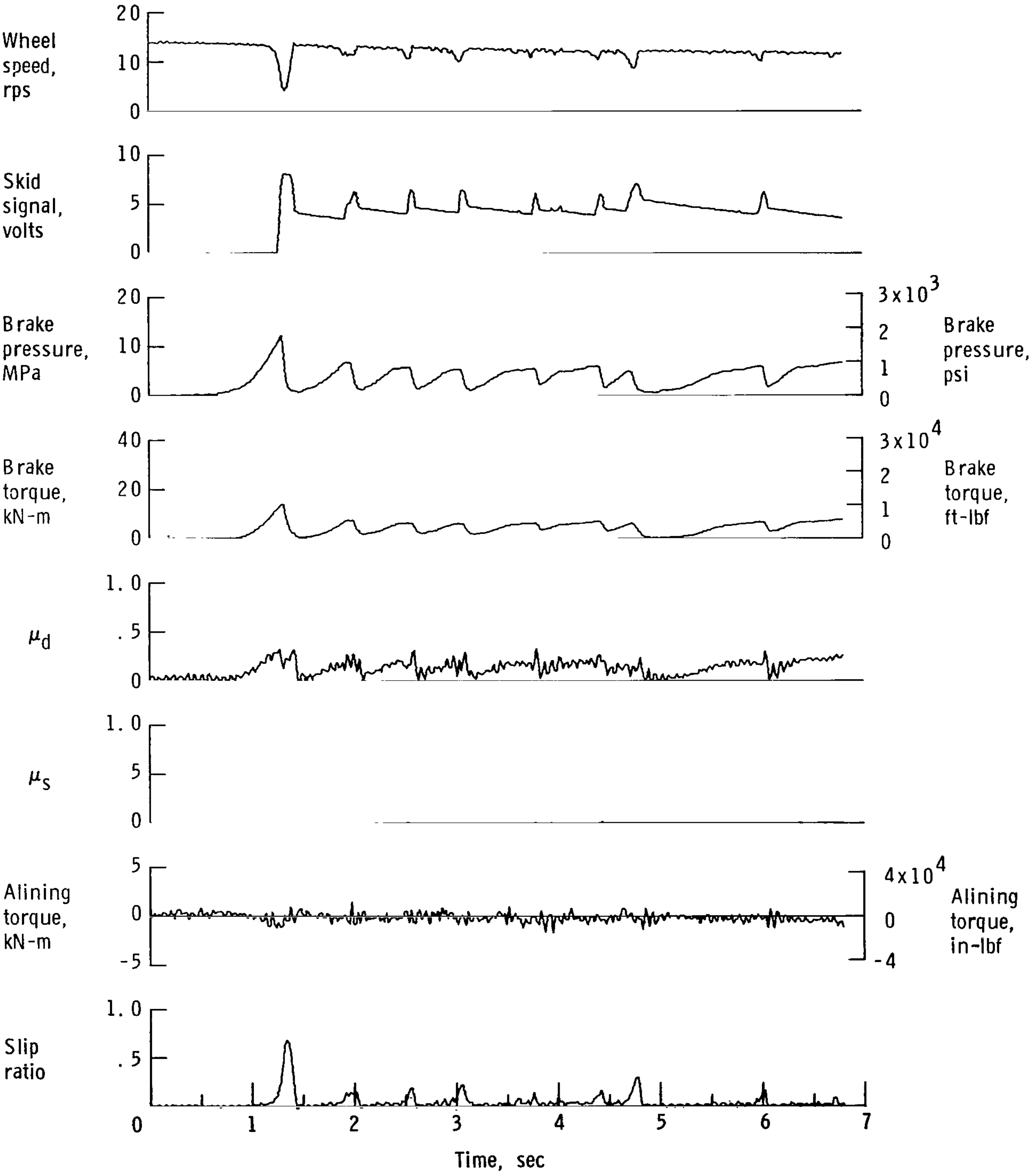

Figure A48.- Time histories for run 48; nominal carriage speed, 76 knots; vertical load, 80.1 kN (18 000 lbf); yaw angle, 0°; surface condition, damp; tire condition, worn; brake pressure, 14 MPa (2000 lbf/in^2).

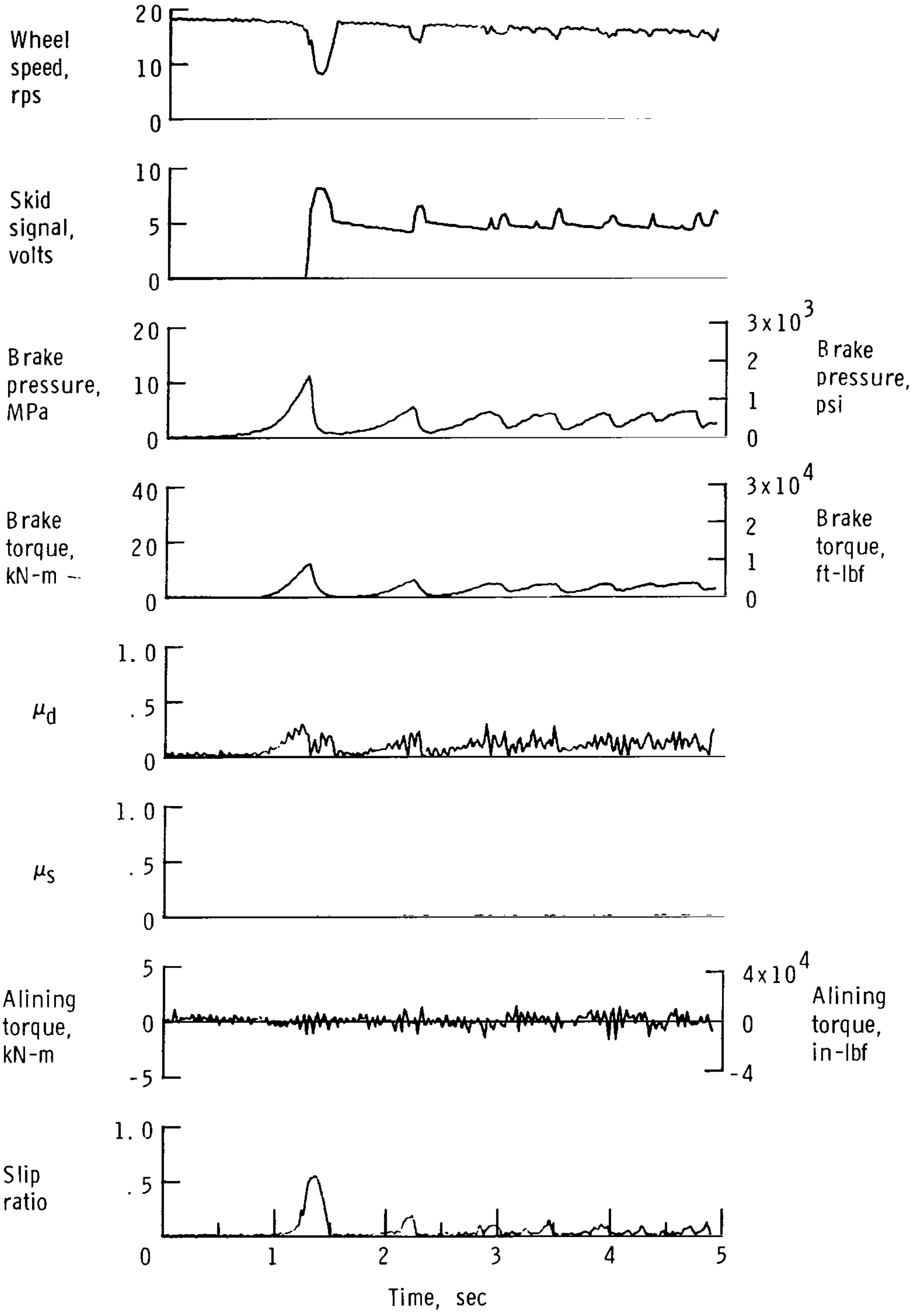

Figure A49.- Time histories for run 49; nominal carriage speed, 102 knots; vertical load, 82.3 kN (18 500 lbf); yaw angle, 0°; surface condition, damp; tire condition, worn; brake pressure, 14 MPa (2000 lbf/in^2).

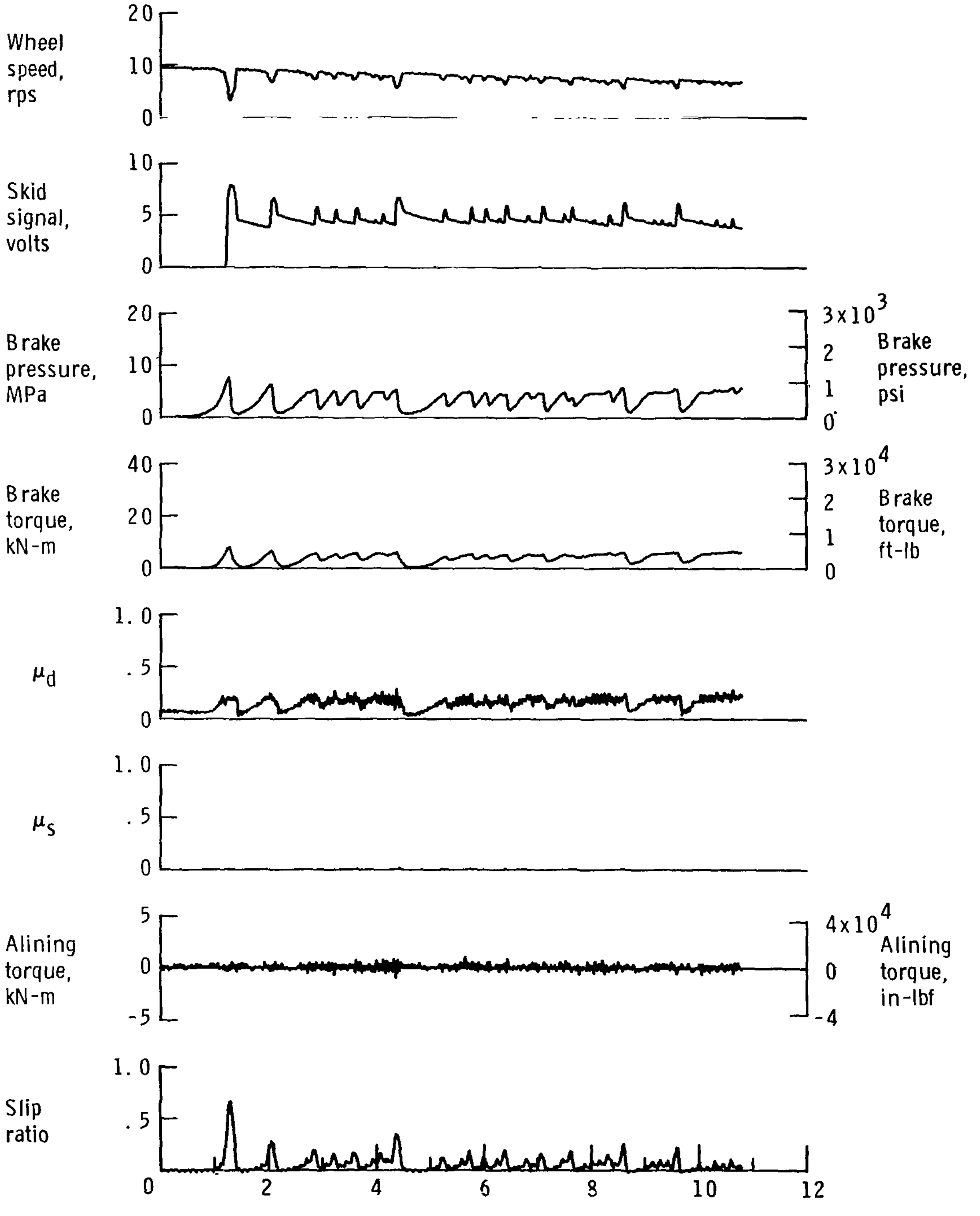

Figure A50.- Time histories for run 50; nominal carriage speed, 48 knots; vertical load, 81.0 kN (18 200 lbf); yaw angle, 0°; surface condition, flooded; tire condition, worn; brake pressure, 14 MPa (2000 lbf/in^2).

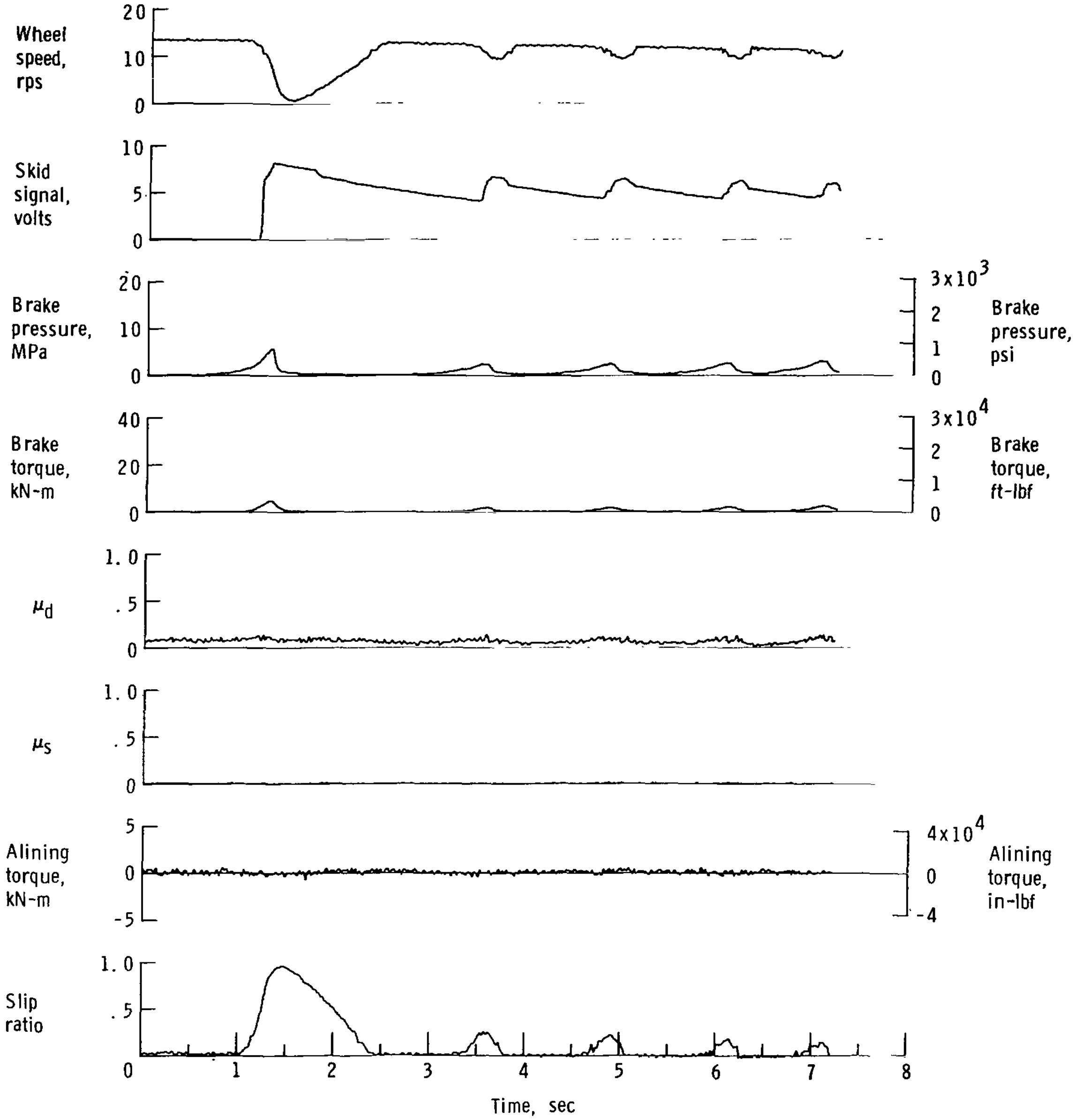

Figure A51.- Time histories for run 51; nominal carriage speed, 75 knots; vertical load, 78.7 kN (17 700 lbf); yaw angle, 0°; surface condition, flooded; tire condition, worn; brake pressure, 14 MPa (2000 lbf/in^2).

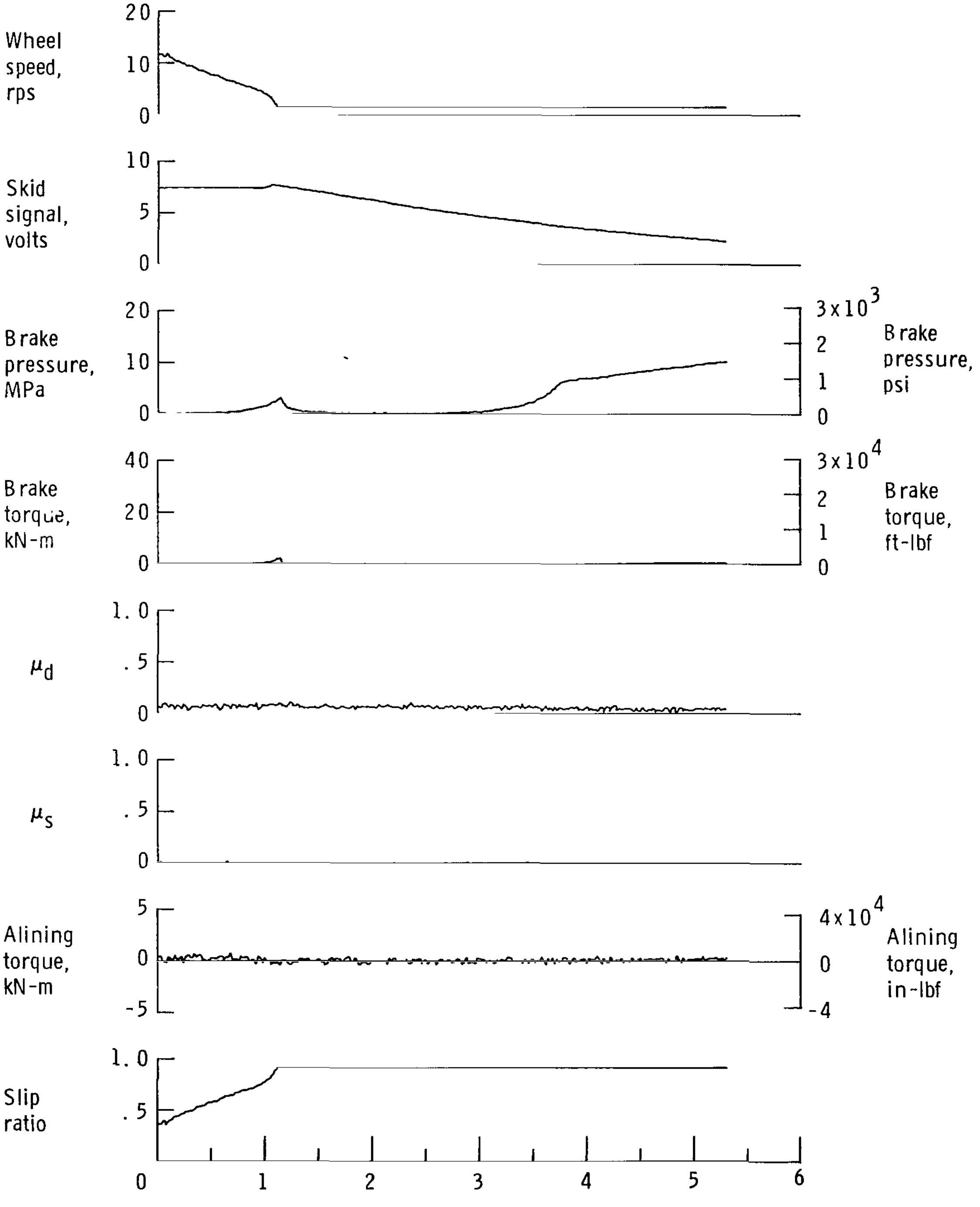

Figure A52.- Time histories for run 52; nominal carriage speed, 99 knots; vertical load, 81.4 kN (18 300 lbf); yaw angle, 0°; surface condition, flooded; tire condition, worn; brake pressure, 14 MPa (2000 lbf/in^2).

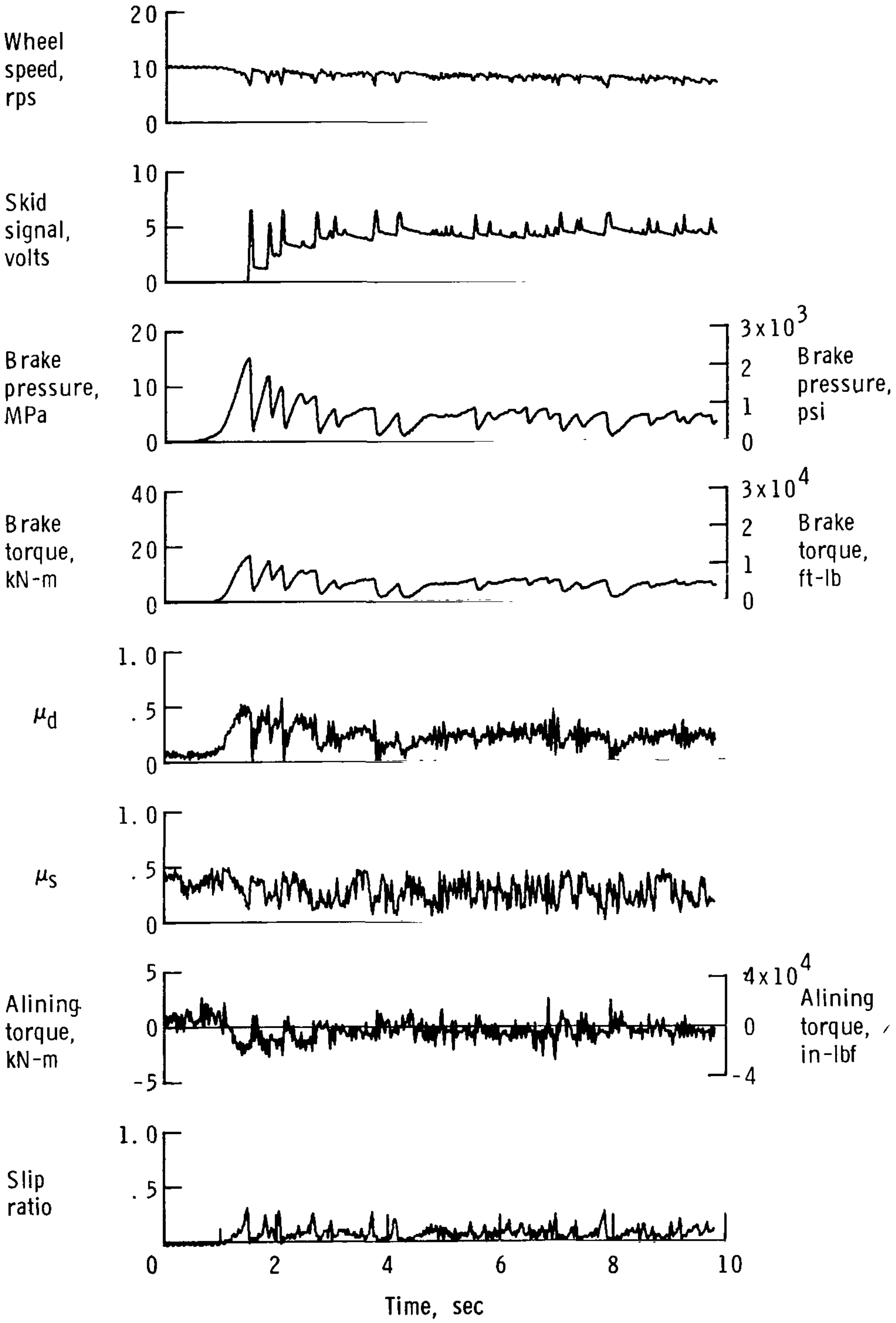

Figure A53.- Time histories for run 53; nominal carriage speed, 52 knots; vertical load, 80.1 kN (18 000 lbf); yaw angle, 6°; surface condition, damp; tire condition, worn; brake pressure, 14 MPa (2000 lbf/in^2).

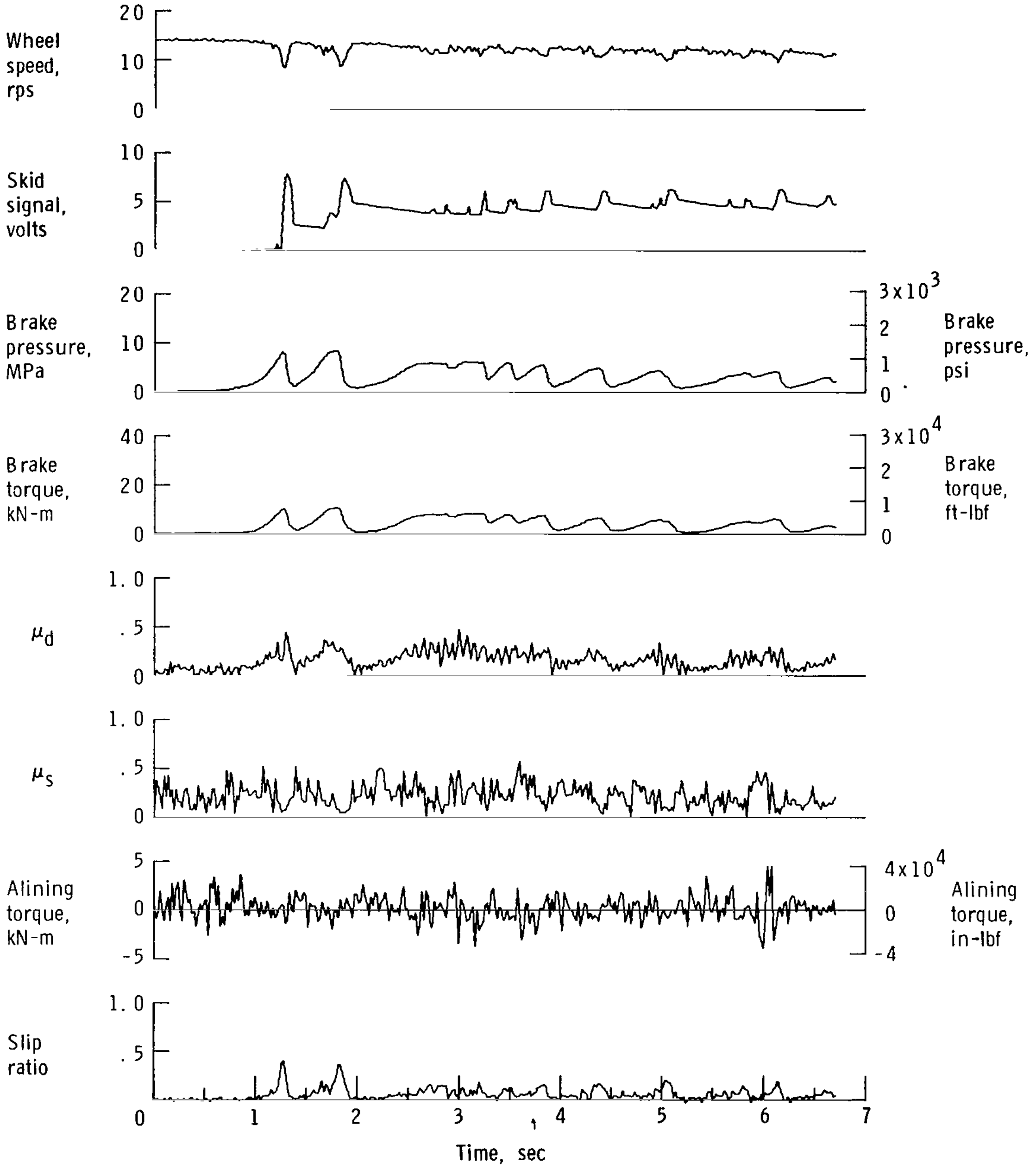

Figure A54.- Time histories for run 54; nominal carriage speed, 77 knots; vertical load, 79.6 kN (17 900 lbf); yaw angle, 6°; surface condition, damp; tire condition, worn; brake pressure, 14 MPa (2000 lbf/in^2).

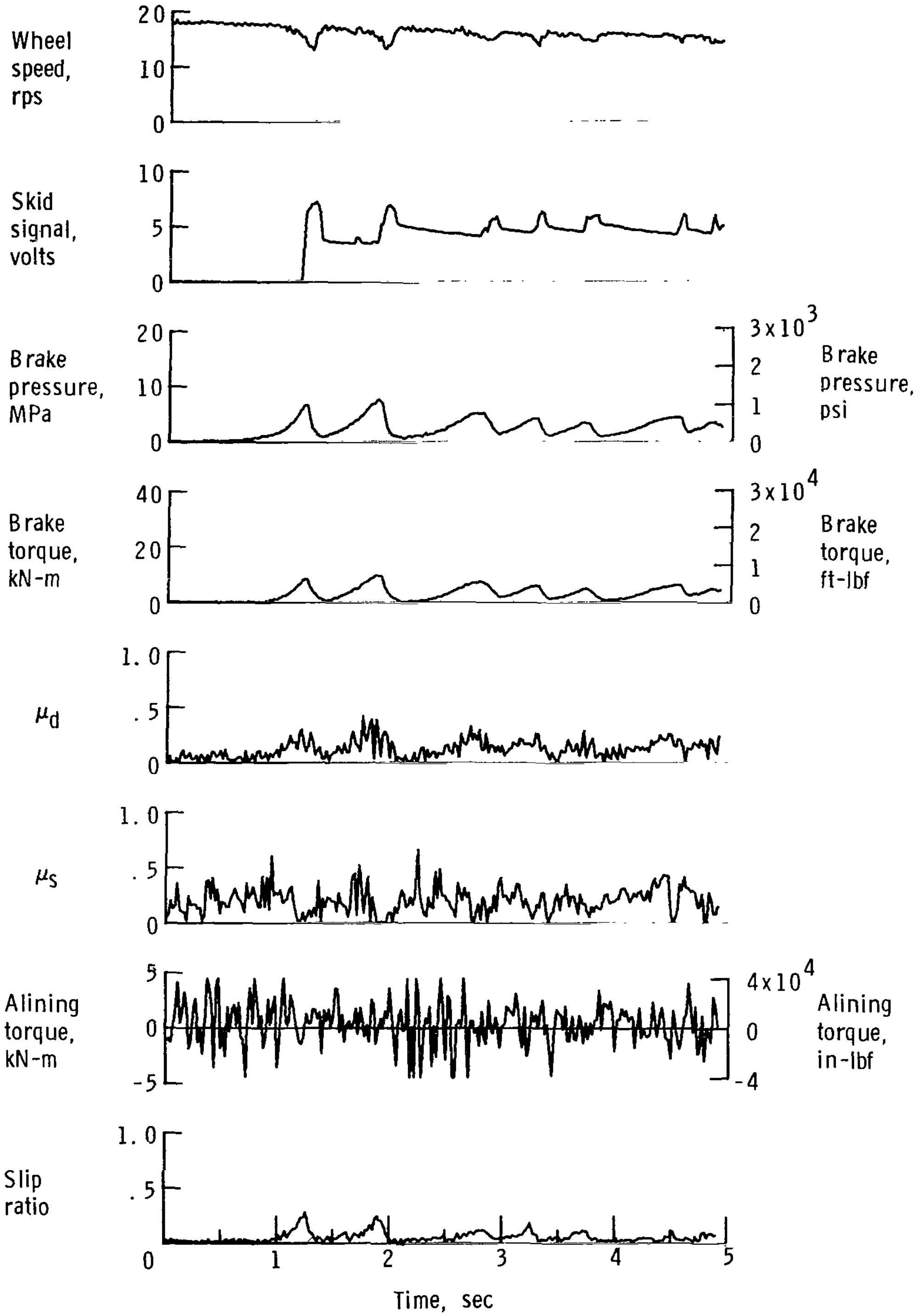

Figure A55.- Time histories for run 55; nominal carriage speed, 102 knots; vertical load, 82.7 kN (18 600 lbf); yaw angle, 6°; surface condition, damp; tire condition, worn; brake pressure, 14 MPa (2000 lbf/in^2).

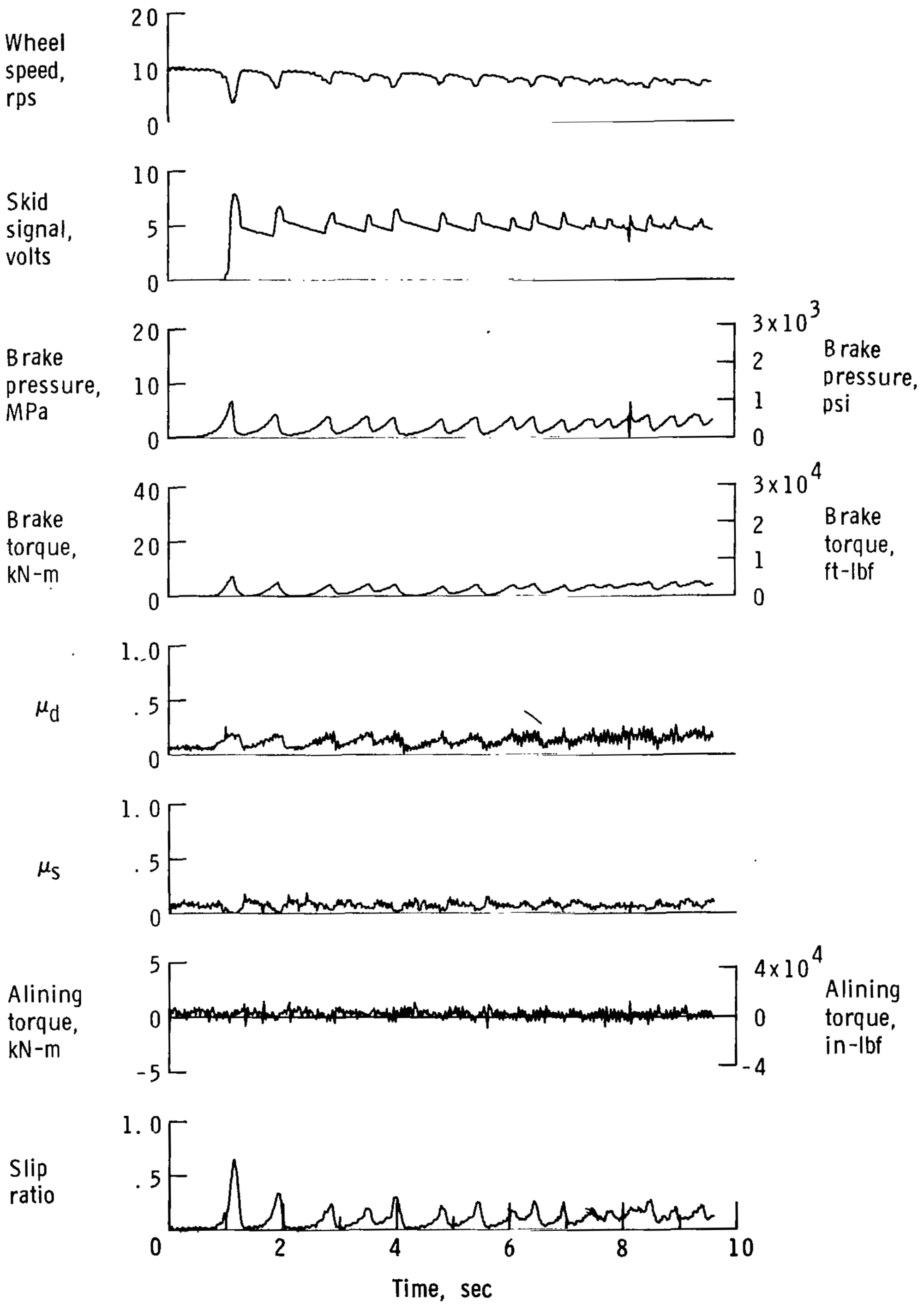

Figure A56.- Time histories for run 56; nominal carriage speed, 47 knots; vertical load, 80.1 kN (18 000 lbf); yaw angle, 6°; surface condition, flooded; tire condition, worn; brake pressure, 14 MPa (2000 lbf/in^2).

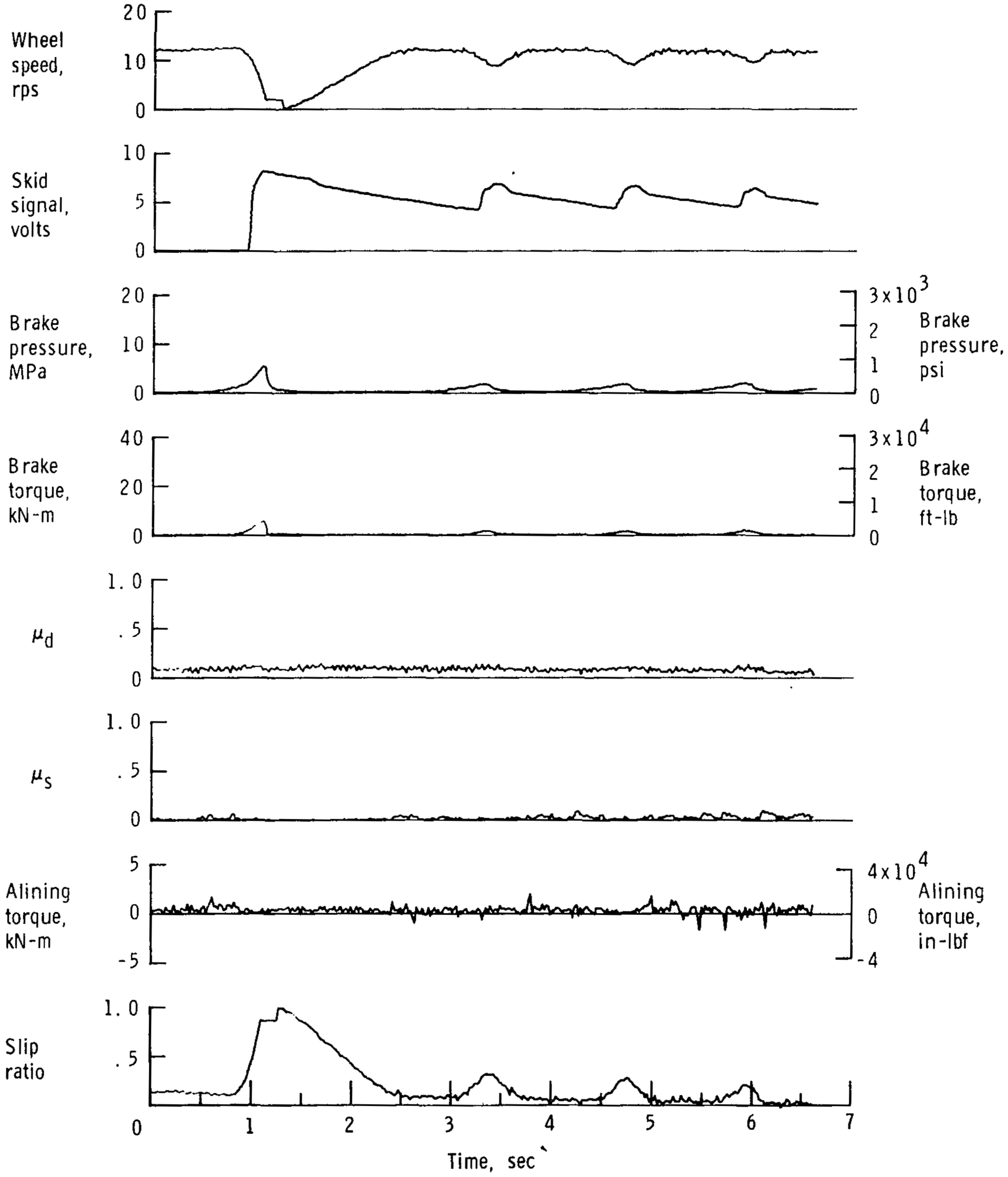

Figure A57.- Time histories for run 57; nominal carriage speed, 76 knots; vertical load, 78.7 kN (17 700 lbf); yaw angle, 6°; surface condition, flooded; tire condition, worn; brake pressure, 14 MPa (2000 lbf/in^2).

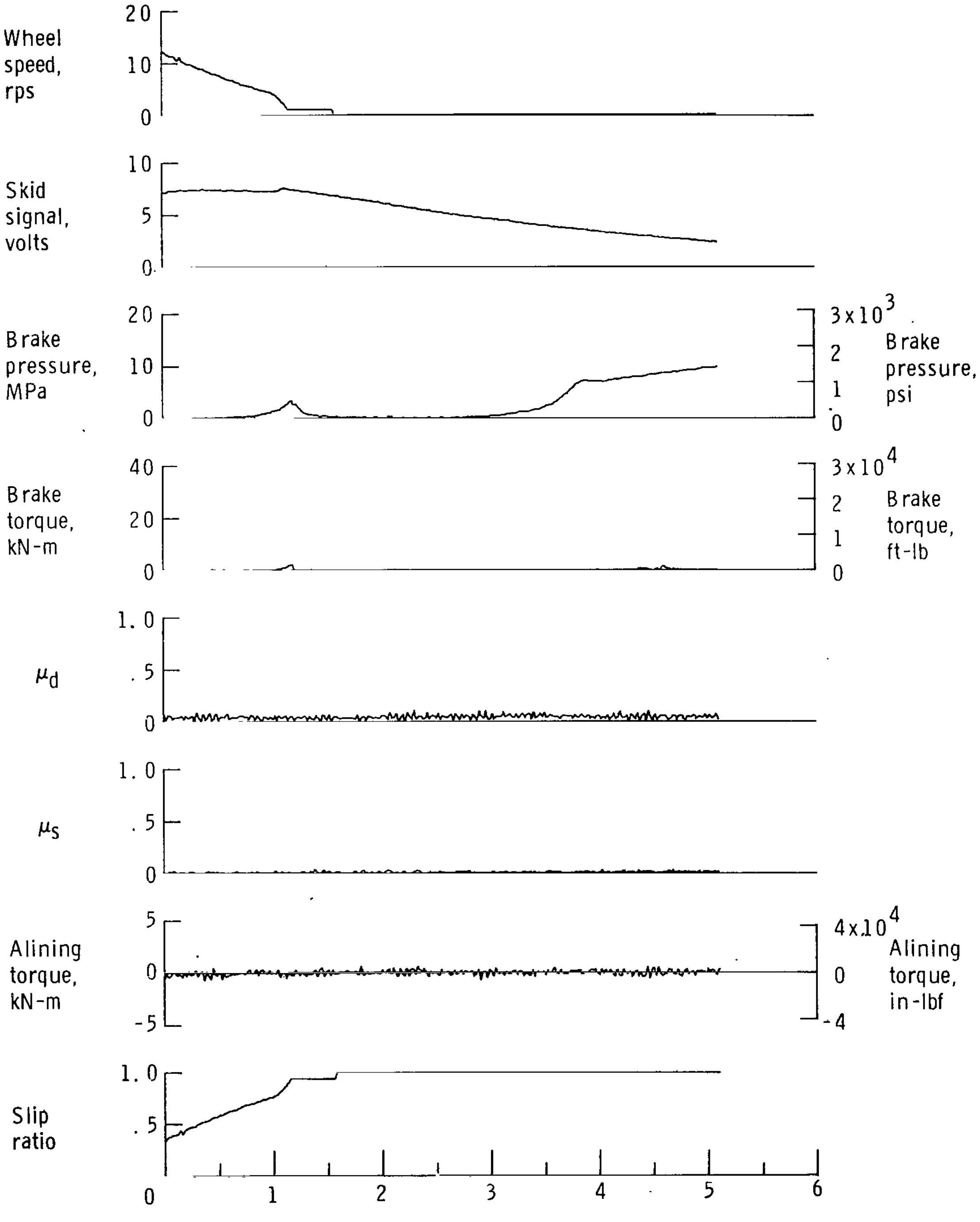

Figure A58.- Time histories for run 58; nominal carriage speed, 100 knots; vertical load, 81.4 kN (18 300 lbf); yaw angle, 6°; surface condition, flooded; tire condition, worn; brake pressure, 14 MPa (2000 lbf/in^2).

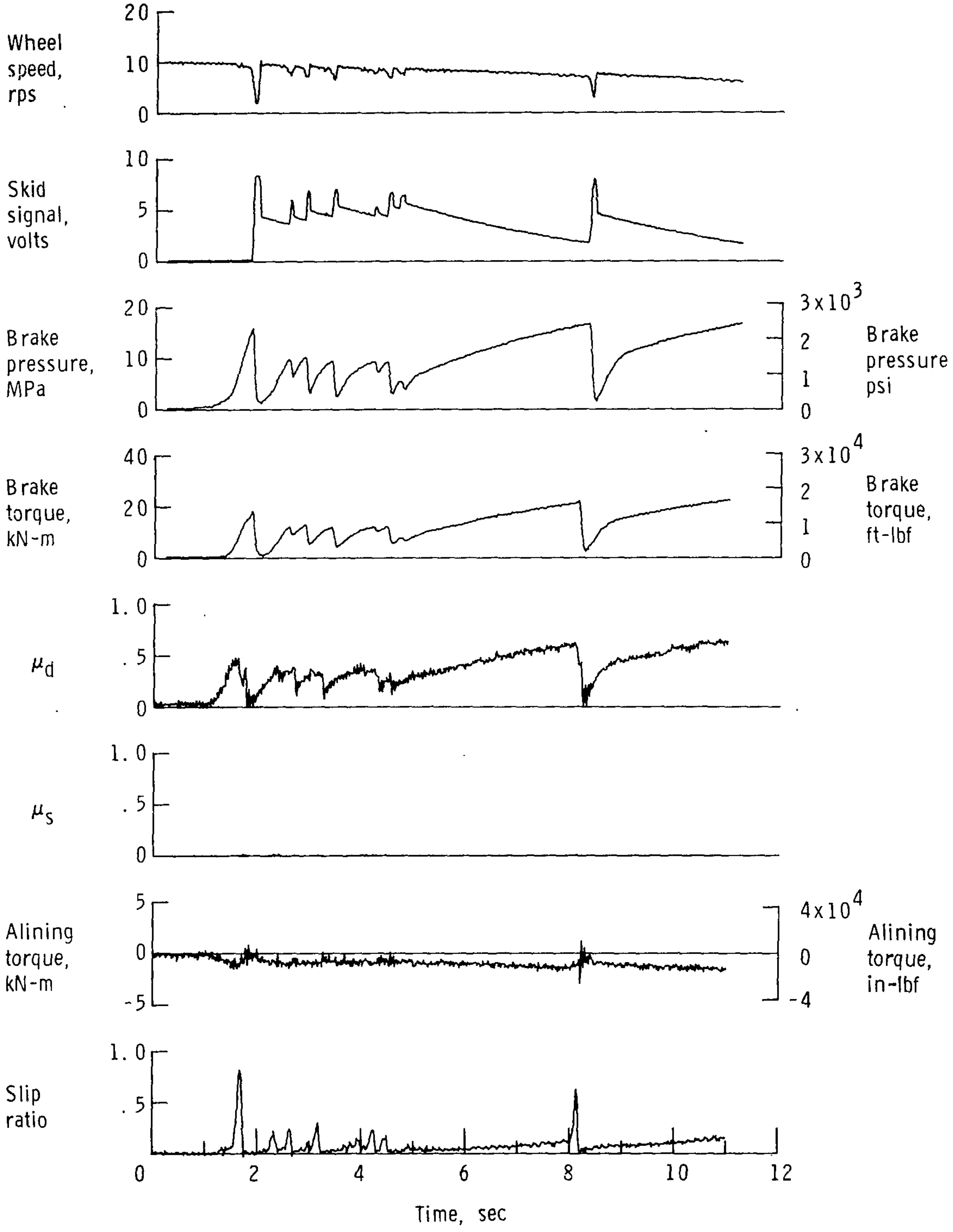

Figure A59.- Time histories for run 59; nominal carriage speed, 50 knots; vertical load, 78.3 kN (17 600 lbf); yaw angle, 0°; surface condition, flooded/dry; tire condition, new; brake pressure, 21 MPa (3000 lbf/in^2).

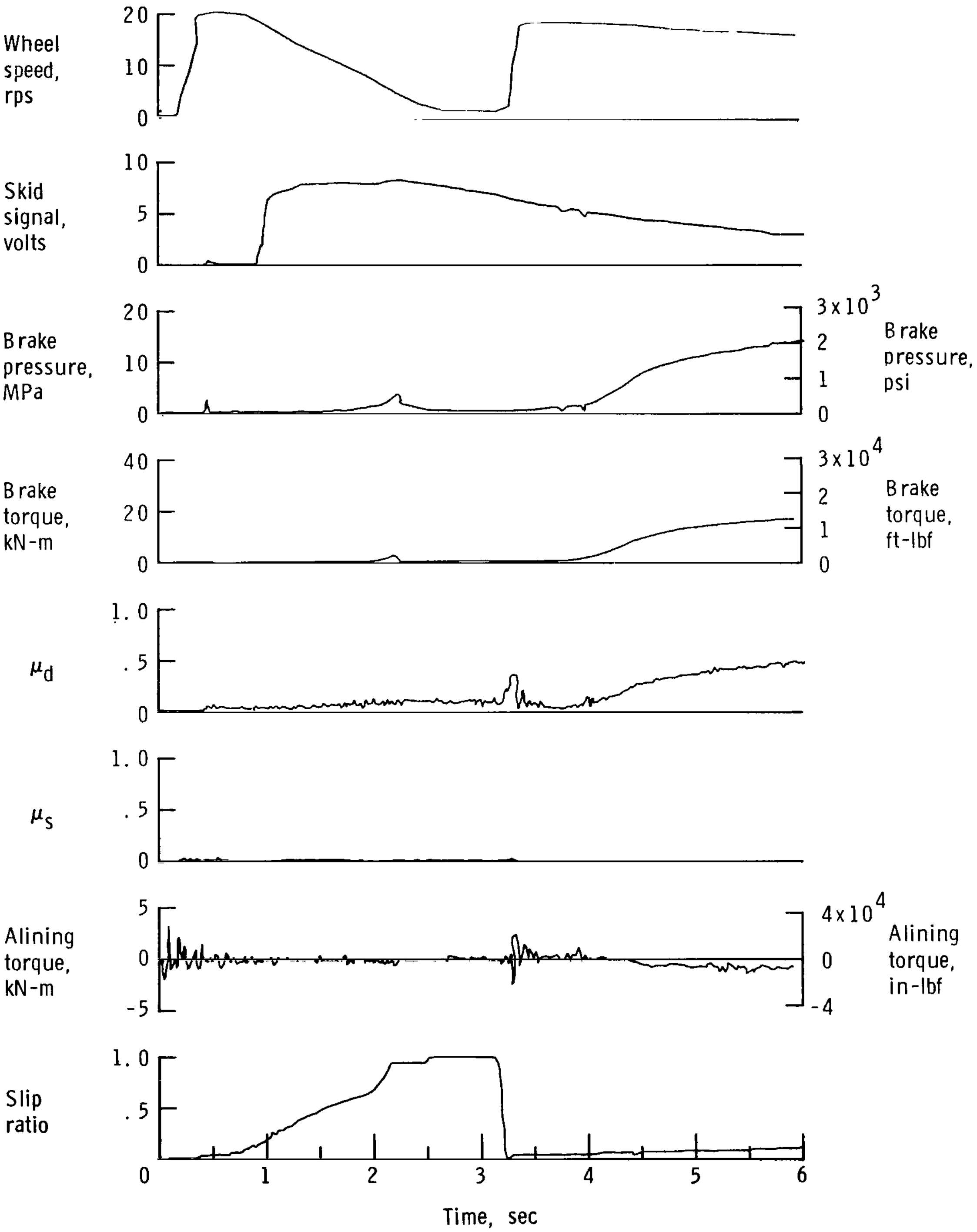

Figure A60.- Time histories for run 60; nominal carriage speed, 101 knots; vertical load, 80.1 kN (18 000 lbf); yaw angle, 0°; surface condition, flooded/dry; tire condition, new; brake pressure, 21 MPa (3000 lbf/in^2).

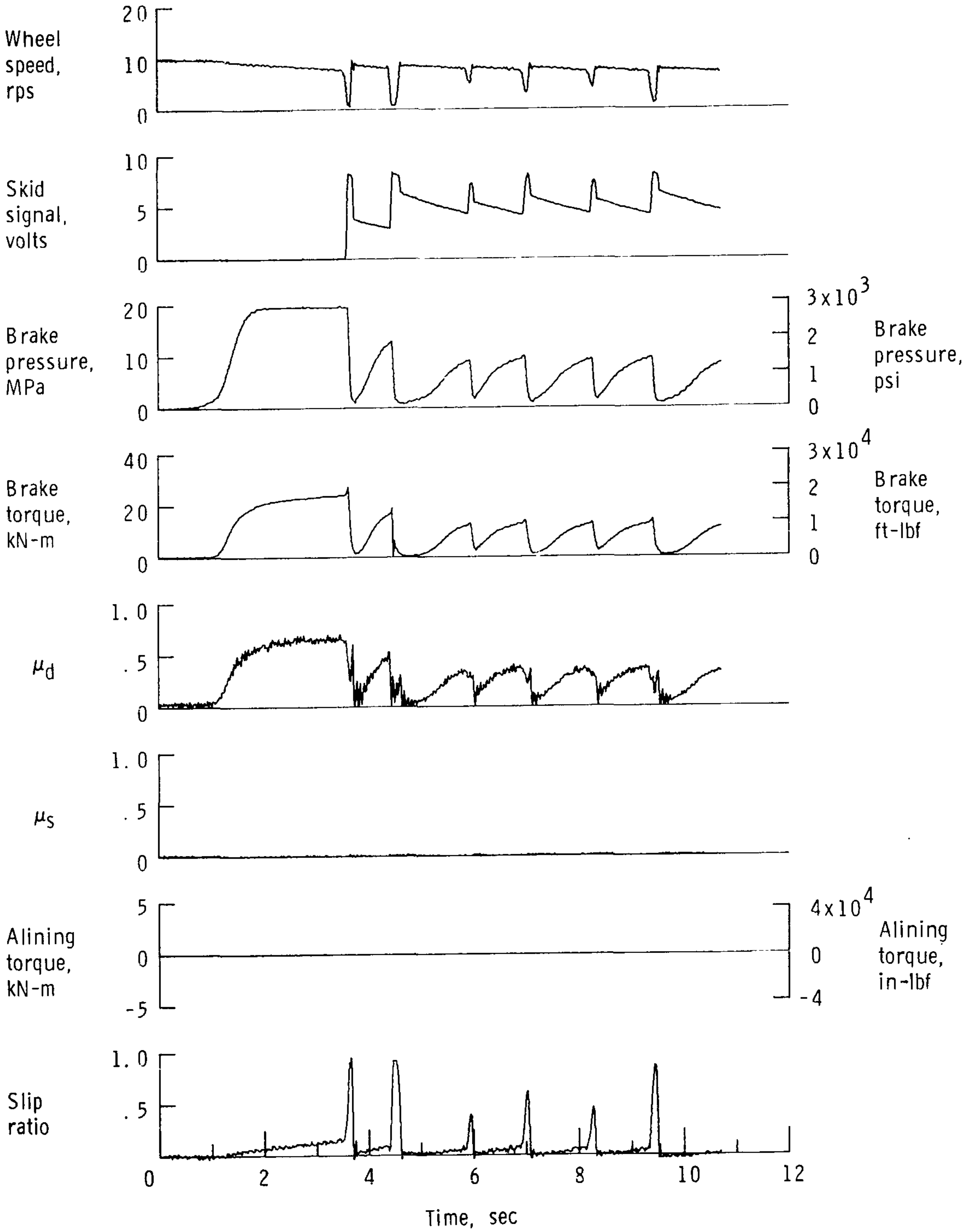

Figure A61.- Time histories for run 61; nominal carriage speed, 49 knots; vertical load, 78.3 kN (17 600 lbf); yaw angle, 0°; surface condition, dry/flooded; tire condition, new; brake pressure, 21 MPa (3000 lbf/in^2).

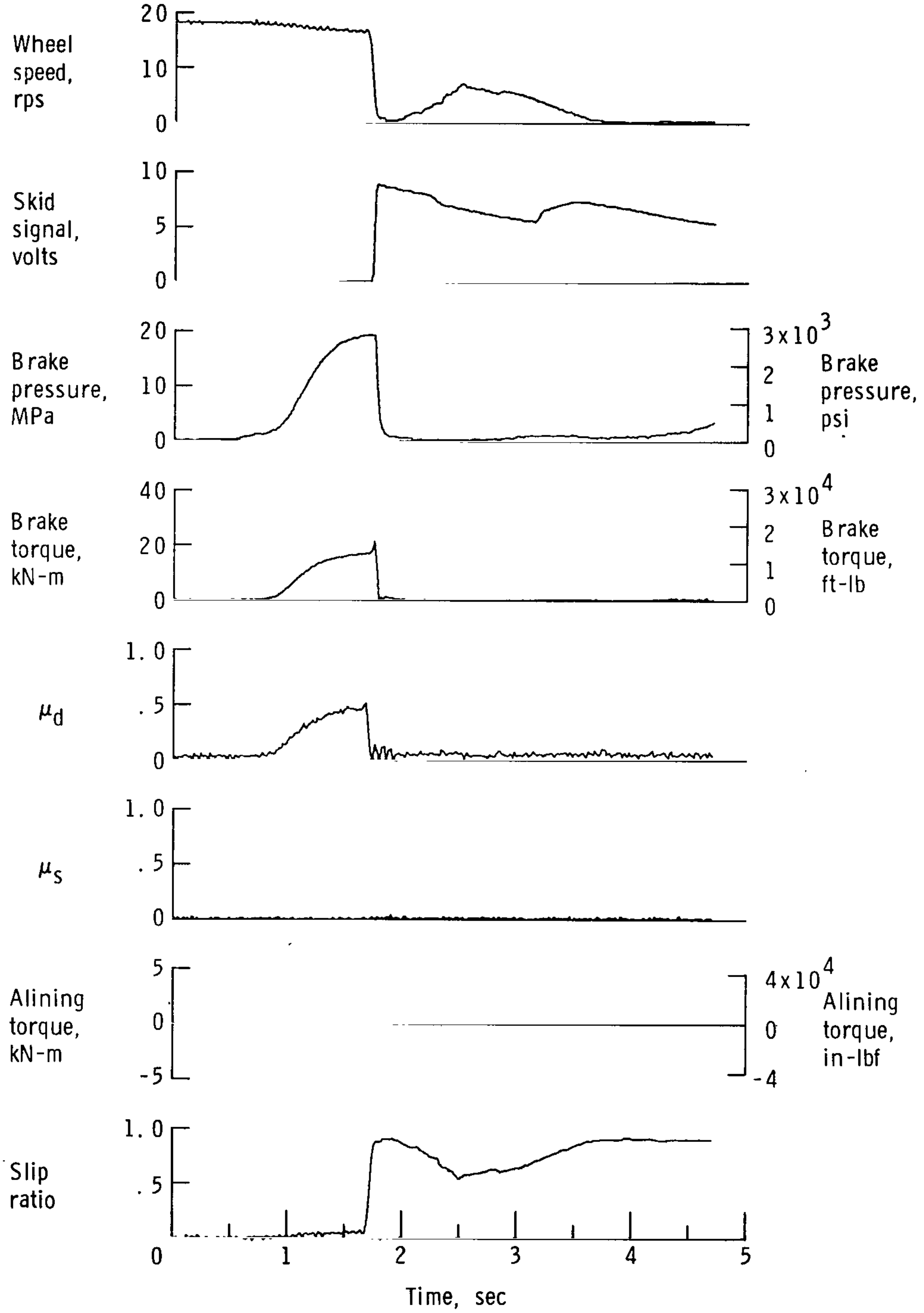

Figure A62.- Time histories for run 62; nominal carriage speed, 103 knots; vertical load, 79.6 kN (17 900 lbf); yaw angle, 0°; surface condition, dry/flooded; tire condition, new; brake pressure, 21 MPa (3000 lbf/in^2).

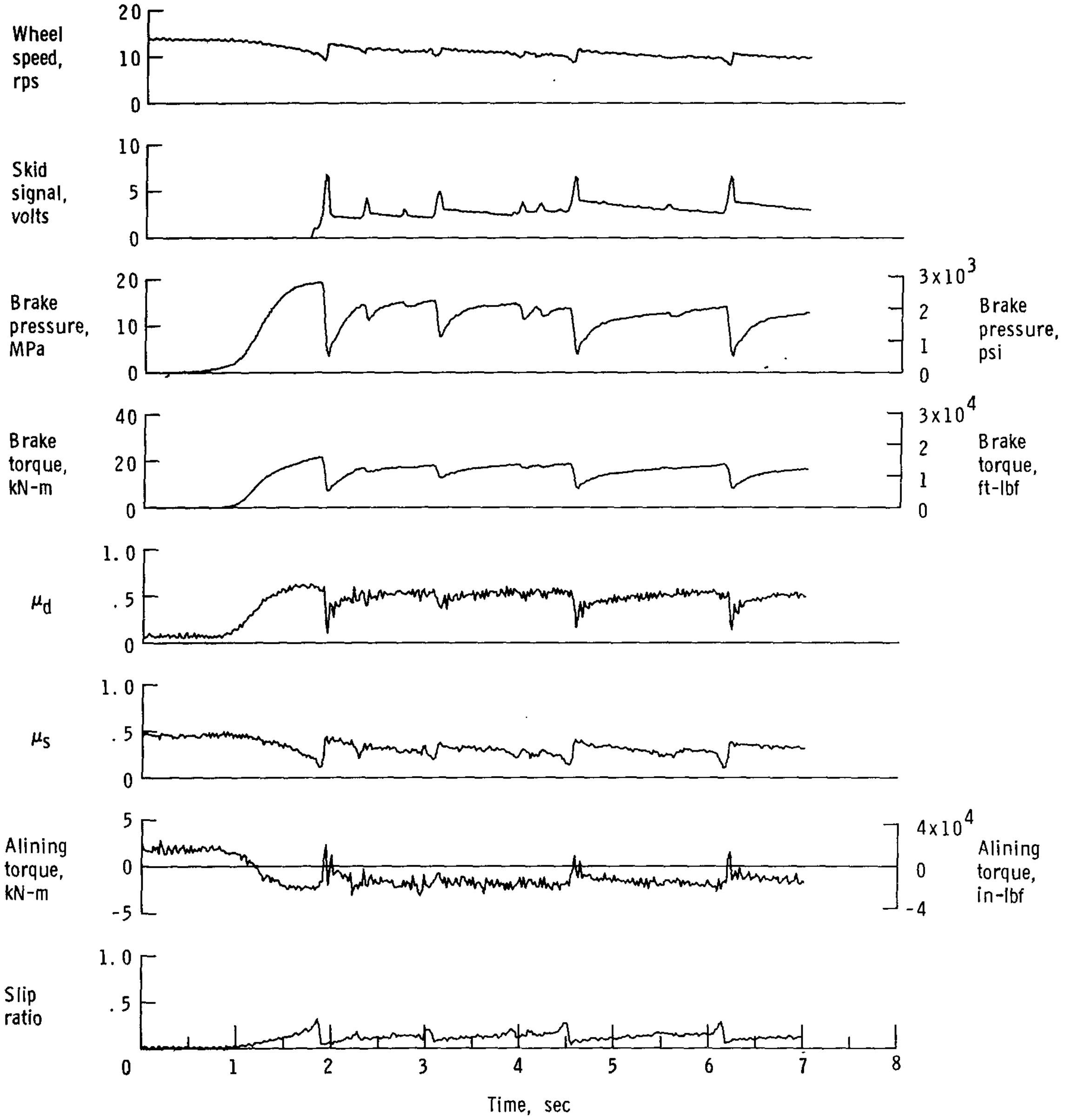

Figure A63.- Time histories for run 63; nominal carriage speed, 75 knots; vertical load, 79.6 kN (17 900 lbf); yaw angle, 6°; surface condition, dry; tire condition, new; brake pressure, 21 MPa (3000 lbf/in^2).

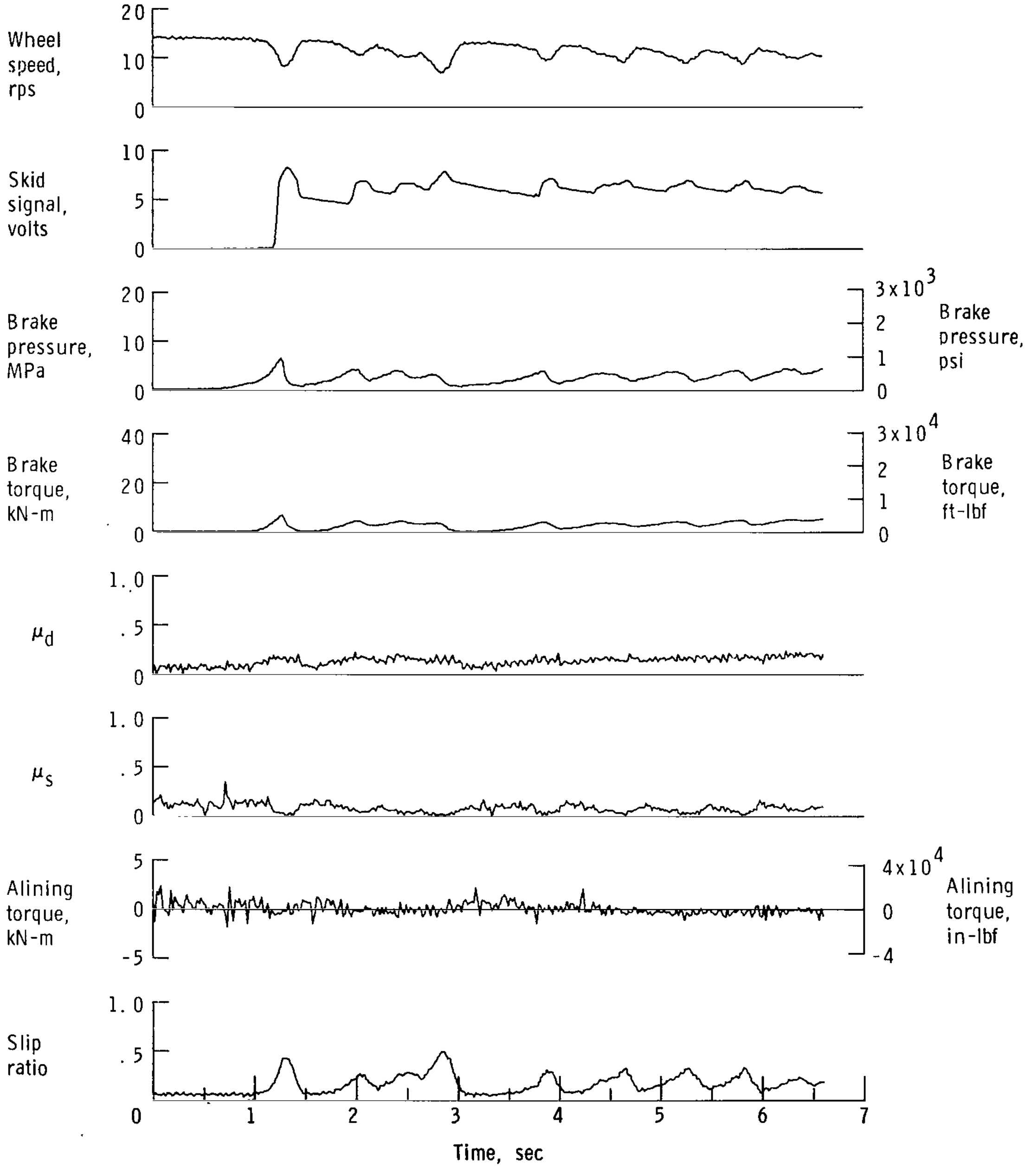

Figure A64.- Time histories for run 64; nominal carriage speed, 80 knots; vertical load, 78.3 kN (17 600 lbf); yaw angle, 6°; surface condition, flooded; tire condition, new; brake pressure, 21 MPa (3000 lbf/in^2).

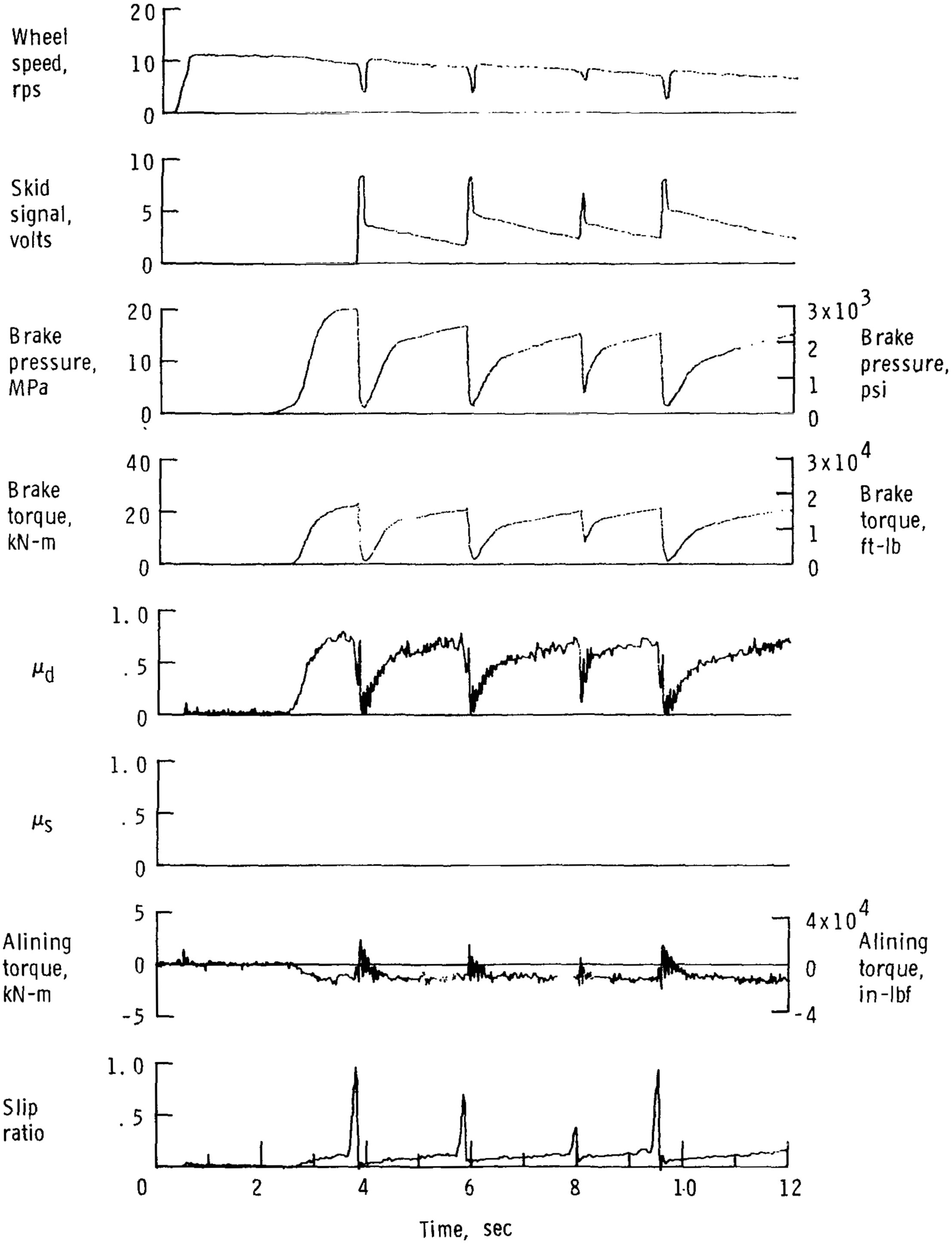

Figure A65.- Time histories for run 65; nominal carriage speed, 49 knots; vertical load, 62.3 kN (14 000 lbf); yaw angle, 0°; surface condition, dry; tire condition, worn; brake pressure, 21 MPa (3000 lbf/in^2).

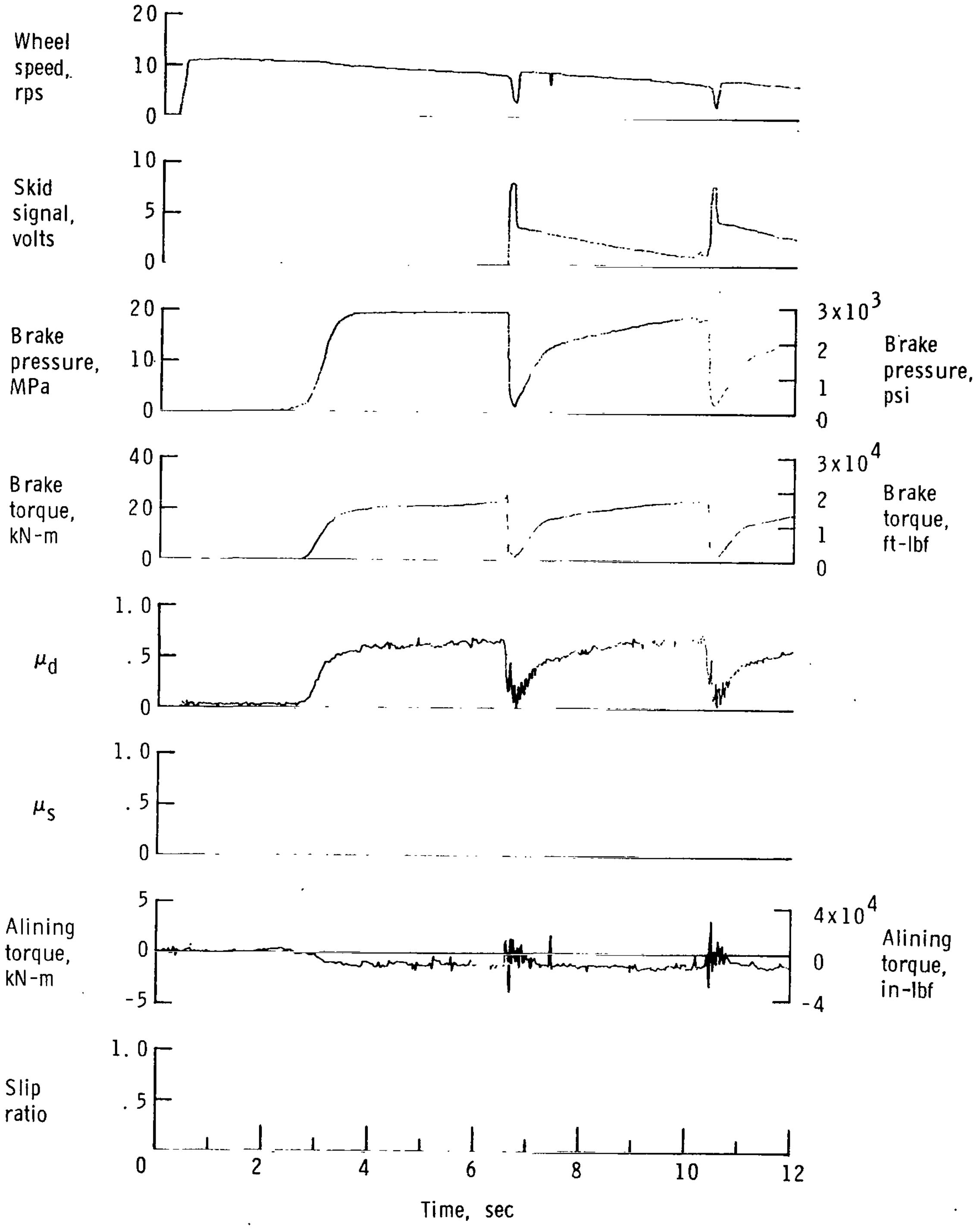

Figure A66.- Time histories for run 66; nominal carriage speed, 48 knots; vertical load, 79.6 kN (17 900 lbf); yaw angle, 0°; surface condition, dry; tire condition, worn; brake pressure, 21 MPa (3000 lbf/in^2).

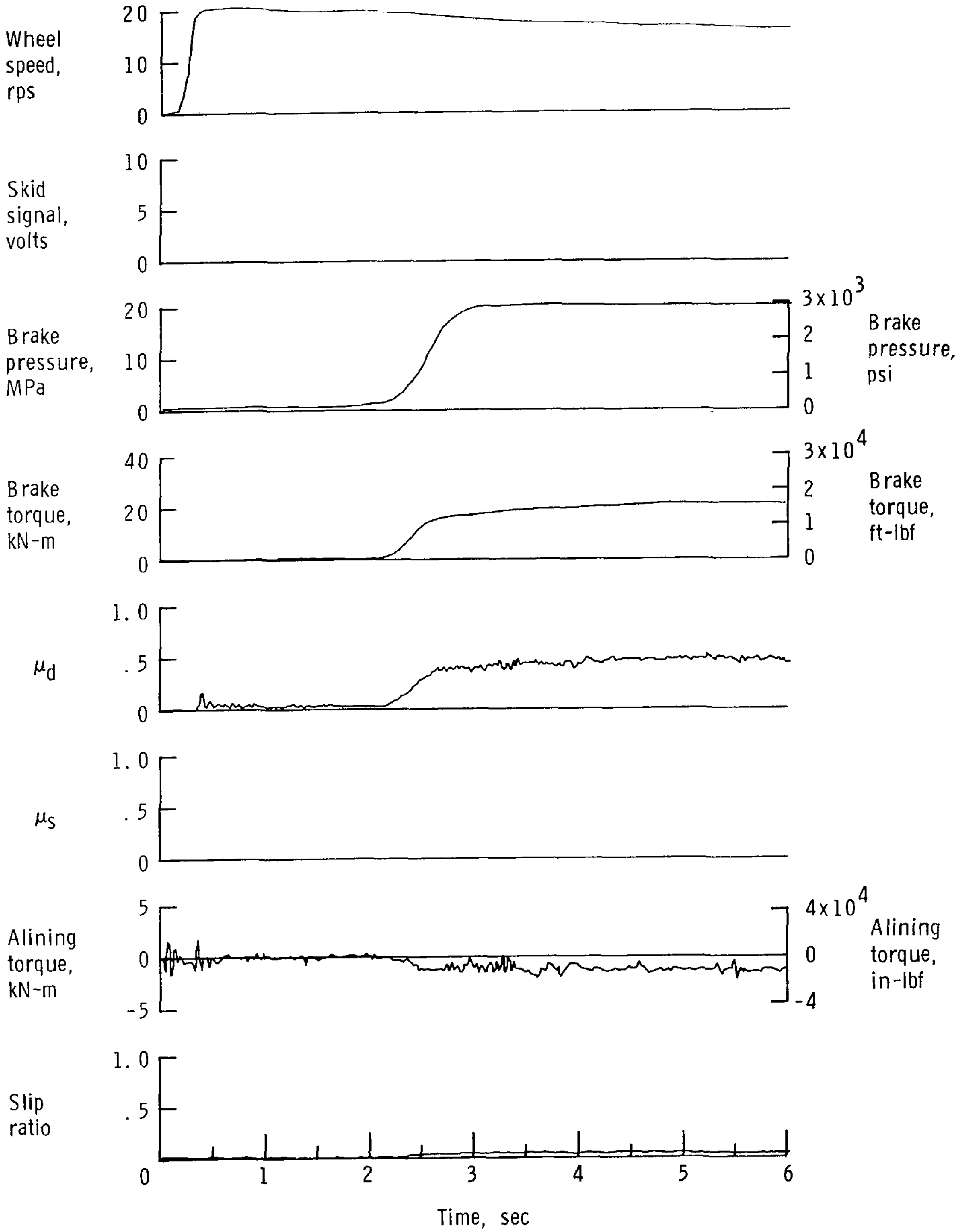

Figure A67.- Time histories for run 67; nominal carriage speed, 100 knots; vertical load, 99.6 kN (22 400 lbf); yaw angle, 0°; surface condition, dry; tire condition, worn; brake pressure, 21 MPa (3000 lbf/in^2).

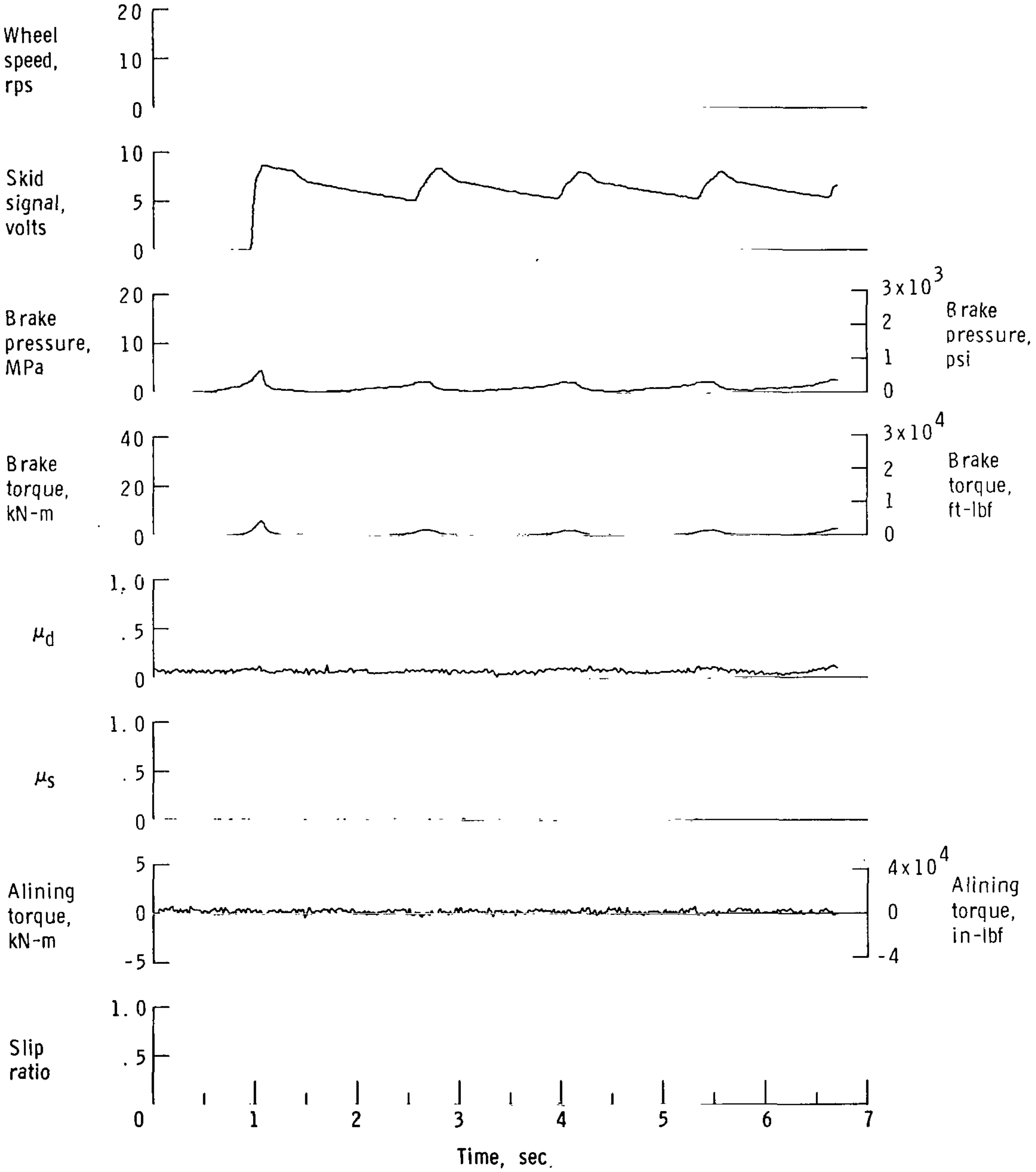

Figure A68.- Time histories for run 68; nominal carriage speed, 76 knots; vertical load, 79.6 kN (17 900 lbf); yaw angle, 0°; surface condition, flooded; tire condition, worn; brake pressure, 21 MPa (3000 lbf/in^2).

NASA-Langley, 1976 L-10976